Towards Patient-Specific Mathematical Radiation Oncology

Russell C. Rockne

A dissertation
submitted in partial fulfillment of the
requirements for the degree of

Doctor of Philosophy

University of Washington

2013

Reading Committee:

Kristin R. Swanson, Chair

Hong Qian

Jason K. Rockhill

Eric T. Shea-Brown

Nathan Sniadecki

Program Authorized to Offer Degree:
Applied Mathematics

University of Washington

Abstract

Towards Patient-Specific
Mathematical Radiation Oncology

Russell C. Rockne

Chair of the Supervisory Committee:
Professor Kristin R. Swanson
Neurological Surgery and Applied Mathematics

The war against cancer continues to take its toll on society, even after many decades of focused, intensive research into its origins and cures. Increasingly, efforts are being made to incorporate physical sciences and mathematical approaches in this battle. The term "integrated mathematical oncology" has been coined, which serves to unify the biological and quantitative sciences to bring a fresh perspective to cancer research. In this vein, mathematical modeling is beginning to serve many purposes, from providing a theoretical framework for biological hypothesis testing, to producing data-driven predictions of future disease behavior, to ultimately laying a foundation for personalized medicine.

Glioblastoma is an aggressive primary brain tumor which presents a particularly significant opportunity for personalized medicine. Glioblastoma is a diffusely invading cancer which blurs the lines between normal brain and malignant tumor. The disease is formally named glioblastoma multiforme (GBM), to emphasize the pathogenic and morphologic heterogeneity of the disease. Despite this heterogeneity, treatment options are limited and somewhat algorithmic. Nearly all patients diagnosed with GBM will receive radiation and chemo-therapy following surgery. The diverse nature of the disease combined with a 12–14 month prognosis and a "one size fits all" approach to treatment, leads to a unique opportunity for integrated mathematical oncology in the form of patient-specific modeling. I present studies and analysis of mathematical models of radiation therapy-induced DNA damage and

repair kinetics, as well as a clinically targeted mathematical model of glioblastoma growth and invasion which incorporates the effects of radiation therapy that links to the concept of personalized medicine by way of estimating patient-specific parameters in a mechanistic model.

Specifically, I present analytic solutions for a nonlinear, two-compartment ODE model of radiation-induced DNA damage and repair, which illustrates orders of magnitude differences between the linearized solution used pervasively in the literature, and the analytic solution to the fully nonlinear model. Further, data-driven parameterization of the DNA damage and repair model reveals superior model prediction and parameter stability across a wide range of experimental conditions compared to current model paradigms. I also present the implications of a patient-specific calibration of a reaction-diffusion model for glioblastoma growth. This patient-specific model is expanded to include delivery and temporally delayed response to radiation therapy to yield a predictive relationship between the net rate of proliferation and radiation sensitivity. The patient-specific radiation therapy model is expanded to include spatially and temporally defined treatment delivery and hypoxia-mediated treatment resistance. This extension advances the patient-specific radiation response model into 3D, improves model accuracy, and demonstrates a multifaceted application of patient-specific mathematical modeling for translation to the clinical setting.

TABLE OF CONTENTS

Page

LIST OF FIGURES

LIST OF TABLES

GLOSSARY

ANGIOGENESIS: the development of new blood vessels

ASTROCYTE: star shaped glial cell of the central nervous system

ASTROCYTOMA: neoplasm of the brain that originates in astrocytes

BED: biologically equivalent dose

BER: DNA base excision repair

BRACHYTHERAPY: a form of radiotherapy where a radiation source is placed inside or next to the area requiring treatment

BRAGG PEAK: a pronounced peak on the Bragg curve which plots the energy loss of ionizing radiation during its travel through matter

DSB: DNA double strand breaks

EUD: equivalent uniform dose

FLAIR: fluid attenuated inversion recovery T2-weighted MRI

GLIA: non-neuronal cells that provide support and protection for neurons in the nervous system

GLIOMA: cancer formed from glial tissue in the brain

GBM: glioblastoma multiforme. World health organization grade 4 astrocytoma.

GREY MATTER: greyish nervous tissue containing cell bodies as well as fibers; forms the cerebral cortex consisting of unmyelinated neurons

GYRUS: a ridge or fold between two clefts on the cerebral surface in the brain

LET: linear energy transfer. Energy locally imparted by radiation per unit length

LQ: linear quadratic radiation dose response model

LQL: linear quadratic linear radiation dose response model

LPL: lethal potentially lethal DNA lesions induced by ionizing radiation

MLQ: modified linear quadratic radiation dose response model

MRI: magnetic resonance image

NECROSIS: the death of a cell due to disease, injury or lack of nutrients

NEOPLASM: abnormal growth of tissue, especially a characteristic of cancer

NER: DNA nucleotide excision repair

NHEJ: non-homologus end joining

ODE: ordinary differential equation

OS: overall survival

PDE: partial differential equation

PET: positron emission tomography

PFS: progression free survival

PSP: pseudo-progression. The appearance of spontaneous resolution of imageable progressive disease following a constant course of therapy.

QUIESCENCE: a state of proliferative dormancy of a cell

RANO: response assessment in neuro-oncology

RECIST: response evaulation criteria in solid tumors

RESECTION: surgical removal

RMF: repair misrepair fixation

RPA: recursive partitioning analysis

RT: radiation therapy

RTOG: radiation therapy oncology group

SER: spherically-equivalent radius

SOBP: spread out Bragg peak is the sum of several Bragg peaks created by modulating radiation intensity

SSB: DNA single strand breaks

T1GD: T1-weighted, gadolinium enhanced MRI

T2: T2-weighted MRI

TCP: tumor control probability

WHITE MATTER: brain tissue composed of mylin-coated nerve cells

DEDICATION

to my girls

Sarah, Chloe and Ella

Chapter 1

BACKGROUND AND SIGNIFICANCE

1.1 Glioma incidence and invasion

Gliomas are primary brain tumors which are known for their ability to aggressively and diffusely invade surrounding tissue, while staying within the confines of the central nervous system [122]. Glioblastoma is the most malignant and aggressive form of glioma. Approximately 13,000 newly diagnosed glioblastoma multiforme (GBM) occur annually, with a median life expectancy of 12–15 months, representing nearly 50% of all primary brain tumors [122, 55]. Over the last 5–6 decades, progress in prolonging survival for patients with GBM has been measured in weeks to months. Perhaps the most recent survival benefit for GBM has come from the "Stupp protocol," which prescribes radiation therapy combined with alkalizing agent and radio-sensitizing temozolomide chemo-therapy, which has set the current standard of care for newly diagnosed GBM, and shown to extend median survival by a modest 2.5 months [175]. Prognostic biomarkers beyond age and mental status are scant, with MGMT promoter methylation status and 1p19q chromosome deletion in oligodendrial tumors providing increased response to chemotherapies and prolonged survival of 5–7 months [3, 109] despite extensive molecular and genetic profiling provided by the cancer genome atlas (TCGA) project [199]. Attempts to further refine prognosis such as the radiation therapy oncology group (RTOG) recursive partitioning analysis (RPA), rely on statistically defined results in groups of "similar patients" [160]. Recently, investigators have become interested in understanding the behavior of glioma dynamics in individual patients rather than the statistical behavior of groups of patients.

Dispersal of glioma cells throughout the brain has been known as being responsible for the failure of surgical resection, no matter how extensive[1], and is suspected to play a critical role in treatment failure of all varieties. Clinical decision making relies primarily on medical

[1]Even hemispherectomies have resulted in tumor recurrence [66].

imaging, which reveals only a small fraction of the diffuse distribution of tumor cells in the brain, and therefore is limited by its own threshold of detection. This leaves an unknown fraction of glioma cells invading the normal-appearing brain parenchyma peripheral to the abnormality seen on imaging. The significance of glioma growth and invasion patterns in the brain have been questioned and investigated for over 70 years [156]. This contemporary view of glioblastoma begs the question, what can be done to quantify the dispersal and proliferation rates of glioma cells in individual patients? Further, how can we use such quantitative understanding to improve current and future therapeutic strategies?

1.2 Mathematical Oncology

The term Mathematical Oncology [67] was coined in 2003 to reflect the burgeoning synergy between mathematical modeling techniques, cancer research, and clinical oncology. This concept then evolved into *Integrated Mathematical Oncology* (IMO) [8] and *Integrative Physical Oncology* [85] to more directly point to the integration of biological and mathematical approaches to a unified whole. In this vein, mathematical modeling is beginning to transition from theoretical to practical studies and serve a variety of roles in cancer research, from providing a theoretical framework for biological hypothesis testing to data-driven predictions of future disease behavior.

Mathematical models that can be tuned to reflect the disease state of an individual patient can serve as virtual controls to characterize baseline behavior of the disease. Deviations from baseline can be used to quantify response to therapy, inherent treatment sensitivity, or predict survival for individual patients, among many other applications. This patient-specific virtual control framework enables the exploration of alternative treatments that can be applied to a virtual copy of the patient's tumor and paves the way towards personalized medicine.

1.2.1 Data-driven modeling

The ethos for IMO, this dissertation work and others like it, is to produce and inform mathematical descriptions of biological processes based on observed data. While this may sound like an obvious and banal statement, it is in fact a relatively new approach to basic cancer

research which goes beyond theoretical studies in mathematics departments, evidenced by new funding calls[2] from national agencies such as the national institutes of health (NIH) and its subdivision the national cancer institute (NCI) as well as the national science foundation (NSF). The use of models to infer behavior and suggest alternate experimental strategies is the essence of hybrid research approaches which combine experiment, theory and data analysis into a single scientific inquiry.

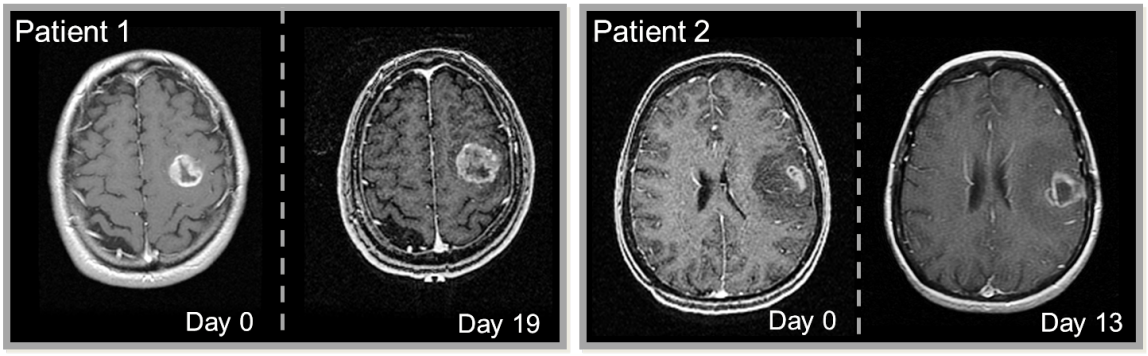

Figure 1.1: Two glioblastoma patients prior to radiation therapy. Patient 1: 48 year old male left parietal lesion. Patient 2: 53 year old female, left parietal lesion. Which of these two patients will respond to radiation therapy? How could we know? How could we predict?

1.3 Personalized medicine

My goal is to test the general hypothesis that a bio-mathematical model can assess and predict treatment response and recurrence following radiation therapy *in vivo* in individual patients. This general hypothesis lends itself to the development of novel tools which can already answer specific questions. For example, when there is recurrence in an individual patient, is it more likely to be the result of increased resistance of migrating cells that tend to be out of the proliferative cycle, or of a relatively low dose of radio- or chemo-therapy having been given that particular site? What is the quantitative importance of resistance factors such as hypoxia in individual patients relative to their dispersal characteristics?

[2]physical sciences oncology centers (PSOC), integrated cancer biology program (ICBP), tumor microenvironment (TMEN), and many more

Answers to these questions can lead to advances in treatment of individual patients. The desire to study response to radiotherapy with mathematical models is not new, with efforts dating back as early as 1972 [47]. However, contemporary clinical challenges demonstrate the limitations and failure of previous studies to translate to clinically applicable metrics of response or useful patient-specific predictions.

By predicting imageable tumor response to therapy, we can spare radiation treatment for those patients the model predicts will have little to no response. Moreover, predictive knowledge can help design more effective clinical trials and design pre-clinical studies which investigate alternate treatment scenarios. Importantly, the model can act as a virtual control against which alternate treatment approaches can be investigated for cost-benefit analysis. Progress in patient-specific modeling and the technical and logistical challenges in translating patient-specific models into clinical applications is reviewed and discussed by Neal et al. [134].

1.3.1 Clinical challenges and modeling opportunities

This thesis work is motivated by studying the human, *in vivo* clinical situation. As such, I chose to frame the research studies contained in this dissertation in the context of clinical challenges which present modeling opportunities. This helps define the scope of the problem as well as the application of the mathematical techniques, analysis and predictions to clinical situations.

Clinical Challenge: Quantifying response to radiation (and other) therapy in gliomas is hindered by significant heterogeneity in growth kinetics and response across patients. Combined with a relatively low incidence rate, heterogeneity can overwhelm the treatment effect associated with the population in modest sized clinical trials.

Model Opportunity: A patient-specific mathematical modeling approach allows us to consider metrics of response not otherwise clinically available. For example, model-predicted untreated virtual controls allow for the estimation of treatment-related metrics of survival, extending beyond the clinical assessment criteria such as the response and evaluation criteria

in solid tumors (RECIST), response assessment in neuro-oncology (RANO), or MacDonald criteria [64, 207, 138, 123]. These metrics rely on changes to observable tumor volume, typically measured with perpendicular diameters from the largest cross-section of imageable tumor. These metrics are coarse and are not prognostic or correlated with outcomes. That is, patients with higher response scores do not necessarily live longer or better than their counterparts with lower response scores. The disconnect between assessment of treatment response and prognosis has much to do with the ignorance of such metrics to tumor growth rates, which can vary by orders of magnitude within patients of the same statistical class, defined by age, performance status, and tumor location. Such approaches provide for a unique opportunity to form of a new generation of model-based metrics of response tuned to each individual patients tumor growth kinetics.

Clinical Challenge: Predictably identify patients as radio-sensitive and radio-resistant prior to therapy and quantify the sensitivity *prior to treatment*, see Figure 1.1.
Model Opportunity: I present a method to non-invasively assess and predict radio-sensitivity for individual patients prior to treatment as well as quantify disease kinetics in terms of net rates of migration and proliferation. This method provides a clinical opportunity to quantify a patient-specific radio-sensitivity using *routinely available* pre-treatment MRI data as the only inputs. The calibration of a patient-specific model to individual tumor growth and response kinetics reflects a paradigm shift in the study of cancer research and provides a novel tool for predicting, quantifying and evaluating sensitivity and response to therapy.

Clinical Challenge: Quantify local regions of environmentally driven tumor radio-resistance and recurrence following radiation therapy in individual patients.
Model Opportunity: Using 3-dimensional patient-specific simulations to quantify inherent radio-sensitivity and *in vivo* imaging data combined with patient-specific models of treatment delivery, response and resistance, we create an opportunity to infer localized treatment resistance and provide a framework for assessing treatment efficacy. For example, take two clinically similar patients with left parietal lesions, similar age and mental status,

as shown in Figure 1.1. With quantitative understanding of each patient's individual tumor invasion and proliferation kinetics, could we determine if either of these patients would see a benefit from dose escalation? How about accelerated or high dose therapy? Quantitative metrics of response, sensitivity, recurrence and growth rates can lead to patient-specific models which answer these questions *in silico* without harming the patient.

1.4 Radiation biology

The study of biological response of cells to radiation-induced DNA damage has historically focused on dose-response relationships. It is common knowledge among radiation biologists that radiation response varies across cell lines, dose rates, experimental conditions, and can be significantly influenced by hypoxia [79]. As a result, dose-response curves have been characterized under a wide variety of experimental conditions, using a wide variety of cell lines, each with a unique relationship to "predict" biological endpoints for doses outside the experimental setting.

Radiation dose-response curves have been characterized and studied since the first therapeutic uses of radiation well over 100 years ago [79]. Radiobiological parameters for dose-response models have been studied extensively and produce consistent ranges across experimental conditions. To date however, these parameters have not been calculated on a patient-specific basis *in vivo* [144]. Furthermore, there is no existing formalism for estimating these parameters from medical imaging. In this respect, the following studies are the first of their kind, and provide a novel mechanism to validate and compare experimental system results with observed *in vivo* quantities in human patients.

Mathematical models of radiation-induced DNA damage, repair, and tumor growth kinetics have been studied and compared with *in vitro* experimental data, with limited success. It is a matter of much debate as to whether or not these models are applicable for single fraction doses beyond 10–12 Gy, commonly used in some clinical treatment paradigms such as radiosurgery [111]. Further, dose-response models do not directly translate to tumor cell kill or tumor control probabilities that can be clearly applied to humans, *in vivo*. Using a reaction-diffusion model for tumor growth, combined with a biologically driven radiation

response model, we present a method for studying radiation biology *in vivo* using routinely available clinical data as inputs. Other tumor treatment modeling efforts have focused on non-clinical situations such as *in vitro* experiments or are not patient-specific due to the large number of parameters to be estimated [149, 60, 194, 172, 16].

1.5 Goldie Locks model

Not unlike the three bears of the Goldie Locks fairytale, the spectrum of models for tumor growth and response to therapy range from overly simple to unwieldingly complex: neither extreme leads to broad applicability or reasonably reflect the clinically observable reality. Simple models of exponential growth neglect the spatial distribution of the disease, and systems of several, even dozens of differential equations produce huge parameter spaces that are all but impossible to resolve within the context of an individual patient. When limiting our focus to the problem of interpreting information available to physicians caring for patients via clinical imaging, we illustrate models that may be just right.

1.5.1 Glioblastoma model

Our proliferation-invasion model for glioblastoma growth and response to radiation therapy is simple enough for parameter values to be calculated for an individual patient, yet complicated enough to model the differential migration of glioma cells throughout the brain and localized, environmentally driven treatment resistance. Our approach further benefits from the few number of parameters, which can be calculated from as few as two magnetic resonance images (MRI) routinely obtained during the course of glioma diagnosis and treatment, eliminating the estimation and exploration of large parameter domains.

1.5.2 Radiation-induced DNA damage and repair model

The repair, misrepair, fixation (RMF) model [37] of radiation-induced DNA damage and repair relies on few adjustable or biological parameters, and instead characterizes biological effect of ionizing radiation in a general framework which includes other mechanistic radiobiological models as special cases. Many of the parameters in the RMF model can be either

directly measured or estimated through radiation transport Monte Carlo simulations. The use of the RMF model as a bridge from conventional dose conformal radiation therapy to biological effect of stereotactic radiosurgery relies on the same modeling ethos employed in the proliferation-invasion model for tumor growth.

I believe these "Goldie Locks" models are *just right* in their scale, predictive value, and ultimately in their clinical applicability.

Chapter 2

DNA DAMAGE AND REPAIR MODELING

Many challenges in clinical radiation oncology can be framed as technical or scientific challenges in radiation physics or radiation biology. Translating the dose of radiation delivered into a biological effect (e.g cell death) is complicated by a variety of factors which can rarely be studied together, in *humans*. Much of our common understanding of radiation-induced effects in humans come from the study of survivors of atomic bomb induced radiation exposure in Hiroshima and Nagasaki [79, 102]. Understanding the mechanisms of action of radiation therapy is essential to a study of clinical applications of a radiation response model applied to patients. To this end, I present studies of a two-compartment ordinary differential equation model which describes the kinetics of radiation-induced DNA damage and repair, and compare this model to the long-standing empirical dose-response model for a wide range of radiation conditions, pertinent to contemporary clinical radiation oncology. Specifically, high dose per fraction treatments, such as stereotactic body radiation therapy (SBRT) and heavy charged particle therapies such as protons and carbon ions, have significant physical and radiobiological challenges associated with translating the prescribed dose into a clinically applicable measure of biological response.

2.1 Dose-response modeling

The fundamental mechanism for cell death from ionizing radiation therapy treatment is damage to DNA in the cell nucleus resulting from the deposition of energy by ionizing radiation. Highly energized particles ionize the atoms which make up the DNA, causing various forms of damage, some of the damage is repaired and the cell survives, or the damage is misrepaired and is lethal to the cell. Although response to radiation therapy goes beyond DNA damage, it is broadly considered the primary mechanism of action driving cellular responses to radiation, since damage to the DNA results in the injured cell being unable to

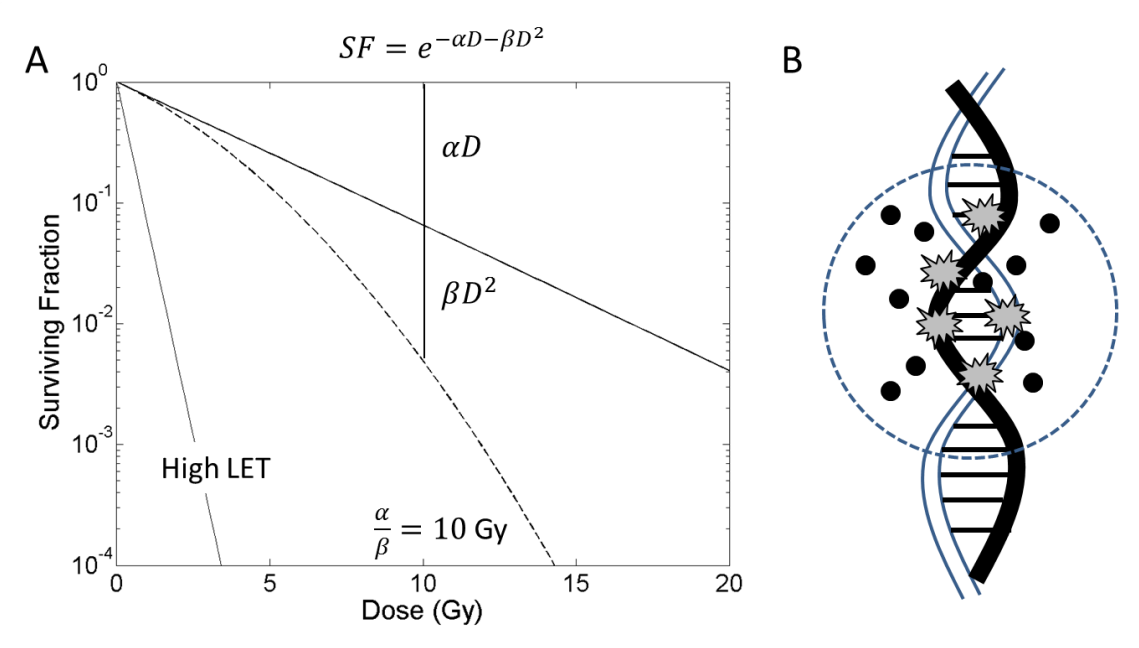

Figure 2.1: A: Surviving fraction of irradiated cells on a log scale versus absorbed dose (Gy) illustrating the linear-quadratic (LQ) parameterization of the dose-response relationship. The ratio of the LQ model parameters, α/β characterizes the steepness of the curve and is generally interpreted as being positively correlated to radio-sensitivity. Radiation with high linear energy transfer (LET) often demonstrates a log-linear relationship, without the quadratic "shoulder." B: Illustration of radiation-induced damage to the DNA.

reproduce itself during a future mitotic phase.

The linear-quadratic (LQ) model is an example of both a *mechanistic* and *empirical* dose-response model; The LQ can be derived from DNA damage and repair kinetic models [153, 30] and fits well to many experimental data sets, under a wide range of biological conditions and radiation types. Because the LQ model may be derived from mechanistic models of DNA damage and repair, utilizing different assumptions about radiation delivery, cellular response, repopulation of cells and duration of dose delivery [29, 128] (see section 2.5), inference into biological processes can be made when fitting the LQ model to dose-response data. However, these inferences and predictions are challenged in the high dose per fraction and high LET radiation situations, presenting a significant **clinical challenge** to radiobiology.

The LQ model relates the physical dose of radiation in units of Gray (Gy) which is the absorption of one joule (J) of radiation energy in one kilogram (kg) of matter, 1 Gy = $\frac{J}{kg}$ to a measure of biological effect (unitless) by the following relationship:

$$\text{biological effect} = \alpha D + \beta D^2, \quad \text{per treatment (fraction)}. \tag{2.1}$$

Let n be the number of treatments (fractions), and d be the dose per fraction, then the total dose D is given by $D = nd$, which is spatially and temporally defined, so that $d = d(x)$, and $D = D(x,t)$. In order to avoid toxic effects to normal tissue, the total dose is typically given in small doses of 1–4 Gy.

As illustrated in Figure 2.1, high LET radiation such as neutrons or heavy ions lack the "shoulder" in the dose response curve, and can be described by a purely exponential relationship between surviving fraction and absorbed dose [79]. This phenomenon motivates the physical intuition that the mechanism of action of DNA damage and repair is different for low and high LET radiations. The ratio of the LQ model parameters, α/β characterizes the steepness of the curve and is generally interpreted as being positively correlated to radio-sensitivity, so that high values of $\alpha/\beta \approx 10$ Gy represent early responding tissues such as actively proliferating tumor cells [79]. Normal tissue and other "radio-resistant" cells which have a shallower dose-response curve have a smaller value of α/β. This perspective motivates the definition of the following quantities, derived from the biological effect in Equation 2.1 :

$$\text{BED} = nd\left(1 + \frac{d}{\alpha/\beta}\right), \quad \text{and} \quad \text{relative effectiveness} = \left(1 + \frac{d}{\alpha/\beta}\right), \tag{2.2}$$

where BED stands for the biologically effective dose, and is a convenient measure of efficacy: total dose times its relative effectiveness and is often used to compare treatments with different number of fractions (n). The definition of BED also leads to the following expression of survival probability of cells exposed to a total dose dose $D(x,t)$,

$$S(\alpha, D(x,t)) = e^{-\alpha BED} \tag{2.3}$$

illustrated in Figure 2.1.

2.2 Radiation therapy for glioblastoma

Current radiation treatment options for primary brain tumors such as glioblastoma, consist of two modalities which are very different in terms of the amount of dose delivered, the distribution of dose in space, and perhaps, the biological effectiveness, illustrated in Figure 2.2 and described below.

2.2.1 Conformal external beam therapy

The current standard of care for primary brain tumors consists of post-operative chemo-radiation using "conformal" or intensity modulated radiation therapy (IMRT) with daily treatments of doses 1.8 – 2 Gy [175, 206]. The clinical target volume (CTV) is often defined relative to the gross tumor volume (GTV) and typically consists of a 2 – 3 cm margin surrounding the frank imaging abnormality to account for sub-clinical infiltrative disease. This treatment typically lasts 6 weeks, consisting of approximately 30 fractions, on a Monday—Friday treatment schedule, to a total dose of approximately 60 Gy (Figure 2.2A). The total "beam on" time required to deliver the dose in each treatment fraction is approximately 5 minutes, depending on the complexity of the treatment plan, number of beams, and location of the tumor. The daily fractionation and low dose per fraction allow for near-complete repair of sub-lethal DNA damage between treatments (inter-fraction repair), and is both a well tolerated dose for the patient and also well predicted with dose-response models such as the linear-quadratic relation.

2.2.2 Radiosurgery

The secondary radiation therapy treatment, considered "salvage therapy" after the patient demonstrates progressive disease following conformal RT, is stereotactic radiosurgery (SRS), or stereotactic body radio surgery (SBRT) [68, 152]. The spatial localization of dose is achieved through the composition of 3–5 mm spherical targets, created with multiple small beams. This is often achieved through 60Co radiation source, unlike conformal or IMRT therapy which is generated with a linear accelerator. SRS is typically high dose, single fraction treatment, with doses of up to 24 Gy or higher. Because of the highly focal target

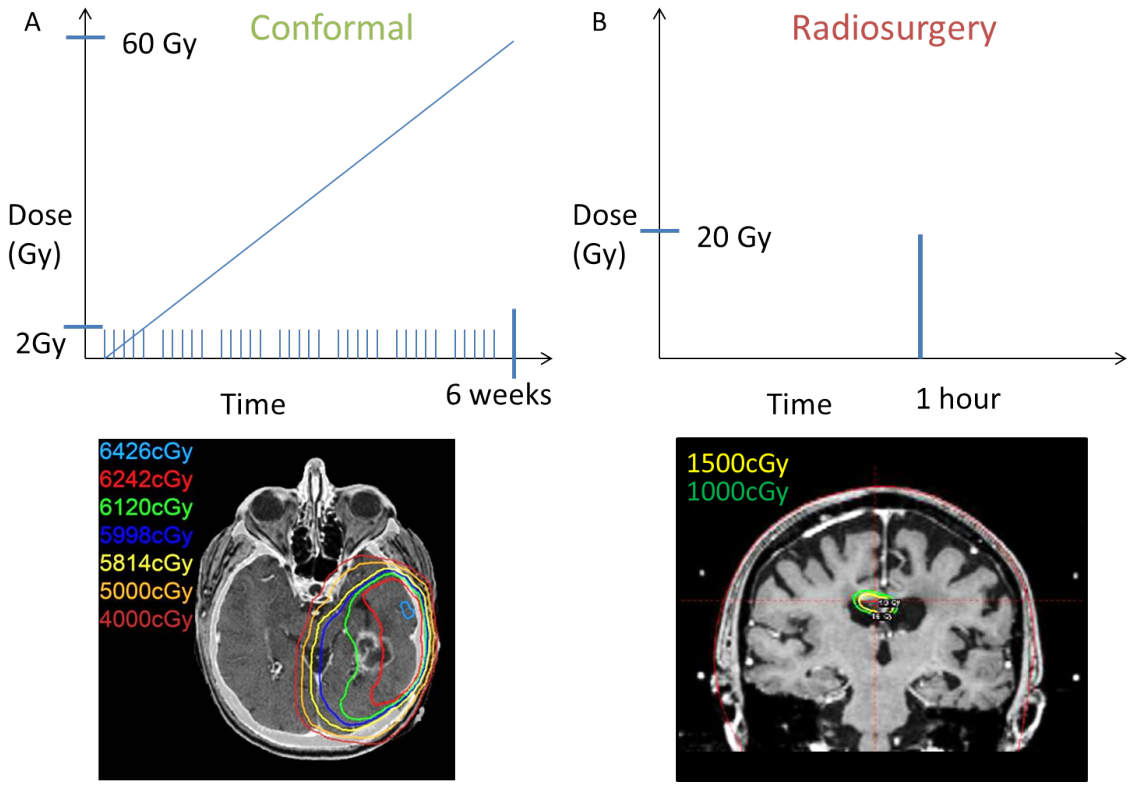

Figure 2.2: Left: Conformal radiation therapy for primary brain tumors typically consists of daily fractions up to 2 Gy over several ($\approx$ 30) fractions to a total dose of 60 Gy. Right: Stereotactic radiosurgery typically consists of a single high dose treatment of up to 24 Gy or higher to a highly focused target.

dose composition, the dose in the treatment volume is often constrained by defining the volume which represents the 50% isodose surface, which permits up to twice the amount of prescribed dose within the treatment volume. Dose delivery "beam on" time can range from approximately 15 minutes for small tumors/target volumes ($<$ 8 cm^3) up to approximately 45 minutes for larger targets ($>$ 8 cm^3, $\approx$ 2 cm diameter), although this can vary with the equipment used to deliver the treatment.

Clinical challenge Use of the linear-quadratic model in the SRS dose regime is a controversial topic, highlighted by a recent point-counterpoint debate in the radiation biology literature [111].

One side of the argument is that the linear-quadratic dose-response model loses validity

to predict biological response to radiation doses above approximately 10 Gy. Arguments for fundamentally different dose-response based biological effects in this high dose regime are often based on the reasoning that radiosurgery doses are ablative to the tissue and may alter one or more of the four R's of radiobiology: repair, reoxygenation, re-assortment into the cell cycle and repopulation. Further, the mechanisms underlying DNA damage may be fundamentally different in this dose regime, due to the biological processing of radiation-induced DNA damage during prolonged treatment delivery times.

On the other side of the argument, dose-response curves continue to demonstrate linear-quadratic behavior, and the cell survival data can be fit just with the LQ model as well beyond 10 Gy as it can below [28], although sometimes with the addition of extra terms to the linear-quadratic equation which are not directly connected to mechanistic rationale [76]. One approach to understanding the physical mechanisms underlying changes in the dose-response curve beyond single fractions of 10–12 Gy is through a DNA repair formalism and mathematical modeling of DNA damage and repair kinetics.

2.3 Repair, Misrepair and Fixation (RMF) model

Several formalisms of radiation-induced DNA damage and repair kinetics exist, on scales ranging from single ionization events to large populations of cells, reviewed in [60, 91, 129]. At the cellular scale, models such as the lethal potentially-lethal (LPL) and linear-quadratic-linear (LQL) [75, 155] use ordinary differential equations to model repairable and fatal radiation-induced DNA damage. The repair misrepair fixation (RMF) model illustrated in Figure 2.3 is a generalization of these models, proposed by Carlson and Stewart [37].

The RMF model The RMF model (Equations 2.4 and 2.5) considers two forms of radiation-induced DNA damage: sub-lethal, potentially rejoinable double strand breaks (DSBs), the number of which is denoted $L(t)$, and lethal DSBs, denoted by $F(t)$. This model considers multiple pathways of DSB formation and repair, including pairwise chromosome interactions formed by single or multiple radiation tracks and follows chromosome breakage and reunion theory [91], where radiation-induced double strand breaks produce chromosome aberrations, such as translocations, ascentric fragments, and dicentric rings,

illustrated in Figure 2.4. The kinetics of DSB induction and repair are described with ordinary differential equations [154]. The RMF model equations are given by:

$$\overbrace{\frac{dL}{dt}}^{\substack{\text{rate of change}\\ \text{of potentially}\\ \text{rejoinable DSBs}}} = \overbrace{f_R \Sigma \dot{D}(t)}^{\substack{\text{creation of}\\ \text{potentially}\\ \text{rejoinable DSBs}}} - \overbrace{(\lambda + \eta f_R \bar{z}_F \Sigma)\, L(t)}^{\substack{\text{first order}\\ \text{non-lethal repair}}} - \overbrace{\eta L^2(t)}^{\substack{\text{second order}\\ \text{non-lethal repair}}} \tag{2.4}$$

$$\overbrace{\frac{dF}{dt}}^{\substack{\text{rate of change}\\ \text{of fatal DSBs}}} = \overbrace{(1 - f_R)\Sigma \dot{D}(t)}^{\substack{\text{creation of}\\ \text{intrinsically}\\ \text{fatal DSBs}}} + \overbrace{(\theta\lambda + \gamma\eta f_R \bar{z}_F \Sigma)\, L(t)}^{\substack{\text{fatal first order}\\ \text{misrepair}}} + \overbrace{\gamma\eta L^2(t)}^{\substack{\text{fatal second order}\\ \text{misrepair}}} \tag{2.5}$$

$$L(t=0) = 0, \quad F(t=0) = 0. \tag{2.6}$$

The model involves 7 parameters: 2 of them are related to the physical properties of the radiation beam, one is included for the sake of generality, and 3 are "adjustable," and biologically driven, summarized in Table 2.1. The parameters Σ, representing the number of DSB per Gy per cell, and $\bar{z}_F$, the frequency-mean specific energy of the radiation (Gy), are determined by the linear energy transfer (LET) of the radiation. The instantaneous radiation dose rate (Gy/hr) at time t is given by $\dot{D}(t)$. A total of $\Sigma\dot{D}(t)$ DSBs are instantaneously created in time dt at the time of the dose, a fraction of which are potentially rejoinable f_R, and the remaining are lethal $(1 - f_R)$. This is to incorporate the concept of "intrinsically fatal" damage and is included primarily for the sake of generality. Repair rate constants λ (/hr), η (L/hr) describe rates of repair and pairwise interactions between DSBs, respectively. The relative sizes of these rate constants is particularly important since they determine the weighting of the linear and quadratic terms in the rate of change of DSB repair and fixation. Specifically, the repair constant λ is the sum of the repair and fixation rate constants, so that $\lambda = \lambda_R + \lambda_F$.

The accumulation of lethal DSB damage, $F(t)$ is given by Equation 2.5. Parameters γ and θ represent proportions of DSB damage which are lethal and non-lethal. The parameter

Parameter	Value	Meaning
λ (1/hr)	**estimated**	1st-order DNA repair rate
Σ (DSBs/Gy/Gbp)	Monte Carlo radiation transport simulation [158]	Number of DSBs per giga-basepair (Gbp) of DNA
$\bar{z}_F$ (Gy)	calculated from LET [37]	Frequency-mean specific energy. Energy deposition in the cell nucleus
η (L/hr)	**estimated**	Binary interaction rate
f_R (%)	1 [37]	Fraction of DSBs that are potentially rejoinable
θ (%)	**estimated**	Proportion of incorrectly rejoined DSBs that are fatal
γ (%)	1/2 [37, 102]	Proportion of incorrectly rejoined DSBs that are fatal

Table 2.1: Parameters of the repair misrepair fixation (RMF) model of radiation-induced DNA damage. Three free parameters are biologically based (λ, η, θ) and are estimated from fitting the model to dose-response data for various cell lines and radiation types. Three parameters are driven by the physical properties of the radiation being delivered ($\Sigma, \bar{z}_F, f_R$).

θ includes a weighted proportion of repaired and fixed damage as

$$\theta = \frac{(1-a)\phi\lambda_R + \lambda_F}{\lambda}. \tag{2.7}$$

f_R is the fraction of DSBs that are potentially repairable, with a and ϕ proportion constants which are not investigated here.

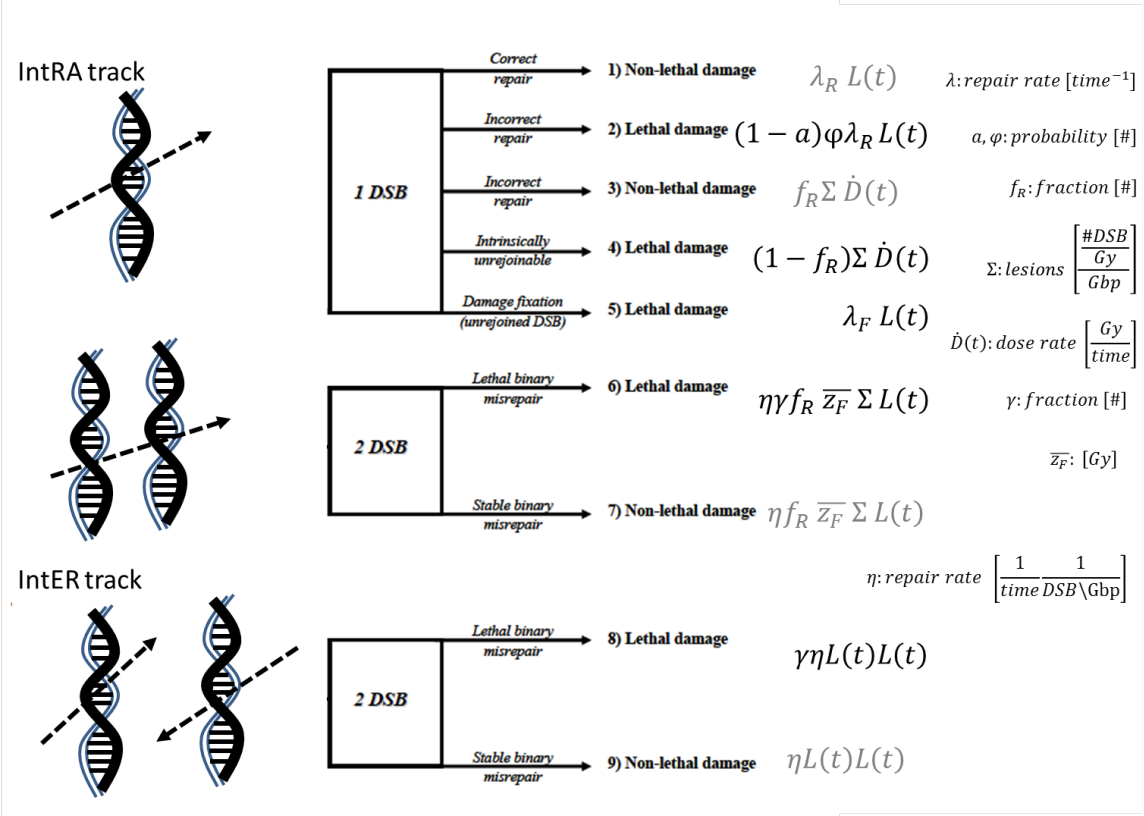

Figure 2.3: Repair misrepair fixation (RMF) model schematic. DNA double strand breaks (DSBs) arise from inter- and intra-track ionization events, which will vary with particle type, energy, and properties of the radiation beam. Lethal misrepair terms of the model are in black, potentially rejoinable DSBs and non-lethal repair is in grey. Brackets $[\ \cdot\ ]$ denote dimensional units of the model parameters. The passive "$R(t)$" class of DSBs which are not potentially rejoinable and non-lethal is not shown. Adapted from Carlson 2006 [35].

2.3.1 Model assumptions

The number of DNA DSBs within a cell population can be modeled as a compound binomial distribution, with each cell representing an independent random variable, with a binomial distribution of DSBs within that cell, as presented in Carlson 2008 [37]. For large numbers of DSBs in a cell, as the case particularly in low LET radiation, the compound binomial approaches a compound Poisson distribution. That is, if we let $p(L)$ denote the probability that exactly L rejoinable DSBs are induced in the DNA of a cell nucleus, then the rate at which DNA break ends associated with two different DSBs are incorrectly rejoined to each other is given by $\eta L(L-1)$, where η is the probability per unit time that break ends interact in pairwise fashion. If we consider the number of breakends in the cell as a distribution, then the expected rate of pairwise DSB rejoining is simply the expectation of the product,

$$\mathrm{E}[\eta L(L-1)] = \eta(\mathrm{E}[L^2] - \mathrm{E}[L]). \tag{2.8}$$

Let δ be the average number of radiation tracks passing through the nucleus of a cell, and let n be the average number of times a radiation track crosses a DNA segment, let Ψ be the probability that a DSB occurs in the DNA segment after a particle crossing. Then the product $n\delta\Psi$ represents the average number of DSBs per Gy per cell. The average number of radiation tracks passing through the cell equals the absorbed dose divided by the frequency-mean specific energy, $\delta = D/\bar{z}_F$ [37]. If the initial distribution of DSBs among a uniformly irradiated population of cells has a compound binomial distribution, with a variance

$$\sigma^2 = n(n-1)\delta\Psi^2 + n\delta\Psi \tag{2.9}$$

then as n becomes large, $n(n-1) \to n^2$, and the compound binomial distribution reduces to a compound Poisson distribution with variance

$$\sigma^2 = n\delta\Psi(1 + n\Psi). \tag{2.10}$$

The expected number of potentially rejoinable DSBs per track is $f_R n\Psi = f_r \bar{z}_F \Sigma$. We assume that the distribution of the number of rejoinable DSBs in a cell is proportional to the initial number of DSBs per cell,

$$\mathrm{E}[L] \approx f_r n\delta\Psi = f_r \Sigma D \tag{2.11}$$

so that the expected rate of pairwise DSB rejoining is given by

$$\mathrm{E}[\eta L(L-1)] = \eta \mathrm{E}[L](\mathrm{E}[L] + f_r \bar{z}_F \Sigma). \tag{2.12}$$

Therefore, the product $\eta f_r \bar{z}_F \Sigma \mathrm{E}[L]$ denotes intra-track pairwise DSB interaction, and $\eta \mathrm{E}[L]\mathrm{E}[L]$ denotes inter-track pairwise DSB repair and misrepair interactions, found in Equations 2.4 and 2.5 for $L(t)$ and $F(t)$ in the RMF model, respectively.

The RMF model has several advantages over other models for radiation-induced DSB creation and repair, namely

1. Few purely adjustable parameters. The quantities $\bar{z}_F, \Sigma$ and γ can be either directly computed, measured, or estimated from physical first principles. Specifically, the frequency-mean specific energy $\bar{z}_F$ can be estimated using the LET of the radiation being used, related to the diameter of a cell. The parameters f_R and Σ can be estimated using Monte Carlo simulations of radiation transport such as the MCDS algorithm [158]. The probability that a binary interaction will be fatal (γ) is idealized to be 1/2, based on the assumption that one lethal dicentric or centric ring is formed from each nonlethal translocation [102]. This leaves repair rate constants λ and η and the proportion of fatally misrepaired DSBs (θ) as adjustable parameters, which are biologically based.

2. The RMF model includes other models as special cases for certain choices of parameters. This provides a generality and framework for investigating a broad class of biological and radiation-driven questions, and enables direct comparisons with other model paradigms, to investigate the *minimum models* needed to describe the phenomenon of interest.

Although no model can include everything involved in complex biological processes, a few obvious limitations exist to the approach presented with the RMF ODE formalism. One such limitation lies in spatial proximity effects in the chromosome breakage and reunion theory which underlies the model. The rate constant governing the pairwise rejoining of DNA DSBs (η), may be a function of space depending on the physical orientation of the

chromosomes within the cell nucleus relative to interactions within and between radiation tracks. Chromosomes which are spatially co-aligned which both experience DNA cleavage from the result of multiple radiation track injury may be more likely to incorrectly rejoin as chromosomes which are distant from each other [91]. Further, the RMF model does not include environmental variables which can cause cell death and may be connected to such phenomenon as the "bystander effect" in which cells not directly exposed to the radiation beam undergo apoptotic or necrotic cell death.

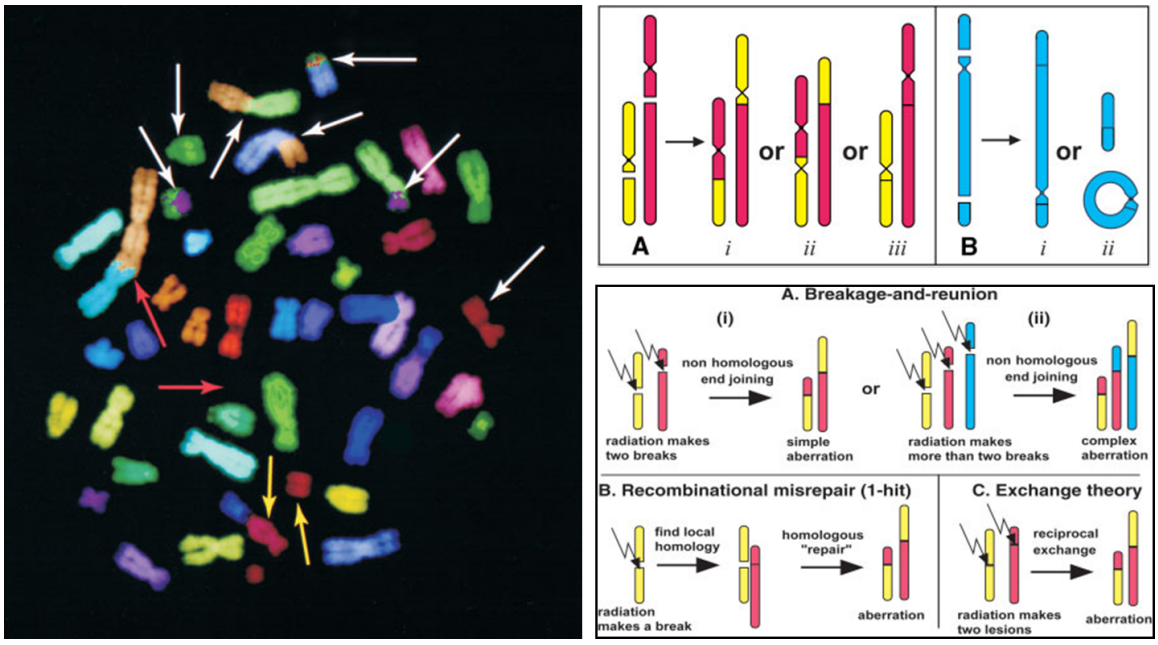

Figure 2.4: DNA breakage and reunion theory which underlies the assumptions of the RMF model. Radiation-induced chromosomal aberrations are visualized with a multispectrum fluorescent in situ hybridization (FISH) technique, revealing ascentric fragments, dicentric rings and translocations. Some chromosomal aberrations are repairable, with repair or misrepair leading to either cell survival or cell death. Adapted from Hlatky et al. 2002 [91].

2.3.2 Conservation of DSBs

Since all damage must be fatal, potentially fatal, or non-fatal, let us introduce the number of non-fatal DSBs that are not potentially repairable, $R(t)$. Since the total number of

instantaneous DSBs induced by radiation dose D in time dt is given by $\Sigma\dot{D}(t)$, we have

$$\frac{d}{dt}\left(L(t)+F(t)+R(t)\right)=\Sigma\dot{D}(t). \tag{2.13}$$

This implies that the rate of change for the non-fatal, non-potentially rejoinable DSBs should include the proportion of DSBs that do not become lethal and do not stay potentially rejoinable,

$$\overbrace{\frac{dR}{dt}}^{\substack{\text{rate of change}\\ \text{of non-fatally}\\ \text{repaired DSBs}}} = \overbrace{\left[(1-\theta)\lambda+(1-\gamma)\eta f_R\bar{z}_F\Sigma\right]L(t)}^{\substack{\text{non-fatal}\\ \text{first order repair}}} + \overbrace{(1-\gamma)\eta L^2(t)}^{\substack{\text{non-fatal}\\ \text{second order repair}}} \quad . \tag{2.14}$$

It would be in good form to give proportion constants to each class of DSB, for example, $f_R,\ f_F,\ f_L$ if we were to study these quantities. Optimistically, we will assume all DBSs are potentially rejoinable and there are no intrinsically fatal DSBs, so that $f_R \equiv 1$, eliminating the need for additional parameters. However, if $f_R \neq 1$, some DSBs are intrinsically unrejoinable. This can be a surrogate for DSB complexity, and could be related to damage resulting from high LET radiations, although we will later show this is assumption is not necessary in order to predict high LET dose-response relationships.

2.3.3 Dose rate functional forms

For most forms of external-beam radiation therapy treatment, the average dose rate is effectively held constant by the treatment delivery machine. In the case of external beam treatment delivered via linear accelerators, the average dose rate can be computed as

$$\dot{D}(t)=\frac{dD}{dt}=\frac{\Delta D}{\Delta t} \tag{2.15}$$

where ΔD represents the total dose administered in the treatment fraction, and Δt is the net sum total time the radiation beam is "on," excluding set-up and beam repositioning time. This differs from the *instantaneous* dose rate, defined by the net flux of radiation through a fixed area, which can vary spatially and temporally based on the specifications

of the radiation treatment, field design, number of beams, attenuation effects of nearby tissue, etc. Figure 2.5 illustrates a piecewise constant dose-rate function with three different treatments, each with their own dose rate and dose delivery time to illustrate the "on-off" nature of this form of treatment, although practically speaking, the dose rate and dose delivery times would not change for a specific patient over the course of their treatment.

Although constant dose-rate external beam radiation therapy is ubiquitous in clinical situations, two important exceptions exist. The first is the degradation of beam dose rate in the radiosurgery context when gamma ray radiation is generated from radioactively decaying sources. A common source is a 60Co, which has an approximately 5.26 year half-life [102]. Although this affects treatment "beam on" times, on short time scales of individual treatments, on the order of minutes, this dose rate is effectively constant during a single treatment.

Another exception is internal source radiation therapy, known as brachytherapy. In brachytherapy, a radiation source is placed directly in the tissue, delivering ionizing radiation by means of radioactive decay. Half-lifes for brachytherapy radiation sources range from 17 days (^{103}Pd γ-ray) to 30 years (^{137}Cs γ-ray). In this case, the dose rate exponentially decays in time, conceptually illustrated in Figure 2.6.

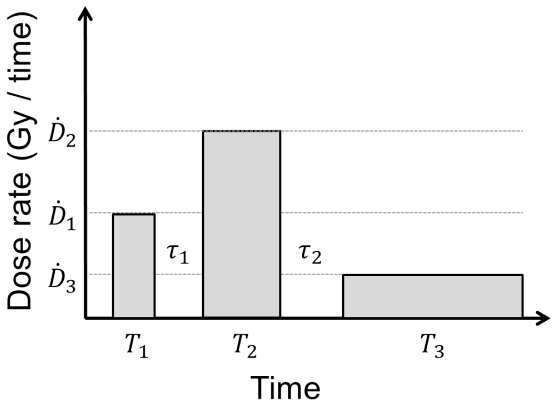

Figure 2.5: An illustration of three treatments with dose rates, treatment durations, and time between treatments denoted by $\dot{D}_i(t)$, T_i and τ_i, respectively.

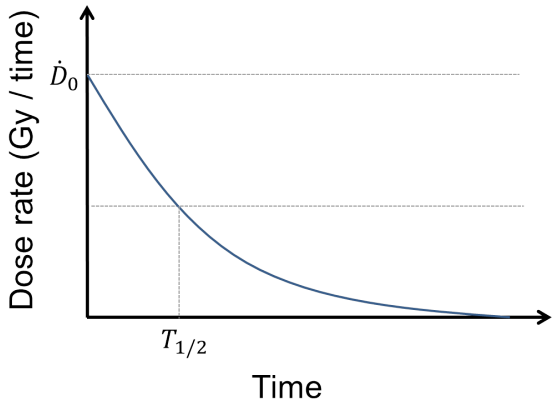

Figure 2.6: Decaying dose rate from initial rate $\dot{D}_0$ for embedded radiation treatments such as brachytherapy.

Mathematically, these dose-rate functional forms can be expressed as follows. For a single fraction treatment starting at time t_i and ending at time t_f with total treatment time $T = t_f - t_i$ and constant dose rate $\dot{D}_0$, the dose rate function is given as

$$\dot{D}(t) = \dot{D}_0 \cdot (\mathcal{H}(t - t_i) - \mathcal{H}(t - t_f)) \tag{2.16}$$

where $\mathcal{H}$ is the Heavyside function defined as

$$\mathcal{H}(t_0) \equiv \begin{cases} 0 & \text{if } t \leq t_0 \\ 1 & \text{if } t > t_0. \end{cases} \tag{2.17}$$

The computation of total dose for this single fraction treatment is then given simply by

$$\begin{aligned} D &= \int_0^\infty \dot{D}(t)dt && (2.18) \\ &= \int_0^\infty \dot{D}_0 \cdot (\mathcal{H}(t - t_i) - \mathcal{H}(t - t_f))dt && (2.19) \\ &= \dot{D}_0 \int_{t_i}^{t_f} dt = \dot{D}_0 \cdot T. && (2.20) \end{aligned}$$

This definition easily extends to N treatment fractions, as

$$\dot{D}(t) = \sum_{n=1}^{N} \dot{D}_n \cdot (\mathcal{H}(t - t_i^n) - \mathcal{H}(t - t_f^n)) \tag{2.21}$$

where t_i^n indicates the start time of the n^{th} fraction, and similarly t_f^n is the stop time. This allows for simple computation of the total dose as

$$D = \int_0^\infty \dot{D}(t)dt = \sum_{n=1}^{N} \dot{D}_n \cdot T_n \tag{2.22}$$

where T_n is the total treatment time for fraction n. Note that $D \neq 0$ for treatment of any duration or dose rate.

The formula for an exponentially decaying radiation source (and therefore dose rates) as is the case in brachytherapy are given by

$$\dot{D}(t) = \dot{D}_0 \exp(-\delta t) \tag{2.23}$$

where δ is a decay constant. This functional form begins at time $t = 0$, at the time of the implantation of the radiation source in the tissue. The total dose is then given by

$$D = \int_0^\infty \dot{D}dt \tag{2.24}$$

$$= \int_0^\infty \dot{D}_0 \exp(-\delta t)dt = \frac{\dot{D}_0}{\delta}. \tag{2.25}$$

2.3.4 Non-dimensionalization

Perturbation analysis and model linearization is prevalent in the radiation biology literature, see references [155, 37, 77, 75, 30] to name only a few. In the case of two compartment kinetic models, perturbation expansions often assume the small parameter involves the nonlinear terms in the model. Previous analysis of the RMF model assumed that the binary interaction rate η is the small parameter in the model, leading to an expansion of the solution in a power series in η of the form $L(t) = L_0(t) + \eta L_1(t)$ [131, 37, 77]. It may not strictly be the case, however that η is the smallest parameter on the time scale of interest, or relative to the radiation type or damage yield, parameters $\Sigma, \bar{z}_F$. If η is not small relative to the number of potentially rejoinable DSBs ($L(t)$), then the resulting linearization will not be valid, therefore a dimensional analysis of the model will provide insight as to the appropriateness, or not, of this assumption and resulting expansion.

There are many ways to scale, or non-dimensionalize the model to best study the size of the solution and parameters relative to each other. Some of them are given below. To

scale the number of potentially rejoinable DNA lesions $L(t)$, relative to radiation quality, rates of repair and rejoining, or radiation efficiency, we can define dimensionless quantities denoted with an overbar, $\bar{}$ as

$$\overbrace{\bar{L} = \frac{L}{\Sigma D}}^{\substack{\text{radiation quality,} \\ \text{total dose}}} \quad , \qquad \overbrace{\bar{L} = \frac{\eta}{\lambda} L}^{\substack{\text{relative repair} \\ \text{rates}}} \quad , \qquad \overbrace{\bar{L} = \frac{L}{\Sigma \bar{z}_F}}^{\substack{\text{relative radiation} \\ \text{efficacy}}} \quad . \tag{2.26}$$

To scale time relative to repair rates, radiation LET and efficiency, we can define the dimensionless variables denoted with an overbar, $\bar{}$ as

$$\overbrace{\bar{t} = \lambda t}^{\substack{\text{first-order} \\ \text{repair}}} \quad , \qquad \overbrace{\bar{t} = \frac{D}{\bar{z}_F} t}^{\substack{\text{time between} \\ \text{ionization events}}} \quad , \qquad \overbrace{\bar{t} = \eta f_R \Sigma \bar{z}_F t}^{\substack{\text{rejoining rate,} \\ \text{radiation efficacy}}} \quad . \tag{2.27}$$

To consider the behavior of the model on the same time scale as the kinetic process of DSB repair and DSB induction relative to radiation quality and dose delivered, for a fixed, single continuous irradiation of total dose D, we define the dimensionless variables with an overbar, $\bar{}$ so that

$$\bar{L} = \frac{L}{\Sigma D}, \qquad \text{where} \quad D = \int_0^\infty \dot{D} dt, \quad \text{and} \quad \bar{t} = \lambda t. \tag{2.28}$$

For a single treatment fraction, the total dose delivered D is strictly positive and so $\bar{L}$ is well defined. Note this is not an appropriate scaling for analyzing multiple fraction scenarios, particularly when the time between fractions is allowed to vary, since in this case the total dose will vary in time. Recall that $\lambda = \lambda_F + \lambda_R$, which are rate constants for the kinetic processes of damage fixation and repair, respectively. Inserting these into the ODE for $L(t)$ given in Equation 2.4, we have

$$\frac{d\bar{L}}{d\bar{t}} = f_R \frac{\dot{D}}{\lambda D} - \left(1 + \frac{\eta}{\lambda} \bar{z}_F \Sigma f_R\right) \bar{L} - \frac{\eta}{\lambda} \Sigma D \bar{L}^2 \tag{2.29}$$

and

$$\frac{d\bar{F}}{d\bar{t}} = \frac{(1 - f_R)\dot{\bar{D}}}{D} + \left(\theta + \frac{\eta}{\lambda} \gamma \bar{z}_F \Sigma f_R\right) \bar{L} + \frac{\eta}{\lambda} \gamma \bar{L}^2 \tag{2.30}$$

where we define the dose rate relative to the dimensionless timescale as

$$\bar{\dot{D}} = \frac{\dot{D}}{\lambda}. \tag{2.31}$$

For convenience, let us define the simplifying variable $\omega \equiv \bar{z}_F \Sigma f_R$ so that the non-dimensional RMF model is given by

$$\frac{d\bar{L}}{d\bar{t}} = f_R \frac{\bar{\dot{D}}}{D} - \left(1 + \frac{\eta}{\lambda}\omega\right)\bar{L} - \frac{\eta}{\lambda}\Sigma D \bar{L}^2, \quad \bar{L}(\bar{t}=0) = 0 \tag{2.32}$$

$$\frac{d\bar{F}}{d\bar{t}} = \frac{(1-f_R)\bar{\dot{D}}}{D} + \left(\theta + \frac{\eta}{\lambda}\gamma\omega\right)\bar{L} + \frac{\eta}{\lambda}\gamma\bar{L}^2, \quad \bar{F}(\bar{t}=0) = 0. \tag{2.33}$$

Size of terms In order to identify the small parameter in this system, we consider the relative order of magnitude of each of the terms in the system. Combining estimates and values in Table 2.1, we have

$$f_R \frac{\dot{D}}{\lambda D} = f_R \frac{\bar{\dot{D}}}{D} = \frac{\mathcal{O}(10^{-1}) \cdot \mathcal{O}(1)}{\mathcal{O}(1)} = \mathcal{O}(10^{-1}) \tag{2.34}$$

$$\left(1 + \frac{\eta}{\lambda}\omega\right) = (\mathcal{O}(10^{0}) + \mathcal{O}(10^{-4}) \cdot \mathcal{O}(10^{-2})) = \mathcal{O}(10^{0}) \tag{2.35}$$

$$\frac{\eta}{\lambda}\Sigma D = \mathcal{O}(10^{-4}) \cdot \mathcal{O}(10) \cdot \mathcal{O}(10^{0}) = \mathcal{O}(10^{-3}). \tag{2.36}$$

We have used the values of the radiation parameters Σ and $\bar{z}_F$ associated with 250 KeV x-rays, and η/λ from Carlson 2008 [37], in which estimates of the following aggregate parameters used in the first-order approximation,

$$\kappa = \frac{\eta}{\lambda}[\gamma - \theta] \tag{2.37}$$

where $\kappa = \mathcal{O}(10^{-5})$ and $\theta = \mathcal{O}(10^{-3})$. Recognizing that the ratio η/λ is much smaller in magnitude than any other parameter, we define

$$\epsilon = \frac{\eta}{\lambda} \tag{2.38}$$

so that the final model takes the form

$$\frac{d\bar{L}}{d\bar{t}} = f_R \frac{\bar{\dot{D}}}{D} - (1 + \epsilon\omega)\bar{L} - \epsilon\Sigma D \bar{L}^2 \tag{2.39}$$

$$\frac{d\bar{F}}{d\bar{t}} = \frac{(1-f_R)\bar{\dot{D}}}{D} + (\theta + \gamma\epsilon\omega)\bar{L} + \gamma\epsilon\bar{L}^2. \tag{2.40}$$

The effect of varying the small parameter on the solution is discussed in the next section. Since the differential equation for $\bar{F}(\bar{t})$ is given by integrating the non-negative function $\bar{L}(\bar{t})$ in time, $\bar{F}(\bar{t})$ will be a monotonically increasing function. It is most informative then, to study the dynamics of $\bar{L}(\bar{t})$.

Solution characterization We note the RMF model is stated for DNA damage and repair kinetics *during the administration of radiation*, so that $\dot{D} \neq 0$. Because external beam radiation therapy is not delivered continuously, in contrast to brachytherapy, the RMF model takes the reduced form to describe DSB repair after the completion of therapy. For clarity, we will denote the model *during treatment* with a subscript $(_D)$, and outside of treatment with a subscript $(_N)$, so that outside of radiation delivery we have the dimensionless model given by

$$\overbrace{\frac{d\bar{L}_N}{d\bar{t}}}^{\substack{\text{rate of change}\\ \text{of potentially}\\ \text{rejoinable DSBs}}} = - \overbrace{(1+\epsilon\omega)\,\bar{L}_N}^{\substack{\text{first order}\\ \text{non-lethal repair}}} - \overbrace{\epsilon\Sigma D\bar{L}_N^2}^{\substack{\text{second order}\\ \text{non-lethal repair}}} \tag{2.41}$$

$$\overbrace{\frac{d\bar{F}_N}{d\bar{t}}}^{\substack{\text{rate of change}\\ \text{of fatal DSBs}}} = \overbrace{(\theta+\gamma\epsilon\omega)\,\bar{L}_N}^{\substack{\text{fatal first order}\\ \text{misrepair}}} + \overbrace{\gamma\epsilon\bar{L}_N^2}^{\substack{\text{fatal second order}\\ \text{misrepair}}} \tag{2.42}$$

with initial conditions given by the RMF solution at the end of treatment of duration $\bar{T}$,

$$\bar{L}_N(\bar{t}=0)=0, \quad \bar{L}_N(\bar{t}=\bar{T})=\bar{L}_D(\bar{t}=(\bar{t}-\bar{T})), \tag{2.43}$$

$$\bar{F}_N(\bar{t}=0)=0, \quad \bar{F}_N(\bar{t}=\bar{T})=\bar{F}_D(\bar{t}=(\bar{t}-\bar{T})). \tag{2.44}$$

We consider the solution behavior in both scenarios, with and without direct irradiation (i.e. with treatment on and with treatment off), from a dynamical systems perspective using fixed point and phase plane analyses.

Fixed points The fixed points of the system are given by setting the derivative of $\bar{L}(\bar{t})$ equal to zero and solving for $\bar{L}(\bar{t})$, which results in the following quadratic equation

$$0 = f_R \dot{\bar{D}} D^{-1} - (1 + \epsilon\omega)\bar{L} - \epsilon\Sigma D \bar{L}^2. \tag{2.45}$$

This, of course, results in two solutions, denoted $\bar{L}_{k1}$ and $\bar{L}_{k2}$. By plotting $d\bar{L}/d\bar{t}$ versus

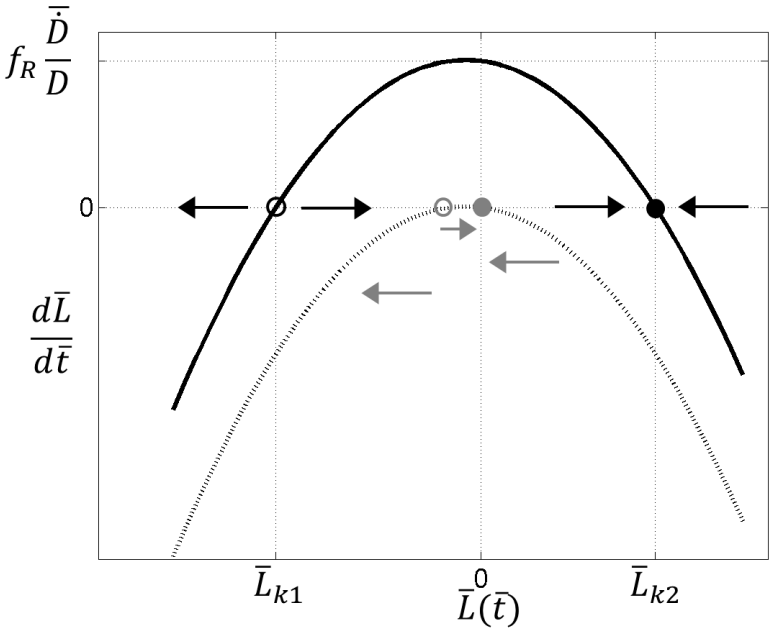

Figure 2.7: Solid line: Two rest points exist for $\bar{L}(\bar{t})$, one positive and one negative for repair dynamics *during therapy*, (i.e. $\bar{L}_D$, and $\dot{\bar{D}} \neq 0$). The Figure shows $\bar{L}_{k2}$ is stable and $\bar{L}_{k1}$ is an unstable fixed point. Dashed line: without therapy, no radiation is delivered (i.e. $\bar{L}_N$, and $\dot{\bar{D}} = 0$), and the potentially rejoinable DSBs ($\bar{L}_N$) go to zero, $\bar{L}_{k2} \to 0$.

$\bar{L}(\bar{t})$, we see that the positive valued fixed point $\bar{L}_{k2}$ is stable, and the other, $\bar{L}_{k1}$ is unstable *during therapy*, (i.e. $\bar{L}_D$, and $\dot{\bar{D}} \neq 0$), shown in Figure 2.7. These values can be computed directly with the quadratic formula to give

$$\bar{L}_{k1,2} = \frac{(1 + \epsilon\omega) \pm \sqrt{(1 + \epsilon\omega)^2 + 4\epsilon\Sigma f_R \dot{\bar{D}} D^{-1}}}{-2\epsilon\Sigma D} \tag{2.46}$$

where $\bar{L}_{k1}$ is the positive root, and $\bar{L}_{k2}$ is the negative root, respectively. Outside treatment delivery, $\bar{L}_N$, we have $\dot{\bar{D}} \equiv 0$ and the reduced equation

$$0 = -(1 + \epsilon\omega)\bar{L}_N - \epsilon\Sigma D\bar{L}_N^2, \tag{2.47}$$

which has solutions given by

$$\bar{L}_{k1} = \frac{-(1 + \epsilon\omega)}{\epsilon\Sigma D}, \quad \bar{L}_{k2} \equiv 0 \tag{2.48}$$

which is also easily seen from setting $\dot{\bar{D}} \equiv 0$ in Equation 2.46, see also Figure 2.7. Solution trajectories during irradiation describing *intra-fraction* repair will approach $\bar{L}_{k2}$ for any starting value $\bar{L}(\bar{t} = 0) = \bar{L}_0$.

In a sense, the presence of treatment can be seen as a perturbation away from rest equilibrium at $\bar{L}(\bar{t}) = 0$, and also as a bifurcation of the system, moving the rest point $\bar{L}_{k2}$ away from zero to some positive value of $\bar{L}_k$. This gives intuition as to the behavior of the system. The natural questions now are the following:

1. how quickly will the sub-lethal, potentially rejoinable DSB formation saturate relative to the total dose delivered D, dose rate $\dot{\bar{D}}$, dose quality $\Sigma, \bar{z}_F$ and repair processes λ, η?

2. Can we characterize the rate the solution approaches the saturating number of sub-lethal/potentially repairable DSBs?

In the time interval outside therapy however, we have the total number of potentially rejoinable double strand breaks going to zero, therefore the rate of change of the number of fatal double strand breaks must also go to zero, $\bar{L}(\bar{t}) \to 0$ and $\dot{\bar{D}} \equiv 0$, therefore $d\bar{F}/d\bar{t} \to 0$ so that $\bar{F} \to \bar{F}(\infty)$. This makes for a sensible model: there should be no fatal DSB creation, and thus no positive rate of change, for long times after therapy administration. The qualitative relationship between $\bar{L}(\bar{t})$ and $\bar{F}(\bar{t})$ is best illustrated with a phase portrait, shown in Figure 2.8.

The effect of varying the small parameter $\epsilon = \eta/\lambda$ in the dimensionless RMF model given in Equations 2.32 and 2.33, is illustrated in Figure 2.10. Although this is a small parameter

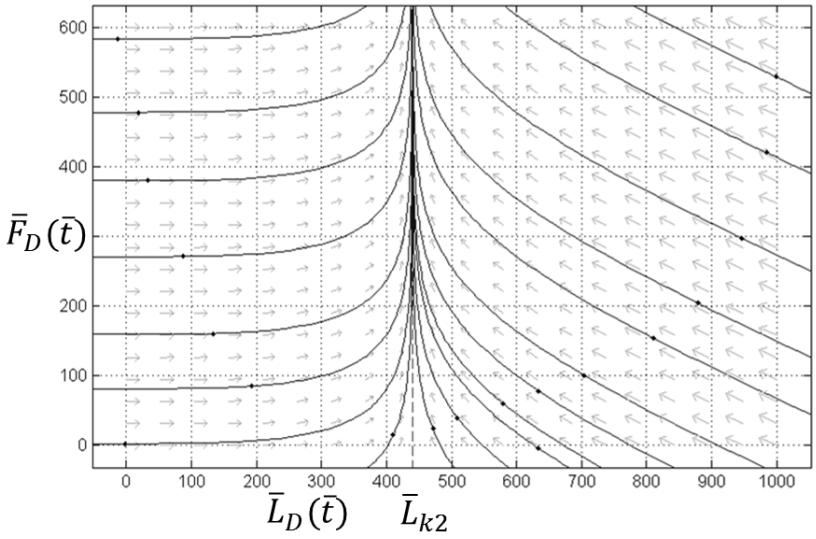

Figure 2.8: Phase portrait for RMF solution dynamics during irradiation ($\bar{L}_D$, $\dot{\bar{D}} > 0$). Potentially rejoinable DSBs will asymptotically approach a stable fixed point, $\bar{L}_k$, while fatal DSBs resulting from misrepair or damage fixation will continue to monotonically increase.

in our model, we do not consider a regular perturbation analysis where $\epsilon \to 0$ since this is both contrary to the very construction of the model, and moreover it is not biologically realistic. With that in mind, we do note that if $\epsilon \to 0$, the RMF model would reduce to a first-order repair model which is one of the mechanistic derivations of the linear-quadratic dose-response model, discussed in detail in Section 2.5. We do however expect the ratio η/λ to be a function of dose rate and perhaps energy deposition or LET, although preliminary evidence suggests this may not be the case, see Section 2.7. As we vary the small parameter ϵ, we see different times required to saturate the number of potentially rejoinable DSBs ($\bar{L}(\bar{t})$), corresponding to low and high predicted radio-sensitivity see Figure 2.9.

Surviving Fraction There exist many rationale for deriving expressions of the surviving fraction (SF) in radiobiology [155, 75]. One explanation is that cell survival should follow a Poisson process such that the probability of survival decreases exponentially with fatal

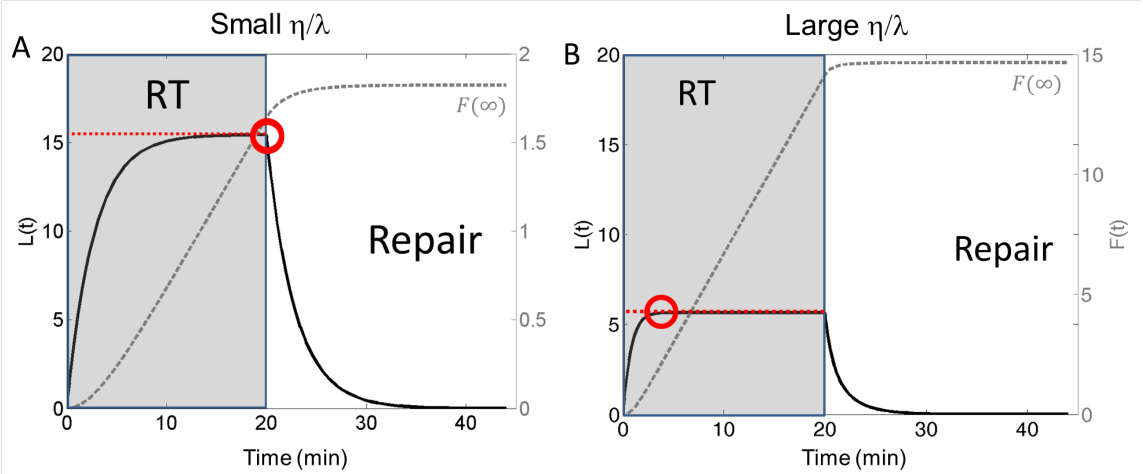

Figure 2.9: As a function of the ratio η/λ, A) The RMF model predicts saturation of sub-lethal damage during prolonged irradiation times. If intra-fraction repair is ignored, the total number of lesions created during the fraction is critical indicated by the red circle for relatively low values of the ratio η/λ. B) When η/λ is large, the total number of potentially rejoinable lesions is completely maximized prior to the completion of the treatment fraction. $F(\infty)$ is long time behavior of $F(t)$ and is related to the overall surviving fraction of cells following irradiation. Small η/λ corresponds to reduced effect and radio-sensitivity ($F(\infty) \approx 1.9$), where large values of η/λ produces a larger effect, and increased radio-sensitivity ($F(\infty) \approx 15$).

DNA double strand breaks, which is represented by the "biological effect" (BE), so that

$$SF = \exp(-BE). \tag{2.49}$$

For the LQ model, the surviving fraction takes the form

$$SF = \exp(-\alpha D - \beta D^2). \tag{2.50}$$

An alternate explanation is that the surviving fraction of cells at time $\bar{t}$, given by $S(\bar{t})$ has a rate of change proportional to $S(\bar{t})$, with rate constant given by $d\bar{F}/d\bar{t}$, so that

$$\frac{dS}{d\bar{t}} = -\frac{d\bar{F}}{d\bar{t}} S(\bar{t}) \tag{2.51}$$

with $S(\bar{t} = 0) = 0$. This formulation rests on the interpretation that the average number of lethal lesions are randomly distributed among a population of cells so that each cell has

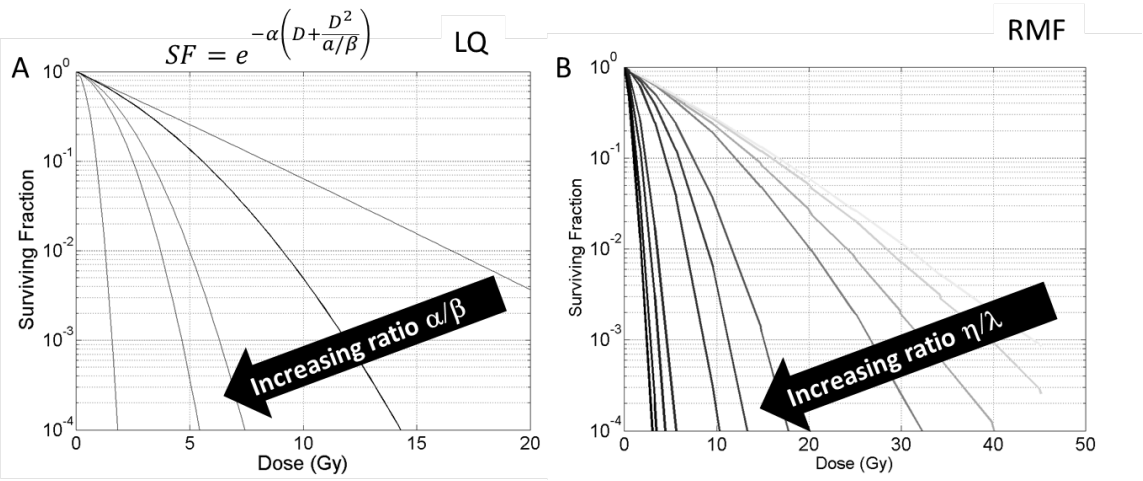

Figure 2.10: The effect of varying the ratio η/λ in the dimensionless RMF model is conceptually similar to varying α/β in the linear-quadratic model, that is to say that it is the ratio of the repair rates, and not their individual variation which contribute to the shape of the curve and characterization of radio-sensitivity. A: Linear-quadratic model. B: RMF model predicted dose-response.

an equal chance of acquiring a lethal lesion, with probability $d\bar{F}/d\bar{t}$. Solving Equation 2.51 gives the same formalism as the Poisson distribution assumption in Equation 2.49, namely that the SF is an exponential function,

$$S(\bar{t}) = \exp(-\bar{F}(\bar{t})) \tag{2.52}$$

where the biological effect is the translation of dose into fatal DNA lesions. Dose response data is generally not collected in a time series, therefore we may regard the terminal surviving fraction of cells after a dose D to be given by the limit as time goes to infinity ($\bar{t} \to \infty$),

$$SF = S(\infty) = \exp(-\bar{F}(\infty)). \tag{2.53}$$

We therefore seek a formalism to give $\bar{F}(\infty)$ for the RMF to translate to a surviving fraction to be compared to the LQ model.

2.4 Exact solutions

Although the RMF model can be solved numerically using "stiff problem" methods in conjunction with judicious time stepping and grid point placement which can account for rapid changes in solution behavior occurring at the beginning and end of irradiation where the dose-rate term in the ODEs appears and disappears, respectively, exact solutions to the model can be found, which avoids these numerical challenges. Because the rate of change of fatal DSB creation and repair ($d\bar{F}/d\bar{t}$) depends only on the number of potentially rejoinable DSBs (i.e. independent of $\bar{F}(\bar{t})$), we need only seek solutions to $\bar{L}(\bar{t})$, which can then be integrated to provide a solution for $\bar{F}(\bar{t})$.

Specifically, closed form solutions can be found for the time evolution of the potentially rejoinable DSBs, $d\bar{L}/d\bar{t}$ given by

$$\frac{d\bar{L}}{d\bar{t}} = f_R \frac{\bar{\dot{D}}}{D} - (1 + \epsilon\omega)\bar{L} - \epsilon\Sigma D\bar{L}^2. \tag{2.54}$$

Solutions can be derived if the dose-rate function $\bar{\dot{D}}(\bar{t})$ is a piecewise constant function, so that $\bar{\dot{D}}(\bar{t}) = \bar{\dot{D}}_0$ for $\bar{t} \in$ treatment. A more precisely stated sufficient condition for a closed form solution to exist is discussed in Section 2.4.1. A constant dose rate implies the cumulative dose is a linear function in time. This is a reasonable assumption for the clinical treatment scenario, and in the case of external beam radiation therapy is almost always the case. The dose rate is held constant regardless of treatment schedule, radiation source, prescribed radiation dose, or beam energy within a single treatment. That is, a radiation delivery system has a characteristic, or set of characteristic average dose rates it is able to deliver, and it is a constant, fixed value. Instantaneous dose rates may fluctuate, however the administered average dose rate defined by the total dose delivered divided by the treatment time is relatively constant. This is not the case for internal, or brachytherapy, in which case the dose rate decays with the isotope used to deliver the ionizing radiation.

Therapeutic application of ionizing radiation is often delivered in multiple fractions. This is the result of decades of clinical experience as well as direct experimental observation relating the 4 R's of radiobiology to the dual goals of maximizing tumor cell kill while minimizing damage to normal tissue [79]. Larger doses of radiation can be tolerated in

fractionated regimens than in large single doses. Radiosurgery is often delivered in a single acute fraction, as is a preponderance of dose-response data, therefore it is most instructive to have analytic solutions to any mechanistic model aimed towards the single fraction scenario [76, 28].

For fixed dose rate therapy, we can consider the dose rate function piecewise constant as defined in Equation 2.16. In this case, the ordinary differential equation for $\bar{L}(\bar{t})$ is a Ricatti equation, which can be solved using a partial fraction decomposition since the equation is separable, or using the following method, which results in a necessary condition for closed form solutions to be found, discussed in Section 2.4.1.

Let $v(t) = \epsilon\Sigma D\bar{L}(\bar{t})$ so that

$$v' = \frac{dv}{dt} = \epsilon\Sigma D\frac{d\bar{L}}{d\bar{t}} = \epsilon\Sigma D(f_R\bar{\dot{D}}_0 D^{-1} - (1+\epsilon\omega)\bar{L} - \epsilon\Sigma D\bar{L}^2) \tag{2.55}$$

$$= f_R\epsilon\Sigma\bar{\dot{D}}_0 - (1+\epsilon\omega)v - v^2. \tag{2.56}$$

Now let

$$v(\bar{t}) = \frac{w'(\bar{t})}{w(\bar{t})} = v^2 - v' \tag{2.57}$$

so that

$$w'' + (1+\epsilon\omega)w' + f_R\epsilon\Sigma\bar{\dot{D}}_0 w = 0. \tag{2.58}$$

For a single treatment, the dose rate is constant, $\bar{\dot{D}}_0$ so that Equation 2.58 is a constant coefficient second order ordinary differential equation, which is straight forward to solve. For $\bar{t}$ in radiation delivery, so that $\bar{t}_i < \bar{t} < \bar{t}_f$, we have the auxiliary equation

$$r^2 + (1+\epsilon\omega)r + f_R\epsilon\Sigma\bar{\dot{D}}_0 = 0 \tag{2.59}$$

which has roots

$$r_{1,2} = \frac{-(1+\epsilon\omega) \pm \sqrt{(1+\epsilon\omega)^2 - 4f_R\epsilon\Sigma\bar{\dot{D}}_0}}{2}. \tag{2.60}$$

This results in solutions to the transformed differential equation for $w(\bar{t})$ in Equation 2.58 as

$$w(\bar{t}) = c_1 e^{r_1\bar{t}} + c_2 e^{r_2\bar{t}} \tag{2.61}$$

where c_1, c_2 are arbitrary constants. The solution for $\bar{L}(\bar{t})$ is given by

$$\bar{L}(\bar{t}) = \frac{-w'}{\eta w} = \frac{-(c_1 r_1 \exp(r_1\bar{t}) + c_2 r_2 \exp(r_2\bar{t}))}{\eta(c_1\exp(r_1\bar{t}) + c_2\exp(r_2\bar{t}))}. \tag{2.62}$$

The roots to the auxiliary equation reduce to $r_1 = -(1+\epsilon\omega)$ and $r_2 = 0$ when $\bar{\dot{D}}_0 \equiv 0$ and that the Ricatti equation becomes a Bernoulli equation commonly known as the logistic equation [132]. Ratios of exponential functions can often be transformed into hyperbolic trigonometric functions, which can serve to simply the expressions and more clearly understand long time scale dynamics. For the solution form given above in Equation 2.62, we transform the solution into the following equivalent form,

$$\bar{L}(\bar{t})_D = \frac{1}{2\epsilon\Sigma D}\left[(1+\epsilon\omega) - \sqrt{\Phi}\tanh\left(\Psi\right)\right] \text{ for } \bar{t} \in \bar{T} \tag{2.63}$$

where the treatment interval is $\bar{T} \equiv \bar{t}_f - \bar{t}_i$ and we define the simplifying variable representing the argument of the hyperbolic tangent Ψ,

$$\Psi \equiv \arg(\tanh) = \frac{\sqrt{\Phi}}{2}\bar{t} - \tanh^{-1}\left(\frac{(1+\epsilon\omega)}{\sqrt{\Phi}}\right). \tag{2.64}$$

and Φ as

$$\Phi \equiv (1+\epsilon\omega)^2 + 4\epsilon f_R \Sigma \bar{\dot{D}}_0. \tag{2.65}$$

It is easy to see that this function satisfies the initial condition $\bar{L}(\bar{t}=0) = 0$, which corresponds to the first fraction of therapy, where it is assumed there are no radiation-induced DSBs. We also see that the function approaches $\bar{L}_{k2}$, by first noting that

$$\lim_{\bar{t}\to\infty} \tanh(\bar{t}) = 1 \tag{2.66}$$

and computing the limit as

$$\begin{aligned}
\lim_{\bar{t}\to\infty} \bar{L}(\bar{t})_D &= \lim_{\bar{t}\to\infty}\left(\frac{1}{2\epsilon\Sigma D}\left[(1+\epsilon\omega) - \sqrt{\Phi}\tanh\left(\Psi\right)\right]\right) &(2.67)\\
&= \lim_{\bar{t}\to\infty}\left(\frac{1}{2\epsilon\Sigma D}\left[(1+\epsilon\omega) - \sqrt{\Phi}\right]\right) &(2.68)\\
&= \frac{(1+\epsilon\omega)+\sqrt{\Phi}}{2\epsilon\Sigma D} \equiv \bar{L}_{k2}, &(2.69)
\end{aligned}$$

as seen in Equation 2.46. Outside of radiation delivery we have the reduced equation

$$\frac{d\bar{L}_N}{d\bar{t}} = -(1+\epsilon\omega)\bar{L}_N - \epsilon\Sigma D\bar{L}_N^2, \quad \text{for } \bar{t} \geq \bar{T} \tag{2.70}$$

which has the solution, denoted $\bar{L}(\bar{t})_N$,

$$\bar{L}(\bar{t})_N = \frac{\bar{L}_D(\bar{T})(1+\epsilon\omega)e^{-(1+\epsilon\omega)(\bar{t}-\bar{T})}}{(1+\epsilon\omega)+\bar{L}_D(\bar{T})\epsilon\Sigma D(1-e^{-(1+\epsilon\omega)(\bar{t}-\bar{T})})}, \quad \text{for } \bar{t} \geq \bar{T}. \tag{2.71}$$

See Murray Chapter 1, Volume 1 for the solution to the logistic equation [132]. This solution satisfies $\bar{L}_N(\bar{t}=\bar{T}) = \bar{L}_D(\bar{T})$, the number of potentially rejoinable DSBs at the end of treatment is the same number as at the beginning of the repair phase after treatment so that the solution is defined piecewise and continuous. The function clearly goes to zero as $\bar{t} \to \infty$, as expected from the fixed point analysis shown in Figure 2.8. Together with the appropriate initial conditions, these two solutions completely define the dynamics of $\bar{L}(\bar{t})$ during and after a single irradiation, so that the complete solution at any time $\bar{t}$ can be given by

$$\bar{L}(\bar{t}) = \begin{cases} \bar{L}(\bar{t})_D & \text{if } \bar{t} \in \text{ therapy} \\ \bar{L}(\bar{t})_N & \text{if } \bar{t} \notin \text{ therapy} \end{cases} \tag{2.72}$$

with $\bar{L}(\bar{t}=0) = 0$ and $\bar{L}(\bar{T})_D = \bar{L}_N((\bar{t}-\bar{T}))$. Since we are considering a single treatment fraction of duration $\bar{T}$, the integrals can be expressed as follows

$$\int_0^\infty = \int_0^{\bar{T}} + \int_{\bar{T}}^\infty \tag{2.73}$$

so we can integrate each piece of the solution independently and ensure continuity of the solution. To compute the log surviving fraction of cells $\ln(S)$, we integrate $\dfrac{d\bar{F}}{d\bar{t}}$,

$$\ln(S) = \bar{F}(\infty) = \int_0^\infty \frac{d\bar{F}}{d\bar{t}} \tag{2.74}$$

$$= \int_0^\infty (1-f_R)D^{-1}\dot{\bar{D}}_0 + (\theta+\gamma\epsilon\omega)\bar{L}(\tau) + \gamma\epsilon\bar{L}^2(\tau)d\tau. \tag{2.75}$$

The first integral is simply the fraction of DSBs which are potentially rejoinable. The second and third integrals require evaluations of the anti-derivative of $\bar{L}(\bar{t})$ and $\bar{L}^2(\bar{t})$.

The anti-derivative of $\bar{L}_D$ is given by integrating the hyperbolic tangent function as follows:

$$\int \tanh(ax)dx = \frac{1}{a}\ln(\cosh(ax)) \tag{2.76}$$

so that we have

$$\int \bar{L}_D d\bar{t} = \frac{1}{2\epsilon\Sigma D}\left[(1+\epsilon\omega)\bar{t} - 2\ln\left(\cosh\left(\Psi\right)\right)\right]. \tag{2.77}$$

The anti-derivative of $\bar{L}_N$ is of the form

$$\int \frac{f'(x)}{f(x)}dx = \ln(f(x)) \tag{2.78}$$

with

$$f(x) = (1+\epsilon\omega) + \bar{L}_D(\bar{T})\epsilon\Sigma D(1 - e^{-(1+\epsilon\omega)(\bar{t}-\bar{T})}) \tag{2.79}$$

which gives

$$\int \bar{L}_N d\bar{t} = \frac{1}{\epsilon\Sigma D}\ln\left((1+\epsilon\omega) + \bar{L}_D(\bar{T})\epsilon\Sigma D\left(1 - e^{-(1+\epsilon\omega)(\bar{t}-\bar{T})}\right)\right). \tag{2.80}$$

To compute $\int_0^\infty \bar{L}^2(\tau)d\tau$ we integrate the original differential equation and note that for a constant dose rate function $\bar{\dot{D}}(\tau) = \bar{\dot{D}}_0$ for all $0 \le \tau \le \bar{T}$, we have

$$\int_0^\infty \frac{d\bar{L}}{d\bar{t}} = \bar{L}(\infty) - \bar{L}(0) = 0 \tag{2.81}$$

so that

$$\int \bar{L}^2(\tau)d\tau = \frac{1}{\epsilon\Sigma D}\left[\int \frac{f_R}{D}\bar{\dot{D}}_0 d\tau - (1+\epsilon\omega)\int \bar{L}(\tau)d\tau\right] \tag{2.82}$$

where the integral from zero to infinity is understood to be broken into the integral during irradiation and outside of radiation, $\int_0^\infty = \int_0^{\bar{T}} + \int_{\bar{T}}^\infty$ so as to not include points of discontinuity in the dose rate function as defined in Equation 2.16. Using this expression, we can obtain a solution for $\bar{F}(\bar{t})$, at some time $\bar{t}$ as follows, recall $\bar{F}(\bar{t}=0) = 0$

$$\begin{aligned}
\int_0^{\bar{t}} \frac{d\bar{F}}{d\bar{t}} &= \bar{F}(\bar{t}) && (2.83)\\
&= \int_0^{\bar{t}} (1-f_R)\frac{\bar{\dot{D}}_0}{D} + (\theta + \epsilon\gamma\omega)\bar{L}(\tau) + \epsilon\gamma\bar{L}^2(\tau)d\tau && (2.84)\\
&= \int_0^{\bar{t}} (1-f_R)\bar{\dot{D}}_0 D^{-1}d\tau + (\theta+\epsilon\gamma\omega)\int_0^{\bar{t}} \bar{L}(\tau)d\tau + ... && (2.85)\\
&\quad \epsilon\gamma\left[\frac{1}{\epsilon\Sigma D}\left(\int_0^{\bar{t}} \frac{f_R}{D}\bar{\dot{D}}_0 d\tau - (1+\epsilon\omega)\int_0^{\bar{t}} \bar{L}(\tau)d\tau\right)\right] && (2.86)\\
&= (1 - f_R(1-\gamma)) + \frac{\Sigma D(\theta+\gamma\epsilon\omega) - \gamma(1+\epsilon\omega)}{\Sigma D}\int_0^{\bar{t}} \bar{L}(\tau)d\tau && (2.87)
\end{aligned}$$

leading to the piecewise defined analytic solution for any time $\bar{t}$,

$$\bar{F}(\bar{t}) = (1 - f_R(1-\gamma)) + \left(\frac{\Sigma D(\theta+\gamma\epsilon\omega) - \gamma(1+\epsilon\omega)}{\Sigma D}\right)\begin{cases} \int \bar{L}_D d\bar{t} & \text{if } \bar{t} \le \bar{T} \\ \int \bar{L}_N d\bar{t} & \text{if } \bar{t} \ge \bar{T}. \end{cases} \tag{2.88}$$

To obtain the surviving fraction after a single dose of length $\bar{T}$ when repair processes have completed, we let $\bar{t} \to \infty$, so that we have the single expression

$$\bar{F}(\infty) = \lim_{\bar{t}\to\infty} \left(\bar{F}(\bar{t})\right) \tag{2.89}$$

$$= (1 - f_R(1-\gamma)) + \left(\frac{\Sigma D(\theta + \gamma\epsilon\omega) - \gamma(1+\epsilon\omega)}{\Sigma D}\right)\ln(\Gamma) \tag{2.90}$$

where we define another simplifying variable

$$\Gamma \equiv (1+\epsilon\omega) + \bar{L}_D(\bar{T})\epsilon\Sigma D(1 - e^{(1+\epsilon\omega)\bar{T}}). \tag{2.91}$$

This beautiful solution reveals the highly nonlinear combination of repair, misrepair and fixation rates that determine the overall fatal DSB yield per total dose D and radiation quality through the non-dimensionalization $\bar{L}(\bar{t}) = L/\Sigma D$, on the relative time scale of first-order repair through the time scaling $\bar{t} = \lambda t$.

Recast in the original, dimensional form, we have the long term fatal DSB yield per cell after a single irradiation of duration T with constant dose rate $\dot{D}_0$ given by

$$F(\infty) = \overbrace{(1 - f_R(1-\gamma))\Sigma \int_0^T \dot{D}_0 d\tau'}^{\text{linear in dose}} + \overbrace{[\lambda(\theta - \gamma\eta) + \gamma\omega\eta(1-\eta)] \int_0^\infty L(\tau)d\tau}^{\text{nonlinear in dose}} \tag{2.92}$$

where

$$\int_0^\infty L(\tau)d\tau = \overbrace{\int_0^T L_D(\tau)d\tau}^{\substack{\text{during} \\ \text{irradiation}}} + \overbrace{\int_T^\infty L_N(\tau)d\tau}^{\substack{\text{after} \\ \text{irradiation}}} \tag{2.93}$$

where functional forms of L_D and L_N are given by

$$L_D(t) = \frac{-(\lambda+\eta\omega) + \sqrt{\phi}\tanh\left((1/2)t\sqrt{\phi} + \tanh^{-1}\left(\frac{(\lambda+\eta\omega)}{\sqrt{\phi}}\right)\right)}{2\eta} \tag{2.94}$$

and

$$L_N(t) = \frac{-(\lambda+\eta\omega)L_0 e^{-(\lambda+\eta\omega)t}}{L_0\eta(e^{-(\lambda+\eta\omega)t} - 1) - (\lambda+\eta\omega)} \tag{2.95}$$

and the anti-derivatives of L_D and L_N are given by

$$\int L_D(\tau)d\tau = \frac{1}{2\eta}\left(-(\lambda+\eta\omega)t + \frac{2}{\sqrt{\phi}}\ln(\cosh(\Psi))\right) \tag{2.96}$$

with

$$\phi \equiv (\lambda+\eta\omega)^2 + 4f_R\dot{D}_0\eta \tag{2.97}$$

and Ψ is the argument of the hyperbolic tangent in $L_D(t)$,

$$\int L_N(\tau)d\tau = \frac{1}{\eta}\ln\left(L_0\eta(e^{-(\lambda+\eta\omega)t}-1) - (\lambda+\eta\omega)\right) \tag{2.98}$$

so that these functions need only be evaluated at the time points of interest to completely determine the fatal DSB yield. The surviving fraction of cells is then given by

$$SF = \exp(-F(\infty)). \tag{2.99}$$

This solution demonstrates consistency with first-order models, to include linear and non-linear dependence on dose, although the nonlinearity takes the form of a natural logarithm which describes repair correction for protracted doses. The complexity of this formalism boils down to the number of parameters and the seldom used hyperbolic trigonometric functions. Simply stated, this solution can be easily programmed into an entry level graphing calculator or onto a personal computing device, which can take dose and dose rate as inputs, and return a surviving fraction or biological effect (net fatal DSB yield) with little effort. There are several advantages of having such a closed form expression, despite its apparent complexity (falsely so). For instance, the explicit dependence on dose rate and radiation quality (Σ) is clear from the first integral, which is not clearly the case in the linear-quadratic formalism, which includes only functional dependence on the dose and repair rates through the dose protraction factor, written out explicitly as

$$\begin{aligned} & \text{linear} && \text{quadratic} \\ & \text{in dose} && \text{in dose} \\ BE &= \overbrace{\alpha D} + \overbrace{\beta G(\lambda,\dot{D},T)D^2} && (2.100) \\ &= \alpha D + \frac{2}{D^2}\int_0^T\int_0^t \exp(-\lambda(t'-\tau))\dot{D}(\tau)\dot{D}(t')dt'd\tau. && (2.101) \end{aligned}$$

The Lea-Catcheside dose-protraction function $G(\lambda, \dot{D}, T)$ and its role in the linear-quadratic model estimates of DNA damage and repair is discussed in more detail in Section 2.5.1.

2.4.1 Sufficient condition for closed form solutions

Since the ODE for $\bar{F}(\bar{t})$ given in Equation 2.33 is independent of $\bar{F}$, we need only find analytic solutions for $\bar{L}(\bar{t})$, which can be found if the second order ODE given in Equation 2.58 has constant coefficients. This is not a necessary condition, only sufficient. Using this solution approach, a necessary condition would be tantamount to finding a sufficient and necessary condition for the solution for a general second order ODE, which has not yet been demonstrated [26].

For an ordinary differential equation of the form

$$w'' + p(\bar{t})w' + q(\bar{t})w = 0 \tag{2.102}$$

from Equation 2.58, make the identifications $p(\bar{t}) = (1 + \epsilon\omega)$, and $q(\bar{t}) = f_R \Sigma \bar{\dot{D}}(\bar{t})$, and consider the transformation

$$x = \int (q(\bar{t}))^{1/2} d\bar{t} \tag{2.103}$$

and note

$$\frac{dw}{d\bar{t}} = \frac{dx}{d\bar{t}}\frac{dw}{dx}, \qquad \frac{d^2w}{d\bar{t}^2} = \left(\frac{dx}{d\bar{t}}\right)^2 \frac{d^2w}{dx^2} + \frac{d^2x}{d\bar{t}^2}\frac{dw}{dx} \tag{2.104}$$

then we have the transformed equation

$$\left(\frac{dx}{d\bar{t}}\right)^2 \frac{d^2w}{d\bar{t}^2} + \left(\frac{d^2x}{d\bar{t}^2} + p(\bar{t})\frac{dx}{d\bar{t}}\right)\frac{dw}{dx} + q(\bar{t})w = 0 \tag{2.105}$$

which will have constant coefficients if

$$\left(\frac{dx}{d\bar{t}}\right)^2 = q(\bar{t}), \quad \iff \quad x = \int (q(\bar{t}))^{1/2} dt \tag{2.106}$$

and,

$$x'' + p(\bar{t})x' = \text{const.}, \quad \iff \quad \frac{q'(\bar{t}) + 2p(\bar{t})q(\bar{t})}{2(q(\bar{t}))^{3/2}} = \text{const.} \tag{2.107}$$

This condition will be satisfied for any piecewise constant dose rate function, such as the function defined during treatment time interval $(\bar{t}_i, \bar{t}_f)$ as

$$\bar{\dot{D}}(\bar{t}) = \bar{\dot{D}}_0 \cdot (\mathcal{H}(\bar{t} - \bar{t}_i) - \mathcal{H}(\bar{t} - \bar{t}_f)). \tag{2.108}$$

In this case, the ratio becomes

$$\frac{q'(\bar{t}) + 2p(\bar{t})q(\bar{t})}{2(q(\bar{t}))^{3/2}} = \frac{0 + 2(1+\epsilon\omega) f_R \Sigma \bar{\dot{D}}_0}{2(f_R \Sigma \bar{\dot{D}}_0)^{3/2}} \tag{2.109}$$

$$= \frac{(1+\epsilon\omega)}{(f_R \Sigma \bar{\dot{D}}_0)^{1/2}} = \text{const.} \tag{2.110}$$

Since $\bar{\dot{D}}_0$ is a constant, the ratio in Equation 2.110, and the ODE given in Equation 2.105 will have constant coefficients, and thus a closed form solution, given in Equation 2.62.

For the case of a decaying dose rate, given by

$$\dot{D}(\bar{t}) = \dot{D}_0 \exp(-\delta/\lambda \bar{t}) \tag{2.111}$$

we have

$$\frac{q'(\bar{t}) + 2p(\bar{t})q(\bar{t})}{2(q(\bar{t}))^{3/2}} = \frac{-\delta \bar{\dot{D}}(\bar{t}) + 2(1+\epsilon\omega) f_R \Sigma \bar{\dot{D}}(\bar{t})}{2(f_R \Sigma \bar{\dot{D}}(\bar{t}))^{3/2}} \tag{2.112}$$

$$= \frac{-\delta/\lambda + 2(1+\epsilon\omega)) f_R \Sigma}{2(f_R \Sigma)^{3/2} (\exp(-\delta/\lambda \bar{t}))^{1/2}}, \tag{2.113}$$

which will not be a constant, since the denominator involves a function of time. In this case, power series solutions may be found to arbitrary order [75].

2.4.2 Multiple fractions

The clinical and practical reality of therapeutic applications of radiation in the context of cancer is one of single daily fractions administered over the course of several weeks. Closed form solutions to a biological effect model must take into account intra- and inter-fraction repair, and must be generalizable to situations in which the timing between and during treatment delivery can be varied. In the case of piecewise constant dose rate ($\bar{\dot{D}}_i = \text{const.}$), the solutions for the RMF model easily extend to n fractions, which is often the case in the clinical scenario. To make more clear the multi-fraction solution formalism, stated in dimensional form, the RMF predicted biological effect at time t after dose n is given by

$$F(t) = \sum_{i=1}^{n} \Sigma \dot{D}_i t_i (1 - f_R(1-\gamma)) + [\lambda(\theta - \gamma\eta) + \gamma\omega\eta(1-\eta)] \int_0^t L(\tau) d\tau \tag{2.114}$$

where the integral is broken into pieces determined by whether treatment is on or off with treatment time T_i and time between treatments τ_i, given by

$$\int_0^t L(\tau)d\tau = \sum_{i=1}^{n}\left(\int_{T_{i-1}}^{T_i} L_D(t')dt' + \int_{T_i}^{T_i+\tau_i} L_N(t'')dt''\right). \tag{2.115}$$

For n identical treatments with constant time between fractions $\tau_i = \tau$ for all i, with the assumption that all repair processes are completed between fractions, i.e. that the time between fractions is sufficiently long (see Section 2.7.5), then the approximation of fraction independence implies the surviving fraction is given simply by $SF = S^n$. Neglecting incomplete inter-fraction repair is equivalent to assuming $L(\tau) = 0$. If the kinetic process which determines the conversion of potentially rejoinable DSBs ($L(t)$) into lethal DSBs ($F(t)$) can be shown to be much more rapid than the inter-fraction time duration (i.e. $\tau \to \infty$), then the simplification results in the formula

$$F(t) = \sum_{i=1}^{n} \Sigma\dot{D}_i t_i[(1 - f_R(1-\gamma))] + [\lambda(\theta - \gamma\eta) + \gamma\omega\eta(1-\eta)]\int_{T_{i-1}}^{T_i} L_D(t')dt' \tag{2.116}$$

for $n = 1, ..., n$ where n is the number of fractions. Since sub-lethal repair processes will be completed,

$$\int_{T_i}^{T_i+\tau_i} L_N(t'')dt'' \approx 0 \tag{2.117}$$

between treatment fractions, i and $(i+1)$. The role of inter-fraction repair is further explored in Section 2.7.5.

2.5 Kinetic models and approximations

In the case where analytic solutions to models of radiation-induced DNA damage and repair cannot be found, approximations are often made to reduce the problem to a more simple, solvable form. Small doses and dose rates are assumed which permit linearization of the problem. For two species models, regardless of their biological interpretations, a reduction of order which reduces the formalism to linear problems will necessarily yield solutions with similar forms. In particular, consider the two species generalization of the RMF model,

given by

$$\frac{dl}{dt} = A\dot{D} - Bl - Cl^2 \tag{2.118}$$

$$\frac{df}{dt} = a\dot{D} + bl + cl^2 \tag{2.119}$$

where the variables l and f correspond to potentially rejoinable DSBs and fatal DSBs in the RMF model, but is not necessarily the case in other contexts. Parameters A, B, C, a, b, c are assumed to be constant, independent of time or dose rate. A simple perturbation analysis in what is assumed to be the small parameter C associated with the quadratic term, yields biological effect predictions $f(\infty)$ of the form

$$f(\infty) = \alpha(a, A, b, B, c, C)D + \beta(a, A, b, B, c, C)D^2. \tag{2.120}$$

It has been argued that the linear-quadratic biological effect relationship is a consequence of many different forms of models, the two species model being the most related to the RMF formalism [30, 77]. Although this is certainly the case, it presents two problems in the context of contemporary radiobiology from a mathematical perspective.

1. Independent of any model formulation, surviving fraction data has repeatedly demonstrated "linear" and "quadratic" relationships. However, a polynomial function of dose is not the only means to describe dose-response data and recapitulate these relationships. Any model which aims to *predict* dose-response data must behave in a qualitatively linear-quadratic manner in order to be consistent with observed data, but other nonlinear formalisms may provide similar, if not better predictions. Further, many of the nonlinear models of DNA damage and repair are "linearized," so they are tractable mathematically, and reduce to equivalent forms.

2. To leading order, and small solutions, higher order polynomials will appear equivalent in a small solution regime. Beyond a critical value in the independent variable, higher order terms and the inherent nonlinearities in the problem will play an increasingly important role. The exclusion of higher order nonlinear terms lies contrary to the construction of the model. This is particularly the case in the high dose per fraction stereotactic radiosurgery dose regime.

Carlson has already derived a first order approximation to the RMF model [37] solutions assuming the small parameter η to give the solution formalism

$$F(\infty) = \alpha'(f_R, \theta, \lambda, \eta, \gamma, \Sigma, \bar{z}_F)D + \beta'(f_R, \theta, \lambda, \eta, \gamma, \Sigma, \bar{z}_F)D^2 \tag{2.121}$$

where

$$\alpha' = [1 - f_R(1-\theta)]\Sigma + \kappa \bar{z}_F (f_R \Sigma)^2, \quad \beta' = (\kappa/2)(f_R\Sigma)^2, \quad \text{with} \quad \kappa = [\eta/\lambda][\gamma - \theta]. \tag{2.122}$$

The functional form of analytic solutions to the RMF model stated in Equation 2.92 can be generalized as

$$F(\infty) = AD + B\ln(f(\dot{D}, T)) \tag{2.123}$$

where the coefficients A and B are functions of the model parameters, and the argument of the natural logarithm is a functional form involving the model parameters, with dependence on dose rate $\dot{D}$ and treatment time T. This solution is *not* simply a power series in dose D. however it is able to recapitulate surviving fraction data across a spectrum of radiation conditions, see Sections 2.7.4 and 2.7.2. The extent to which a surviving fraction expression is a power series in dose, as given in the LQ model and linearizations of other kinetic models, versus the linear-log solution formalism given by exact solutions to the RMF model is the focus of the remainder of the Chapter.

2.5.1 Lea-Catcheside dose-protraction factor

When derived from kinetic models as described above, the "mechanistic" perspective on the LQ model includes the Lea-Catcheside dose-protraction function which arises from first-order repair kinetics and is not strictly a power series in dose. From the "empirical" model perspective, the dose-protraction function is included as a "correction" term in the linear-quadratic formalism. This function is often assigned the letter G, which takes two arguments: the first-order repair rate constant λ and the dose irradiation time T, with the dose function itself defined by the temporal variation (or not) of the dose rate. The function is given in the form of an integral in order to allow for spatial and temporal variation in dose delivery,

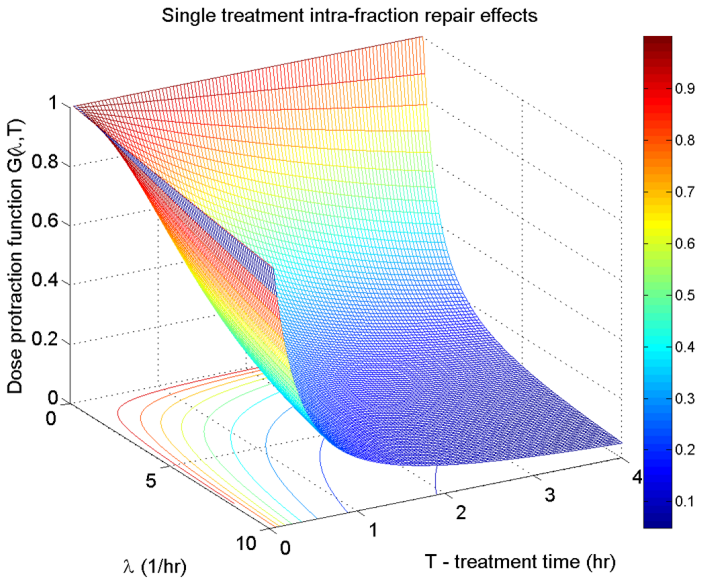

Figure 2.11: Single fraction intra-fraction repair effects defined by the Lea-Catcheside dose-protraction function [155]. The function takes values between zero and one. For a fixed repair rate constant λ, greater than ≈ 2 /hr, the dose-protraction function precipitously drops from unity towards zero as the irradiation time increases. Similarly, for a fixed irradiation time, the intra-fraction repair effects can range from modest, near unity, to near zero. Note that for $\lambda < 1$ /hr, the function $G(\lambda, \dot{D}, T) \approx 1$ for all T.

$$G(\lambda, \dot{D}, T) = \frac{2}{D^2} \int_0^T \int_0^t \exp(-\lambda(t' - \tau)) \dot{D}(\tau) \dot{D}(t') dt' d\tau. \tag{2.124}$$

The dose-protraction function is viewed as a correction to the β parameter in the linear-quadratic model to account for prolonged radiation delivery times so that

$$SF = \exp(-\alpha D - \beta G(\lambda, \dot{D}, T) D^2). \tag{2.125}$$

For a single fraction dose with constant dose rate, the integral in Equation 2.124 can be computed, and the resulting dose protraction function $G(\lambda, T)$ is given by

$$G(\lambda, T) = \frac{2}{(\lambda T)^2} \left(e^{-\lambda T} + \lambda T - 1 \right). \tag{2.126}$$

It is easy to see that for a single fraction, as the radiation time $T \to 0$, the protraction function $G(\lambda, T) \to 1$, with an application of L'Hospital's rule,

$$\lim_{T\to 0} G(\lambda, T) = \lim_{T\to 0} \left(\frac{2}{(\lambda T)^2} \left(e^{-\lambda T} + \lambda T - 1 \right) \right) \tag{2.127}$$

$$\overset{\left[\frac{0}{0}\right]}{\underset{\text{H}}{=}} \lim_{T\to 0} \frac{(-e^{-\lambda T} + 1)}{\lambda T} \tag{2.128}$$

$$\overset{\left[\frac{0}{0}\right]}{\underset{\text{H}}{=}} \lim_{T\to 0} e^{-\lambda T} = 1. \tag{2.129}$$

The behavior of the protraction function in terms of the repair rate constant λ, constant dose rate and irradiation time T can be seen in Figure 2.11. When the function takes values close to zero, the quadratic term of the LQ surviving fraction also goes to zero, yielding a purely linear relationship between dose and log surviving fraction. Note that for $\lambda < 1$ /hr, and a constant dose rate, the function $G(\lambda, T) \approx 1$ for all T and no protraction effects are seen.

2.5.2 Second-order perturbation expansion

In response to arguments that first order approximations produce similar dose-response relationships [30], we considered a second order expansion of the RMF model to be compared to a first order linearization. Carrying out a power series expansion to second-order will result in an one or more higher order terms in the expression for the biological effect, yielding a cubic polynomial expression in dose. For the dimensional RMF model given in Equations 2.4, and 2.5, we consider extending the expansion to a second order term in the dimensional form of the RMF model for a single irradiation so that it can be directly compared to the expansion investigated by Carlson [37], namely, let

$$L(t) \approx L_0 + \eta L_1(t) + \eta^2 L_2(t). \tag{2.130}$$

First, we integrate Equation 2.4 representing the rate of change of potentially rejoinable DSBs with respect to time,

$$\int_0^\infty \frac{dL}{dt} = \int_0^\infty f_R \Sigma \dot{D}(t) dt - (\lambda + \eta\omega) \int_0^\infty L(t) dt - \eta \int_0^\infty L^2(t) dt \tag{2.131}$$

where $\omega \equiv f_R \bar{z}_F \Sigma$, and note that

$$\int_0^\infty \frac{dL}{dt} = L(\infty) - L(0) = 0 \tag{2.132}$$

since we assume there are no DSBs prior to irradiation at some time $t > 0$ and all potentially rejoinable DSBs are either fatally or non-fatally rejoined as $t \to \infty$. With the cumulative dose expressed as

$$D = \int_0^\infty \dot{D}(t)dt \tag{2.133}$$

we have the resulting integral equation for $L(t)$ given by

$$0 = f_R \Sigma D - (\lambda + \eta\omega) \int_0^\infty L(t)dt - \eta \int_0^\infty L^2(t)dt. \tag{2.134}$$

Substituting our expansion $L(t) \approx L_0 + \eta L_1(t) + \eta^2 L_2(t)$ into the integral Equation 2.134, we have

$$0 = f_R \Sigma D - (\lambda+\eta\omega) \int_0^\infty (L_0+\eta L_1(t)+\eta^2 L_2(t))dt - \eta \int_0^\infty (L_0+\eta L_1(t)+\eta^2 L_2(t))^2 dt. \tag{2.135}$$

Equating powers of η, we have to zeroth order,

$$\eta^0 : \quad 0 = f_R \Sigma D - \lambda \int_0^\infty L_0(t)dt \tag{2.136}$$

which gives

$$\int_0^\infty L_0(t)dt = \frac{f_R \Sigma D}{\lambda}. \tag{2.137}$$

To first order, we have

$$\eta^1 : \quad 0 = \lambda \int_0^\infty L_1(t)dt - \omega \int_0^\infty L_0(t) - \int_0^\infty L_0^2(t)dt \tag{2.138}$$

which gives an expression for $\int_0^\infty L_1(t)dt$ as

$$\int_0^\infty L_1(t)dt = \frac{-1}{\lambda} \left[\omega \int_0^\infty L_0(t)dt + \int_0^\infty L_0^2(t)dt \right]. \tag{2.139}$$

Now if we substitute Equation 2.130 into the original ODE for $L(t)$ given in Equation 2.4, we have

$$\begin{aligned} L_0'(t) + \eta L_1'(t) + \eta^2 L_2'(t) &= f_R \Sigma \dot{D}(t) - (\lambda + \eta\omega)(L_0 + \eta L_1(t) & (2.140) \\ &+ \eta^2 L_2(t))\eta(L_0 + \eta L_1(t) + \eta^2 L_2(t))^2 & (2.141) \end{aligned}$$

where the hash indicates differentiation with respect to time, $' \equiv d/dt$. Equating powers of η, we have to zero order,

$$\eta^0 : \quad L_0'(t) = f_R \Sigma \dot{D}(t) - \lambda L_0(t). \tag{2.142}$$

This first order equation is straight forward to solve, using an integrating factor $e^{\lambda t}$,

$$\frac{d}{dt}\left[e^{\lambda t} L_0(t)\right] = e^{\lambda t} f_R \Sigma \dot{D}(t) \tag{2.143}$$

$$L_0(t) = f_R \Sigma e^{-\lambda t} \int_0^t e^{\lambda \tau} \dot{D}(\tau) d\tau \tag{2.144}$$

which satisfies the initial condition $L_0(t=0) = 0$. Similarly, to first order, we have

$$\eta^1 : \quad L_1'(t) = -\lambda L_1(t) - \omega L_0(t) - L_0^2(t). \tag{2.145}$$

We again use an integrating factor $e^{\lambda t}$, to give

$$\frac{d}{dt}\left[e^{\lambda t} L_1(t)\right] = -e^{\lambda t}[\omega L_0(t) + L_0^2(t)] \tag{2.146}$$

$$L_1(t) = -e^{-\lambda t}\left[\omega \int_0^t e^{\lambda \tau}\left(L_0(\tau) + L_0^2(\tau)\right) d\tau\right] \tag{2.147}$$

which satisfies the initial condition $L_1(t=0) = 0$. To compute $\int L_0^2(t)dt$, we use integration by parts as follows

$$\int_0^\infty L_0^2(t)dt = L_0(\tau) \cdot \int L_0(\tau)d\tau \Big|_0^\infty - \int_0^\infty \left(\frac{d}{dt} L_0(t)\right) L_0(\tau) d\tau \tag{2.148}$$

$$\int_0^\infty L_0^2(t)dt = \frac{(f_R \Sigma)^2}{2\lambda}\, GD^2 \tag{2.149}$$

where G is defined by

$$G \equiv \frac{2}{D^2} \int_0^\infty \int_0^t e^{-\lambda(t-\tau)} \dot{D}(t) \dot{D}(\tau) d\tau dt. \tag{2.150}$$

This is the classical Lea-Catcheside dose-protraction function which arises from first-order linear repair processes [155]. Now we consider the expansion of L in η in the differential equation for lethal DSBs. We first express Equation 2.5 in integral form, and note that

$$\int_0^\infty \frac{dF}{dt} = F(\infty) - F(0) = F(\infty) \tag{2.151}$$

since it is assumed that there are no fatal DSBs prior to irradiation, $F(t=0)=0$. Substituting Equation 2.130 into Equation 2.5 and integrating from zero to infinity gives

$$\begin{aligned} F(\infty) &= (1-f_R)\Sigma D + (\theta\lambda+\gamma\eta\omega)\int_0^\infty (L_0(t)+\eta L_1(t)+\eta^2 L_2(t))dt & (2.152)\\ &+ \gamma\eta\int_0^\infty (L_0(t)+\eta L_1(t)+\eta^2 L_2(t))^2 dt. & (2.153)\end{aligned}$$

Carlson has already evaluated the terms to zeroth and first order [35], so we consider the second order terms, $\mathcal{O}(\eta^2)$, which are

$$2\gamma\eta^2\int_0^\infty L_0(t)L_1(t)dt, \quad \gamma\omega\eta^2\int_0^\infty L_1(t)dt, \quad \text{and} \quad \theta\lambda\eta^2\int_0^\infty L_1(t)dt. \tag{2.154}$$

The terms involving $\int_0^\infty L_1(t)dt$ are straight forward to compute from Equation 2.155, using Equations 2.137, and 2.149,

$$\int_0^\infty L_1(t)dt = \frac{-1}{\lambda}\left[\omega\frac{f_R\Sigma D}{\lambda}+\frac{(f_R\Sigma)^2}{2\lambda}GD^2\right]. \tag{2.155}$$

These terms are linear and quadratic in dose, D. The mixed integral involving both zero and first order approximations of $L(t)$ will be computed with integration by parts. For the integral

$$2\gamma\eta^2\int_0^\infty L_0(t)L_1(t)dt, \tag{2.156}$$

let $dv = L_1(t)dt$ and $u = L_0(t)$, so that

$$dv = L_1(t) \quad \rightarrow \quad v = \int L_1(t)dt \tag{2.157}$$

which is given in Equation 2.155. To compute du, we use the fundamental theorem of calculus

$$\begin{aligned} u = L_0(t) &= e^{-\lambda t} f_R\Sigma\int_0^t e^{\lambda\tau}\dot{D}(\tau)d\tau & (2.158)\\ du = dL_0(t) &= f_R\Sigma\left(-\lambda L_0(t) + e^{-\lambda t}\left[e^{\lambda\tau}\dot{D}(\tau)\right]_0^t dt\right) & (2.159)\\ du &= f_R\Sigma(-\lambda L_0(t)+\dot{D}(t)) & (2.160)\end{aligned}$$

and note that $\dot{D}(t=0)=0$. The product $uv|_0^\infty$ is identically zero, since $L_0(\infty)=0$ and $L_0(0)=0$. The remainder of the integral can now be computed by first integrating with

respect to τ as

$$
\begin{aligned}
-\int_0^\infty v du &= -\int_0^\infty \int_0^\infty L_1(\tau) f_R\Sigma(-\lambda L_0(t) + \dot{D}(t)) d\tau dt && (2.161)\\
&= \frac{(f_R\Sigma)^2}{\lambda^2}\int_0^\infty \left(\omega D + \frac{f_R\Sigma}{2} D^2 G\right)\left(-\lambda L_0(t) + \dot{D}(t)\right) dt && (2.162)\\
&= \frac{(f_R\Sigma)^2}{\lambda^2}\int_0^\infty \Big(-\omega\lambda D L_0(t) + \omega D\dot{D}(t) \ldots && (2.163)\\
&- \frac{\lambda f_R\Sigma}{2} D^2 G L_0(t) + \frac{f_R\Sigma}{2} D^2 G\dot{D}(t)\Big) dt && (2.164)
\end{aligned}
$$

since the dose-protraction function G is a constant determined by the repair rate λ and the irradiation time T, it is independent of t, and the integral reduces to

$$
\begin{aligned}
\int_0^\infty v du &= \frac{(f_R\Sigma)^2}{\lambda^2}\left(-\omega\lambda D\int_0^\infty L_0(t)dt + \omega D\int_0^\infty \dot{D}(t)dt \ldots && (2.165)\\
&- \frac{\lambda f_R\Sigma}{2} D^2 G\int_0^\infty L_0(t)dt + \frac{f_R\Sigma}{2} D^2 G\int_0^\infty \dot{D}(t)dt\right) && (2.166)\\
&= \left[2\gamma\eta^2\omega\left(\frac{f_R\Sigma}{\lambda}\right)^2(1 - f_R\Sigma)\right] D^2 \ldots && (2.167)\\
&+ \left[2\gamma\eta^2 G\left(\frac{(f_R\Sigma)^3}{2\lambda^2}\right)(1 - f_R\Sigma)\right] D^3, && (2.168)
\end{aligned}
$$

using Equations 2.133 and 2.137 to compute the integrals for $\dot{D}(t)$ and $L_0(t)$ respectively. Thus the mixed integral given in Equation 2.156 contributes to quadratic and now cubic powers of the total dose, D. The other two terms are given simply by

$$
\begin{aligned}
\gamma\eta^2\omega\int_0^\infty L_1(t)dt &= \left[\frac{-\gamma\eta^2\omega^2 f_R\Sigma}{\lambda}\right] D - \left[\frac{\gamma\eta^2(f_R\Sigma)^2 G}{2\lambda}\right] D^2 && (2.169)\\
\theta\gamma\eta^2\int_0^\infty L_1(t)dt &= \left[\frac{-\theta\eta^2\omega f_R\Sigma}{\lambda}\right] D - \left[\frac{\theta\eta^2(f_R\Sigma)^2 G}{2\lambda}\right] D^2. && (2.170)
\end{aligned}
$$

Substituting these into Equation 2.152 for $F(\infty)$ and grouping terms in powers of D, we have

$$F(\infty) = \alpha D + \beta G D^2 + \delta G D^3 \qquad (2.171)$$

where the coefficients are given in ascending powers of η,

$$
\begin{aligned}
\alpha &= (1 - f_R)\Sigma + \theta f_R\Sigma + \frac{\eta}{\lambda}[\gamma - \theta]\omega f_R\Sigma - \frac{\gamma\eta^2\omega^2 f_R\Sigma - \theta\eta^2\omega f_R\Sigma}{\lambda} && (2.172)\\
\beta &= \frac{\eta}{2\lambda}[\gamma - \theta](f_R\Sigma)^2 - \frac{[\gamma - \theta](\eta f_R\Sigma)^2}{2\lambda} + 2\gamma\eta^2\omega\left(\frac{f_R\Sigma}{\lambda}\right)^2\frac{(1 - f_R\Sigma)}{G} && (2.173)\\
\delta &= 2\gamma\eta^2\left(\frac{f_R\Sigma}{\lambda}\right)^2(1 - f_R\Sigma). && (2.174)
\end{aligned}
$$

All terms of order $\mathcal{O}(\eta^2)$ are newly derived, beyond Carlson 2008 [37], including the entire

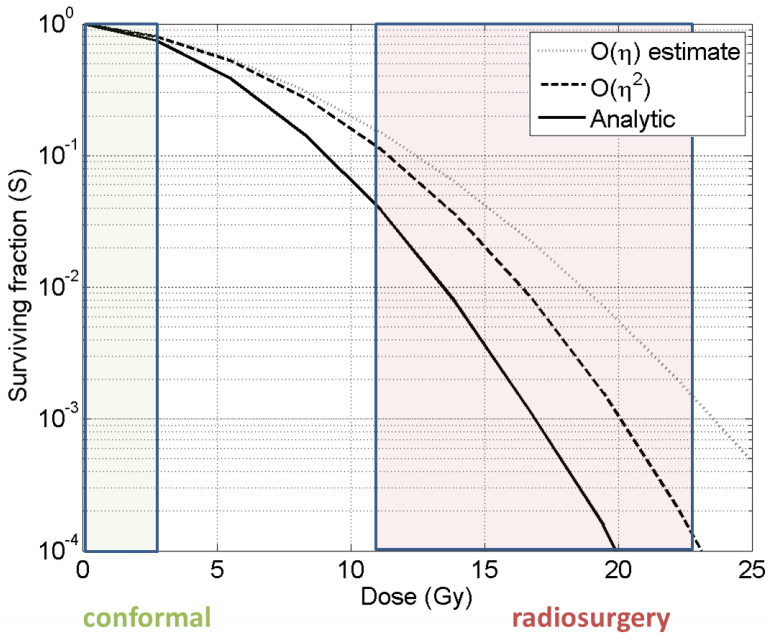

Figure 2.12: First and second order approximations to the RMF model predicted surviving fraction. The approximation agrees well with the exact solution at low doses of 0–2 Gy but diverges significantly around 5 Gy, suggesting that this approximation will not be accurate even to the order of magnitude in the high dose per fraction radiosurgery dose regime.

cubic term $\delta G D^3$. It is convenient to redefine terms to clarify the order of terms within the aggregate α, β and δ coefficients in order to illustrate the role of the dose-protraction function G and η on the higher order approximations. Let the subscript (i, j) indicate the order of the term with respect to η, and index the terms within that order, so that

$$\alpha_{0,1} = (1-(1-\theta)f_R)\Sigma, \quad \alpha_{1,1} = \left(\frac{[\gamma-\theta]}{\lambda} f_R \Sigma \omega\right)\eta, \quad \alpha_{2,1} = \left(\frac{[\gamma\omega+\theta]}{\lambda} f_R \Sigma \omega\right)\eta^2 \tag{2.175}$$

$$\beta_{0,1} = 0, \quad \beta_{1,1} = \left(\frac{1}{2}\frac{[\gamma-\theta]}{\lambda}(f_R\Sigma)^2\right)\eta, \tag{2.176}$$

$$\beta_{2,1} = \left(\frac{1}{2}\frac{[\gamma+\theta]}{\lambda}(f_R\Sigma)^2\right)\eta^2, \quad \beta_{2,2} = \left(2\gamma\omega\left(\frac{f_R\Sigma}{\lambda}\right)^2(1-f_R\Sigma)\right)\eta^2 \tag{2.177}$$

$$\delta_{2,1} = \frac{\beta_{2,2}}{\omega} = \left(2\gamma\left(\frac{f_R\Sigma}{\lambda}\right)^2(1-f_R\Sigma)\right)\eta^2. \tag{2.178}$$

Ordering terms in powers of η and grouping terms involving the dose protraction function G, to reflect those previously estimated by Carlson, we see

$$F(\infty) = \overbrace{(\alpha_{0,1} + \alpha_{1,1})D + \beta_{1,1}GD^2}^{\text{zero and first order terms}} - \overbrace{\alpha_{2,1}D + (\beta_{2,2} - \beta_{2,1}G)D^2 + \delta_{2,1}GD^3}^{\text{second order terms}}. \quad (2.179)$$

The difference in predicted surviving fraction ($SF = \exp(-F(\infty))$) between the exact solution, first and second order approximations can be seen in Figure 2.12. As expected, the approximations hold only for small solutions, in the dose range of approximately 0–2 Gy, and diverge significantly beyond that range.

The higher order terms reduce the linear contribution to cell killing in α, an additional contribution to quadratic cell killing, inversely proportional the the dose-protraction, countered by a reduction in the quadratic cell killing proportional to G, as well as the inclusion of a cubic cell killing term, proportional to G. This is also seen in the non-dimensionalization of the system in section 2.3.4. The ratio λ/η is conceptually similar to α/β in the LQ model, illustrated in Figure 2.10.

Second order terms $\beta_{2,2}$ and $\delta_{2,1}$ vanish when

$$1 - f_R\Sigma = 0, \quad \iff \quad f_R\Sigma = 1 \quad (2.180)$$

that is, when the product of the fraction of instantaneously created potentially rejoinable DSBs and the number of DSBs created per Gy, per cell is unity. That is, when f_R is relatively small, $f_R = \mathcal{O}(10^{-2})$, which implies a large percentage of the instantaneously created DSBs are inherently unrejoinable and thus fatal. This would be the case in high LET radiation where relatively fewer ionization events occur and a dominant linear dose-response relationship is often seen. Further, high LET radiation is associated with increased DNA damage complexity, which produces prolonged repair times and may also produce intrinsically unrepairable DSBs [102].

First order correction terms vanish when

$$\gamma - \theta = 0, \quad \iff \quad \gamma = \theta \quad (2.181)$$

that is, when the proportion of one-track induced DSBs that undergo fatal first order misrepair or fixation is equal to the proportion of fatal binary exchanges between two DSBs

created via one-track or two-track action are equal. This would be the case in low LET radiation where many ionization events take place, and the dose-response relationship is dominantly nonlinear, perhaps quadratic. Figure 2.12 illustrates the difference between the true analytical solution and its first and second order approximations increases with dose. The decreasing quality of the approximation for doses outside the 0–2 Gy single daily fraction range compels the use of the full nonlinear model for dose-response data which extends beyond this range.

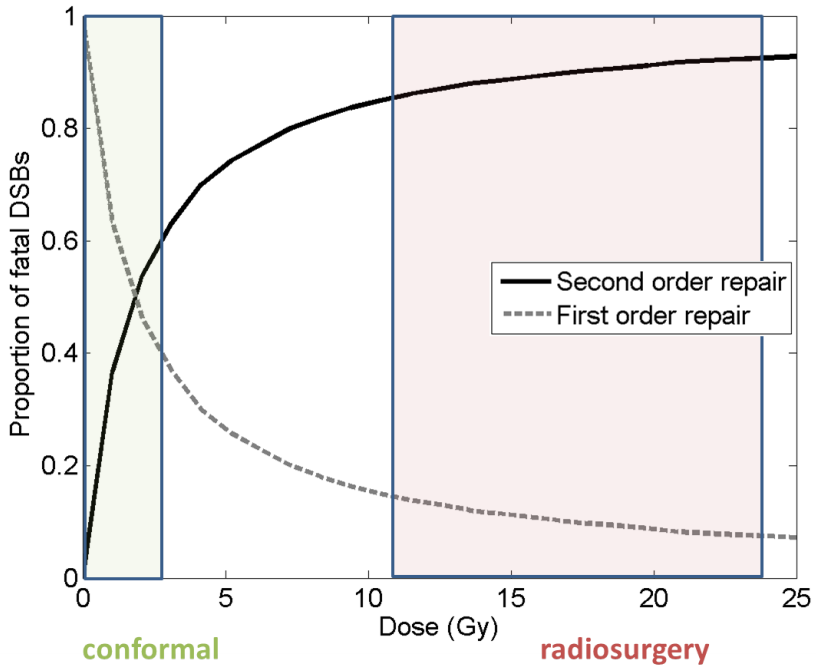

Figure 2.13: Relative proportions of fatal DSBs, composed of first and second-order misrepair processes. As expected, for doses less than 3 Gy, the first order repair processes dominate over the pairwise rejoining resulting from inter-track damage, determined by the quadratic term in Equation 2.4 for potentially rejoinable DBSs $L(t)$. However, the entire remainder of the dose range is dominated by nonlinear second order misrepair kinetics. This suggests the quadratic terms in DNA repair kinetic models such as the RMF should not be ignored or approximated in the radiosurgery high dose regime, and may play an "equal" role in the low dose regime of 0–3 Gy conformal therapy.

2.6 Conformal versus radiosurgery

Clinical challenge High dose per fraction radiosurgery treatments may induce intra-fraction repair, that is, DNA repair processes taking place during the prolonged irradiation time, which can last up to one hour or more of "beam on" time, particularly for large lesions (see Table 2.2). A significant clinical challenge lies in translating high dose per fraction radiation into a meaningful biological effect, with the still unresolved debate as to the applicability of the LQ model at doses beyond 10 Gy, in the SRS dose regime. To address this clinical challenge, we compare RMF and LQ model predictions for high and low dose per fraction therapies to demonstrate the role of intra-fraction repair, and potential mechanisms underlying the failure–or not–of the LQ at high doses. Clinical dose rates are estimated for conformal and SRS in Table 2.2.

Repair kinetics We can use the RMF model to investigate relative contributions of first and second order repair kinetics in the low dose conformal and high dose per fraction radiosurgery dose regimes. Although dose-response data consistently demonstrates a linear-quadratic relationship between absorbed dose and surviving fraction of cells, even into the high dose per fraction ($>$ 10 Gy) dose regime, the mechanisms of repair and cell death pathways are debated [111]. Using the estimations for clinical dose rates given in Table 2.2, and biological parameters estimated from 250 keV x-ray data [37], we solve the RMF model for a range of absorbed doses which include the conformal and radiosurgery dose ranges. As illustrated in Figure 2.13, for doses less than 3 Gy, the first order repair processes dominate over the pairwise interactions determined by the quadratic term in Equation 2.4 for potentially rejoinable DBSs $L(t)$. However, the entire remainder of the space is dominated by the ηL^2 term in the ODE for $F(t)$ given in Equation 2.5. This suggests the quadratic terms in DNA repair kinetic models such as the RMF should not be ignored or approximated in the radiosurgery high dose regime, and may play an "equal" role in the low dose regime of 0–3 Gy conformal therapy, as expected from the linearization analysis.

Characterizing intra-fraction repair Although the RMF model permits saturation of sublethal damage, fatal damage is a monotonically increasing function in time during

Treatment	"Beam on" time (Δt)	Dose (ΔD)	Avg. dose rate ($\dot{D} = \Delta D/\Delta t$)
conformal	2 min	2 Gy	1 Gy/min, 60 Gy/hr
radiosurgery	20 min	20 Gy	1 Gy/min, 60 Gy/hr

Table 2.2: Approximate dose rates for conformal and stereotactic radiosurgery computed based on a typical treatment for an average size brain lesion, not greater than 4 cm in radius. "Beam on" time excludes setup and beam repositioning.

irradiation, however, potentially rejoinable DSBs saturate, as shown in Figure 2.9. Several radiobiological modeling investigations [75, 30, 37] *assume* an acute dose so that there is no repair during treatment, regardless of the relative time scales of dose delivery and repair. Specifically, if we consider the dimensional form of the equation for potentially rejoinable DSBs, given in Equation 2.4 and assume no repair during the irradiation time as in [75], so that the number of potentially rejoinable DSBs at the end of a single fraction with constant dose rate $\dot{D}_0$ as defined in Equation 2.16 and duration T is given by,

$$\int_0^\infty \frac{dL}{dt} = \int_0^\infty f_R \Sigma \dot{D}_0 d\tau = f_R \Sigma D. \tag{2.182}$$

We see from the explicit intra-fraction solution given by $\bar{L}(\bar{t})_D$ that the rate of change of $\bar{L}(\bar{t})$ is most strongly influenced by the quantities $(1 + \epsilon\omega)$ and $\sqrt{\Phi}$. Ironically, this is made most clear not by the original differential equation for the rate of changed of $\bar{L}$, but rather from the derivative of the solution as a function of time, given by

$$\begin{aligned} \frac{d}{d\bar{t}}\left[\bar{L}(\bar{t})_D\right] &= \frac{d}{d\bar{t}}\left[\frac{1}{2\epsilon\Sigma D}\left[(1+\epsilon\omega) - \sqrt{\Phi}\tanh(\Psi)\right]\right] &(2.183)\\ &= \frac{\Phi}{2}\left[1 - \tanh^2(\Psi)\right]. &(2.184)\end{aligned}$$

Since $0 \leq |\tanh(x)| < 1$, then $\tanh^2(x) << 1$, the least upper bound on $\bar{L}(\bar{t})'$ is given by

$$\sup_{0\leq t\leq T} \frac{d}{d\bar{t}}\left[\bar{L}(\bar{t})_D\right] = \frac{\Phi}{2}. \tag{2.185}$$

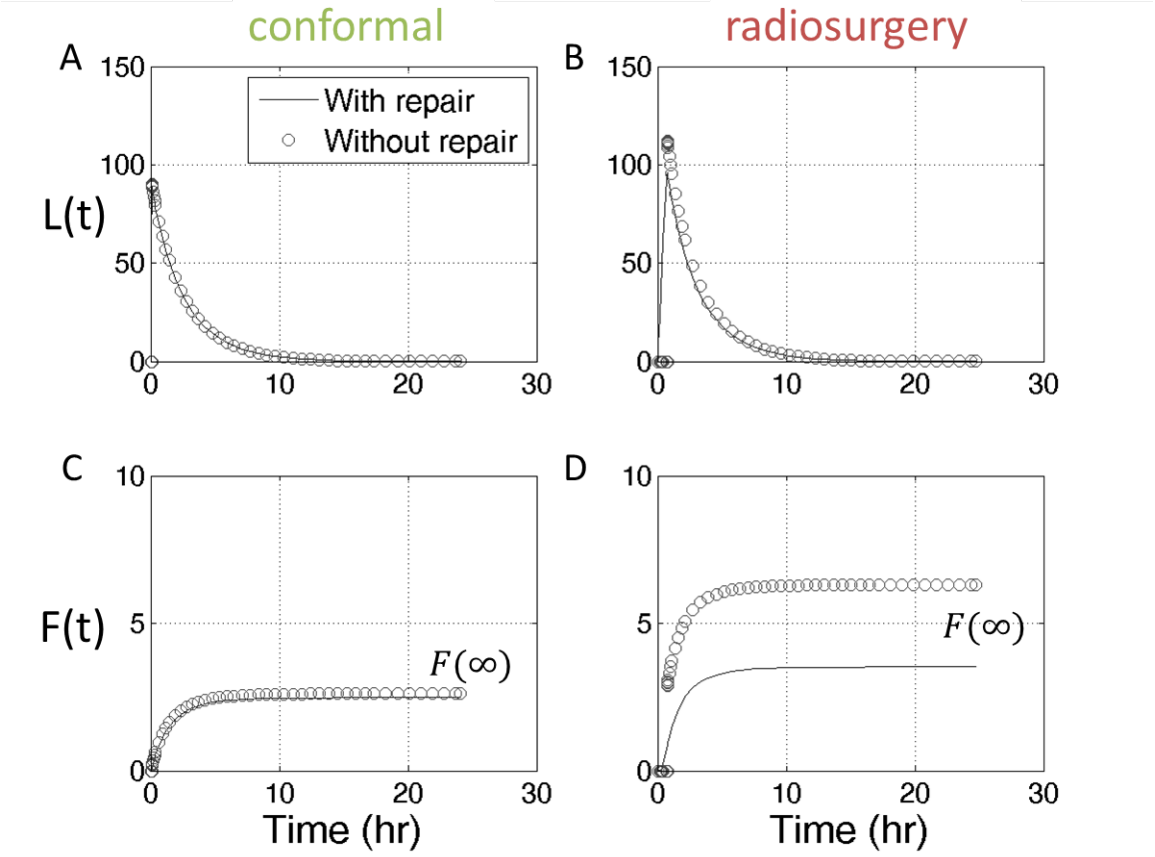

Figure 2.14: Left column A and C: Conformal delivery consisting of 1.8 Gy delivered in 5 mins at a constant dose rate of $\dot{D} = 18$ Gy/hr. Right column B and D: stereotactic radiosurgery dose 14 Gy delivered at the same dose rate, for a protracted delivery time of 45 min. The circles represent the linearized model which neglects intra-fraction repair. The line represents the full nonlinear, time dependent solution of the RMF model. Biological effect is given by the long term behavior of the fatal lesion creation ($F(\infty)$) in C and D, summarized in Table 2.6.

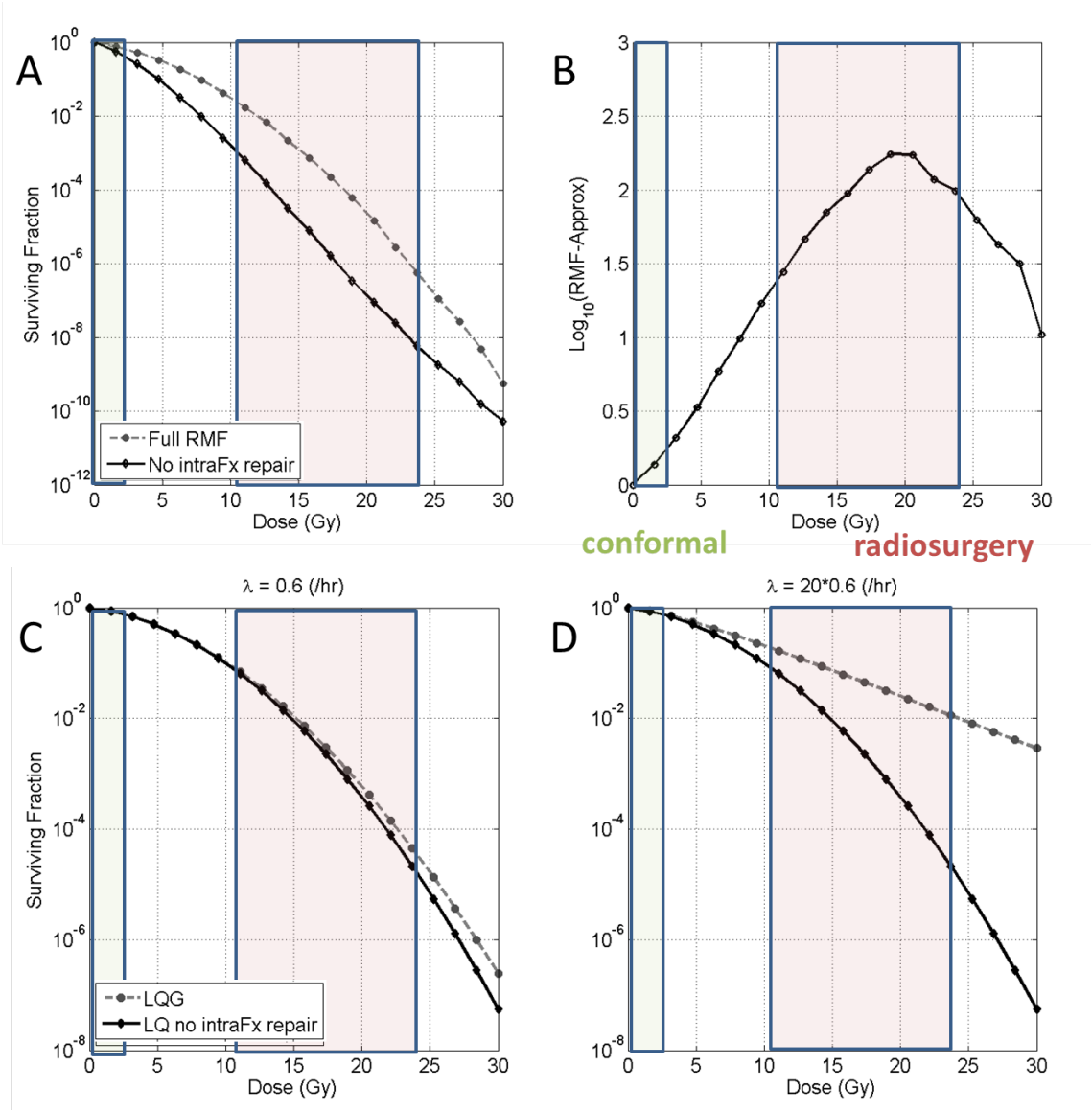

Figure 2.15: A: RMF with and without intra-fraction repair for a fixed constant dose rate of 55 Gy/hr. B: Log base 10 of the difference between the RMF and acute dose delivery approximation indicating a maximum difference between the curves at approximately 20 Gy, in the radiosurgery dose regime, where the model predictions differ by two orders of magnitude. C: Linear-quadratic dose-response curve with and without the dose-protraction factor $G(\lambda, T)$. The dose-protraction function does not produce drastically different surviving fraction predictions. D: By increasing the repair rate 20 fold, we see differences in the repair-no repair situation comparable to that seen in the RMF model, suggesting that for the *same repair constant parameter* (λ), the RMF and LQ models produce drastically different estimates of intra-fraction repair.

	Conformal	Radiosurgery
$\dot{D}$ (Gy/hr)	18	18
D (Gy)	1.8	14
T (min)	5	45
With repair: $F(\infty)$	2.5	**3.5**
Without repair: $F(\infty)$	2.6	**6.3**

Table 2.3: Intra-fraction repair effects for protracted stereotactic delivery shown in Figure 2.14. The difference between the simplified model and the full nonlinear RMF solution is small for conformal therapy, but are three orders of magnitude different for radiosurgery. Biological effect (BE) is given by the long term fatal damage yield $F(\infty)$.

The rate at which the solution approaches its fixed point is also determined by the relative rate at which the hyperbolic tangent approaches unity. Therefore we consider the relative contributions of the y-intercept versus slope of the line defined by the argument function

$$\Psi = \arg(\tanh) = \frac{\sqrt{\bar{\Phi}}}{2}\bar{t} + \tanh^{-1}\left(\frac{(1+\epsilon\omega)}{\sqrt{\bar{\Phi}}}\right). \tag{2.186}$$

Clearly the rate of change of this linear function is given by the slope, $\sqrt{\bar{\Phi}}/2$, however, the range of the inverse hyperbolic tangent function is all real numbers, $-\infty < \tanh^{-1}(x) < \infty$. This leads us to consider the argument of this function, as the y-intercept could be sufficiently large as to overwhelm the contribution of the slope to bringing the argument to infinity and thus the tanh function value towards unity and $\bar{L}(\bar{t}) \to \bar{L}_{k2}$. Specifically, how close is the argument of $\tanh^{-1}$ to unity,

$$\frac{(1+\epsilon\omega)}{\sqrt{\bar{\Phi}}} \approx 1? \tag{2.187}$$

We can expand the square root in the denominator using the generalized binomial theorem,

$$(a+b)^n \approx a^n + na^{n-1}b + ... \tag{2.188}$$

which is valid for integer and rational values of n and is a good approximation when $a > b$. Using this, we have

$$\sqrt{\bar{\Phi}} = \sqrt{(1+\epsilon\omega)^2 + 4\epsilon\Sigma f_R \bar{\dot{D}}} = (1+\epsilon\omega) + \frac{2\epsilon\Sigma f_R \bar{\dot{D}}}{(1+\epsilon\omega)} + ... \tag{2.189}$$

Substituting this into our relation and simplifying, we see

$$\frac{(1+\epsilon\omega)}{\sqrt{\bar{\Phi}}} \approx 1 \quad \Rightarrow (1+\epsilon\omega) \approx \sqrt{\bar{\Phi}} \tag{2.190}$$

$$(1+\epsilon\omega) \approx (1+\epsilon\omega) + \frac{2\epsilon\Sigma f_R \bar{\dot{D}}}{(1+\epsilon\omega)} \tag{2.191}$$

$$0 \approx \frac{2\epsilon\Sigma f_R \bar{\dot{D}}}{(1+\epsilon\omega)} \tag{2.192}$$

which will not hold in general for our parameter ranges. The numerator will be $\mathcal{O}(10^{-2})$ and the denominator $\mathcal{O}(1)$. This reinforces the previous result observed by differentiating $\bar{L}(\bar{t})_D$ with respect to time: the principle driver of the rate of change is Φ. This reveals the strong dependence on the ratio η/λ, since $f_R, \bar{z}_F, \bar{\dot{D}}, \Sigma$ are parameters to be determined from the physical properties of the irradiation. Therefore the RMF model *predicts* differential behavior as a function of radio-sensitivity based on the physical properties of the radiation.

2.6.1 Comparing RMF and LQG forms of intra-fraction repair

The incorporation of first-order repair mechanisms in the linear-quadratic dose-response model can be directly included in a nonlinear regression with the data so that 3 parameters, α, β, λ are simultaneously optimized to fit the data. An alternative approach is to consider the direct translation of the linear repair rate constant λ from the estimates in the RMF model to the LQ, to be treated as a constant and optimize only α and β. To illustrate the minimal impact the incorporation of the dose-protraction function $G(\lambda, T)$ has on the LQ dose-response predictions for a constant dose rate, we compute $G(\lambda, T)$ for the clinically relevant dose-rate regime data and fix λ, taken from the RMF data regression, results shown in Table 2.4.

Given that the LQ coefficients vary by 2–3 orders of magnitude across the dose-rate range, a 9% decrease in β provided by G is a small modulation of the relative contribution of two-track action, pairwise misrepair effects taking place in the high dose regime, as suggested by the RMF model. Fitting the linear-quadratic model to wide ranging dose data is challenging and a recognized limitation of the model, not easily accommodated at high doses without additional terms [65, 76].

Lethal DNA damage overestimates The effect of assuming acute dose delivery and thus overestimating the net lesion creation during a prolonged dose delivery time, as in radiosurgery can be illustrated with the analytic closed form solution of the dimensional RMF model (Equations 2.4 and 2.5), see Figure 2.14. Conformal delivery consisting of 1.8 Gy delivered in 5 mins at a constant dose rate of $\dot{D} = 18$ Gy/hr and stereotactic radiosurgery with dose 14 Gy delivered at the same dose rate, for a protracted delivery time of 45 min are simulated with the RMF model. The difference between the simplified model which assumes acute dose delivery and therefore no repair during the irradiation time and the full nonlinear RMF solution is small for conformal therapy, but are three orders of magnitude different for radiosurgery, as measured by the biological effect (BE), given by the long term fatal damage yield $F(\infty)$, summarized in Table 2.6.

We contrast the RMF model *predicted* intra-fraction repair to that predicted from the LQ model, which accounts for intra-fraction repair via the Lea-Catcheside dose protraction factor in Figure 2.15. The RMF is solved with and without intra-fraction repair for a fixed, clinically deliverable dose rate of 55 Gy/hr, and the LQ model with and without the dose-protraction factor $G(\lambda, T)$ for the same value of the first-order repair rate, λ. For the LQ model, the dose-protraction function does not produce drastically different surviving fraction predictions, in contrast to the difference between the RMF and acute dose delivery approximation indicating a maximum difference between the curves at approximately 20 Gy, in the radiosurgery dose regime, where the model predictions differ by two orders of magnitude. Only by increasing the repair rate 20 fold, we see differences in the repair-no repair situation comparable to that seen in the RMF model, suggesting that for the *same repair constant parameter* (λ), the RMF and LQ models produce drastically different estimates of intra-fraction repair. Table 2.4 demonstrates the modest effect of the dose-protraction function at clinical dose rates. This suggests that the linearization of damage and repair models which produce the dose-protraction correction function do not sufficiently account for the contribution of nonlinear repair processes at high doses per fraction. This speaks directly to the debate over the relevance of the LQ model in the high dose regime.

$G(\lambda, T)$	Dose (Gy)			
$\lambda = 0.6$ / hr	2	5	10	20
45 Gy/hr	0.9912	0.9781	0.9570	0.9167
55 Gy/hr	0.9928	0.9821	0.9646	0.9311

Table 2.4: The linear-quadratic dose-protraction function for single acute doses evaluated at $\lambda = 0.6$ /hr for two clinically deliverable dose rates. The dose-protraction function effectively modulates the coefficient of the quadratic component of cell killing (β). In this context, the scale factor decreases the empirical β by at most 9% (45 Gy/hr at 20 Gy) in stark contrast to the drastic effects of intra-fraction repair predicted by the RMF model for the same parameters (Figure 2.15).

2.7 Model comparisons

To more directly address how the RMF model differs from the LQ and the linearized RMF model in the context of clinical challenges, we test these models against data for a wide range of doses, dose rates, energies and fraction timing scenarios. Specifically, we wish to compare the predictions from the analytical solution to the RMF model to the LQ and linearized RMF, given below.

Linear-quadratic with dose-protraction, (LQG)

$$SF = \exp\left(-\alpha D - \beta G(\lambda, T) D^2\right) \tag{2.193}$$

where

$$G(\lambda, \dot{D}, T) = \frac{2}{D^2} \int_0^T \int_0^t \exp(-\lambda(t' - \tau)) \dot{D}(\tau) \dot{D}(t') dt' d\tau. \tag{2.194}$$

The analytic solution to the RMF model given in dimensional form in Equations 2.4 and 2.5,

$$SF = \exp\left(\hat{\alpha} \int_0^T \dot{D}(\tau') d\tau' + \hat{\beta} \int_0^\infty L(\tau) d\tau\right) \tag{2.195}$$

with

$$\hat{\alpha} = \Sigma(1 - f_R(1 - \gamma)), \quad \hat{\beta} = [(\theta\lambda + \eta\omega) - \gamma(\lambda + \eta\omega)], \tag{2.196}$$

and we also consider the linearized version of the RMF model in terms of the linear-quadratic equivalent coefficients (LQG_{RMF}), derived in Section 2.5.2,

$$\alpha' = [1 - f_R(1-\theta)]\Sigma + \kappa\bar{z}_F(f_R\Sigma)^2, \quad \beta' = (\kappa/2)(f_R\Sigma)^2 \tag{2.197}$$

with

$$\kappa = [\eta/\lambda][\gamma - \theta]. \tag{2.198}$$

2.7.1 Parameter estimation

One advantage of the RMF model over other DNA kinetic models is the estimation parameters by properties of the radiation beam. The DSB yield Σ and mean specific energy $\bar{z}_F$ can be estimated from Monte Carlo simulations of radiation transport [37], and conceptually, the value of γ, which is the probability that a single radiation track creates either a discentric or ascentric fragment (fatal) or reciprocal translocation (non-fatal) should be equal to $1/2$ to reflect the decreasing rate of dicentric fragments created after the time of irradiation [102].

This leaves the parameters η, λ and θ to be estimated from data. Recall further that the rate constant η is related to inter-track exchanges between two DNA fragments, and governs the nonlinear contribution towards the rate of DSB repair or fatal misrepair. The rate constant λ is determines the rate of repair or misrepair for intra-track damage, and is conceptually equivalent to the rate constant found in the Lea-Catcheside dose protraction function. To some degree, these rate constants should be intrinsic to the cell line, with radiation-specific effects determined by Σ and $\bar{z}_F$.

With $\Sigma, \bar{z}_F, \gamma$ fixed parameters, we now regard the surviving fraction as a function of the free parameters λ, η and θ, so that for the analytically derived surviving fraction to the full RMF model (SF_{RMF}), we have clear dependence on the free parameters

$$SF_{\mathrm{RMF}} = SF_{\mathrm{RMF}}(\lambda, \eta, \theta) \tag{2.199}$$

and the LQ-equivalent parameters from the linearized RMF solution (α', β'),

$$\alpha' = \alpha'(\lambda, \eta, \theta), \quad \beta' = \beta'(\lambda, \eta, \theta). \tag{2.200}$$

Nonlinear regression To perform the nonlinear regression to estimate model parameters, we use the nlinfit routine in the MATLAB statistics toolbox, which performs a Levenberg—Marquardt damped Gauss—Newton gradient descent method [127]. This routine requires an initial guess of the values of the model parameters to be estimated, denoted by b_0. Trial and error was used to estimate b_0 which provided good model-data agreement to within 95% confidence intervals. In order to test the robustness of the regression and whether the optimization identified a local minimum, several initial values were used to perform the regression after a suitable starting value was identified.

2.7.2 Dose-rate effects

The effect of the rate of dose delivery can have a substantial impact on cell killing, due to the increasingly stochastic nature of ionization events as the dose rate goes to zero [48], relevant to brachytherapy. Surviving fraction dose-response data in which the dose rate is varied is a good a test of the versatility of an ODE radiation-induced DNA damage and repair model. Using nonlinear regression, biological parameters that are considered variable across cell populations and conditions are the repair constants λ, η and θ, the binary fatal misrepair probability. Chinese hamster ovarian (CHO) cell line 10B2 from Stackhouse and Bedford (1993) under a range of radiation doses, from 0–20 Gy and dose rates 0.12–45 Gy/hr [170, 171] and C3H 10T1/2 mouse cells ranging from 0–70 Gy and dose rates of 0.06–55 Gy/hr (Wells and Bedford 1983) [205] are used to estimate model parameters. These two cell lines have distinct radiosensitivities which allows us to compare model parameters in the two situations. CHO 10B2 cells behave similarly to late-responding tissues (low α/β or low η/λ), and C3H 10T1/2 cells are more similar to early-responding tissues (large α/β, η/λ) [170].

Using the CHO and C3H datasets, the RMF, LQG and SF_{RMF} models are fitted to the data using nonlinear regression for a wide range of dose-response from 0 – 70 Gy and dose rates from 0.12–55 Gy/hr within clinically deliverable ranges for both 3D conformal and radiosurgery treatments (Figure 2.16) [171].

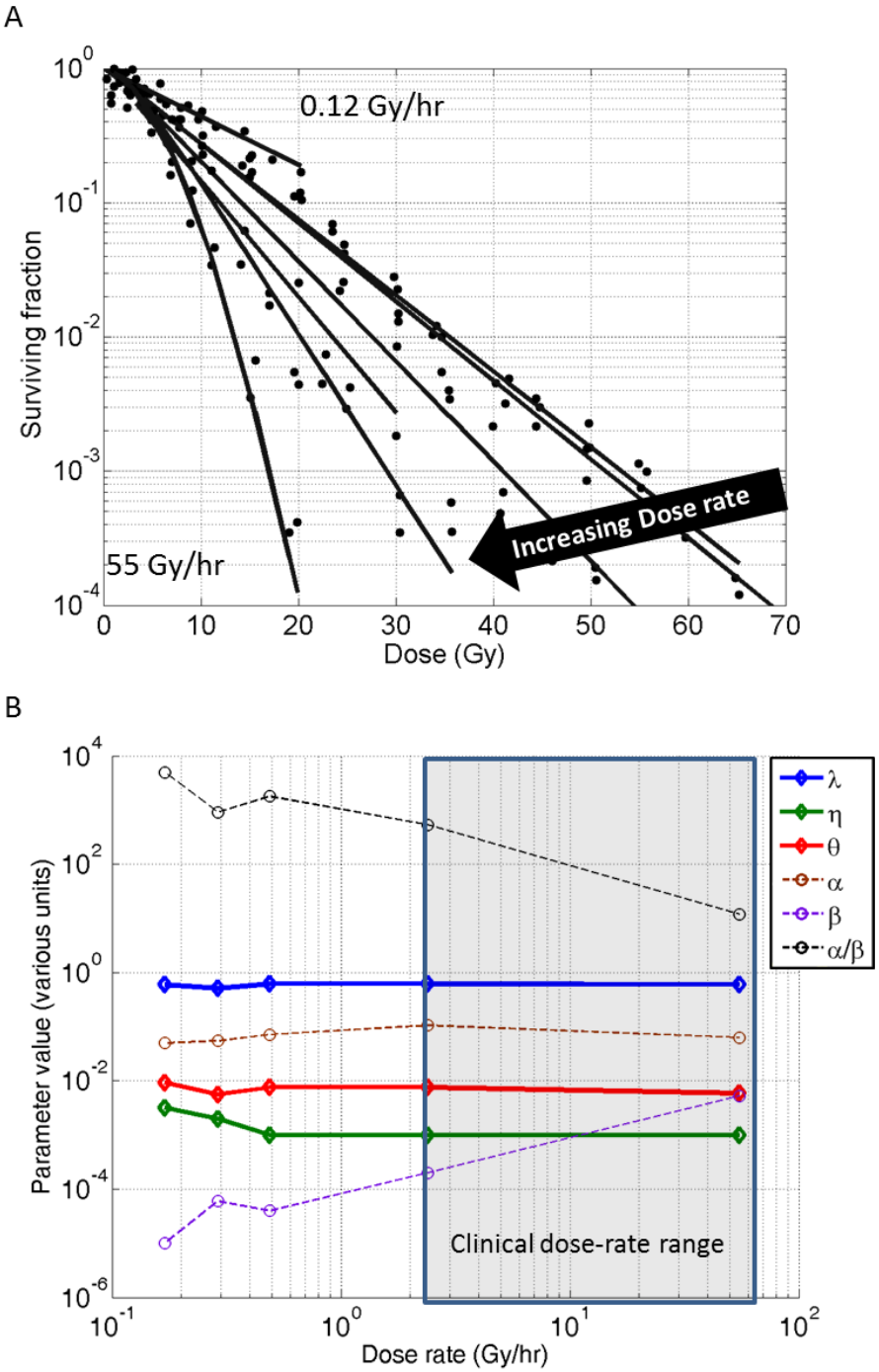

Figure 2.16: A: RMF model is fit to each dose rate set from 0.12–55 Gy/hr, and *predicts* a wide range of behaviors from linear at low and very high doses (70 Gy) and nonlinear "shoulder" behavior at intermediate doses and dose rates (CHO and C3H data sets from Wells (1983) and Stackhouse (1993) [205, 171]). B: RMF parameters λ, η, θ and LQG α, β estimated fit to a range of dose-rate data demonstrates small variation in fitted parameter values across a wide range of dose rates, the grey box represents dose-rates that are clinically relevant. Linear-quadratic model parameters vary at least two orders of magnitude in this range, while RMF model parameters are stable to within a single order of magnitude, suggesting the RMF model is more robust to stable predictions, particularly within the clinical dose-rate range.

2.7.3 Parameter stability

The linear-quadratic model fits to the CHO and C3H data sets demonstrates wide variation across clinical dose rate ranges, suggesting the RMF model is more robust to predictions within this dose delivery range, see Figure 2.16. The wide variation in α and β is due to the coefficient of the nonlinear term going to zero as the dose-response relationship behaves more linearly and less parabolically. This is not required of the RMF model, which is capable of producing both linear and parabolic dose-response curves with relatively little change in the parameters. Because the full mechanistic model is solved which is not simply a power series in dose, the affects of intra-fraction repair and low dose rate damage induction are included in the dynamic process. The incorporation of first-order repair in a linear-quadratic model fit to the data does not sufficiently account for dose-rate effects. The RMF model therefore is more robust to *predictions* produced by modeling changes in the experimental conditions, in contrast to *fitting* parameters. The inability of the LQ to predict dose-rate effects as measured by dose-response data without large variations in the parameters undermines confidence in the biological inferences which can be made from the fitted parameters.

Clinical dose rates In order to parameterize the RMF model at clinically deliverable dose rates, we estimate the average dose rate used for conformal and radiosurgery treatments by dividing the prescribed dose by an estimated average treatment time defined as the net "beam on" time. Using the definition of dose rate computed as in Equation 2.15, we compute ranges of dose rates for conformal and radiosurgery treatments to be roughly the same, at 1 Gy/min = 60 Gy/hr as follows in Table 2.2.

We restrict the data set fitting to the 45 and 55 Gy/hr data sets to estimate RMF model parameters that most closely resemble clinically deliverable dose rates from a linear accelerator, radiation source or cyclotron. RMF model predictions and 95% confidence intervals for these data sets are shown in Figure 2.17. The parameters estimated are shown in Table 2.5.

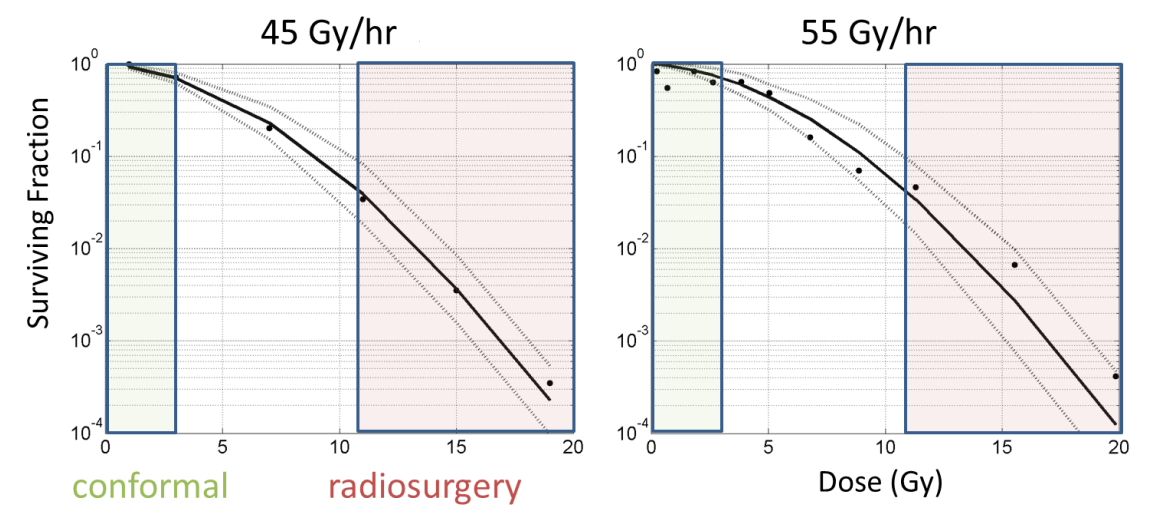

Figure 2.17: Radiation dose rates most closely resembling clinically deliverable therapy, as estimated in Table 2.2. Left: RMF model fit using nonlinear regression to vary repair rate constants λ and η as well as the fatal misrepair probability θ, with 95% confidence intervals to 45 Gy/hr data for C3H cells from Wells and Bedford (1983) [205]. Right: Same for 55 Gy/hr data for CHO cells from Stackhouse and Bedford (1993) [170]. Parameter estimates from this regression provide reasonable estimates of DNA repair times, summarized in Table 2.5.

2.7.4 Particle type and energy

Clinical challenge Heavy charged particles are increasingly of interest as a treatment for cancer. With heavy ions becoming more popular, there is an increased desire to use models to predict differential response beyond the "relative biological effectiveness" (RBE) between conventional photon or x-ray therapy and alternative particle types and energies (LET). That is, models which are able to capture a wide range of dose-response dynamics induced by high LET radiation.

The biological effects of particle energy deposition (LET) are incorporated in the RMF model through the parameters relating the energy and dose to double strand break induction and repair. Specifically, the number of DSBs induced per Gray of radiation, per giga-base pair of DNA (Σ) and the mean-specific energy ($\bar{z}_F$), are determined by LET [37]. Moreover, the fraction of DSBs that are potentially rejoinable (f_R) is inversely correlated with LET. As

Parameter	45 Gy/hr	55 Gy/hr
λ (/hr)	0.5946	0.6017
	(0.2498 - 0.9393)	(0.6006 - 0.6029)
η (pot. repairable	0.0010	0.0010
DSBs/hr)	(0.0010 - 0.0010)	(0 - 0.0037)
θ (% fatally	0.006	0.0059
misrepaired DSBs)	(0 - 0.0154)	(0 - 0.0165)

Table 2.5: Biological and adjustable parameters of the RMF model estimated from nonlinear regression on 45 Gy/hr data for C3H cells from Wells and Bedford (1983) [205] and 55 Gy/hr data for CHO cells from Stackhouse and Bedford (1993) [170]. Parentheses indicate 95% confidence intervals.

a test of these assumptions and their incorporation into a DNA damage and repair model, dose-response data Barendsen 1966 [18] for cells exposed to deuterons ($2H^+$) with kinetic energies from 3 MeV to 14.9 MeV (LET: 5.6–20 keV/μm) and to α particles ($4He^{2+}$) with energies from 3.1 to 26.8 MeV (LET: 24.6–200 keV/μm). Nonlinear regression is used to fit the RMF and LQG models (3 free parameters each) to 200 kVp x-ray data with absorbed dose rate of 29.19 Gy/hr, and doses from 0.5–13.9 Gy [17]. These parameters are then used to predict surviving fraction for different LETs by varying only Σ and $\bar{z}_F$, estimated for each energy using the MCDS algorithm [158].

The regression yielded estimates for parameters λ, η and θ which were applied to each of the 12 dose-response datasets, with only the physical parameters Σ and $\bar{z}_F$ adjusted based on the physical properties of the radiation. This process was performed using both the full RMF model, and its first order linear-quadratic approximation. Results are shown in Figure 2.18, revealing good qualitative agreement with the data for all energies/LETs, with mean absolute errors 4.71×10^{-4} and -2.4×10^{-3} for LQG and RMF respectively. Further, the distributions of absolute error between data and model prediction for RMF and LQG are not statistically different (paired t-test $p > 0.9$), suggesting that within this dose and energy range, the first-order linear approximation to the RMF model provides equal predictive

value. This is expected from the linearization analysis, and consistent with conventional wisdom that the LQ model is valid in the 0–10 Gy dose range. Further studies for doses beyond 10 Gy are needed to show significant differences between the nonlinear RMF model and the linearized approximation (LQG).

2.7.5 Inter-fraction repair

Split dose experiment RMF model parameter calibration is further refined with setting adjustable parameters with a split dose data set of CHO cells from Stackhouse and Bedford (1993) [171], in which two fractions of 8 Gy are delivered at a constant dose rate of 45 Gy/hr, with the time between fractions allowed to vary, see Figure 2.19. A time of zero corresponds to a single fraction of 16 Gy in which case the cell killing effect is additive due the absence of inter- or intra-fraction repair processes. Cell killing is maximized (i.e. surviving fraction is minimized) when no inter-fraction repair is involved. When the time between fractions extends beyond approximately six hours, the doses are effectively independent, and all repair processes have taken place between fractions. Nonlinear regression gives an estimate of the repair rate as $\lambda = 0.571$ /hr. If we consider this to be the characteristic repair time scale, so that the net repair rate λ_{net} is given by

$$\lambda_{\text{net}} = (\lambda + \eta\omega) \tag{2.201}$$

and consider the repair half time,

$$\lambda_{\text{net}} = \frac{\ln(2)}{\tau_{1/2}} \tag{2.202}$$

then $\tau_{1/2} \approx 1.2$ hrs. This implies that after approximately 5 hours $\approx 4\tau_{1/2}$, approximately 95% of repair should have taken place. This is consistent with the observed data in Figure 2.19 in which cell killing levels off after 6 hours between irradiation fractions. Moreover, the value of λ estimated from the regression is consistent with parameter values estimated from the 45 Gy/hr and 55 Gy/hr Wells and Stackhouse datasets (Figure 2.16, and Table 2.5).

2.8 Summary

Solutions and approximations Analytic solutions are found for the repair-misrepair fixation (RMF) DNA damage induction and repair ordinary differential equation model.

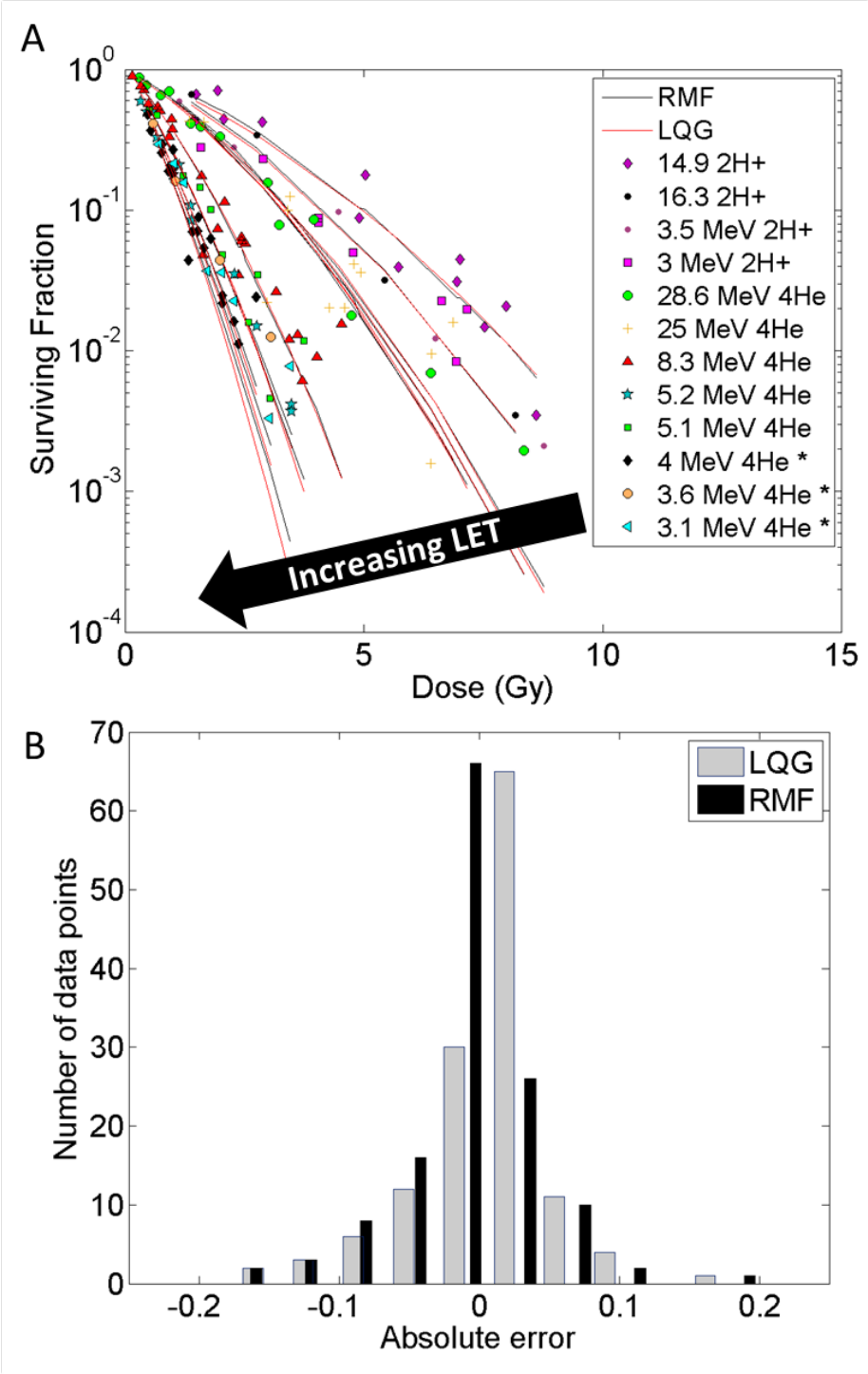

Figure 2.18: Dose-response data from Barendsen 1966 [18] for cells exposed to deuterons ($2H^+$) with LET from 5.6–20 keV/μm and to α particles ($4He^{2+}$) with LETs from 24.6–200 keV/μm. Nonlinear regression is used to fit the RMF and LQG models (3 free parameters each) to 200 kVp x-ray data [17]. These parameters are then used to predict surviving fraction for different LETs by varying only Σ and $\bar{z}_F$, estimated for each energy using the MCDS algorithm [158]. A) RMF and LQG model predictions and data for LETs ranging from 5.6–200 keV/μm. B) Absolute error between data and model prediction for RMF (black) and LQG (grey). Distributions of error are not statistically different (paired t-test $p > 0.9$), suggesting that within this dose and energy range, the first-order linear approximation to the RMF model provides equal *predictive value* in this dose range.

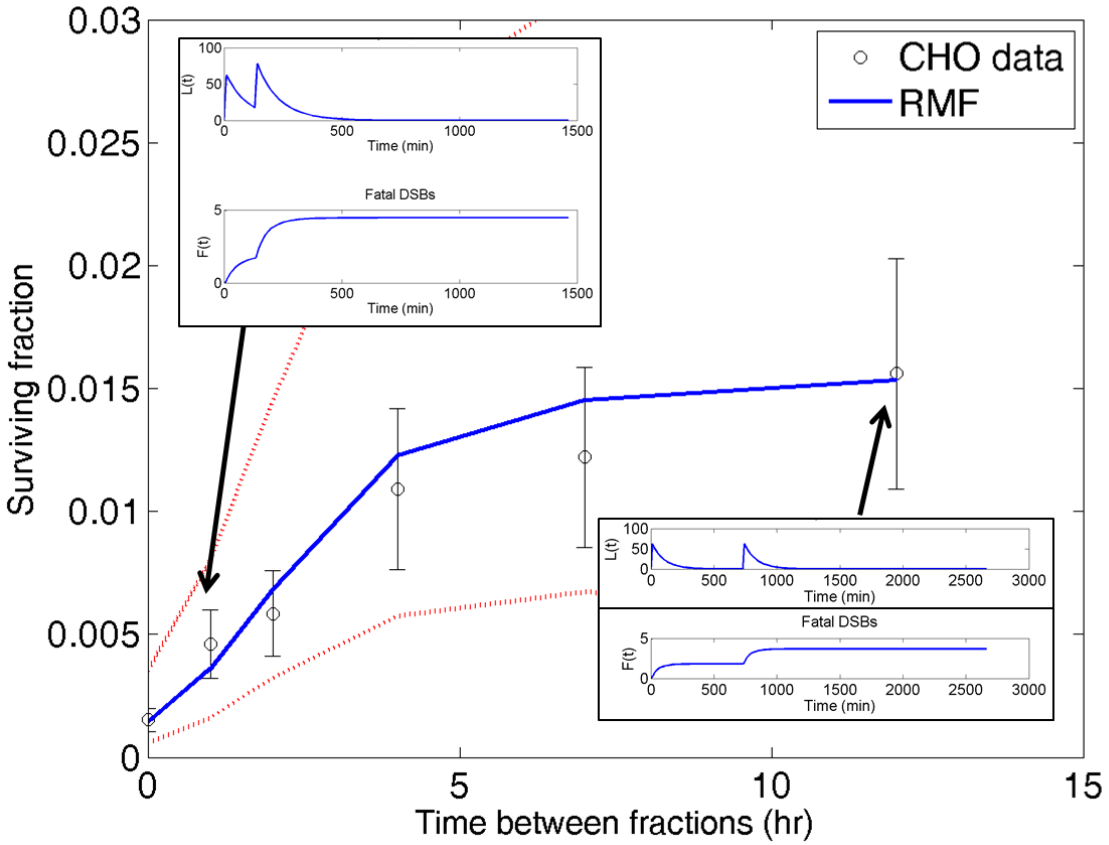

Figure 2.19: Surviving fraction of cells resulting from two fractions of 8 Gy are spaced apart by time τ on the horizontal axis with an estimated standard error of 30%, for CHO cells from Stackhouse and Bedford (1993) [171]. Solid line indicates RMF model prediction based on nonlinear regression with λ, η, θ adjustable parameters. Inset: upper left $\tau = 2$ hours. Lower right $\tau = 12$ hours.

The analytical solutions illustrate orders of magnitude differences between the linearized solution used pervasively in the literature and the analytic solution to the fully nonlinear model, Figures 2.12 and 2.15. Moreover, the role of intra-fraction repair has a maximum effect near 20 Gy for protracted doses such as those delivered during radiosurgery. The large differences in model predictions between the linearized and analytical solution to the model play an important role in model parameter estimation and biological inferences from those parameters.

Relevance to high dose per fraction radiosurgery This mathematical analysis speaks directly to a current debate regarding the relevance of mathematical models in high radiation dose treatment. The inability of the first-order repair processes included in the Lea-Catcheside dose protraction function to significantly affect the nonlinear term in the linear-quadratic dose-response model speaks to the necessity of consideration of fully nonlinear mechanistic models in this dose regime, Table 2.4 and Figure 2.15. Other extensions of the linear-quadratic model to include correction terms to accommodate high dose per fraction treatment such as radiosurgery are largely empirically driven and not mechanistic, which does not speak directly to the debate as to whether or not the linear-quadratic model is conceptually correct at high doses [77, 28, 203].

From a mathematical perspective, naive perturbation expansions without regard to relative size of terms (non-dimensionalization) in the nonlinear models are often invalid in the high dose per fraction dose regime and furthermore, ignore analytical solutions which are not prohibitively complicated to implement or analyze. Moreover, including additional terms in perturbation expansion solutions do not improve model predictions for high dose radiation, as these expansions are not valid in the dose range of interest (> 10 Gy) and in fact provide worse approximations to the solutions of the fully nonlinear model, Figure 2.12.

Model parameterization and predictive value Data-driven parameterization of the DNA damage model reveals improved model prediction and parameter stability across a wide range of radiation delivery dose rates compared to the current linear-quadratic model

paradigm, in which the model parameters must vary orders of magnitude in order to capture linear dose-response behavior seen at low dose rates, Figure 2.16. This suggests that the RMF and more generally, a class of nonlinear DNA damage induction and repair ODE models are capable of describing simple and complex DNA damage repair across a spectrum of dose and dose rate conditions which include the radiobiological challenges faced by high dose per fraction radiation treatment such as stereotactic radiosurgery. Response to, and effects of, radiation therapy is certainly more than DNA damage, and involves changes to the tissue micro-environment and can include more exotic phenomena such as the "bystander effect," whereby cells not directly exposed to ionizing radiation undergo necrotic or mitotic catastrophe cell death [33]. Further, micro-environmental variables such as oxygen concentration, radiation beam energy, particle type and quality all can have significant effects on DNA induction, repair and overall radiation response, many of these scenarios have been investigated with the RMF model [173, 37].

Making a distinction between fitting a model to data and *predicting phenomena* from a mechanistic model which is robust to a wide variety of experimental conditions is at the heart of these results. In the context of the debate regarding the appropriateness of the linear-quadratic model in the high dose per fraction regime, these results suggest that mechanistic models of DNA damage and repair are able to not only agree with empirical models at small doses (where linearizations are valid, resulting in power series dose-response functional forms), but are robust and valid in the high dose situation. Finally, the RMF model suggests that the fundamental mechanism of DNA repair lies in the nonlinear terms of the model which are not captured by empirical models or linearizations of the mechanistic model.

Chapter 3

PROLIFERATION, INVASION, RADIATION THERAPY (PIRT) MODEL FOR GLIOBLASTOMA

The form of a model depends on the question being asked of it. Continuum, density scale models, agent based models and stochastic / Monte Carlo models, each have a role in answering questions of the data that drives them, depending on the nature and scale of the problem reviewed in [14, 9]. The scale of the model is dictated by the scale of the data, and in this regard, we present a tumor cell density model which describes the macroscopic invasion and proliferation of malignant tumor cells throughout the brain on a scale which is observable by medical imaging.

Cancer is a dynamic biological process in which homeostatic regulation processes are inhibited or overcome, from the molecular to the organ scales. A useful analogy can be drawn to the world of physics, where mathematical models which describe observable phenomenon are potentially incompatible, or at least not subsuming of each other. Take for example the macroscopic phenomenon of a mass experiencing the force of gravity, perfectly described by Newton's law, $F = ma$, in contrast to the microscopic scale of and more complex standard model of quantum mechanics which describe interactions between atomic and sub-atomic particles. On the macroscopic scale of throwing a football, landing an airplane, or taking an elevator, the very simple $F = ma$ model perfectly describes any aspect of the time evolution of the location of a mass experiencing the force of gravity. This minimal model with *one parameter* is more than sufficient to recapitulate observed data, and make predictions of the same. In this model, virtually any object can be treated as a single point, located at the center of mass of the object. This model is clearly not sufficient to describe the strong and weak nuclear forces which bind the molecules which constitute the mass of the object, nor does it intend to. We present a mathematical model which is calibrated by, and is intended to give insight and predictions into the invasion of tumor cells throughout the brain via mass

transport of tumor cells under Fickian diffusion which proliferate with density-dependence, analogous to the macroscopic $F = ma$ scale.

3.1 Proliferation and invasion (PI) model

Gliomas are primary brain tumors which arise from glial cells in the brain [122]. Glioblastoma multiforme (GBM) is the most aggressive form of glioma, and is characterized by diffuse invasion of the normal appearing brain far beyond the bulk tumor mass. Median survival for a patient diagnosed with GBM is 12–15 months with the current standard of care [175, 174], which consists of surgical resection, radiation therapy concurrent with chemo-therapy, followed by "maintenance" chemotherapy until the disease progresses. The extensive invasion of tumor cells throughout the brain can be likened to an iceberg of invisible, "sub-clinical" disease illustrated in Figure 3.1, which can be found as far away as 4 centimeters from the bulk tumor [42] and cannot be seen intra-operatively, or revealed by medical imaging such as computed tomography (CT) or magnetic resonance imaging (MRI) [137]. This invasion of the brain paranchyma is influenced by the anatomy of the brain: tumor cells preferentially migrate along the axons of neurons composing the white matter, and move more randomly, and slowly, through the dense grey matter composed of neuronal bodies, glial cells, and other brain tissue which compose the cortical surface and some internal structures of the brain [69, 97, 176]. This differential motility of tumor cells throughout the brain presents a challenge to understanding the true extent of the sub-clinical disease, as tumor dispersal speeds can vary up to 100 fold between pioneering cells in white matter compared to the random Brownian motion characterizing the tumor cells in the core of the tumor and in grey matter [122, 97, 176].

Clinically, glioblastoma progression and response to therapy is monitored with MRI [206, 137]. For the last two decades, routine clinical imaging protocols for glioblastoma have consisted of T1-weighted and T2-weighted MRI sequences, with the addition of the gadolinium contrast agent on T1 MRI (T1Gd) as well as fluid attenuation inversion recovery (FLAIR) based on the T2 MRI [31]. The contrast agent in the T1Gd MRI will appear only where the blood brain barrier has been compromised. This is often the case in regions of tumor growth, where new blood vessels are created. The tumor-induced neo-vasculature is

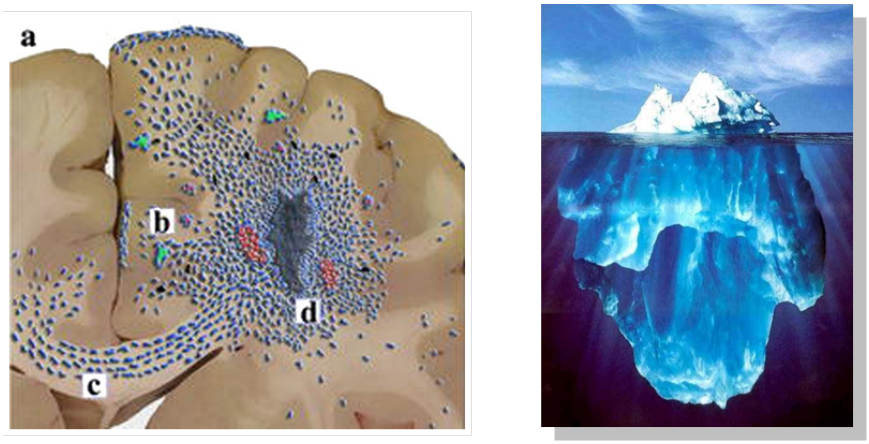

Figure 3.1: Left: Glioblastoma tumor cells migrate extensively throughout the brain, with differential motility between grey and white matter regions of the brain defining the migration patters and overall geometry of the tumor. Right: The extensive, diffuse infiltration of the normal appearing brain is often invisible, and can be likened to the submarine portion of an iceberg. Adapted from Claes et al. 2007 [43].

often malformed, tortuous and "leaky," to the extent that the gadolinium contrast agent is allowed to pass through. Therefore, regions of hyper-intensity on the T1Gd MRI correlate with high tumor cell density and "bulk tumor." In contrast, the T2 and FLAIR MRI modalities reflect vasogenic edema, or swelling, typically associated with inflammatory response to infiltrating tumor cells, at a much lower density than found on the T1Gd region, which is almost always a subset of the T2/FLAIR abnormality.

Our biologically-based model for glioma invasion and proliferation is based on the hypothesis that, from a clinical standpoint, gliomas can be quantitatively characterized by two net rates: proliferation (ρ) and invasion (D) (PI model) [176, 178]. Let $c = c(\mathbf{x}, t)$ represent the concentration of tumor cells per volume (mm^3) at a location $\mathbf{x} = (x, y, z)$ at time t where the domain $\mathcal{B}$ (brain) is closed and bounded. The model is a reaction-diffusion partial differential equation which describes both the net diffusion and proliferation of tumor

cells as follows:

$$\overbrace{\frac{\partial c}{\partial t}}^{\substack{\text{rate of change}\\ \text{of glioma cell}\\ \text{density}}} = \overbrace{\nabla \cdot (D(\mathbf{x})\nabla c)}^{\substack{\text{net dispersal}\\ \text{of glioma cells}}} + \overbrace{\rho c\left(1 - \frac{c}{K}\right)}^{\substack{\text{net proliferation}\\ \text{of glioma cells}}} \tag{3.1}$$

$$\mathbf{x} \in \mathcal{B}, \quad t \geq 0 \tag{3.2}$$

$$\mathbf{n} \cdot \nabla c = 0 \text{ on } \partial\mathcal{B}, \quad c((x_0, y_0, z_0), t = 0) = c_0, \tag{3.3}$$

$$D(\mathbf{x}) = \begin{cases} D_w & \text{if } \mathbf{x} \in \text{white matter} \\ D_g & \text{if } \mathbf{x} \in \text{grey matter} \\ 0 & \text{else} \end{cases} \tag{3.4}$$

where $D(\mathbf{x})$ is the spatially resolved diffusion coefficient with units mm^2/year, ρ is the net rate of proliferation per year, and K is the carrying capacity of the tissue assuming a 10 μm diameter spherical cell [27],

$$K \approx \frac{1 \text{ cell}}{5.24 \times 10^2 \mu\text{m}^3} \left(\frac{10^3 \mu\text{m}}{1 \text{ mm}}\right)^3 = 1.91 \times 10^6 \text{cells/mm}^3. \tag{3.5}$$

No flux boundary conditions $\mathbf{n} \cdot \nabla c = 0$ prevents cells from leaving the brain domain, $\mathcal{B}$, at its boundary $\partial\mathcal{B}$. This model allows the diffusion coefficient to be a tensor to account for the complex geometry and preferential directions for cell migration in the brain [97]. For the scalar case, the migration rate in white matter is considerably higher than that in grey matter, $D_w \gg D_g$. The "PI" model has been studied and analyzed extensively [176, 177, 180, 181, 183, 182] and many more, see Murray 2003, Volumes I and II for a summary [132, 133]. Quantification of glioma growth and invasion has been of interest for over 20 years, lead predominantly by neuropathologist Dr. Ellsworth C. Alvord Jr., as early as 1991 [6]. A review of mathematical modeling methods in glioblastoma is given by Hatzikirou et al. [86] with additional history provided by Harpold et al. [83] and clinical applications by Baldock et al. [14].

3.1.1 Fisher-KPP equation

The "PI" model is a variant on the Fisher-KPP equation from the classic papers by Fisher (1937) and Kolmogoroff (1937), famously studied by Fisher to model the propagation wave of advantageous genes in a population [62]. The KPP equation in one spatial dimension x and with unitless variables denoted with an overbar $^-$ is given by

$$\frac{\partial \bar{u}}{\partial \bar{t}} = \nabla^2 \bar{u} + \bar{u}(1-\bar{u}), \quad c(x, t=0) = f(x). \tag{3.6}$$

The spatial and temporal domains may be infinite, semi-infinite, or finite. A vast literature exists on this equation, which has been used extensively in genetics, biology, ecology, and here for the growth and proliferation of tumor cells [133]. The model describes migration in terms of a diffusion process via the spatial derivatives resulting from the Laplacian operator ∇, and density-dependent logistic growth. Although no closed-form solutions can be given for the Fisher-KPP equation, uniformly valid asymptotic approximations exist for the Cauchy problem defined on the infinite line, as well as a spatial and temporal characterization of the solution in terms of a traveling wave [132].

3.1.2 Proliferation-invasion model assumptions

The PI model assumes glioma cell invasion throughout the brain is a Fickian diffusion process with diffusion coefficient $D(\mathbf{x})$ (mm^2/year). The model also assumes logistic growth of the tumor cell population, so that the net proliferation rate, ρ (/year) is lower in regions of high cell density where $c \approx K$, than in regions of low cell density where c is much less than the carrying capacity K. It is further assumed that the T1Gd MRI is smaller than the T2 MRI during untreated growth, consistent with the association with high and low cell densities, respectively (see Figure 3.2).

Traveling wave solutions An essential characteristic of this model (4.1) is the formation of a traveling wave solution in the case of a spatially uniform diffusion coefficient $D(\mathbf{x}) = D$. In one spatial dimension with homogeneous diffusion, the PI model reduces to the classic Fisher-Kolmogoroff model

$$\frac{\partial c}{\partial t} = D\frac{\partial^2 c}{\partial x^2} + \rho c\left(1 - \frac{c}{K}\right), \tag{3.7}$$

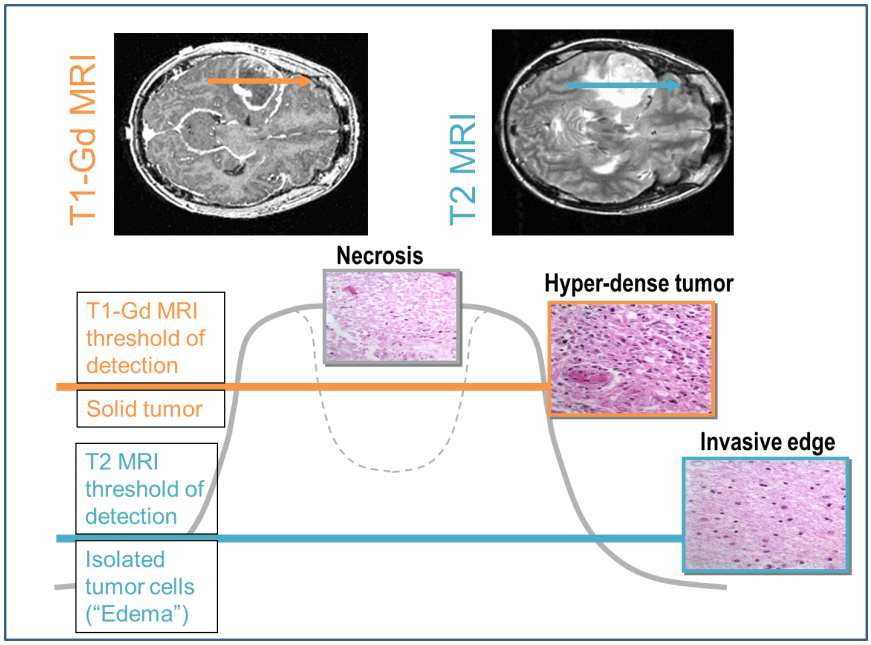

Figure 3.2: Tumor cell isodensities associated with MRI threshold of detection for T1-weighted gadolinium-enhanced (T1Gd) and T2-weighted MRI. T1Gd abnormality indicates regions of neoangiogenesis and increased tumor cell density, approximately 80% of the carrying capacity. T2 MRI abnormality indicates edema caused by microvascular proliferation and invading tumor cells, and reveals roughly 5-fold more tumor cell concentration, approximately 16% of the carrying capacity [49], where throughout the gradient, tumor cells are intermingled with normal brain [163].

$$c(x,0) = \delta(x), \ x \in \mathbb{R}. \tag{3.8}$$

with a Dirac delta point source initial condition. If a traveling wave solution exists of the form $c(x,t) = C(z)$ where $z = x - vt$ where v is the wave speed ($v > 0$), then the equation can be transformed into an ordinary differential equation,

$$DC'' + vC' + \rho C\left(1 - \frac{C}{K}\right) = 0 \tag{3.9}$$

where the prime $'$ indicates differentiation with respect to the traveling coordinate z. This second order nonlinear ordinary differential equation can be restated as a coupled pair of

first order equations as

$$C' = G \tag{3.10}$$

$$DG' = -vG - \rho C\left(1 - \frac{C}{K}\right). \tag{3.11}$$

This system (C, G) has two fixed points: (0,0) and (1,0). In order to derive the condition for the wave speed v, consider a linear stability analysis about the fixed point located at the origin. In order to do this, we compute the Jacobian (J) of the system which is given by

$$J = \begin{bmatrix} 0 & 1 \\ -\frac{\rho}{D} + 2\frac{\rho c}{DK} & -\frac{v}{D} \end{bmatrix},$$

which has characteristic polynomial given by $\det(J - \lambda I)$,

$$\det(J - \lambda I) = \lambda^2 + \lambda\frac{v}{D} + \frac{\rho}{D} - 2\frac{\rho c}{DK}. \tag{3.12}$$

Evaluated at the fixed point $(0, 0)$, we have

$$\det(J - \lambda I) = \lambda^2 + \lambda\frac{v}{D} + \frac{\rho}{D}. \tag{3.13}$$

The roots of this second degree characteristic polynomial are given by the quadratic formula as

$$\lambda_{\pm} = \frac{1}{2}\left(-\frac{v}{D} \pm \sqrt{\left(\frac{v}{D}\right)^2 - 4\frac{\rho}{D}}\right). \tag{3.14}$$

The fixed point will be a stable node if the discriminant is strictly positive, giving the condition

$$\left(\frac{v}{D}\right)^2 \geq 4\frac{\rho}{D}, \quad \Rightarrow \quad v \geq 2\sqrt{D\rho}. \tag{3.15}$$

Thus a range of wave speeds are possible, with the minimum wavespeed given by $v = 2\sqrt{D\rho}$, Fisher's approximation [62, 132]. Although $c(x, t)$ could represent any tumor population, this simple reaction-diffusion equation is an appropriate model for gliomas in particular for the following reasons:

1. Unlike tumors in other regions of the body, the highly diffuse nature and recurrence patterns [2, 6] of gliomas agrees with essential properties of the model. Specifically,

in as few as 7 days after tumor induction in a rat brain, glioma cells can be identified throughout the central nervous system [70] intermingled with normal brain [163], analogous to the instantaneous non-zero solution of the diffusion equation on any finite domain [74]. Additionally, recurrence of glioma growth at the boundary of the surgical resection mirrors the perpetual proliferation and dispersal of any non-zero tumor cell concentration at any time point, and that a gradient of tumor cell density exists throughout the brain [49] consistent with Fickian diffusion. Moreover, glioma cells do not metastasize outside of the brain [5].

2. *In vivo* evidence suggests the observably advancing tumor front travels radially at approximately a constant rate [125], and, in the absence of treatment or physical barriers of brain anatomy, grows with spherical symmetry, aligning with Fisher's approximation. Moreover, the constant velocity of untreated growth suggests that D and ρ are characteristics intrinsic to the tumor, discussed in Chapter 4. A constant velocity of MR imageable growth has been demonstrated for 27 untreated low grade gliomas [125] and for at least one untreated high grade glioma [177].

3. So-called "go or grow" models of glioma invasion which focus on individual cell behavior and the dichotomous state of being motile or proliferative, have been shown to result in reaction-diffusion style equations when translated to the cell-density scale [84].

3.2 Radiation therapy (RT) model

A vast majority of glioblastoma patients receive daily fractionated radiation therapy, which targets the gross tumor volume with an added margin to include invasive disease peripheral to the imaging modality. Radiation therapy is a favored treatment for brain lesions because of the independence of the blood brain barrier, ability to sculpt and deliver dose to specific regions of the tumor, and because of the demonstrated survival benefit when given concurrently with alkylating agent temozolomide, albeit a modest few months [175]. Radiation treatment plans are often sculpted to avoid critical brain structures, but often do

not account for differential response across patients.

3.2.1 Linear-quadratic model

The linear-quadratic (LQ) model of radiation efficacy, which is a dose-response function is used to extend the PI model to include radiation delivery and biological effect. The motivation for using the LQ model lies in the ability to communicate the model in a language familiar to radiation oncology colleagues, as well as the clinical relevance, versatility and robustness of the model *in the clinical dose range* of 0–5 Gy.

The LQ model relates the physical dose of radiation in units of Gray (Gy) which is the absorption of one joule (J) of radiation energy in one kilogram (kg) of matter, 1 Gy $= \frac{J}{kg}$ to a measure of biological effect (unitless) by the following relationship:

$$\textit{biological effect} = \alpha Dose + \beta Dose^2. \tag{3.16}$$

Let n be the number of treatments (fractions), and *dose* be the dose per fraction, then the total dose $Dose$[1] is given by $Dose = n \cdot dose$, which is spatially and temporally defined, so that

$$dose = dose(\mathbf{x}), \quad \text{and} \quad Dose = Dose(\mathbf{x}, t). \tag{3.17}$$

In order to avoid toxic effects to normal tissue, the total dose is typically given in small doses of 1–4 Gy.

The ratio α/β represents the dose at which the linear and quadratic terms contribute equally to cell killing. In low dose photon conformal radiation, the ratio α/β can be assumed to be constant at 10 Gy, to represent early responding tissues such as actively proliferating tumor cells [79]. This motivates the definition of the following quantities, derived from the *biological effect* (Equation 3.16) :

$$BED = ndose\left(1 + \frac{dose}{\alpha/\beta}\right), \quad \textit{relative effectiveness} = \left(1 + \frac{dose}{\alpha/\beta}\right) \tag{3.18}$$

[1] we use "*Dose*" (Gy) in order to avoid confusion with the diffusion coefficient, D (mm^2/year)

where n is the number of treatments and BED stands for the *biologically effective dose*, and is a convenient measure of efficacy: total dose times its relative effectiveness. This formulation is particularly convenient for comparing biological effects of alternate fractionation schemes, in which the number of treatments n and the dose per treatment are varied. The definition of BED also leads to the following expression of survival probability, for a single fraction or total dose,

$$S(\alpha, Dose(\mathbf{x}, t)) = e^{-\alpha Dose - \beta Dose^2} = e^{-\alpha BED}. \tag{3.19}$$

With the ratio α/β fixed, and the number of treatments (n) and $Dose$ determined by the treatment schedule, the strong dependence on the single parameter α (Gy^{-1}) is made clear [150, 151]. Large α implies high susceptibility to therapy, whereas small α implies low susceptibility: we therefore regard α as our radiation sensitivity parameter. While the true biological effects of RT are complicated [15], the clinical utility of the biologically effective dose remains valid for computing equivalent fractionation schedules and translating absorbed dose into an estimated treatment effect [117, 102, 79].

3.2.2 Proliferation-invasion radiation therapy (PIRT) model

Now that we have established the survival probability, S, as a function of the radiation sensitivity parameter α and the dose distribution $Dose = Dose(\mathbf{x}, t)$ per fraction, the quantity $(1 - S)$ represents the probability of cell death per fraction delivery time (f_t), and we can incorporate radiation biological effect into the proliferation-invasion (PIRT) glioma model as follows:

$$\frac{\partial c}{\partial t} = \nabla \cdot (D(\mathbf{x})\nabla c) + (\rho - \overbrace{R(\alpha, Dose(\mathbf{x}, t))}^{\text{loss due to radiation therapy}})c\left(1 - \frac{c}{K}\right) \tag{3.20}$$

$$\mathbf{x} \in \mathcal{B}, t \geq 0 \tag{3.21}$$

$$\mathbf{n} \cdot \nabla = 0 \quad \text{ on } \partial\mathcal{B}, c(\mathbf{x}, t = 0) = c_0\delta(\mathbf{x}), \tag{3.22}$$

where

$$R(\alpha, Dose(\mathbf{x},t)) = \begin{cases} 0, & \text{for } t \notin \text{therapy} \\ (1 - S(\alpha, Dose(\mathbf{x},t)))/f_t & \text{for } t \in \text{therapy.} \end{cases} \tag{3.23}$$

The loss term $R(\alpha, Dose(\mathbf{x},t))$ is the probability of cell death per treatment fraction time (f_t), which occurs on a per day time scale so that $f_t = 1$ day.

Several of the well known variations on the LQ model including cellular re-population or loss rate and effective doubling time [155, 29, 104, 103, 128], are included in the net growth rate ρ in the PIRT model, Equation (3.20). These models do not include a spatial component to the proliferation or invasion of the tumor or differential response to radiation based on tumor cell density, hypoxia. Mathematical models of radiation therapy response in solid tumors has been studied by a wide range of perspectives, for over 40 years, with some of the earliest work done by Cunningh in 1972 [47], to more recent studies which cover a spectrum, from more theoretical studies [143, 172, 149] to data-driven models [60, 110, 53], to name only a few. A more detailed discussion can be found in Chapter 4, section 4.2.

The rate of change of the tumor cell population due to radiation-induced cell death is proportional to $c(1 - c/K)$ since RT will have a greater impact on proliferating cells in regions of low cell concentration than in dense regions with tumor cell concentration close to the carrying capacity, K. This assumption is based on resistance mechanisms of increased interstitial pressure and hypoxic environmental conditions that exist within the core of the tumor. This formalism also allows for quiescent cell death in which the tumor cell continues to engage with its environment and consume nutrients but does not undergo necrosis or apoptosis. In this view, the cell is not cleared from the tissue as it would if it were dead, rather, it counts towards an overall tumor cell density. Alternative interpretations of radiation-induced cell killing in the form of mitotic, apoptotic/necrotic and senescent cell "death" can alter the forms of this loss term, for example linear loss,

$$\frac{\partial c}{\partial t} = \nabla \cdot (D(\mathbf{x})\nabla c) + \rho c \left(1 - \frac{c}{K}\right) - \overbrace{R(\alpha, Dose(\mathbf{x},t))c}^{\substack{\text{loss due to} \\ \text{radiation therapy}}} \tag{3.24}$$

and $R(\alpha, Dose(\mathbf{x},t))\delta(t-\tau)$ for $\tau \in$ therapy have also been investigated [150], resulting

in the conclusion that the density dependent formalism given by the logistic loss term better reflects the clinical data. The analysis using the linear and Dirac forms of radiation effect are not presented here for this reason.

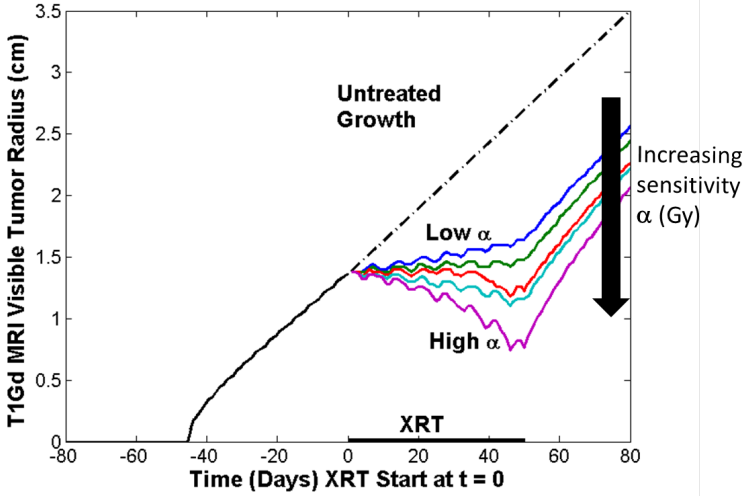

Figure 3.3: Untreated tumor growth serves as a "virtual control" is shown, against which relative treatment effect can be assessed. Simulated radiation therapy using a spatially resolved radiation dose distribution of 1.8 Gy delivered to the MRI associated isodensities plus margin for increasing values of the radiation response parameter α. Low values of α correspond to small deflection from untreated growth, high values of α correspond to high response and large deflection from untreated growth. The ratio α/β is held fixed at $\alpha/\beta = 10$ Gy. Adapted from Rockne 2008 [150].

An additional consequence of the logistic radiation therapy loss term formalism is a maximum rate of cell killing per fraction of radiation therapy as a function of the tumor cell density. Specifically, consider the maximum instantaneous rate of cell kill for a fixed time, t', we define

$$\mathcal{R} = R(\alpha, Dose(\mathbf{x}, t))c\left(1 - \frac{c}{K}\right) \tag{3.25}$$

and consider

$$\max_{c(\mathbf{x},t')}(\mathcal{R}) = \max_{c(\mathbf{x},t')}\left[R(\alpha, Dose(\mathbf{x}, t))c\left(1 - \frac{c}{K}\right)\right]. \tag{3.26}$$

Taking the partial derivative of $\mathcal{R}$ with respect to c gives

$$\frac{\partial \mathcal{R}}{\partial c} = R(\alpha, Dose)\left[1 - \frac{2c}{K}\right]. \tag{3.27}$$

Setting the derivative equal to zero to find the extrema, we see a maximum is achieved at the half-max, $c^* = K/2$,

$$\frac{\partial \mathcal{R}}{\partial c} = 0 \quad \Rightarrow \quad c^* = \frac{K}{2} \tag{3.28}$$

since $R(\alpha, Dose) > 0$ during therapy, by construction. Evaluating $\mathcal{R}$ at c^*, we see that the maximum instantaneous rate of change of cell killing during a fraction of radiation therapy is given by

$$\mathcal{R}(c^*) = R(\alpha, Dose)c^* \left(1 - \frac{c^*}{K}\right) = \frac{K}{4} R(\alpha, Dose). \tag{3.29}$$

The radiation response coefficient can be viewed as a probability of cell death per treatment delivery time, which takes values between zero and unity, giving an overall maximum in space for a fixed time t' as

$$\max_{c(\mathbf{x},t')} (\mathcal{R}) = \frac{K}{4}. \tag{3.30}$$

This is shown in Figure 3.4. This model term implicitly includes biological mechanisms which mitigate cell kill via reducing ionizing radiation-induced DNA damage to the cells. These effects include increased interstitial pressure, hypoxia, necrosis, and higher cell density, yielding a lower dose per cell ratio via reduction in the probability any given cell will be directly damaged by the radiation [79, 102, 155]. These effects are modeled in more detail, including the effects of focal hypoxia in Chapter 4. Note that the linear model as well as the Dirac instantaneous delivery models of radiation therapy do not have this spatial variability and resulting constraint on the radiation efficacy.

3.2.3 Spherical symmetry

To investigate the PIRT model via direct numerical computation of the spatial and temporal evolution of the solution, we simplify the problem by considering the model in the case of spherical symmetry. That is, treat the tumor as a growing sphere in the absence of brain anatomy. *In vitro* experiments using glioma cell lines often are referred to as "spheriods" because they tend to grow in this manner in certain types of cell culture. We do not consider reduction to one spatial dimension without spherical growth, as this relates the tumor to a growing line, which is not biological reasonable. The one dimensional model and the spherically symmetric model are very similar except for the behavior at the origin.

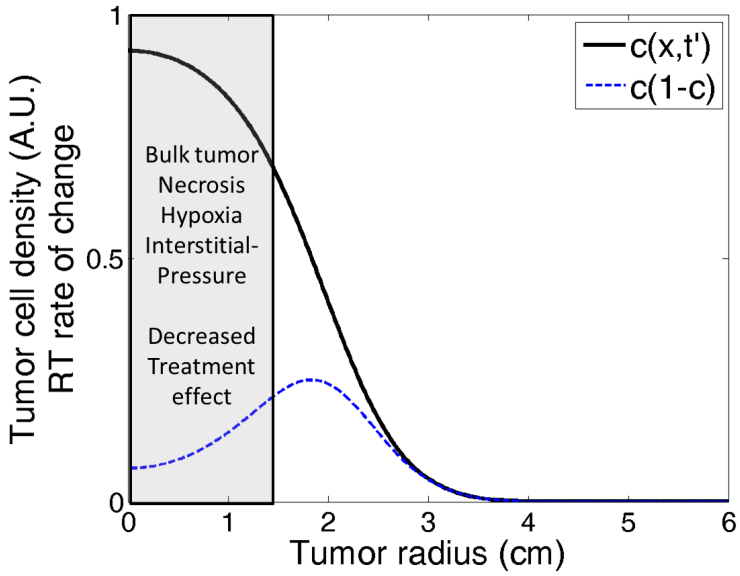

Figure 3.4: Maximal instantaneous rate of change as a fraction of the tumor cell carrying capacity K of radiation-induced cell kill in the PIRT model using a logistic formalism to include density-dependent treatment effect.

The spatially resolved PI model equation given by

$$\frac{\partial c}{\partial t} = \nabla \cdot (D(\mathbf{x})\nabla c) + (\rho - R(\alpha, Dose(\mathbf{x}, t)))c\left(1 - \frac{c}{k}\right) \tag{3.31}$$

where

$$D(\mathbf{x}) = \begin{cases} D_w & \text{if } \mathbf{x} \in \text{white matter} \\ D_g & \text{if } \mathbf{x} \in \text{grey matter} \end{cases} \tag{3.32}$$

includes differential motility of glioma cells through the grey and white tissue of the brain. To initially study the PIRT model, we consider spatially homogeneous environment where the model equation (3.31) can be simplified to

$$\frac{\partial c}{\partial t} = D\nabla^2 c + (\rho - R(\alpha, Dose(\mathbf{x}, t)))c\left(1 - \frac{c}{k}\right). \tag{3.33}$$

The Laplacian operator, ∇^2 is defined in Cartesian coordinates as

$$\nabla^2 f = \sum_{i=1}^{3} \frac{\partial^2 f}{\partial x_i^2} \tag{3.34}$$

where the $(x_1, x_2, x_3) = (x, y, z)$. In spherical coordinates, the Laplacian operator is given by

$$\nabla^2 f = \frac{1}{r^2}\frac{\partial}{\partial r}\left(r^2\frac{\partial f}{\partial r}\right) + \frac{1}{r^2\sin\varphi}\frac{\partial}{\partial\varphi}\left(\sin\varphi\frac{\partial f}{\partial\varphi}\right) + \frac{1}{r^2\sin^2\varphi}\frac{\partial^2 f}{\partial\theta^2} \tag{3.35}$$

where θ is the azimulthal angle and φ is the zenith angle, and r is the radius. If we consider the case of *radial symmetry*, then $\partial f/\partial\varphi$ and $\partial f/\partial\theta$ are both identically zero, and we have the following expression of the Laplacian,

$$\nabla^2 f = \frac{1}{r^2}\frac{\partial}{\partial r}\left(r^2\frac{\partial f}{\partial r}\right) \tag{3.36}$$

$$= \frac{\partial^2 f}{\partial r^2} + \frac{2}{r}\frac{\partial f}{\partial r}. \tag{3.37}$$

Substituting this expression into our simplified equation (3.33), we have the spherically symmetric form

$$\frac{\partial c}{\partial t} = D\left(\frac{\partial^2 c}{\partial r^2} + \frac{2}{r}\frac{\partial c}{\partial r}\right) + (\rho - R(\alpha, Dose(r,t)))c\left(1 - \frac{c}{k}\right), \tag{3.38}$$

where the tumor cell density is now a function of tumor radius and time, as $c = c(r,t)$.

3.2.4 Non-dimensionalization

We scale our original equation (3.33) by introducing the following unitless variables,

$$\bar{t} = \rho t, \qquad \bar{c} = \frac{c}{K}, \qquad \bar{r} = \frac{r}{L}. \tag{3.39}$$

where L is the dimensional radial length of the spherical brain domain, typically taken to be $L = 12$ cm. Plugging these values into our equation (3.33), we have the scaled equation

$$\frac{\partial \bar{c}}{\partial \bar{t}} = \bar{D}\nabla^2\bar{c} + (1 - \bar{R}(\bar{r},\bar{t}))\bar{c}\,(1 - \bar{c}), \tag{3.40}$$

where the unitless diffusion coefficient $\bar{D}$ is given by

$$\bar{D} = \frac{D}{\rho L^2}. \tag{3.41}$$

We will use this reduced form of the equation with $c(r,t) \in [0,1]$, $r \in [0,1]$ and $t \geq 0$ with the radially symmetric form of the differential operator ∇^2 given in (3.36). The

radiation therapy extension is formally unaffected by these scalings since the term includes no derivatives and simply results in the following reduced equation

$$\frac{\partial \bar{c}}{\partial \bar{t}} = \bar{D}\nabla^2 \bar{c} + (1 - \bar{R}(\bar{r}, \bar{t}))\bar{c}\,(1 - \bar{c})\,. \tag{3.42}$$

where

$$\bar{R}(\bar{r}, \bar{t}) = \frac{(1 - S(\alpha, Dose(\bar{r}, \bar{t}))}{\rho}$$

with initial and boundary data given by

$$\bar{c}(\bar{r}, 0) = \bar{f}(\bar{r}), \quad \bar{r} \in \mathcal{L}, \quad \bar{t} \geq 0 \tag{3.43}$$

$$\nabla \bar{c} \cdot \mathbf{n} = 0, \nabla \text{ on } \partial\mathcal{L}. \tag{3.44}$$

Dimensionless space is denoted by $\mathcal{L}$. Since the radiation therapy dose is predetermined on an arbitrary spatial and temporal Cartesian grid, the grid itself is scaled. Further, because the dose is point-wise defined and not a formal function of space and time, a non-dimensional analog does not exist, rather, it is implicit in the definition of the spatial and temporal grids on which the dose is defined.

3.2.5 Numerical methods

The Crank-Nicolson method is a second order centered finite difference method for solving parabolic partial differential equations and is straight forward to implement in Cartesian coordinates. The method is less straight forward in the case of spherical symmetry due to the $1/r$ term in the spherical Laplacian operator,

$$\nabla^2 = \left(\frac{\partial^2}{\partial r^2} + \frac{2}{r}\frac{\partial}{\partial r}\right). \tag{3.45}$$

Here we detail the numerical methods needed to solve the PI or PIRT models in spherical symmetry which accounts for the singularity at the origin as well as the no-flux Neumann boundary conditions [192, 119].

For simulations in the homogeneous, $(D(x) = D)$ spherically symmetric case we have, we use the form of the Laplacian given in Equation 3.38 in spatial domain of size R, $r \in [0, R]$ with M spatial nodes so that $R = hM$, the six-point stencil

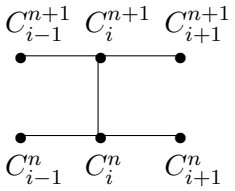

yields

$$\frac{C_i^{n+1} - C_i^n}{k} = \frac{D}{2}\left[\mathcal{D}_i^n + \mathcal{D}_i^{n+1}\right], \tag{3.46}$$

where the discrete spherically symmetric Laplacian ($\mathcal{D}$) is given by

$$\mathcal{D}_i^n = \left(\frac{C_{i-1}^n - 2C_i^n + C_{i+1}^n}{h^2} + \frac{2}{r}\frac{C_{i+1}^n - C_{i-1}^n}{2h}\right). \tag{3.47}$$

Grouping terms and replacing r with ih we get

$$\frac{C_i^{n+1} - C_i^n}{k} = \frac{D}{2h^2}\left[A_i^{n+1} + A_i^n\right], \tag{3.48}$$

where

$$A_i^n = \left[\left(1 - \frac{1}{i}\right)C_{i-1}^n - 2C_i^n + \left(1 + \frac{1}{i}\right)C_{i+1}^n\right] \tag{3.49}$$

at the interior nodes $i = 1, 2, 3, ..., M-1$. At the right boundary, where $i = M$, we have the no-flux boundary condition at the right boundary gives the Neumann condition

$$\frac{\partial c}{\partial r}(R, t) = 0. \tag{3.50}$$

Discretizing, we get

$$\frac{1}{2}\left[\frac{C_{M+1}^n - C_{M-1}^n}{2h} + \frac{C_{M+1}^{n+1} - C_{M-1}^{n+1}}{2h}\right] = 0$$

$$C_{M+1}^n + C_{M+1}^{n+1} = C_{M-1}^n + C_{M-1}^{n+1}.$$

Replacing $C_{M+1}^n + C_{M+1}^{n+1}$ with $C_{M-1}^n + C_{M-1}^{n+1}$ in the discretization for the interior nodes and simplifying we get

$$\frac{C_M^{n+1} - C_M^n}{k} = \frac{D}{h^2}\left[C_{M-1}^{n+1} - C_M^{n+1} + C_{M-1}^n - C_M^n\right], \tag{3.51}$$

at the right boundary $i = M$. At the left boundary, where $i = 0$, we have a singularity due to the $\frac{2}{r}$ term in the Laplacian. Using L'Hospital's rule, we see that in the limit as $r \to 0$,

$$\lim_{r\to 0} \frac{2}{r}\frac{\partial c}{\partial r} \underset{\text{H}}{\overset{\left[\frac{0}{0}\right]}{=}} 2\frac{\frac{\partial c}{\partial r}\frac{\partial c}{\partial r}}{\frac{\partial c}{\partial r}r} = 2\frac{\partial^2 c}{\partial r^2}. \tag{3.52}$$

Replacing $\frac{2}{r}\frac{\partial c}{\partial r}$ with $2\frac{\partial^2 c}{\partial r^2}$ at the left boundary gives

$$\frac{\partial c}{\partial t} = 3D\left(\frac{\partial^2 c}{\partial r^2}\right). \tag{3.53}$$

The discretization now becomes

$$\frac{C_0^{n+1} - C_0^n}{k} = 3D\left(\frac{C_{-1}^n - 2C_0^n + C_1^n}{h^2}\right). \tag{3.54}$$

At $i = 0$ we have the Neumann, no flux boundary condition

$$\frac{\partial c}{\partial r}(0, t) = 0 \tag{3.55}$$

which gives

$$\frac{C_1^n - C_{-1}^n}{2h} = 0 \quad \Rightarrow \quad C_1^n = C_{-1}^n. \tag{3.56}$$

Replacing C_{-1}^n with C_1^n in the discretization at the left boundary, $i = 0$, we have

$$\frac{C_1^m - C_0^n}{k} = 6D\left(\frac{C_1^n - C_0^n}{h^2}\right). \tag{3.57}$$

The right boundary we have

$$(1+s)C_M^{n+1} - sC_{M-1}1^{n+1} = (1-s)C_M^n + sC_{M-1}^n, \tag{3.58}$$

and at the origin, we have

$$(1+3s)C_0^{n+1} - 3sC_1^{n+1} = (1-3s)C_0^n + 3sC_i^n, \tag{3.59}$$

where we define s as

$$s = \frac{Dk}{h^2}. \tag{3.60}$$

This method is accurate to $\mathcal{O}(h^2 + k^2)$ and unconditionally stable [119]. We take the time step so that

$$k \leq \frac{h^2}{2D} \tag{3.61}$$

in order to resolve the wave front. The resulting matrix equation is solved iteratively with the conjugate gradient method [72].

3.3 Dose distributions and margins

Clinical challenge Where to place dose relative to the frank tumor as presented on medical imaging is a daily clinical challenge in radiation oncology. To date, no survival improvement beyond that demonstrated by the Stupp chemo-radiation protocol has been shown, from whole-brain radiation therapy (WBRT) to carefully sculpted fields based on MRI defined frank tumor and irradiation margins [141]. The clinical goal is to minimize dose to normal tissue, and maximize dose to the tumor target volume. The challenge in the case of glioblastoma to account for sub-clinical, invisible tumor cell infiltration which is interwoven with healthy, normal brain.

Where previous methods of dose sculpting and dose field design fall short, is not in typical irradiation margins, which often include over 90% of PIRT model predicted sub-clinical disease. The opportunity for modeling in dose distributions, lies in the ability to account for differential response to radiation therapy across patients. In order to use the PIRT model to investigate the role of conventional radiation dose margins and fraction size on imageable tumor response, we must first have a model for these fields and treatment paradigms and understand the sensitivity of the PIRT model predictions to variations in dose.

Dose margins Although our model allows for any imaginable treatment schedule or dose distribution, the standard dose prescription used for radiation treatment includes margins beyond the bulk contrast-enhancing tumor to account for invasive disease, denoted the "target volume" (TV). Typically, external beam conformal radiation treatment consists of the following

1. 6 weeks of treatment, using a 5 days on, 2 days off schedule to allow for weekends

2. 1.8 Gy to the T2 enhancing region plus a 25 mm margin for 28 days

3. followed by 1.8 Gy to the T1Gd enhancing tumor region plus a 20 mm margin for the remaining 6 days, yielding 61.2 Gy total max dose to the tumor bed [175, 96].

The spatial region and temporal duration of the final 6 days of treatment is considered the boost time (BT) and boost region (BR), respectively. For simplicity, all treatment simulations are assumed to begin on a Monday so that 5 consecutive days of therapy can be applied before the 2 day rest period is implemented. In the spherically symmetric case, our dose profile approximation is given by

$$Dose(\bar{x},\bar{t}) = \begin{cases} 1.8 \pm 5\% \text{ Gy} & \text{TV}, \\ \dfrac{1}{\bar{r}^2} & \text{outside the TV}. \end{cases} \tag{3.62}$$

Figure 3.11 shows the relationship of the planning target volume relative to the T1Gd and T2 contrast-enhancing abnormality in a one-dimensional radially symmetric profile. The approximation is based on analysis of a typical 3-dimensional radiation dose plan, shown in Figures 3.5 and 3.11. The dose is fairly uniform, to within $\pm$ 5 % within the target volume, and drops precipitously outside the TV.

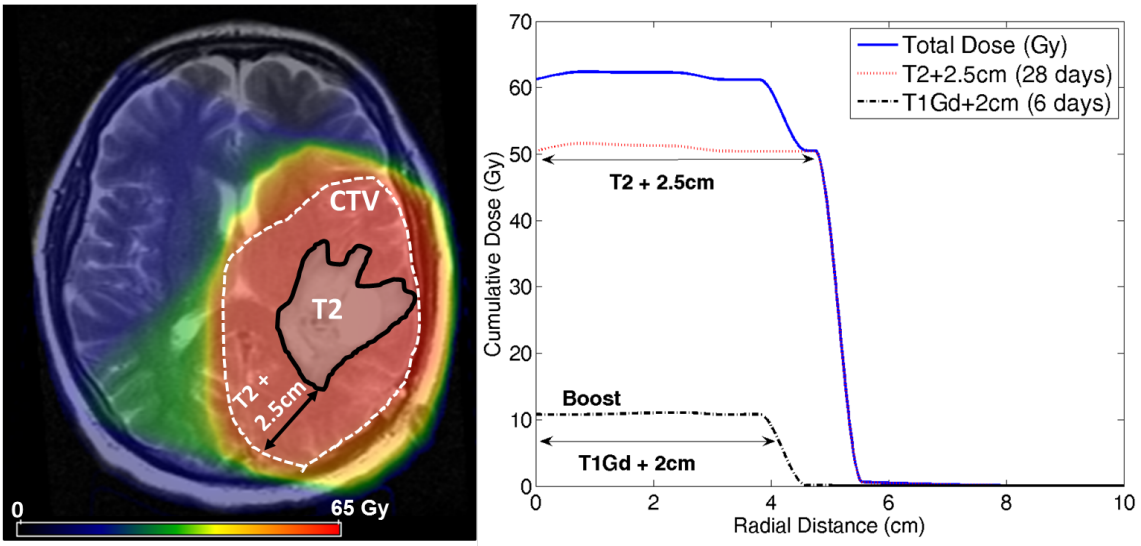

Figure 3.5: Creation of radially symmetric dose distributions based on clinical and target radiation volumes. The T2-weighted MRI abnormality and T1+Gd bulk tumor mass are dosed with fairly uniform radiation, with additional margin to include invasive sub-clinical disease. Left: clinical target volume (CTV) includes the imageable tumor (T2) plus 2.5 centimeter margin, with approximately 5% variation in dose [96]. Right: radial approximation based on target volumes and margins, adapted from Rockne 2008 [150].

We consider quantifying the effect of spatial dose variation on the predicted tumor evolution by considering using maximum, mean, median, and minimum radial dose profiles from the isocenter of a full three-dimensional clinical dose plan Figure 3.11, holding radiosensitivity α, constant. As seen in Figure 3.11 panel D, only the maximum radial dose profile provides a noticeable reduction in tumor volume: mean, median and minimum dose profiles all produce similar tumor size following the completion of RT. Upon closer examination of the dose profiles in panel C, the maximum dose profile places more dose at the tumor periphery, where dose per cell will be much higher than the core of the tumor. This suggests that subtle variations in dose near the core of the tumor will not yield drastic changes to the model-predicted tumor size following therapy. These results further suggest that biologically guided dose distributions which sculpt the dose field to the model-predicted tumor cell distribution may provide better tumor control from the perspective of overall tumor size reduction following therapy.

3.4 Radiation-induced arrest of tumor proliferation

Clinical challenge In addition to determining optimal radiation dose margins which minimize dose to normal tissue and include therapeutic dose to the tumor periphery which includes occult invasive disease, the challenge of *how much dose* to give the frank tumor is limited by the physical properties of the radiation modality being used, as well as the anatomical location of the tumor. As with treatment field design, dose escalation studies have failed to produce a meaningful survival benefit in glioblastoma [39].

In absence of these limitations, the model opportunity is to provide an estimate of the critical dose required to arrest tumor growth as a function of the tumor-specific proliferation (ρ) *and radio-response* (α) *rates.* In order to arrest the tumor proliferation, we require that the biological effects of radiation therapy negate the effect of the proliferation, so that the overall rate of change of the tumor cell density is zero or decreasing in space and in time. Specifically, in the absence of the diffusion process, we have tumor proliferation arrest when

$$\frac{dc}{dt} = 0 \quad \Rightarrow \quad 0 = (\rho - R(\alpha, Dose))c(1-c) \tag{3.63}$$

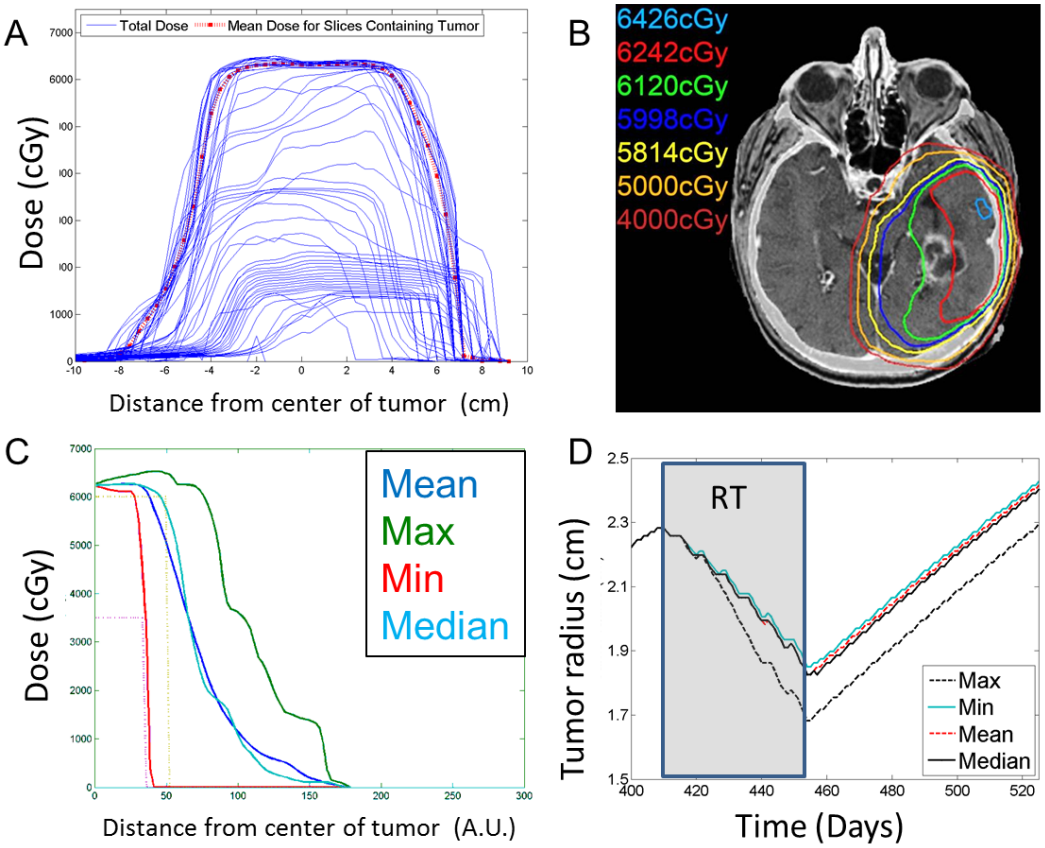

Figure 3.6: A: Three-dimensional radiation dose plans are converted to radial profiles by averaging lines through the pixels of highest dose in the volume to create an aggregate profile. B: fusion of MRI and treatment planning CT with isodoses. C: Radial profiles based on the min, mean, median and maximum radial profile from A. D: Spherically symmetric simulations of the PIRT model with fixed radio-sensitivity and varying dose profile. A, B and C adapted from Rockne 2010 supplementary material [151].

so that for $c(x,t) \neq 0$ or $c(x,t) \neq 1$, we require

$$\rho = R(\alpha, Dose). \tag{3.64}$$

If we consider a spatially uniform dose, which would be analogous to whole brain radiation therapy (WBRT), then we may derive a critical dose, $Dose_{crit}$, beyond which the tumor growth would arrest as follows. The condition above implies that per treatment fraction

time, we have

$$\rho \leq (1 - S)/Fx/day \tag{3.65}$$

where the number of fractions per day is unity, so that we have $Fx/day \equiv 1$, and

$$\begin{aligned} \rho &\leq (1 - \exp(-\alpha Dose - \beta Dose^2)) && (3.66) \\ -\beta Dose^2 - \alpha Dose &\leq \ln(1 - \rho) && (3.67) \end{aligned}$$

clearly we require that in units per day, $0 \leq \rho < 1$. This is equivalent to requiring a tumor cell doubling time of $\tau = \ln(2)/\rho$ so that $\tau \lesssim 0.6931$ per day, or $\tau \lesssim 253$ per year, which is biologically reasonable. We can find the critical uniform dose $Dose_{crit}$ with the quadratic equation to give

$$Dose_{crit} = \frac{-\alpha \pm \sqrt{\alpha^2 - 4\beta \ln(1 - \rho)}}{2\beta}. \tag{3.68}$$

In order for $Dose_{crit}$ to be real-valued, we require the discriminant to be non-negative, giving the condition

$$\alpha^2 - 4\beta \ln(1 - \rho) > 0 \tag{3.69}$$

and further, the following relation must hold

$$\alpha \geq 4\frac{\beta}{\alpha} \ln(1 - \rho). \tag{3.70}$$

This relationship will always hold since $\rho < 1$ /day implies that $\ln(1 - \rho) < 0$, and since $\alpha, \beta > 0$, we have this condition satisfied by construction. The ratio α/β in units Gy, can be viewed as the rate of change of the dose-response relationship: higher values of α/β correspond to early responding tissue, such as tumor cells, and low α/β values correspond to later responding tissue, such as normal tissue. This is roughly correlated with radio-sensitivity of the tissue or cell line, as well as the net proliferation rate of the irradiated cells. Now the condition for a real valued $Dose_{crit}$ can be viewed as a relationship between the natural logarithm of one minus the net proliferation rate to the radio-sensitivity parameter. Finally, we require that $Dose_{crit}$ take positive values, so that $Dose_{crit} \geq 0$, which is the positive root, so that

$$Dose_{crit} = \frac{-\alpha + \sqrt{\alpha^2 - 4\beta \ln(1 - \rho)}}{2\beta}. \tag{3.71}$$

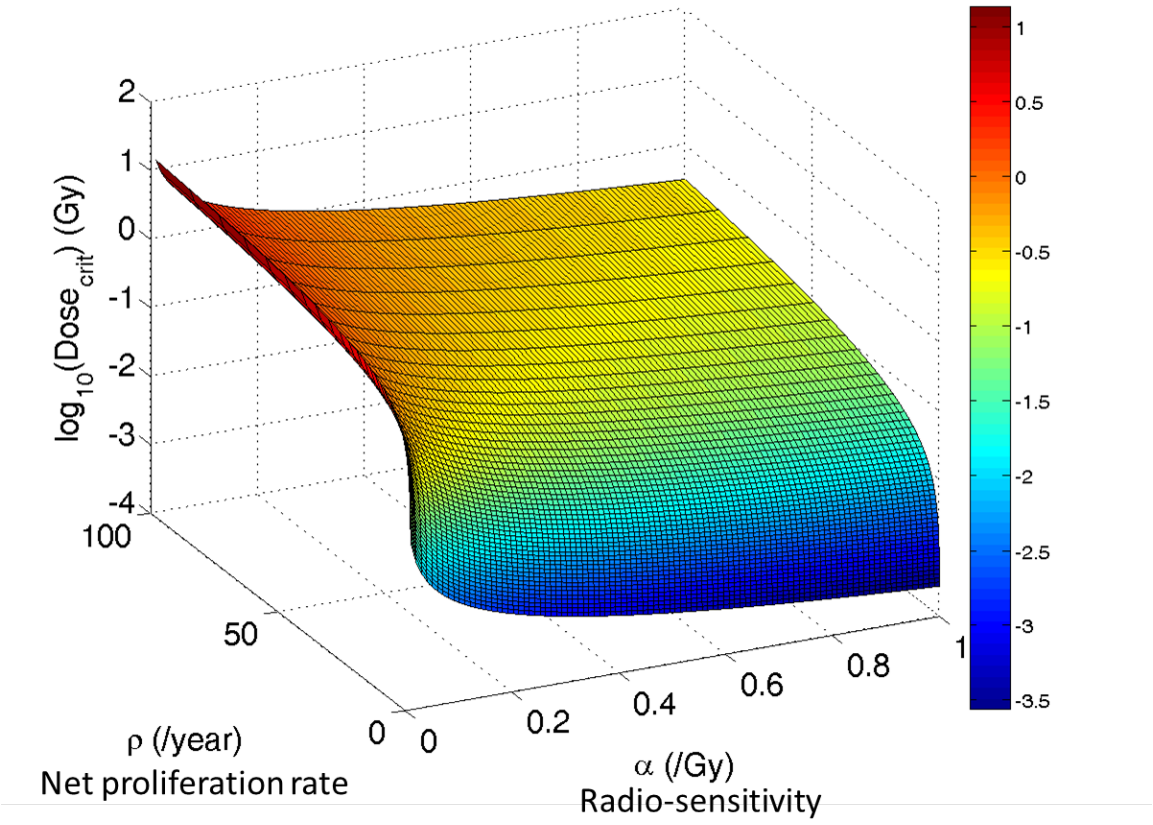

Figure 3.7: $\log_{10}(Dose_{crit})$ is plotted as a function of radiosensitivity (α) and net proliferation rate (ρ). $Dose_{crit}$ is the minimum spatially uniform dose of radiation needed to arrest tumor proliferation.

$Dose_{crit}$ is plotted as a function of α and ρ in Figure 3.7. For parameter values $0 \leq \alpha \leq 1$ (/Gy) and $0.1 \leq \rho \leq 100$ (/year), $Dose_{crit}$ takes values between $1 \times 10^{-3.5} \leq Dose_{crit} \leq 1 \times 10^{1}$ (Gy). Daily radiation doses are typically given on the order of 2–5 Gy per day, with the exception of radiosurgery, which permits single fraction doses up to 20 Gy, suggesting that an arresting dose of radiation is achievable in the clinical radiation treatment paradigm, if we include high dose radiosurgery. Radiosurgery is discussed in Chapter 2. Although such a dose is theoretically achievable, many other processes such as environmentally driven resistance and delayed effects of therapy prevent radiation from being a curative therapy in glioblastoma. This is explored in Chapter 4.

3.5 Homogeneous therapy delivery

Clinical challenge In addition to the patient's quality of life and mental status, changes in imageable tumor volume is a routine clinical metric of assessing response to therapy of any kind. Specifically, translating radiation dose to biological response, and further translating to changes in tumor size is at the core of a clinical application of "mathematical radiation oncology."

In order to estimate the effect of changing the radio response parameter α on tumor growth, we again consider the simplified situation in which the radiation dose is homogeneous in space and is a function only of time. Moreover, we consider the case where the tumor has not yet reached carrying capacity so that the growth and response to therapy can be approximated with linear growth and decay terms respectively. On the infinite two-dimensional domain, the simplified PIRT model for this case is given by

$$\frac{\partial c}{\partial t} = D\left(\frac{\partial^2 c}{\partial x^2} + \frac{\partial^2 c}{\partial y^2}\right) + \rho c - Rc, \quad (x, y) \in \mathbb{R}^2,\ t > 0 \tag{3.72}$$

with initial conditions given by a point source of cells at the origin, so that

$$c(x, y, t = 0) = c_0 \delta(r), \tag{3.73}$$

where we define $r = \sqrt{x^2 + y^2}$. The radiation loss term no longer depends on the spatial

variable, and is given per fraction time f_t by

$$R(\alpha, Dose(t)) = \begin{cases} 0, & \text{for } t \notin \text{therapy} \\ (1 - S(\alpha, Dose(t)))/f_t, & \text{for } t \in \text{therapy.} \end{cases} \tag{3.74}$$

The radiation dose is homogeneous in space so that

$$Dose(t) = \begin{cases} d, & \text{for all } \ x,\ y,\ t \in \text{therapy} \\ 0, & \text{for } t \notin \text{therapy.} \end{cases} \tag{3.75}$$

As discussed previously, the standard of care for conformal external beam radiation therapy is 1.8 Gy per day with fairly homogeneous dose delivered to the bulk tumor mass, shown in Figure 3.5. We use this simplification because the cross sectional area of the contrast-enhancing tumor mass is often used as a clinical measure of response. We therefore seek 2D planar solutions of the form

$$c(x, y, t) = v(t)w(x, y, t) \tag{3.76}$$

where the functions $v(t)$ and $w(x, y, t)$ satisfy the following differential equations

$$\frac{dv}{dt} = (\rho - R(t))\, v, \qquad v(0) = 1 \tag{3.77}$$

and

$$\frac{\partial w}{\partial t} = D\left(\frac{\partial^2 c}{\partial x^2} + \frac{\partial^2 c}{\partial y^2}\right), \qquad w(x, y, t = 0) = \delta(r). \tag{3.78}$$

Solving these equations, we obtain

$$v(t) = \exp\left(\rho t - \int_0^t R(\tau) d\tau\right) \tag{3.79}$$

and the heat kernel solution, given by

$$w(x, y, t) = \frac{1}{4\pi D t} \exp\left(\frac{-(x^2 + y^2)}{4Dt}\right) \tag{3.80}$$

so that the solution is given by

$$c(x, y, t) = \frac{1}{4\pi D t} \exp\left(\rho t - \int_0^t R(\tau) d\tau - \frac{r^2}{4Dt}\right) \tag{3.81}$$

$$c(x, y, t = 0) = \delta(r), \quad t > 0. \tag{3.82}$$

For fixed tumor density threshold, c^* with corresponding radius r^*, we have the following

$$c^* = \frac{1}{4\pi Dt} \exp\left(\rho t - \int_0^t R(\tau)d\tau - \frac{(r^*)^2}{4Dt}\right), \quad t > 0. \tag{3.83}$$

Rearranging this equation, we have the following expression which relates the tumor radius for a fixed isodensity as a function of time to the parameters D, ρ, α by

$$r^* = \sqrt{4D\left(\rho t^2 - t\int_0^t R(\tau)d\tau - t\ln(4\pi Dtc^*)\right)}. \tag{3.84}$$

where

$$t\int_0^t R(\tau)d\tau = t\int_0^t (1 - \exp(-\alpha Dose - \beta Dose^2))d\tau \tag{3.85}$$

$$= \begin{cases} \left(1 - \exp\left(-\alpha\left(Dose + \frac{Dose^2}{\alpha/\beta}\right)\right)\right)t^2 & \text{for } t \in \text{ therapy} \\ 0 & \text{for } t \notin \text{therapy.} \end{cases} \tag{3.86}$$

The typical external beam conformal treatment for glioblastoma is composed of 34 treatments (fractions) of 1.8 Gy, administered daily to a total dose of 61.2 Gy. We can use this information to compute the treatment parameter value needed to obtain a 50% reduction in tumor size relative to the size at the start of therapy as follows. Define the time at the end of therapy, T, and the pre- and post-treatment tumor radii for a fixed isodensity of tumor cells to be r_{pre} and r_{post}, respectively. Here we ignore the two day break in treatment associated with weekends and consider the total treatment time to be the summation of the individual days of treatment. We further consider the growth of the tumor between fractions to be negligible so that the radiation treatment can be considered a continuous variable on the time scale of a single day. We compute the net treatment effect after treatment duration T by evaluating the expression above at $t = T$. In particular, if we take $\alpha/\beta = 10$ Gy, we have the survival probability simplify to

$$(1 - S) = \left(1 - \exp\left(-\alpha\left(Dose + \frac{Dose^2}{\alpha/\beta}\right)\right)\right) \tag{3.87}$$

$$= (1 - \exp(-E\alpha)) \tag{3.88}$$

where E is a constant, defined by computing $(Dose + Dose^2/\alpha/\beta)$ where $Dose = 1.8$ Gy and $\alpha/\beta = 10$ /Gy, so that the tumor radius at the end of radiation therapy treatment of

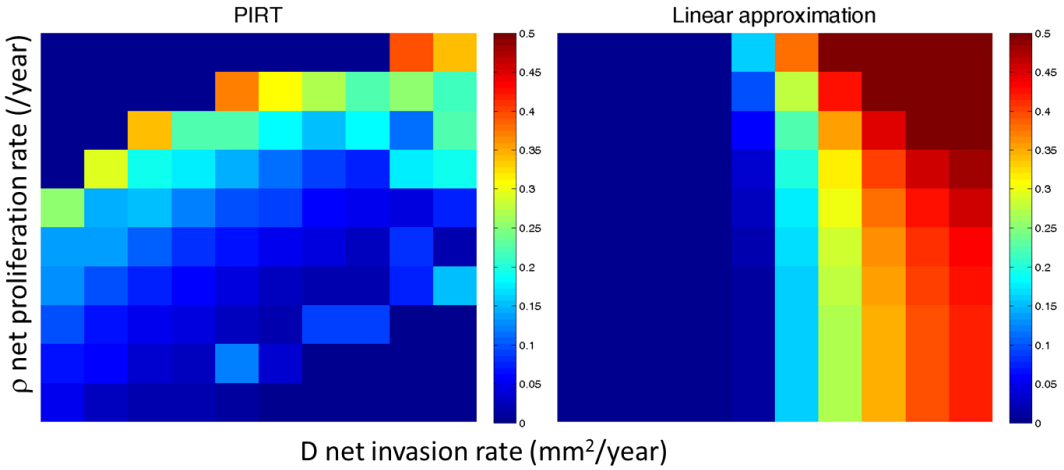

Figure 3.8: Net invasion rate (D) versus the net proliferation rate (ρ) A) numerical solution of the PIRT model with conventional 3D conformal dose plan delivered to the MRI defined isodensity target volumes. Color indicates value of radio-sensitivity α (/Gy) needed to reduce the tumor radius by 50%. B) Linear approximation provided by Equation 3.90. The differences reveal the significant role played by the nonlinear dose profile, response and proliferation terms in the PIRT model (Equation 3.20). Qualitative agreement to the same order of magnitude, suggests the linear approximation is a reasonable first order estimate of radio-response based on model parameters D and ρ.

duration T is given by,

$$r^*(T) = \sqrt{4D\left(\rho T^2 - R(T) - T\ln(4\pi DTc^*)\right)}. \tag{3.89}$$

To compute the radio-sensitivity needed to reduce the pre-treatment tumor volume by 50%, so that $r^*(T) = r_{post} = r_{pre}/2$, for a conventional 34 fraction treatment, we evaluate the expression above and solve for α, to give

$$\alpha_{1/2} = \frac{-1}{E}\ln\left(\frac{r_{pre}^2}{16D} - \rho T + T\ln(4\pi DTc^*) + 1\right). \tag{3.90}$$

As is seen in Figure 3.8, the linear approximation does not capture the same qualitative behavior of the fully nonlinear simulation of the PIRT model (Equation 3.20) with spatial and temporal variations in radiation dose, as is the case in the clinical scenario. This is due to the significant role of the nonlinearities in proliferation and response kinetics. The linear approximation given above in Equation 3.90 is correct to an order of magnitude,

however, scale factors of up to 4 times the values of $\alpha_{1/2}$ can mean unacceptable normal tissue toxicities when treating patients.

3.5.1 Pseudo-progression

Clinical challenge Understanding complicated imaging changes following the completion of radiation therapy, and differentiating pseudo-progression from true progression.

Response assessment to radiation therapy on imaging alone provides many challenges in the clinical setting [4, 50]. Among them is the phenomenon of pseudo-progression (PsP), characterized by increased progressive enhancement on radiographic imaging occurring within 12 weeks post chemo-radiotherapy which may or may not be accompanied by clinical deterioration or changes in neurological status and which spontaneously resolves with no further clinical intervention [187]. The phenomenon of pseduo-progression of disease following radiation therapy may be a realization of delayed or late radiotherapy biological effect. PsP has posed a significant clinical challenge in the management of high grade gliomas. Recent studies estimate that up to 50% of patients who underwent re-resection and a change in chemotherapeutic regimen for progressive contrast enhancement on T1Gd and T2 MRI within 100 days of chemo-radiotherapy with temozolomide did not exhibit true progressive disease, but rather PsP. Radiation response predictions should be robust to choice of MRI modality and observation following RT, controlling for variations in Stupp-defined adjuvant chemotherapy. It has been shown that the PI model alone is capable of differentiating true progression from pseudo progression using novel, patient-specific metrics of response based on PI model predicted pre-treatment growth [135], discussed in more detail in Chapter 4, section 4.2.

3.6 PIRT-D Delay model

Effective radiation-induced cell death can follow apoptotic/necrotic, senescent/quiescent or mitotic pathways. In the necrotic pathway, the cell's DNA is damaged and undergoes cell death processes which dissolve the cell membrane and remove the cell from the net tumor cell concentration. In the quiescent death pathway, the tumor simply remains dormant but may continue to consume nutrients and engage with the micro-environment without

further proliferation and contribution to the net tumor cell population. In the mitotic death pathway, the exposed cell may undergo one or even several additional mitoses before becoming quiescent or necrotic. Mitotic cell death, including damage to mitochondrial DNA creates heritable effects within the clonogenic daughter cells and may evolve treatment resistance.

Mitotic cell death may lead to delayed radiation effects, allowing portions of the tumor to continue to disperse and proliferate. To investigate the role of mitotic catastrophe cell death resulting from radiation therapy, we define a subpopulation of tumor cells exposed to radiation at time t and location $\mathbf{x}$ as $r(\mathbf{x}, t)$ as follows:

$$\overbrace{\frac{\partial c}{\partial t}}^{\substack{\text{rate of change}\\ \text{of un-irradiated}\\ \text{tumor cells}}} = \overbrace{\nabla \cdot (D\nabla c) + \rho c\left(1 - \frac{(c+r)}{K}\right)}^{\substack{\text{diffusion and proliferation}\\ \text{of un-irradiated tumor cells}}} - \overbrace{R(S, c(x,t))}^{\substack{\text{irradiated}\\ \text{tumor cells}}} \tag{3.91}$$

$$\overbrace{\frac{\partial r}{\partial t}}^{\substack{\text{rate of change}\\ \text{of irradiated}\\ \text{tumor cells}}} = \overbrace{R(S, c(\mathbf{x}, t))}^{\substack{\text{irradiated}\\ \text{tumor cells}}} - \overbrace{\rho_r r}^{\substack{\text{irradiated cell death}\\ \text{after proliferation cycle}}} \tag{3.92}$$

the proportion of cells exposed to radiation per treatment fraction time (f_t) is given by

$$R(S, c(\mathbf{x}, t)) = \begin{cases} 0 & \text{for } t \notin \text{ treatment} \\ \dfrac{(1 - S(Dose(\mathbf{x}, t), \alpha, \beta))}{f_t} c\left(1 - \dfrac{(c+r)}{K}\right) & \text{for } t \in \text{ treatment} \end{cases} \tag{3.93}$$

with the probability of surviving radiation exposure given by the linear-quadratic surviving fraction dose-response function,

$$S(Dose(\mathbf{x}, t), \alpha, \beta) = \exp\left(-\alpha\left(Dose(\mathbf{x}, t) + \frac{Dose^2(\mathbf{x}, t)}{\alpha/\beta}\right)\right) \tag{3.94}$$

with initial conditions and domain given by

$$c(\mathbf{x}, 0) = f(\mathbf{x}), \quad r(\mathbf{x}, 0) = 0, \tag{3.95}$$

$$\mathbf{x} \in \mathcal{B}, \quad t \geq 0, \quad \nabla c \cdot \mathbf{n} = 0, \ \nabla r \cdot \mathbf{n} = 0 \text{ on } \partial\mathcal{B}. \tag{3.96}$$

The irradiated tumor cells are the fraction of cells doomed by radiation exposure, given by the term $R(S, c(\mathbf{x}, t))$, so that this proportion of cells is removed from the "normal," or un-irradiated tumor cell population and added to the irradiated population, $c(\mathbf{x}, t)$. It is assumed that the irradiated cells do not migrate or diffuse. The rationale for this assumption is that once the cell is damaged by radiation, the cell is stationary while damage repair takes place. No flux boundary conditions prevent both the irradiated and non-irradiated tumor cell populations from leaving the brain. Because of the spatial shape of the function $R(S, c(\mathbf{x}, t))$, shown in Figure 3.4, competition for space is not required in the diffusion term, but is required in the logistic growth term. The irradiated cells consume space as the other tumor cells do, and therefore compete for space and contribute to the overall tissue carrying capacity in an additive way so that the total tumor volume is given by $T = c + r$.

Delayed radiation-induced cell death The cells in the irradiated sub-population $r(\mathbf{x}, t)$ undergo radiation-induced mitotic cell death at the next cell cycle, at a rate ρ_r. The rate of loss from radiation-induced cell death ρ_r, need not necessarily equal the un-irradiated tumor cell net proliferation rate ρ, although we assume this to be the case in the following analysis and studies. There are alternative formalisms for considering time-delays, such as integro-differential equations and time-shifted terms in the model. These approaches will be investigated in future work.

3.6.1 Non-dimensionalization

We introduce the non-dimensional variables in one spatial dimension as

$$\bar{c} = \frac{c}{K}, \quad \bar{t} = \rho t, \quad \bar{x} = x \left(\frac{\rho}{D}\right)^{1/2} \tag{3.97}$$

resulting in the scaled system

$$\frac{\partial \bar{c}}{\partial \bar{t}} = \bar{D}\nabla^2 \bar{c} + (1 - \bar{R}(S, \bar{c}))\ \bar{c}(1 - \bar{c} - \bar{r}) \tag{3.98}$$

$$\frac{\partial \bar{r}}{\partial \bar{t}} = \bar{R}(S, \bar{c})\ \bar{c}(1 - \bar{c} - \bar{r}) - \bar{d}_r \bar{r} \tag{3.99}$$

where we have the scaled radiotherapy term $\bar{R}$ given by

$$\bar{R}(S,\bar{c}) = R(S,\bar{c})/\rho \tag{3.100}$$

with the dimensionless rate of diffusion, $\bar{D}$ radiation-induced delay constant $\bar{d_r}$ given by

$$\bar{D} = \sqrt{\frac{D}{\rho}}, \quad \bar{d_r} = \frac{\rho_r}{\rho}. \tag{3.101}$$

Because we have $\bar{R} = (1 - S)$ where $0 \leq S \leq 1$, the scaling of the survival probability is implicit in the numerical grid in space and time. That is, the dose in Gy is defined on the computational grid and is independent of specific values of x and t, therefore the survival probability function is implicitly scaled through the scaling of $\bar{c}(\bar{x},\bar{t})$. Initial conditions and boundary data are given by

$$\bar{c}(\bar{x},0) = \bar{f}(\bar{x}), \quad \bar{r}(\bar{x},0) = 0, \tag{3.102}$$

$$\bar{x} \in \bar{\mathcal{B}}, \quad \bar{t} \geq 0, \quad \nabla\bar{c}\cdot\mathbf{n} = 0, \nabla\bar{r}\cdot\mathbf{n} = 0 \text{ on } \partial\bar{\mathcal{B}}. \tag{3.103}$$

Spherical symmetry Simulations of the delay model in spherical symmetry using the Laplacian in spherical coordinates given by Equation 3.36 results in the following non-dimensional system,

$$\frac{\partial\bar{c}}{\partial\bar{t}} = \bar{D}\left(\bar{c}_{\bar{r_*}\bar{r_*}} + \frac{2}{\bar{r_*}}\bar{c}_{\bar{r_*}}\right) + (1 - \bar{R}(S,\bar{c}))\ \bar{c}(1 - \bar{c} - \bar{r}) \tag{3.104}$$

$$\frac{\partial\bar{r}}{\partial\bar{t}} = \bar{R}(S,\bar{c})\ \bar{c}(1 - \bar{c} - \bar{r}) - \bar{d_r}\bar{r} \tag{3.105}$$

where the subscript denotes partial derivative with respect to the non-dimensional radial coordinate, $\bar{r_*}$ so as not to be confused with the irradiated cell population $\bar{r}$. Initial and boundary data can be restated as

$$\bar{c}(\bar{r_*},0) = \bar{f}(\bar{r_*}), \quad \bar{r}(\bar{r_*},0) = 0, \tag{3.106}$$

$$\bar{r_*} \in \bar{\mathcal{B}}, \quad \bar{t} \geq 0, \quad \nabla\bar{c}\cdot\mathbf{n} = 0, \nabla\bar{r}\cdot\mathbf{n} = 0 \text{ on } \partial\bar{\mathcal{B}}. \tag{3.107}$$

3.6.2 Stability analysis

To investigate the qualitative role the irradiated cell population has on the total tumor growth, we perform a fixed point and phase plane analysis on the system in the absence of diffusion.

Fixed points In order to consider fixed points of the system, we assume the diffusion process is negligible during the irradiation time when $\bar{R}(S,\bar{c}) \neq 0$, and that the radiation dose is spatially uniform, $Dose(x,t) = Dose_0$ so that the radiation loss term becomes a constant and the system reduces to the pair of ordinary differential equations given by

$$\frac{\partial \bar{c}}{\partial \bar{t}} = (1-\bar{R}(S,\bar{c}))\ \bar{c}(1-\bar{c}-\bar{r}) \tag{3.108}$$

$$\frac{\partial \bar{r}}{\partial \bar{t}} = \bar{R}(S,\bar{c})\ \bar{c}(1-\bar{c}-\bar{r}) - \bar{d_r}\bar{r} \tag{3.109}$$

for $t \in treatment$, i.e. $R > 0$, and with initial conditions given by

$$\bar{c}(\bar{t}=0) = \bar{c}_0, \quad \bar{r}(\bar{t}=0) = 0 \tag{3.110}$$

so that time starts at the beginning of a radiation therapy treatment cycle. The equilibrium points of the non-dimensional ODE system are given by setting $\bar{c}_{\bar{t}} = 0$, and $\bar{r}_{\bar{t}} = 0$, to give the following conditions

$$0 = (1-\bar{R}(S,\bar{c}))\ \bar{c}(1-\bar{c}-\bar{r}) \quad \Rightarrow \quad c=0, \quad c+r=1 \tag{3.111}$$

$$0 = \bar{R}(S,\bar{c})\ \bar{c}(1-\bar{c}-\bar{r}) - \bar{d_r}\bar{r} \quad \Rightarrow \quad r=0 \tag{3.112}$$

so that the fixed points for the pair $(\bar{c},\bar{r})$ are given by $(0,0)$ and $(1,0)$. In the $(\bar{c},\bar{r})$ phase plane, the nullclines are given by

$$\bar{c} \equiv 0, \quad \bar{r} = 1-\bar{c}, \quad \bar{r} = \frac{\bar{R}\bar{c}(1-\bar{c})}{\bar{d_r}(1+\bar{R}\bar{c})}. \tag{3.113}$$

The nullclines are shown in Figure 3.10, for varying values of net radiation response $\bar{R}$. Solution trajectories depend on both $\bar{R}$ and $\bar{d_r}$, the dimensionless rate constant which determines the delay time between cell irradiation and cell death. The equilibrium points (0,0) and (1,0) exchange stability based on the bifurcation parameter R as shown in Table 3.1.

To examine the stability of the equilibrium points, we compute the Jacobian as

$$J(\bar{c},\bar{r}) = \begin{bmatrix} (1-\bar{R})[1-2\bar{c}-\bar{r}] & -\bar{c}(1-\bar{R}) \\ \bar{R}[1-2\bar{c}-\bar{r}] & -(\bar{R}\bar{c}+\bar{d_r}) \end{bmatrix}. \tag{3.114}$$

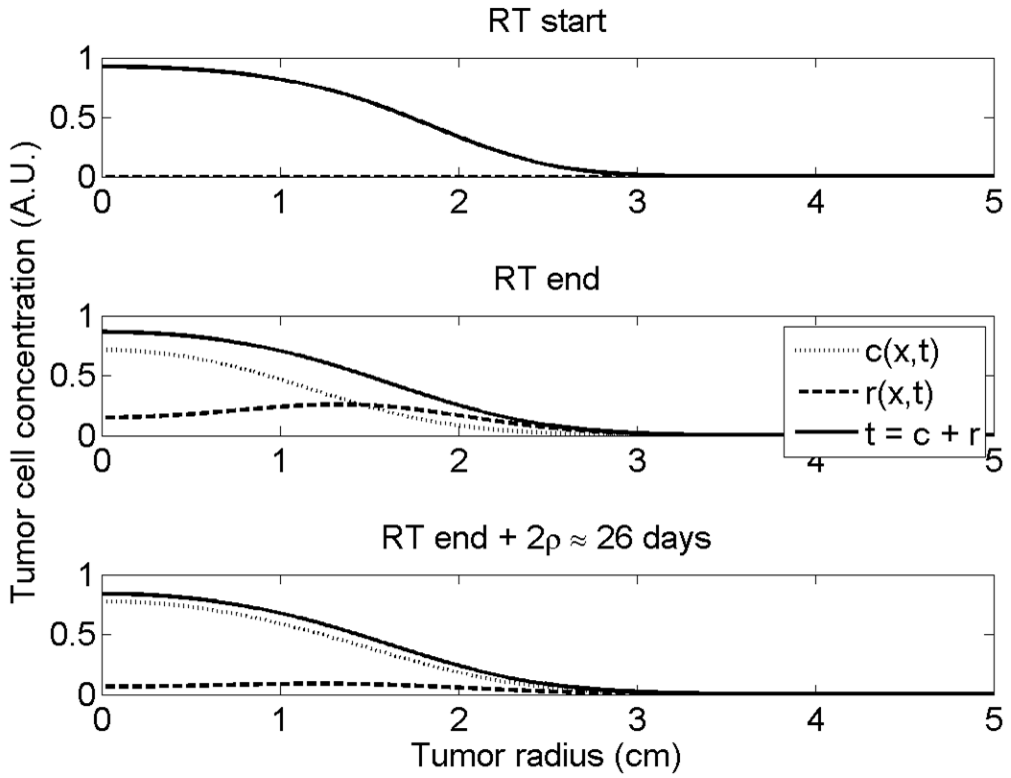

Figure 3.9: Spatial solutions at the beginning, during and end of radiation therapy for the spherically symmetric PIRT-D delay model.

	(0,0)	(1,0)
$\bar{R} < 1$	saddle	node
$\bar{R} > 1$	node	saddle

Table 3.1: Fixed point stability based on values of the dimensionless radiation response $\bar{R}$.

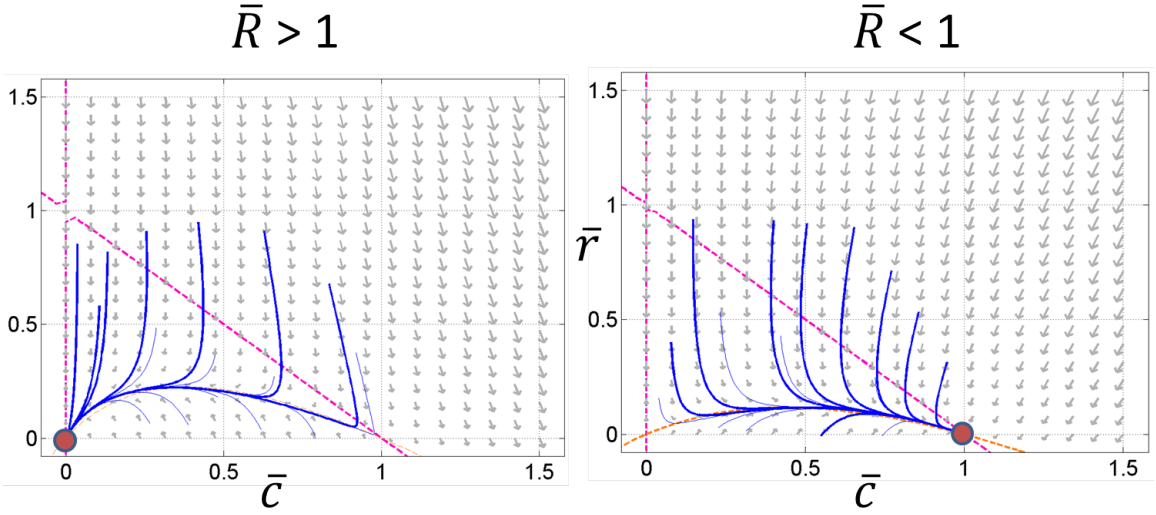

Figure 3.10: Phase portrait in $(\bar{c}, \bar{r})$ space for PIRT-D in the absence of diffusion. Left: Stable node equilibrium at (0,0) when the net radiation effect is greater than unity ($\bar{R} > 1$). Right: exchange of stability when $\bar{R} < 1$, with the stable node equilibrium at (1,0) and (0,0) a saddle point. Nullclines are shown as dashed lines.

The characteristic polynomial for the Jacobian evaluated at the fixed point $(0, 0)$ is given by $\det(J(0, 0) - \lambda I)$, as

$$((1 - \bar{R}) - \lambda)(-\bar{d}_r - \lambda) = 0, \quad \Rightarrow \quad \lambda = -\bar{d}_r, \ (1 - \bar{R}). \tag{3.115}$$

When $(1 - \bar{R}) > 0$ the equilibrium point is a saddle. This corresponds to the case when $\bar{R} < 1$, that is that the rate of change of the tumor cell population due to radiation therapy-induced cell death is less than the net proliferation rate. When $(1 - \bar{R}) < 0$, the equilibrium point is a stable node. This corresponds to the case when the radiation effect is greater

than the proliferation rate so that the tumor cell population $\bar{c}$ is eradicated, along with the irradiated cell population $\bar{r}$.

For the equilibrium point $(1, 0)$, we have the characteristic polynomial given by

$$\det(J(1,0) - \lambda I) = \lambda^2 + (1 + \bar{d_r})\lambda + (2\bar{R} + \bar{d_r})(1 - \bar{R}) = 0. \tag{3.116}$$

The quadratic formula gives

$$\lambda_{\pm} = \frac{-(1 + \bar{d_r}) \pm \sqrt{(1 + \bar{d_r})^2 - 4(2\bar{R} + \bar{d_r})(1 - \bar{R})}}{2}. \tag{3.117}$$

In order to obtain real eigenvalues, the discriminant to be non-negative, giving the condition

$$(1 + \bar{d_r})^2 - 4(2\bar{R} + \bar{d_r})(1 - \bar{R}) > 0. \tag{3.118}$$

Since we have $\bar{R} > 0$ and $\bar{d_c} > 0$, the inequality holds only when we have $1 - \bar{R} < 0$, that is $\bar{R} > 1$. We can think of R as a bifurcation parameter since we have $\bar{R} \neq 0$ during treatment and $\bar{R} \equiv 0$ outside of treatment.

3.7 Quantifying patient-specific radio-sensitivity

Clinical challenge Perhaps the single largest challenge to clinical radiation oncology lies in the *a priori* knowledge of which patients will, or will not, respond to treatment. Quantifying radiation sensitivity and providing metrics of response which tailor treatment decisions to features of the individual patient's growing tumor/lesion could be transformative to the practice of radiation oncology.

Metrics of response Current metrics of response in the clinical setting rely on changes in tumor volume prior to and following completion of a given therapy. Most notably, these metrics are the response evaluation criteria in solid tumors (RECIST), response assessment in neuro-oncology (RANO) and the most general, MacDonald criteria, [64, 123, 138, 145]. These metrics place response into categories, loosely described as complete response (CR), partial response (PR) and progressive disease (PD). None of these methods however are able to differentiate small response from a slow growing tumor from a large response from a rapidly growing tumor, principally because none of them require the estimation of growth

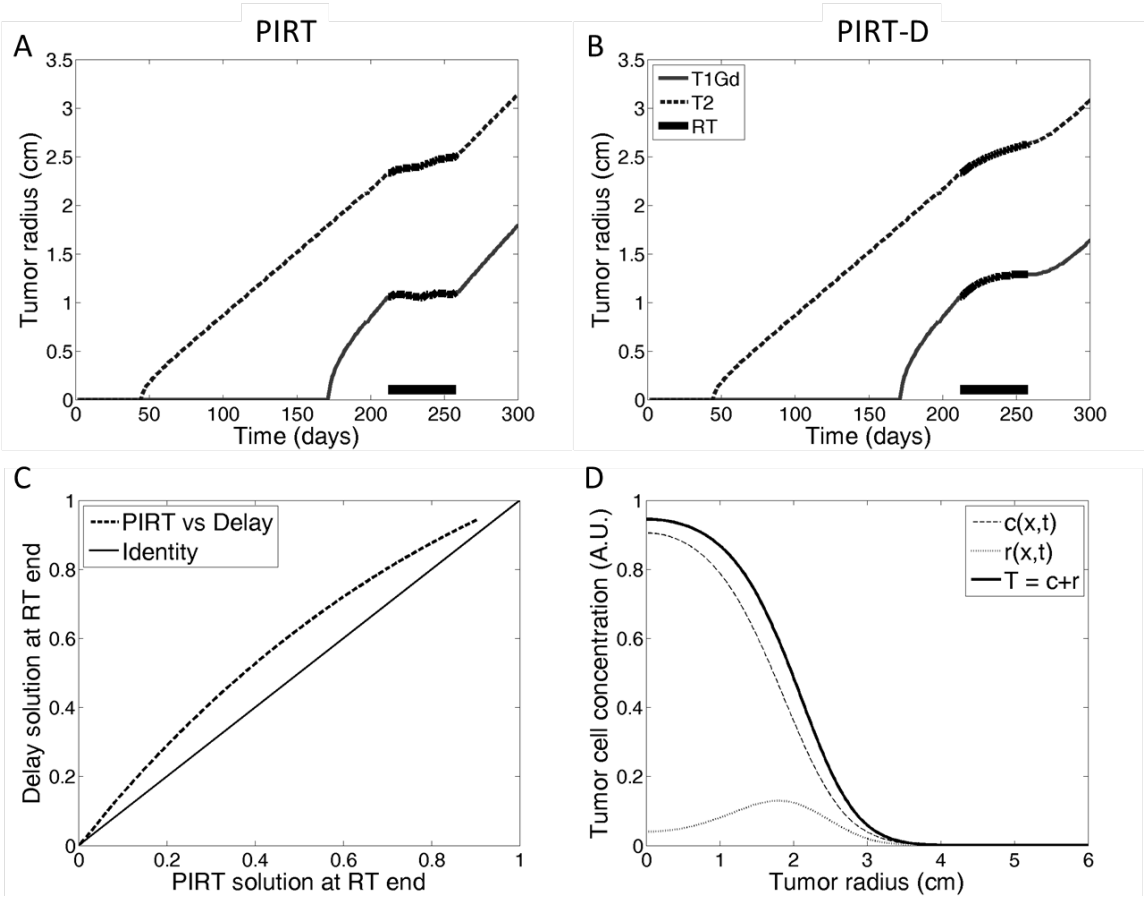

Figure 3.11: The addition of an irradiated population which decays at rate ρ effectively "smooths out" the radius versus time curve response to radiation therapy. A) PIRT model simulation, B) PIRT-D delay model simulation with the same parameters, radiation treatment, radiation dose. C) PIRT solution $\bar{c}_{PIRT}(\bar{x}, RTend)$ plotted against the delay model solution $\bar{c}(\bar{x}, RTend)$ along with the line of identity, revealing increased net tumor cells in the delay model over the PIRT. This is due to the irradiated cell population contributing to the overall tumor volume. D) the delay model solution at $\bar{t} = RTend$, illustrating the irradiated/quiescent tumor cell fraction of the total tumor cell population.

rate, or velocity *prior to treatment*. Acknowledging that radiation response is much more complicated than any imaging modality can reveal [71], we present a quantification of radiation response which is patient-specific and relies on pre-treatment growth kinetics in order to provide a biological rationale for our response measure. Moreover, we present a method to estimate patient-specific radio-sensitivity in addition to the degree of response

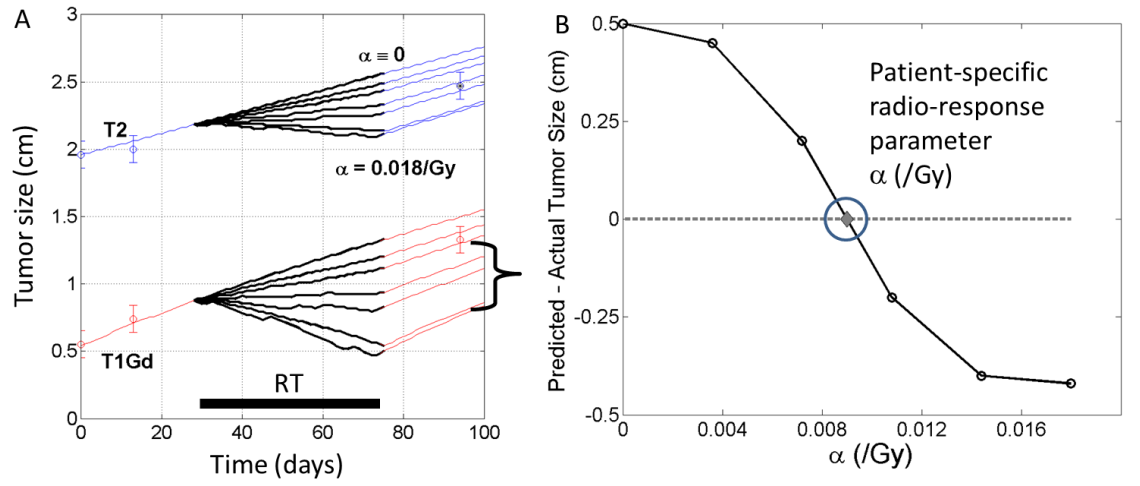

Figure 3.12: A) Tumor volume data pre- and post-treatment is plotted along with spherically symmetric radial tumor growth and radiation therapy for six values of α ranging from zero (no effect) to 0.018 /Gy (high effect). B) The optimal value of α which minimizes error between the model and the data following therapy lies in the interval $0.008 \leq \alpha \leq 0.012$. The optimal value for α is computed using linear interpolation. Figure A adapted from Rockne 2010 [151].

to radiation therapy.

In order to estimate the radiation response model parameter α (Gy^{-1}) (3.20) for a specific patient, a range of values for α are chosen and RT is simulated for each, with the difference between the simulated T1Gd and T2 radii and the measured data are recorded for each patient (Figure 3.12). The model predicted tumor volume is fitted to match the tumor size as measured on the first post-RT MRI. As demonstrated with the linear approximation analysis, the relationship between D, ρ, and α is nonlinear and spatially variable according to the patient-specific dose distribution and schedule. As such, RT is simulated several times, with a range of α values, yielding a relationship between α and the simulated imageable RT response, unique to the patient [151]. Regression is performed to yield a value of α that minimizes the difference between the simulated and actual target radius. To ensure that our quantification of radiation response is robust to imaging modality, optimal values for α are computed using both T1Gd and T2 post-RT tumor size, see Figure 3.12.

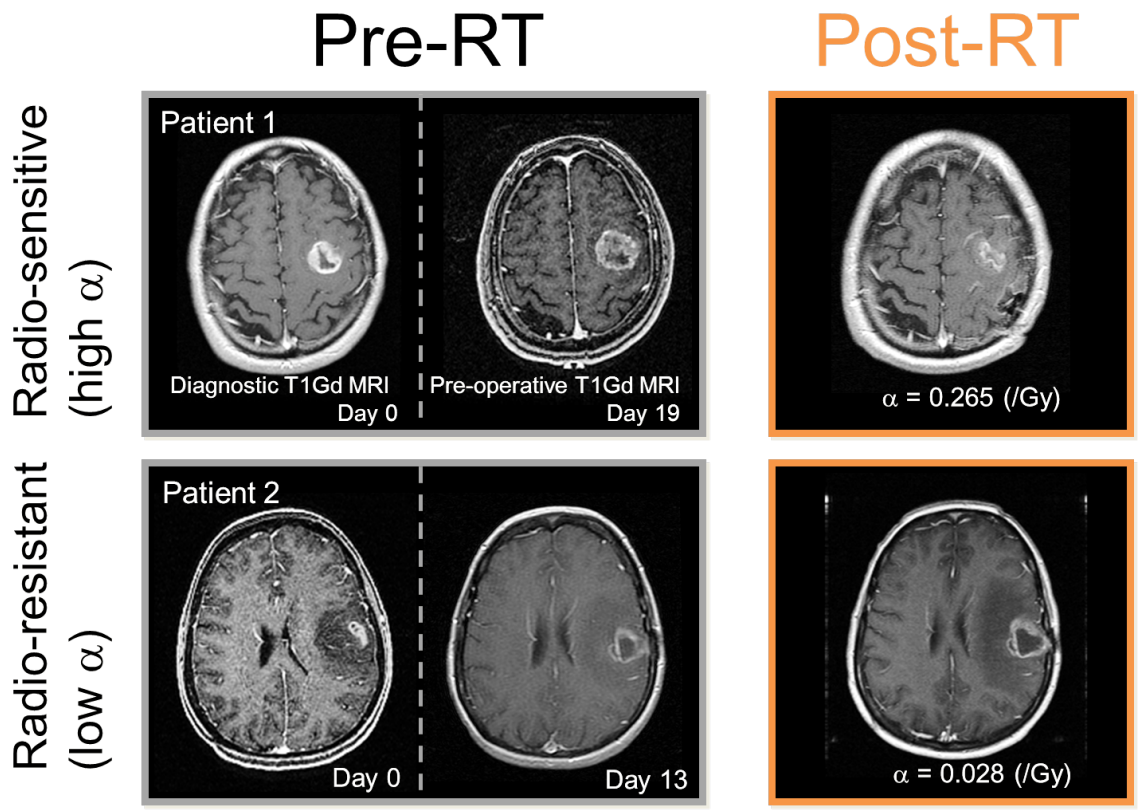

Figure 3.13: Two patients that have quantifiable disease growth and response kinetics provided by a patient-specific radiographic calibration of the proliferation-invasion model of glioblastoma. First two columns are MRIs taken prior to conformal radiation therapy (RT). The third column is taken approximately 30 days following conformal radiation therapy. Computation of α for each patient provides a means to quantitatively differentiate response rates between individuals. Adapted from Rockne 2010 [151].

Patients that cannot meet the T1Gd or T2 post-RT target radius for any non-negative value of α can be thought of having an α value of zero, and would not have deviated from their untreated virtual control baseline behavior. Such a patient would have a velocity of growth during treatment greater than that measured prior to treatment, implying an accelerating effect of RT on the tumor growth, ($\alpha < 0$), which is assumed not to exist. In the case when the radio-sensitivity parameter value is zero $\alpha \equiv 0$, this corresponds to the situation in which the net proliferation of the tumor overwhelms the treatment response and the patient theoretically receives no benefit from the therapy, and the model-predicted growth is unaffected by the treatment.

This presents an interesting paradox: patients that are most likely to respond to therapy (high ρ) are also the patients whose tumors recover and progress the fastest and, as a corollary, have worse prognosis. On the other hand, patients who are likely to see little to no benefit from therapy (low ρ), are also the tumors which grow slower and therefore have a better overall prognosis.

The effects of chemotherapy and alkalizing agents such as temozolomide specified by the "Stupp protocol [175]" are considered to be incorporated into the net radiobiological effect parameter α. Due to a dearth of glioblastoma patients receiving RT only, without concurrent chemotherapy, the specific effects of chemotherapy on response are not explicitly modeled, although this has been studied in the context of the PI model [196, 181]. However, an alternative PIRT model may help understand delayed or late effects of radiation not directly linked to the therapeutic effects of adjuvant chemotherapy.

3.7.1 Data analysis

Twenty four ($N = 24$) glioblastoma patients were used to investigate the relationship between the net-proliferation rate and the radio-sensitivity by simulation of their treatment plans, Table 3.2. The method for computing D and ρ for each patient is detailed in Chapter 4.

patient	D (cm^2/year)	ρ (/year)	$\alpha_{\text{PIRT-D}}$ (/Gy)	α_{PIRT} (/Gy)	RT dose (Gy)	Survival Days
1	0.352	6.904	0.087	0.019	59.4	92
2	0.810	41.877	0.242	0.217	61.2	681
3	0.378	35.196	0.117	0.116	59.4	1336
4	0.105	137.018	0.287	0.000	59.4	115
5	0.184	35.135	0.247	0.162	59.4	2356
6	0.277	3.587	0.009	0.005	59.4	823
7	0.079	15.244	0.000	0.000	69.0	375
8	0.262	54.374	0.167	0.167	61.2	572
9	0.499	16.794	0.047	0.046	60.0	508
10	1.098	66.567	0.357	0.293	61.2	286
11	0.379	55.847	0.173	0.143	60.0	331
12	0.035	4.968	0.000	0.000	59.4	1276
13	0.140	20.976	0.023	0.023	61.2	753
14	0.136	57.068	0.396	0.265	61.2	334
15	0.089	50.288	0.422	0.265	59.4	552
16	0.507	13.883	0.039	0.028	61.2	377
17	0.035	5.540	0.000	0.000	64.8	266
18	0.501	18.330	0.079	0.055	61.2	826
19	0.126	7.993	0.080	0.032	65.0	453
20	0.013	28.844	0.045	0.045	61.2	351
21	0.066	17.042	0.108	0.084	60.4	617
22	0.244	33.542	0.133	0.105	60.0	345
23	0.044	18.367	0.221	0.106	60.0	428
24	0.286	8.158	0.036	0.024	61.2	417

Table 3.2: Data for N = 24 glioblastoma patients analyzed with both the PIRT and PIRT-D models.

3.7.2 Predicting radiation response

The mathematical relationship between radiation response (α) and net proliferation rate (ρ) in the PIRT-D model is complicated by the spatial and temporal variation of radiation dose and response throughout the tumor. A positive correlation is found between the *pre-treatment* proliferation rate ρ and the patient's radio-sensitivity α (Figure 3.14), so that tumors with a higher net-proliferation rate are more radio-sensitive. A similar result was found on a smaller set of patients ($N = 9$) with the PIRT model [151]. To test the predictive value of this relationship, a leave-one-out cross validation (LOOCV) was performed on the data set [159]. This analysis systematically removes one patient from the population, computes a new line of regression between α and ρ, and uses the regression to estimate the radio-sensitivity for the patient removed from the data set. Then a PIRT-D simulation is performed with the estimated value of α and the difference between the model-predicted tumor size and the observed tumor size is recorded. The radio-sensitivity (α) calculated using the PIRT model is positively correlated with that calculated for the PIRT-D model, with the value of α computed for the PIRT-D model less than or equal to that computed for the PIRT model (Figure 3.15). Patients for whom the value of α calculated using PIRT and PIRT-D models would have little to no component of their response to radiation altered by delayed effects. We would expect the patients for whom the value of α computed using the delay model is much greater than that computed with the PIRT model to be likely candidates for pseudoprogression, as this would imply a large component of their tumor size following radiation therapy to be influenced by delayed radiation effects.

Resection Surgical resection is ubiquitous in the treatment of glioblastoma. At minimum, a tissue based diagnosis is required to establish the relevant treatment paradigm. Modeling surgical resection is critical for a data-driven, patient-specific modeling approach. In order to approximate surgical resection, we simply truncate the computational domain and preserve the no-flux boundary condition at the relocated origin point, to match the spherically equivalent radius of the volume of residual tumor, with the solution value set to zero inside the resection cavity. This approach to approximating surgical resection presents a chal-

lenge for resections which are highly irregularly shaped and cannot be well approximated by removing a volume from the center of the tumor bed. In these cases, full 3-dimensional models are needed.

Assessment of response to radiation therapy using MRI alone is difficult, and likely confounded by a number of factors related to normal tissue response, selection for resistant tumor cell clones, changes to the tumor micro-environment, and wound healing processes, to name a few. However, cellular DNA repair kinetic analysis suggests it may be possible to measure intrinsic radio-sensitivity of a cell [51]. Moreover, velocity of growth may be used to predict response relative to untreated baseline growth [183].

Changes in MRI tumor volume have shown to be correlated with response [197], however, these results do not provide a *predictive* relationship from pre-treatment imaging data. Moreover, the RTOG recursive partitioning analysis is predictive [160] of overall survival, but does not differentiate between patients, rather, partitions them into statistically similar groups with no regard to individual variations in disease kinetics or overall treatment response.

3.8 Discussion

Factors impacting the ability to accurately calculate patient-specific PIRT model parameters, such as pre-operative steroids which reduce inflammation and therefore the edema associated with the T2/FLAIR regions of hyper-intensity. This would result in an underestimate of the ratio D/ρ, as the low density tumor profile would be reduced, which would steepen the tumor cell gradient, resulting in a relatively higher proliferation rate relative to the diffusion rate for a fixed growth velocity. The steroid effect is likely to be most prominent in patients with extended periods of time between two pre-operative MRIs, for high-dose steroids to take effect and impact imageable disease. This may additionally contribute to reduced observed volumetric velocity of growth on the T2/FLAIR sequence. A fundamental assumption of the PI model is that the tumor grows at a positive rate. These effects could further explain differences in T1Gd and T2 velocity of growth.

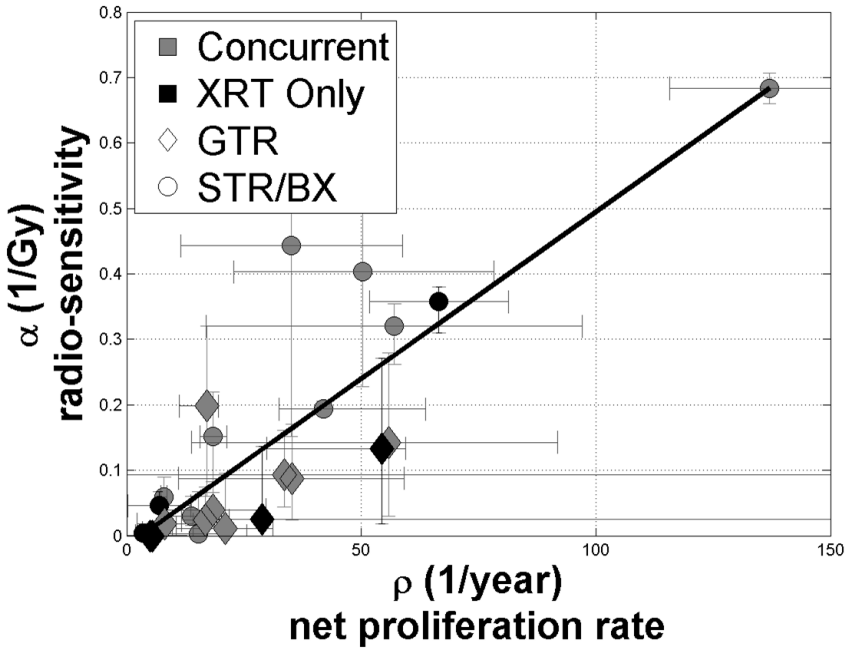

Figure 3.14: Relationship between radiation response and tumor proliferation rate parameters α (/Gy) and ρ (/year), respectively, r=0.85, p<0.001, N=24 for the two species delayed effects PIRT-D radiation model. Concurrent: chemotherapy administered with radiation therapy. GTR: gross total resection. STR: sub-total resection. Bx: biopsy. Uncertainty in calculated radio-sensitivity was calculated using a leave-one-out cross validation analysis [159].

Estimation of radiobiological parameters *in vivo* Through a meta-analysis of clinical data, Qi et al. have estimated linear-quadratic radiobioloical parameters for astrocytomas of low and high grade, including glioblastoma [144], however this analysis relies on assumptions of tumor growth and response rates and treats all patients within a histologic category the same. Although differential radiobiological parameters are calculated across histologic grades, the parameter range observed encompasses the entire range of observable parameter space, $\alpha \in [0.06 \pm 0.05]$ /Gy, and $\alpha/\beta \in [10 \pm 15.1]$ Gy, with tumor doubling times in the enormous range of $T_d = 50 \pm 30$ days.

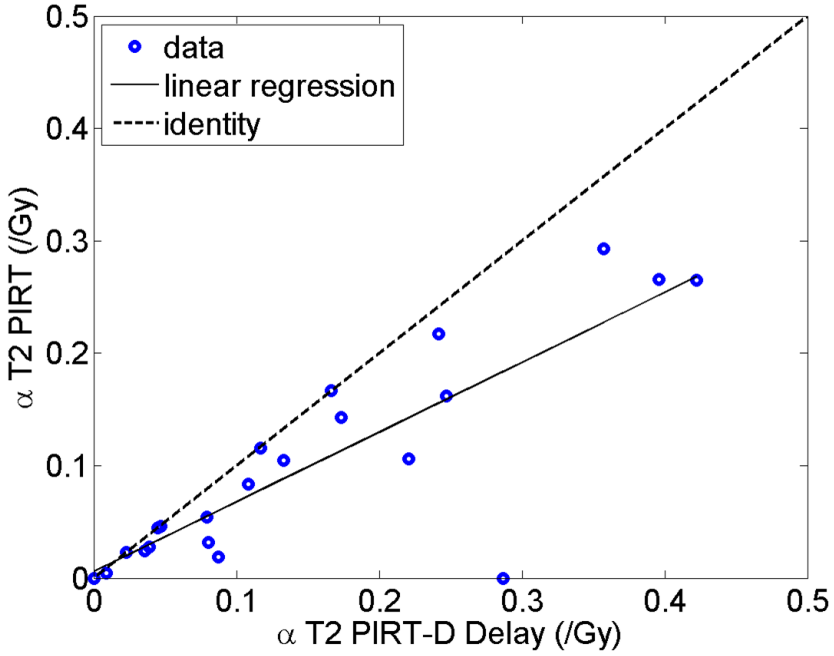

Figure 3.15: Relationship between radiation response response parameters estimated for the PIRT and PIRT-D models α (/Gy) respectively, r=0.85, p<0.001, N=24. The value of α computed with the PIRT-D model is always less than or equal to that computed with the PIRT model. In cases where the parameter estimates are equal, we expect little effect of delay in determining post RT tumor size. In cases where α is much greater using the PIRT-D model (4–5 data points below the line of linear regression) we expect the role of delayed response to RT to have a larger effect, implying these patients could experience pseudoprogression on subsequent MRI scans following the completion of RT.

Normal tissue toxicity Normal tissue response is not included in the PIRT or PIRT-D model formalisms, however the importance of normal tissue toxicity and tolerance doses in the clinical setting cannot be understated. In the PI model, tumor cell migration through brain tissue is not modeled, nor is the damage, inflammation and response of normal tissue to radiation therapy, which can confound imaging-based metrics of response [71]. Both normal tissue toxicity and healing kinetics [82] as well as toxicity related effects of radiation therapy should be considered in future models, particularly in the context of altered delivery schedules such as hypo and hyper fractionation in which the dose is delivered in fewer, larger and more, smaller doses respectively. For a fixed parameters D and ρ without normal tissue

toxicity considered, the standard daily fraction delivery is shown to give improved tumor control [150]. However, this analysis does not take into account the role of normal tissue damage, toxicity, or differences in model parameters. One might expect tumors with higher proliferation rate ρ to be better candidates for hyper fractionation such that the radiation treatment creates a resonant effect with the cells in the tumor such that the re-assortment into the cell cycle is timed with the treatment delivery. Convergence of cell cycle times in periodically delivered radiation therapy has been observed [79, 102].

Dose optimization Radiation dose optimization and dose "painting," are often attempted, but without regard to patient-specific growth and response kinetics, provided by the PIRT and PIRT-D models. Biological optimization of radiation dose is possible using multi objective evolutionary algorithms (MOEA) which utilize the patient-specific tumor cell density profiles and radiation sensitivity metrics provided by the PIRT(D) models [92, 93]. However, many studies have shown that dose escalation and restricted or expanded dose margins have not produced statistically significant changes in overall survival for glioblastoma patients [141], and overall radiation response and prognosis has changed very little [19] despite extensive, whole-brain irradiation. Attempts to sculpt radiation dose based on biological parameters which are not patient-specific have resulted in theoretical or modest changes to overall response [108, 1]. Irradiation margins based on advanced imaging inferences of tumor cell invasion of the normal appearing brain have not been compared to clinical data or validated *in vivo* [98]. See Moghaddasi et al. for a recent review of mathematical model-driven tumor irradiation volume delineation [129].

Chapter 4

QUANTIFYING HYPOXIA-MODULATED RADIATION-RESISTANCE IN HUMAN GLIOBLASTOMA *IN VIVO*

The four R's of radiobiology are rexoygenation, repopulation, repair and reassortment into the cell cycle. Each of these influences response of tissues to ionizing radiation, and each should be considered when translating physical dose into biological effect [79][+more]. Hypoxia, or lack of oxygen reduces free-radical based DNA damage induced by ionizing radiation. The lack of oxygen in the environment permits fewer free-radical species to be formed from ionizing events, and therefore fewer lesions to the cell's DNA [166], and is a known factor in treatment resistance [7], particularly in glioblastoma [61]. The oxygenation effect varies with radiation energy, particle, cell line and tissue environment. The role of hypoxia in defining response to ionizing radiation has been well characterized *in vitro*, and in animal experiments *in vivo*, however, there exists few mechanisms to study this in humans.

Glioblastoma is a particularly hypoxic primary brain tumor. The disease is, in part, histologically defined by the presence of neoangiogensis and necrosis arising from the tumor growth. The cascade of events which initiate and propagate neoangiogenesis may involve both acute and chronic hypoxic events. A hallmark of glioblastoma on radiographic imaging is the presence of a contrast-enhancing ring surrounding a region of hypo-intensity [122, 31]. These regions correspond directly to tumor-induced angiogenesis and necrosis, respectively. Although the human brain is oxygen rich in its native state, glioblastoma tumor cells consume oxygen through both cooption of existing vasculature, as well as stimulation of new vasculature [122]. Increased hypoxia is a hallmark of aggressive tumor growth [61, 186, 112] and is negatively correlated with prognosis, although this is debated [63]. In order to better understand patient-specific metrics of radiation response and the role of hypoxia in mediating that response, we consider a patient-specific mathematical model which incorporates tumor proliferation and invasion, coupled with a spatially and temporally defined radia-

tion response and resistance model, which is parameterized by routine clinical imaging and functional positron emission tomography (PET) respectively [40, 113].

The ultimate motivation however is the need for more quantitative and individualized medicine. We present an application of a patient-specific, biologically-based mathematical model for glioma growth that quantifies response to radiation therapy (RT) using *in vivo* human data. The model is based on estimates of tumor growth, characterized by net rates of proliferation and invasion, that incorporates cell-kill subsequent to radiation therapy with the linear-quadratic dose-response model. Using only routinely available pre-treatment MRI, the model provides patient-specific 4-dimensional simulations of tumor growth and radiation therapy.

We have previously demonstrated that estimates of the growth kinetics are prognostic for outcome and that metrics of biological aggressiveness derived from these estimates are related to relative hypoxia within the tumor [186]. Additionally, these model parameters can predict the extent of radio-sensitivity of individual glioblastoma patients. Despite the ability to characterize patients prior to treatment, to date, there have been no clear advantage of using these models in the design of treatment plans. To our knowledge, this work presents the first patient-specific mathematical model to quantify radio-sensitivity based on *in vivo* glioma data utilizing the complex 3D architecture of the human brain.

4.1 Patient-specific calibration of the PI model

The goal for patient-specific modeling in the context of cancer is to create a virtual copy of the disease process being observed, which captures essential behavior and is focused at the appropriate scale relative to the quantity of interest. The model should be no more complicated than necessary, and should be able to recapitulate the data from which it is derived.

"All models are wrong, but some are useful." George E. P. Box

We present here a method to characterize glioblastoma growth and invasion on a patient-specific basis by using a fitting process to parameterize a reaction-diffusion partial differential equation which describes the differential motility of glioblastoma tumor cells throughout

the brain, in addition to density-dependent net proliferation. Once parameterized for an individual patient, based on routine clinical imaging data, the model is able to provide a quantitative characterization of the tumor invasion and evolution which is predictive of survival, response to therapy and overall aggressiveness.

The proliferation-invasion model of glioma growth is given as follows. Let $c = c(\mathbf{x}, t)$ represent the concentration of tumor cells per volume (mm^3) at a location $\mathbf{x} = (x, y, z)$ at time t where the domain $\mathcal{B}$ (brain) is closed and bounded. The model is a reaction-diffusion partial differential equation which describes both the net diffusion and proliferation of tumor cells as follows:

$$\overbrace{\frac{\partial c}{\partial t}}^{\substack{\text{rate of change} \\ \text{of glioma cell} \\ \text{density}}} = \overbrace{\nabla \cdot (D(\mathbf{x}) \nabla c)}^{\substack{\text{net dispersal} \\ \text{of glioma cells}}} + \overbrace{\rho c \left(1 - \frac{c}{K}\right)}^{\substack{\text{net proliferation} \\ \text{of glioma cells}}} \tag{4.1}$$

$$\mathbf{x} \in \mathcal{B}, \quad t \geq 0 \tag{4.2}$$

$$\mathbf{n} \cdot \nabla c = 0 \text{ on } \partial\mathcal{B}, \quad c((x_0, y_0, z_0), t = 0) = c_0, \tag{4.3}$$

$$D(\mathbf{x}) = \begin{cases} D_w & \text{if } \mathbf{x} \in \text{white matter} \\ D_g & \text{if } \mathbf{x} \in \text{grey matter} \\ 0 & \text{else} \end{cases} \tag{4.4}$$

where $D(\mathbf{x})$ is the spatially resolved diffusion coefficient with units mm^2/year, ρ is the net rate of proliferation per year, K is the carrying capacity of the tissue assuming a 10 μm diameter spherical cell [27],

$$K \approx \frac{1 \text{ cell}}{5.24 \times 10^2 \mu\text{m}^3} \left(\frac{10^3 \mu\text{m}}{1 \text{ mm}}\right)^3 = 1.91 \times 10^6 \text{cells/mm}^3. \tag{4.5}$$

No flux boundary conditions $\mathbf{n} \cdot \nabla c = 0$ which prevents cells from leaving the brain domain, $\mathcal{B}$, at its boundary $\partial\mathcal{B}$ and initial distribution of tumor cells $c_0(\mathbf{x}, t = 0)$. This model allows the diffusion coefficient to be a tensor to account for the complex geometry and preferential directions for cell migration in the brain. For the scalar case, the migration rate in white matter is considerably higher than that in grey matter, $D_w \gg D_g$.

In order to adapt the proliferation-invasion (PI) model to patient-specific data, we must relate the model parameters to data so that they are uniquely determined, but without attempting to solve an inverse problem. A closed-form solution has not been found for the PI model with spatially resolved diffusion coefficient $D(x)$. However, we may regard a homogenized diffusion coefficient to be the effective diffusion rate, D_{eff} to be a weighted average of the scalar diffusion rates in gray (g) and white (w) matter with weight constants γ and ω, so that

$$D_{\text{eff}} = \omega w D_w + \gamma g D_g. \tag{4.6}$$

As the tumor grows within the brain, for a fixed iso-density, the relative proportions of grey and white matter within the tumor will change in time. Moreover, the inverse heat equation is ill posed, meaning that small changes in initial data lead to large changes in solution behavior [74]. A more tractable approach is to solve the spatially uniform diffusion problem, the Fisher-Kolmogoroff model where we regard the calculated diffusion coefficient (D) to simply be an estimate of D_w, the faster of the two rates D_w and D_g, so that we have

$$\frac{\partial c}{\partial t} = D\nabla^2 c + \rho c(1 - c/K). \tag{4.7}$$

More tractable still, is a linear proliferation model, for which exact solutions exist. In one dimension on an infinite domain

$$\frac{\partial c}{\partial t} = D\nabla^2 c + \rho c \tag{4.8}$$

$$c(x, t = 0) = c_0\delta(x), \quad x \in \mathbb{R}. \tag{4.9}$$

With initial point-source tumor cell concentration given by a scaled Dirac delta function at the origin, the solution is given by

$$c(r, t) = \frac{c_0}{(4\pi D t)^{1/2}} \exp\left(\rho t - \frac{r^2}{4Dt}\right) \tag{4.10}$$

in the axially symmetric radial coordinate r [133]. The form given in Equation 4.10 should be close to the solution for the nonlinear model when c much less than the carrying capacity K, so that

$$\rho c\left(1 - \frac{c}{K}\right) = \rho c - \rho\frac{c^2}{K} \approx \rho c \quad \text{for} \quad c \ll K. \tag{4.11}$$

With a closed form solution to the linear problem with constant diffusion coefficient, the solution can be rearranged to give the evolution of the tumor radius in time for a fixed isodensity c^*, as

$$r^* = 2\sqrt{D\rho}\, t\sqrt{1 - \frac{1}{\rho t}\ln\left((4\pi Dt)^{1/2}c^*/c_0\right)}. \tag{4.12}$$

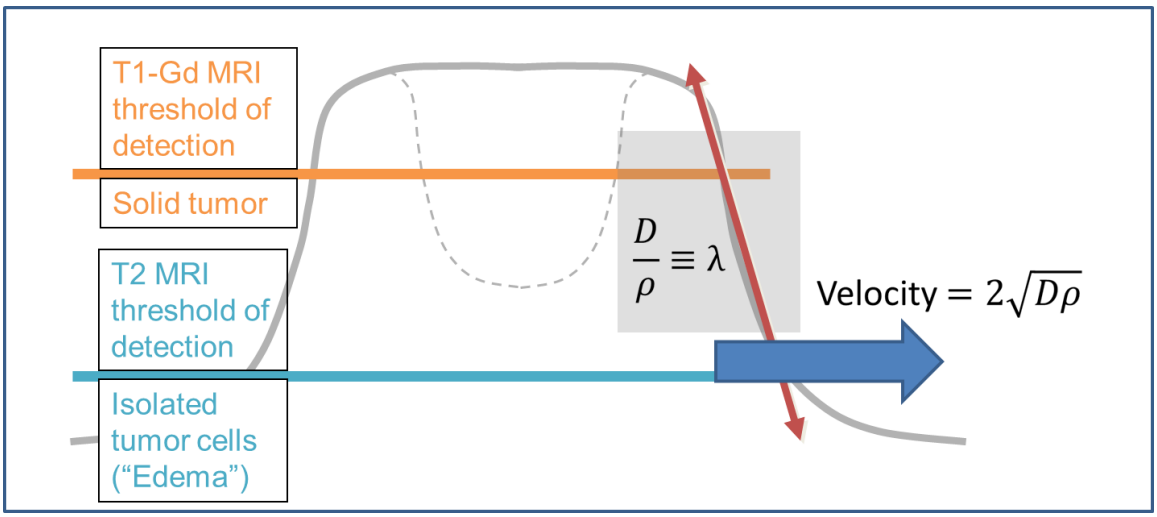

Figure 4.1: Illustration of relationship between imaging features and tumor cell isodensities used to calibrate patient-specific model parameters. The relative invasiveness ratio $\lambda \equiv D/\rho$ is correlated to the slope of the half-max of the tumor cell concentration curve. The velocity of radial expansion is related to the model parameters by Fisher's approximation $v = 2\sqrt{D\rho}$. Together, these two equations uniquely define the model parameters for each patient.

The boundary of the hyperdense angiogenic tissue and necrotic regions are detected by T1-Gd-MRI ("T1Gd") imaging while the boundary of the edema is detected by T2/FLAIR-MRI ("T2/FL") imaging. The diffuse invasion of tumor cells extends well past the T2-imaging-detected boundary. The orange horizontal line in Figure 4.1 shows the concentration threshold for T1Gd-imaging detection and the blue horizontal line shows the concentration threshold for T2-imaging detection, respectively. The lines of isodensity form a concentration-gradient wave front which moves outward. The position of the wave front varies linearly with time, which asymptotically approaches a constant wave-front velocity $2\sqrt{D\rho}$ [62, 132]. In fact, the wave-front velocity may initially be nonlinear, but asymp-

totically approaches linear radial growth and thus a constant velocity, as seen in Figure 4.2.

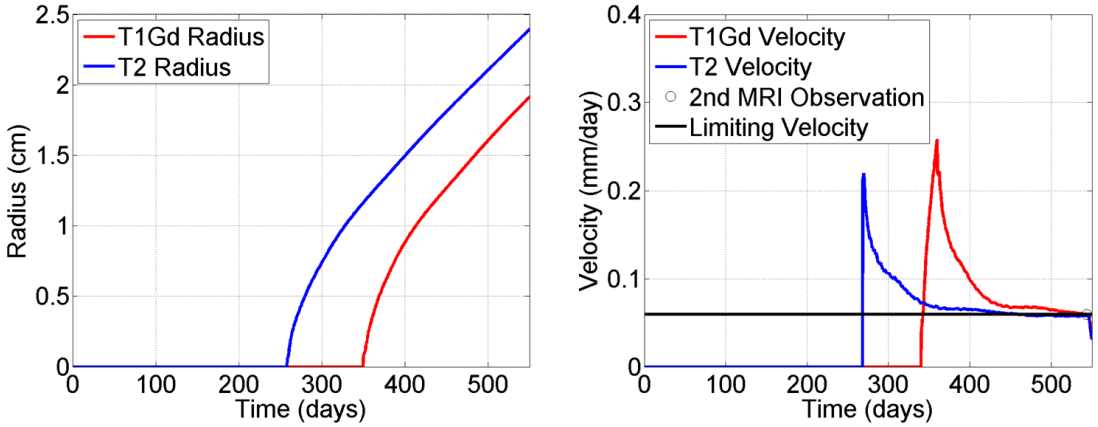

Figure 4.2: Left: PI model solutions with time evolution of T1GD and T2 spherically equivalent radii which grow linearly in time following a brief nonlinear period. Right: Velocity of radial growth approaching a constant value provided by Fisher's approximation.

The wave front may be defined by spherically equivalent radii (r_{T1GD}, r_{T2}) at isodensities relative to the tumor cell carrying capacity K, as $0.80K$ and $0.16K$ respectively. Accordingly, we consider the axially symmetric form of the PI model as follows. The spherical tumor of volume equal to the volumes of the tumor at times t_1 and t_2. An average linear rate of expansion of the tumor along directions normal to surface of the tumor is computed as the wave-front velocity. Thus, two different MRI images are used to compute velocity v, as:

$$v_{T1Gd,T2} = 2\sqrt{D\rho} = \frac{r_2^{(T1Gd,T2)} - r_1^{(T1Gd,T2)}}{t_2 - t_1} \tag{4.13}$$

depending on whether the T1GD or T2 velocity is measured, v_{T1Gd} and v_{T2}, respectively. Here the subscripts indicate the chronological ordering of time points of the data so that r_1 is the first time point and r_2 is the second time point MRI observation of the tumor. The gross tumor volume (GTV) extracted from three-dimensional segmentation of MR images [44, 21] is translated to a spherically-equivalent radius (SER) by inverting the formula for

the volume of a sphere, so that

$$r = \left(\frac{3}{4\pi}v\right)^{1/3}. \tag{4.14}$$

A second equation relating the two unknown parameters ρ and D is needed in order to uniquely determine them for an individual patient/tumor. Specifically, we seek the ratio D/ρ to describe the patient-specific tumor density profile, denoted by λ. The ability to estimate patient-specific parameters from only two pre-treatment MRI studies is enabled by the calculation of a patient-specific value of the invisibility index, or the ratio of the net invasion rate to the net proliferation rate, D/ρ. Combined with Fisher's approximation, D and ρ can be estimated for a patient, with the following relationships

$$\lambda = \frac{D}{\rho}, \quad v = 2\sqrt{D\rho}. \tag{4.15}$$

Applications of patient-specific parameter estimates have been studied extensively, and have been shown to have prognostic value [201, 135], predict response to therapy [151, 136] and quantify biological aggressiveness [186].

An analytical solution for the Cauchy problem formulation of the constant coefficient linear reaction-diffusion model on an infinite spatial domain and semi-infinite time in 3-dimensions

$$\frac{\partial c}{\partial t} = D\nabla^2 c + \rho c \tag{4.16}$$

$$\mathbf{x} \in \mathbb{R}^3,\ t \geq 0, \quad c(\mathbf{x_0}, t = 0) = c_0\delta(\mathbf{x_0}) \tag{4.17}$$

where $\mathbf{x} = (x, y, z)$ is given by

$$c(\mathbf{x}, t) = \frac{c_0}{(4\pi Dt)^{3/2}} \exp\left(\rho t - \frac{r^2}{4Dt}\right) \tag{4.18}$$

So that the equation which determines the radial evolution of the tumor in time for isodensity c^* in three spatial dimensions is given by

$$r^* = 2\sqrt{D\rho}t\sqrt{1 - \frac{1}{\rho t}\ln\left(\frac{(4\pi Dt)^{3/2}c^*}{c_0}\right)}. \tag{4.19}$$

From Equation 4.19 with image isodensity thresholds c_{T1GD} and c_{T2}, an equation for the ratio of ρ to D can be given by

$$\lambda_f = \left(\frac{\rho}{D}\right)_f = \left[4\frac{\ln(c_{T2}/c_{T1Gd})}{\left(r_{T2}^2 - r_{T1Gd}^2\right)}\right]\left(\frac{r_{T1Gd}^2 \ln(c_{T2}/c_{T1Gd})}{\left(r_{T2}^2 - r_{T1GD}^2\right)} + \ln\left(\frac{c_{T2}}{c_0}\right)\frac{\pi(r_{T2}^2 - r_{T1Gd}^2)}{\ln(c_{T2}/c_{T1Gd})^{3/2}}\right). \tag{4.20}$$

This expression relates isodensities and spherically equivalent radii to the ratio ρ/D so that from a single pair of T1Gd and T2 MRI scans we can obtain a quantitative metric of relative invasiveness and characterize phenotype, presented in United States patent # US 12/709,367 [184]. The ratio D/ρ is not correlated to a simple algebraic relationship between the spherically equivalent radii observed on MRI. Moreover, the value of λ is not constant throughout the solution evolution in time.

4.1.1 Non-dimensionalization

For the isotropic, constant diffusion coefficient case in axial symmetry given by

$$\frac{\partial c}{\partial t} = D\left(\frac{\partial^2 c}{\partial r^2} + \frac{2}{r}\frac{\partial c}{\partial r}\right) + \rho c\left(1 - \frac{c}{K}\right) \tag{4.21}$$

the following scaling of the radial coordinate variable r as

$$\bar{r} = r\sqrt{\left(\frac{\rho}{D}\right)} \tag{4.22}$$

is preferable to resolve solutions with steep wave fronts. Specifically, define non-dimensional variables

$$\bar{r} = r\sqrt{\left(\frac{\rho}{D}\right)}, \quad \bar{t} = \rho t, \quad \bar{c} = \frac{c}{K} \tag{4.23}$$

which results in the following dimensionless equation

$$\frac{\partial \bar{c}}{\partial \bar{t}} = \bar{D}\left(\frac{\partial^2 \bar{c}}{\partial \bar{r}^2} + \frac{2}{\bar{r}}\frac{\partial \bar{c}}{\partial \bar{r}}\right) + \bar{c}(1 - \bar{c}) \tag{4.24}$$

where

$$\bar{D} = \sqrt{\frac{D}{\rho}}. \tag{4.25}$$

This non-dimensionalization eliminates one of the parameters, and scales the effective diffusion coefficient to the square root of the ratio (D/ρ).

The shape of the tumor wave front depends on the shape of the initial tumor cell distribution [132]. Kolmogoroff showed that if the initial condition has compact support, then the solution will develop a traveling wave solution (Kolmogoroff 1937). The analytic solution assumes a point-source Dirac delta concentration of tumor cells. Any other initial condition form would impact the shape of the final solution by convolution of the point-source solution with the initial tumor density distribution function. We therefore chose the initial condition to be the analytic solution to the linear equation evaluated after one-proliferation cycle of the cells $t = 1/\rho$ to give

$$c_0(r, t = 1/\rho) = \frac{C_0}{(4\pi D/\rho)^{3/2}} \exp\left(\frac{1}{\rho} - \frac{r^2}{4D/\rho}\right). \tag{4.26}$$

The choice of initial number of tumor cells C_0 is arbitrary, provided it is less than the carrying capacity and greater than zero. This choice of initial condition ensures the shape of the wave front stays close to the analytic solution to the linear equation with a point-source initial condition. Our spatial mesh, which may be on the scale of MRI resolution and moreover, what is measurable on MRI, $\approx$ 1 mm, which is the minimum detectable measurement of tumor growth and response to therapy.

4.2 Patient-specific rates of invasion and proliferation

As the field of "mathematical oncology" continues to develop, some investigators have looked towards patient-specific models, and methodologies of parameter estimation. The advantage of the PI model parameter space is that it is limited: two parameters can be computed from two measurements, and provide a finite parameter space which may be explored with relative ease. Models with many, even dozens of biological parameters are difficult to "tune" and even more so to patient-specific data in the context of glioblastoma and imaging-scale models. Generally speaking, prior work in the area of mathematical model parameter estimation can be grouped into the following categories, which are separate and distinct from the patient-specific model calibration presented here.

1. Patient-specific, but not predictive of treatment response, [57, 81].

2. Patient-specific, model of treatment response, but not validated with clinical data, or not predictive of response [59, 172].

3. Patient-specific and prognostic, but provides limited biological insight into the disease or mechanisms driving treatment response [139].

4. Patient-specific, but tissue based, limiting the applicability to carefully chosen tissue samples, and requires surgical intervention [88], and provides only a *static* snapshot of a dynamic process.

5. Patient-specific prognostic imaging based studies which do not quantify disease or response kinetics [80].

6. Not patient specific, but predictive of response [103, 160], which limits the ability to consider alternate treatment regimens for patients which are predicted to respond poorly to treatment.

7. Not patient-specific, purely theoretical investigations, perhaps without any real parameter estimation or predictive value [22, 24, 116, 114].

The patient-specific model provided by the PI and PIRT models yields validated, clinically meaningful metrics of aggressiveness and hypoxic burden [186], prognosis [201, 136], extent of infiltration [177], response to radiation therapy [151], response to anti-angiogenic therapy [87], extent of resection [180], and differentiation between true and pseudo progression following chemoradiation therapy [135]. The distinction between the patient-specific PI model (PS-PI) and any other study is clear.

4.2.1 Glioblastoma heterogeneity quantified with D/ρ

A cohort of 63 glioblastoma patients have been analyzed and their model parameters calculated[1]. Days between pre-treatment MRIs ranged from 2 to 266 days, with a median

[1]Research involving human subjects was approved by the University of Washington and University of California, Los Angeles institutional review boards. Written informed consent was obtained for the collec-

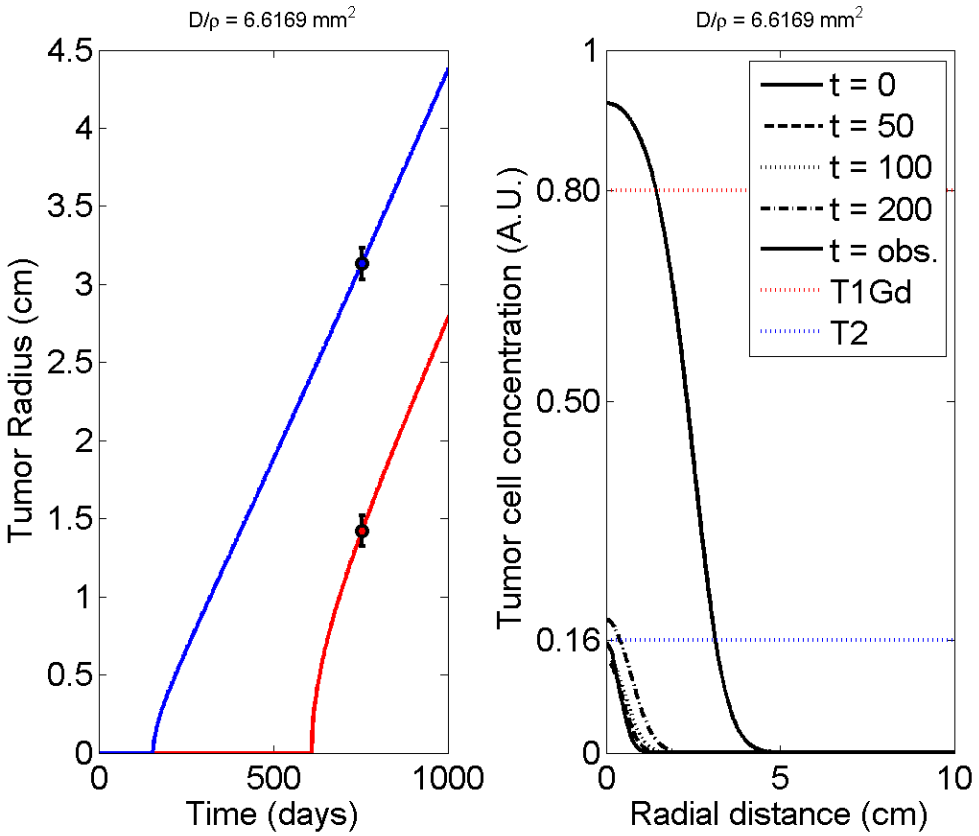

Figure 4.3: Model solutions with data for the maximum value of D/ρ observed in a 63 patient cohort of glioblastomas. Error bars correspond to $\pm$ 1 mm from the mean tumor radius from 2 independent volume measurements. Left: tumor radius versus time. Right: tumor cell density versus space plotted for several points in the tumor's evolution, including the time point at which the ratio D/ρ was calculated (Obs.).

of 11 days. The age at diagnosis ranged from 19 years old to 88 years, with a median of 55 years. The tumor sizes ranged from 5 mm in spherically-equivalent radius as measured volumetrically on T1Gd MRI, to 36 mm, with a median of 17 mm. A wide range of growth kinetics are observed, with model parameters, D, ρ, velocity and D/ρ, varying up to two orders of magnitude, Figure 4.5. This observation is possible only by measurement of individual growth rates by direct calculation of λ and velocity of radial expansion. The

---

tion of all patient data, and the investigation was conducted according to the principles of the Declaration of Helsinki.

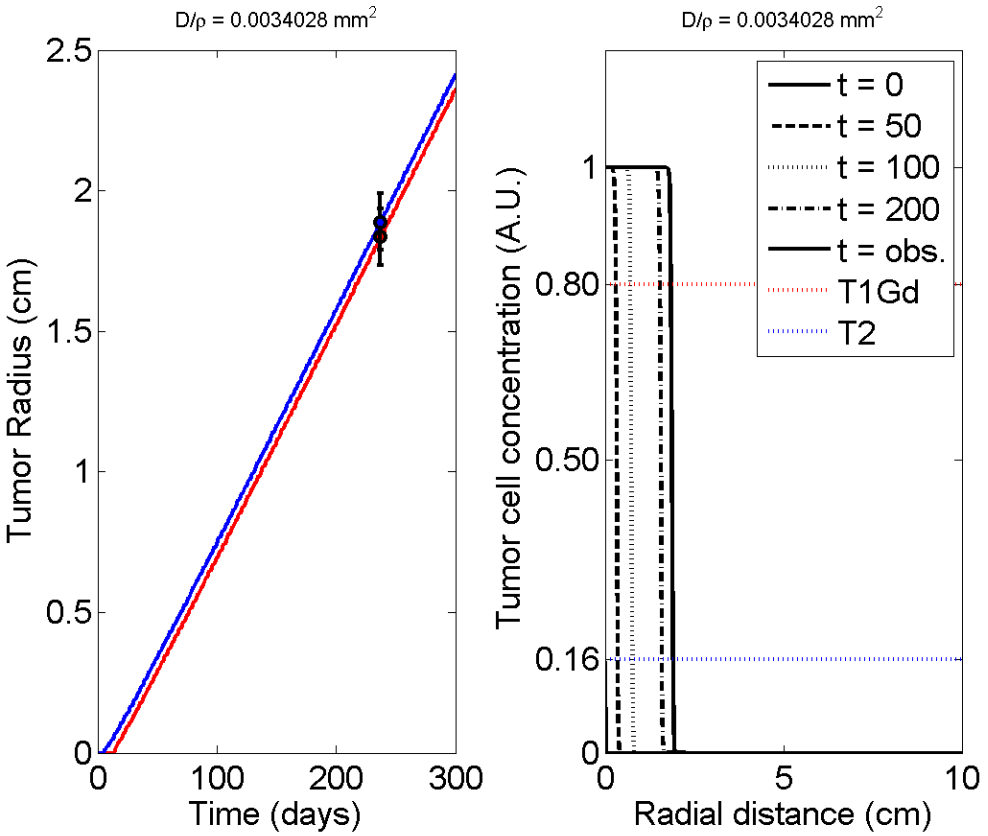

Figure 4.4: Model solutions with data for the minimum value of D/ρ observed in a 63 patient cohort of glioblastomas. Error bars correspond to $\pm$ 1 mm from the mean tumor radius from 2 independent volume measurements. Left: tumor radius versus time. Right: tumor cell density versus space plotted for several points in the tumor's evolution, including the time point at which the ratio D/ρ was calculated (Obs.).

parameter space spectrum of invasion and proliferation rates is shown in Figure 4.6 for N = 63 glioblastoma patients, color-coded for size at diagnosis.

It is evident in Figure 4.6 that the cases are almost equally distributed around a relative invasiveness, D/ρ, of 1 mm^2, but quite differently distributed by velocities, most being quite fast, greater than 20 mm/year, but about 10% tailing off to quite slow, down to 2 mm/year. About half of the patients have a radial growth velocity of greater than 40 mm/yr, 17% have a velocity between 20-40 mm/yr and 11% have a velocity less than 20 mm/yr. The color-coding for size (T1Gd radius at diagnosis) in Figure 4.6 suggests a rather

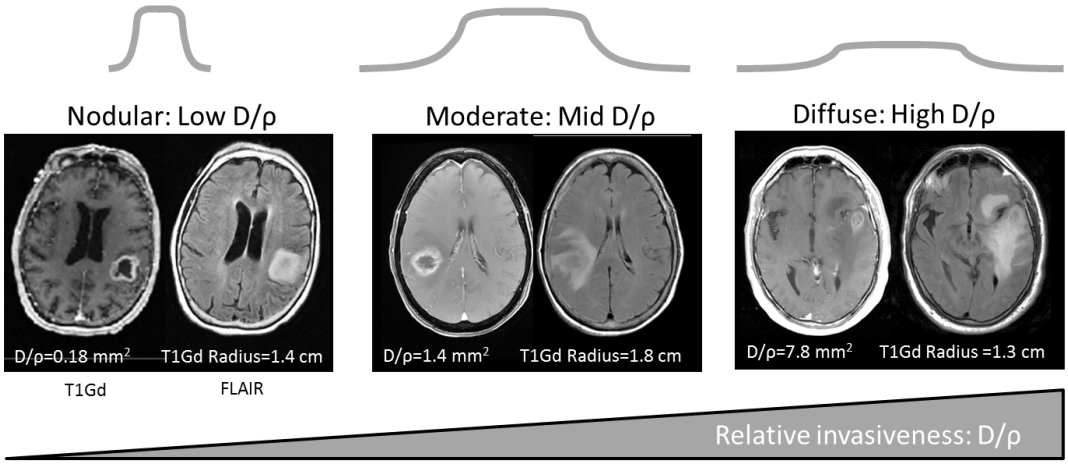

Figure 4.5: By calibrating the proliferation-invasion (PI) model to individual patient imaging characteristics, we are able to define patient-specific metrics of relative invasiveness, and quantify biological aggressiveness in addition to quantitatively defining the tumor phenotype via the ratio $\lambda = D/\rho$.

even distribution of sizes, with a few more of the largest (red and orange) being among the fastest growing. A recent study by Pallud et al. have shown volumetric velocity of growth to be correlated with duration of survival and may be used as a clinical prognostic factor in low grade gliomas, who are followed serially without intervening treatment for long periods of time in the absence of symptoms, allowing for an accurate measure of velocity [139].

The variation in overall invasive phenotype quantified by $\lambda = D/\rho$ provides a means to place tumors into relatively nodular or invasive categories, using the ratio as a dichotomous variable with the line of division at $D/\rho = 1$ mm^2. In this regard, we may connect the model-derived, data-driven characterization of tumor phenotype to the tumor evolution and response to therapy as follows.

Nodular These tumors have high proliferation relative to their migration potential, and tend to be more hypoxic [186], with a larger relative percent of bulk tumor mass composed of necrosis. These tumors deplete the nutrients of the local tissue and are generally more angiogenic, which produces focal regions of both chronic and acute hypoxia. These

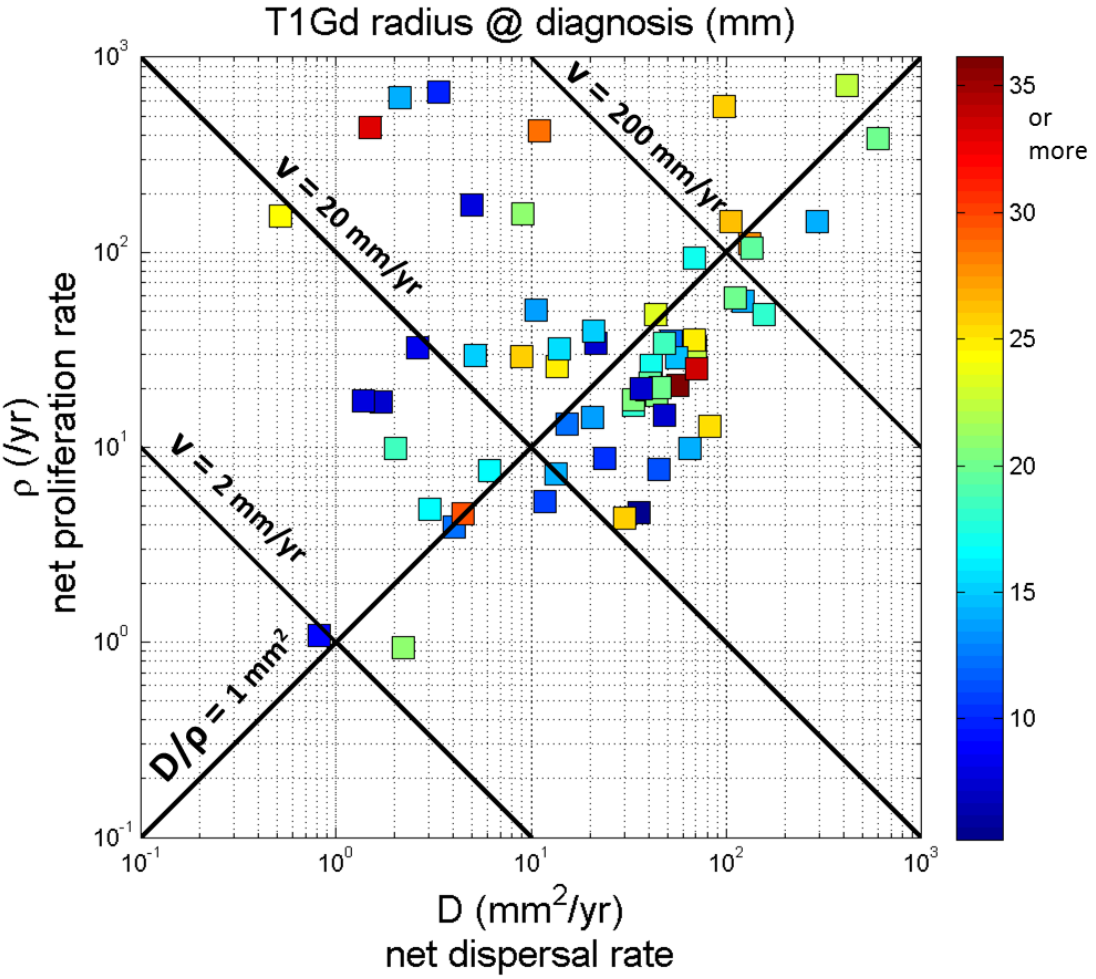

Figure 4.6: Log-log plot of invasion rate versus proliferation rate for N = 63 glioblastoma patients demonstrating a wide range of growth kinetics quantified by the patient-specific PI model and parameter estimation algorithm [184]. Model parameters are computed using radial velocity of growth computed on T1Gd MRI. Color indicates tumor size at diagnosis (mm). Lines of constant velocity ($2\sqrt{D\rho}$) and $\lambda = D/\rho$ are shown.

tumors have a steep tumor cell density profile and would be considered favorable candidates for extensive surgical resection of the contrast-enhancing bulk tumor mass. Furthermore, because of the relatively steep tumor cell density profile and relatively decreased diffusive invasion of the normal appearing brain, these patients may benefit from reduced radiation therapy margins in order to preserve more normal tissue which may have insufficient tumor cell density to warrant the cognitive side effects from increased dose to the tumor periphery. In the context of a "go or grow" perspective on cellular behavior, these tumors would be more inclined to grow rather than go, and likely have increased interstitial pressure and degradation of the normal tissue architecture due to the increased bulk tumor mass, tumor-induced angiogenesis and central necrosis [84].

Diffuse In contrast, the invasive phenotype is one which relies heavily on co-option of the native brain vasculature and has a relatively shallow tumor cell density profile. This phenotype includes increased sub-clinical disease due to relatively high migration relative to proliferation, and may take longer periods of time to undergo malignant transformation from an initial lesion to a contrast-enhancing glioblastoma [185]. This phenotype also includes highly invasive low grade gliomas (LGG) which rely on vascular co-option of the brain than neoangiogensis of their high grade GBM counterparts, to the extent that some LGGs do not contrast-enhance on T1Gd MRI and present only as edema or T2/FLAIR regions of hyper-intensity. These tumors are strongly associated with secondary glioblastomas for this reason: the process of malignant progression from a low to high grade cancer is associated with increased glycolosis due to plentiful oxygen.

These tumors are poor candidates for surgical excision due to the increased proportion of sub-clinical disease. For the same reason, these tumors would require extensive radiation therapy margins to capture the diffuse component of the disease, which would deliver increased dose to normal tissues, producing increased cognitive and other radiation-induced side effects. Due to the increased co-option of normal blood vessels, these tumors may respond well to chemotherapy agents which cross the blood-brain barrier, providing additional drug penetration into the tumor mass as well as the invasive cells at the tumor periphery at the leading edge [196].

Although these pheontypes may appear obvious from the perspective of clinical imag-

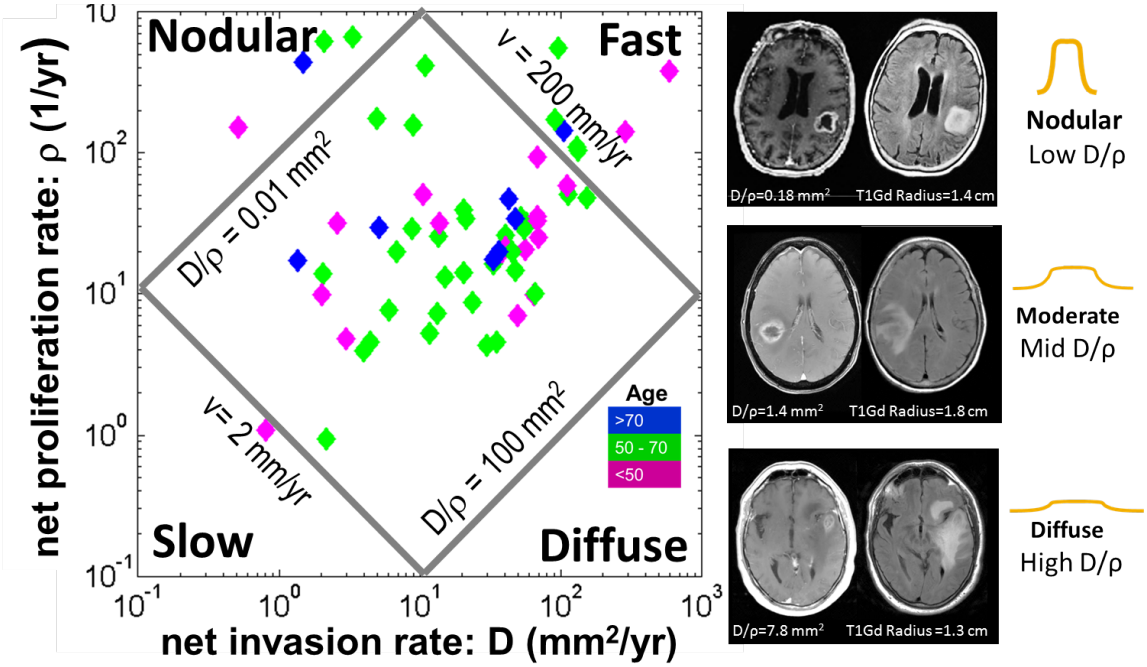

Figure 4.7: Log-log plot of net invasion rate versus net proliferation rate for N = 63 glioblastoma patients, defining regions of PI model parameter space that quantifies tumor phenotype and growth kinetics into slow, fast, diffuse and nodular classes. Patient-specific estimates of net invasion and net proliferation rates enables this quantitative characterization of an individual patient's disease.

ing, likening the ratio D/ρ to some algebraic relationship between the T1Gd and T2 MRI sequences, without the quantitative metric provided by the model parameters, these qualitative and subjective classifications would provide no clear distinction between subgroups, and would perhaps miscategorize patients in the middle which are neither overtly nodular or diffuse. In fact, such a qualitative judgment may correctly identify patients at these extremes, however, without a quantitative understanding of how this tumor cell density profile evolves in time and influences response to therapy, these surrogates would ultimately break down.

4.2.2 Accuracy

In order to quantify the quality of fit provided by the look up table we calculate the observed invasiveness ratio $(D/\rho)_o$ for the cohort of 63 glioblastoma patients and use this ratio to run the model simulation forward in time to recapitulate the observed T1Gd and T2 spherically-equivalent tumor radii. The T1Gd SER is used as a reference point to determine when the model simulation has reached the tumor size. The error in model prediction then lies in the difference between the T2/FLAIR isodensity SER and the T2 data point for each value of $(D/\rho)_o$. Shown in Figure 4.8 is the ratio $(D/\rho)_o$ versus T2 SER, colored for absolute error between model predicted T2 size and the actual tumor T2 size. Data points are colored black if they are below the resolution of MRI and the inter-observer variation in tumor volume delineation, both approximately 1 mm in SER [200]. Therefore colored data points are the only data pairs which have measurable differences between the model-predicted and actual tumor data. Figure 4.8A reveals 98% of T1Gd SER data is below measurable error, and 83% of T2 data points fall below this threshold, these points correspond to the black dots in Figure 4.8B.

Sensitivity Using inter-observer uncertainty of $\pm$ 1 mm, with a 95% confidence interval, we assume gross tumor volume (GTV) to be indicative of the fundamental level of uncertainty in our model and propagate the error in our calculations of the ratio D/ρ and velocity to obtain 95% confidence intervals for each parameter. Since α is determined by regression fitting the model to the data, we suppose a $\pm$ 10% variation as the confidence interval.

We then performed Latin hypercube sampling (LHS) [89] uncertainty analysis. Specifically, applying LHS to the parameter ranges resulting from the tumor radius uncertainty to our model parameter estimation. Unlike standard sensitivity analysis for which only one parameter is typically varied, in LHS all parameters (D, ρ, α) are allowed to vary at the same time. Assuming the parameter values are normally distributed, the mean and standard deviation of 100 LHS simulations are compared with the patients post radiation therapy tumor size, revealing robust predictions of $\pm$ 2–3 mm, only slightly more than inter-observer uncertainty in tumor size. Further, the LHS technique generates a sensitivity measure for each parameter varied, in the form of a partial rank correlation. Applying this to the LHS simulations results reveal that the imageable tumor radius post-radiotherapy is most sensitive to variations in the ratio D/ρ and the radiotherapy response parameter α. We note that the ratio D/ρ provided by the look up table need not remain constant throughout the untreated growth. This is due to the initial nonlinear portion of the radius versus time curve in which the relative differences between the low and high tumor cell density profiles is exaggerated.

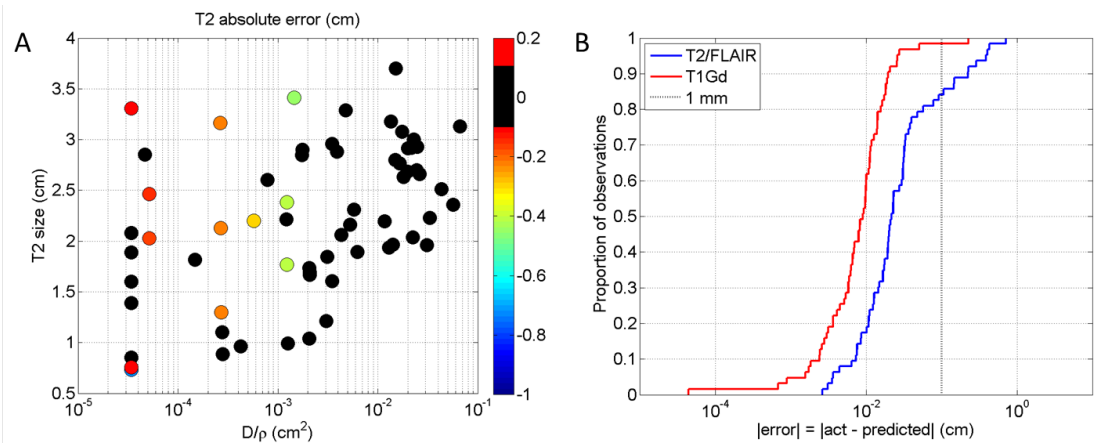

Figure 4.8: A) Invasion profile defined by the ratio (D/ρ) (cm^2) versus T2 spherically-equivalent radius size (cm) colored for absolute error between observed tumor size and model-predicted T2 tumor size. Black data points indicate the error is less than inter-observer tumor volume error, which has been estimated at $\pm$ 1 mm = 0.1 cm. B) Empirical cumulative distribution of errors between model-predicted tumor size on T2/FLAIR and the actual SER observed. Dashed line indicates the resolution of MRI and estimated inter-observer uncertainty in tumor volume delineation.

4.2.3 Differential motility

As stated in the PI model given in Equation 4.1, glioma cells migrate preferentially along axons and blood vessels, giving anisotropy and preferential migration direction [97]. The differential rates of invasion in white and grey matter of the brain D_w and D_g respectively, can be back-calculated once the isotropic, homogeneous parameters D and ρ are known, through percolation and homogenization theory [105], as well as level-set methods. These techniques are not presented here.

4.2.4 Untreated virtual control

The concept of the untreated virtual control (UVC) is central to the utility of a patient-specific model of any process, but particularly so in cancer. The UVC is a tool created by the mathematical model which can assess the impact of therapy, compare alternate treatment strategies, and ultimately lead to model-based patient-specific predictions. The UVC is not as meaningful without patient-specific tuning of the model, especially when a wide range of process dynamics and rate constants exist in the problem of interest. The UVC provides prognostic metrics of treatment through a relative quantification of tumor growth and deflection of untreated growth due to therapy, by way of a metric coined "days gained," [135, 136]. The UVC further enables quantification of differential response to treatment relative to other treatment paradigms, and provides a baseline, reference growth prediction against which any therapy may be compared.

Fatal tumor burden A model-predicted survial can be computed from the patient-specific rates of invasion and proliferation with the concept of a fatal tumor burden (FTB) or fatal tumor size. Acknowledging that death from glioblastoma is multi-factorial, involving mass effect from the expanding tumor in a closed space, to treatment related illness, stroke, cognitive decline and other factors [164], a FTB is a reasonable assumption, in light of the short prognosis and rapid growth rates observed in human glioblastomas. A first estimate of a FTB of 35 mm in tumor radius is used in Swanson et al. [183], based upon autopsy findings from patients in the early 1960's [46].

Age at diag.	Extent of resection	T1Gd MRI Volume (cc)	T2 MRI Volume (cc)	Hypoxic Volume (cc)
73	BX	18.8	44.0	2.4

Table 4.1: Clinical characteristics for the study patient.

4.3 Glioblastoma patient case study

Now that we have a patient-specific proliferation-invasion and radiotherapy (PIRT) model by way of calculation of model parameters D, ρ and α, we apply our patient-specific modeling techniques to a single patient in detail to study the environmental effects of treatment resistance in the form of focal hypoxia defined by 18F-fluoromisonidazole (FMISO) PET [13, 148, 169] and quantify response to radiation therapy in three dimensions using an anatomically accurate simulation domain.

4.3.1 Natural history and diagnosis

The subject of this study approved by the University of Washington IRB is a 73 year-old man who provided informed consent to participate in an observational study. The patient had no abnormalities on an initial MRI at 386 days prior to the onset of memory difficulties. A repeat MRI obtained at the time of presentation demonstrated a left temporal lobe lesion surrounded by significant edema. A needle biopsy of the left temporal lobe lesion was performed and multiple tissue sections microscopically revealed hemorrhage and eosinophilic necrosis. Thickened walls were seen within areas of necrosis with no viable endothelium. A review of frozen section material revealed larger areas of glial neoplasm as well as areas of necrosis with associated pseudopalisading of neoplastic nuclei. On the basis of these pathological findings, the biopsy was most consistent with WHO grade IV GBM.

4.3.2 Imaging data

Routine clinical MRI modalities used to follow GBMs include T1-weighted gadolinium enhanced (T1Gd) and T2-weighted MRI. The patients diagnostic and pre-operative MRIs were performed 13 days apart, which allowed for the calculation of a volumetric velocity of growth. Prior to the initiation of radiation therapy (RT), the patient also underwent an FMISO PET study on an IRB-approved research protocol.

The patient underwent an MRI study three days following the completion of RT and another MRI two months later. Following RT, the patient continued temozolomide chemotherapy for a total of 14 months and was followed with serial MRI every two months. The MRI and PET images were spatially co-aligned to a common coordinate system using a rigid body transformation to the brainweb phantom using the PFUS package within the PMOD software [190] and statistical parametric mapping, available through the MATLAB software suite [10]. The brainweb phantom provides a spatial probability tissue classification, partitioning the brain into gray and white matter in addition to cerebrospinal fluid (CSF), shown in Figure 4.9 [45], on a 1 mm^3 Cartesian grid. Tumor volumes were measured using a semi-automated threshold-based pixel intensity background subtraction software, developed in MATLAB , with accuracy and reproducibility comparable to manual tumor delineation [100]. Specifically, tumor volume V (cm^3) is calculated using the formula

$$V = \sum_{i=1}^{N} A_i dz_i \tag{4.27}$$

where the image series is composed of N two-dimensional slices, typically acquired in the axial plane, and slice i has thickness dz_i, and tumor area A_i.

MRI Protocol The MRIs were acquired using a 1.5 Tesla GE system. The pre-operative Stealth navigation studies included axial T1 with contrast (3D gradient echo, TE/TR minimal, 1.3 mm slice thickness with no skip), axial T2 FSE (TE 97.3, TR 4000, 1.7 mm slice thickness with no skip). Follow-up scans including standard gadolinium-enhanced T1-weighted (TE minimal, TR 350), T2-weighted (TE 102, TR 4300) were obtained in 2D mode with a spin echo sequence and slice thickness of 5 mm with no inter-slice spacing.

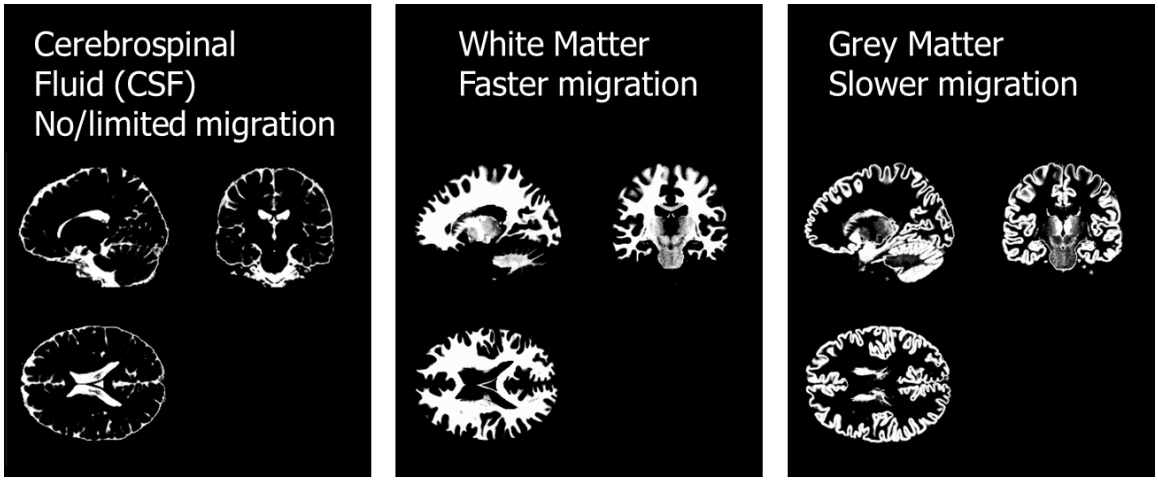

Figure 4.9: Brainweb phantom and atlas provides a voxel-wise defined probability map used as a tissue classifier in 3D model simulations. Each voxel is composed of grey matter, white matter and/or cerebrospinal fluid (CSF) in relative proportions such that the sum of all tissues in each voxel is unity. The phantom is defined on a cubic 1 mm $\times$ 1 mm $\times$ 1 mm $\times$ $= 1$ mm^3 Cartesian grid.

Quantifying hypoxia *in vivo* The co-registered FMISO-PET images were scaled to the average venous blood concentration of FMISO activity to produce tumor/blood (T/B) ratios. A T/B ratio greater than or equal to 1.2 (T/B $\geq$ 1.2) was associated with regions of hypoxia, and used to calculate the total hypoxic volume (HV) [169]. PET imaging is inherently noisy and there can be signal of FMISO uptake scattered in isolated voxels throughout the brain; defining HV as T/B $\geq$1.2 and restricting the FMISO signal to the T2-weighted MRI abnormality region largely excludes this noise and isolates the FMISO signal to the tumor area [169, 183]. The preponderance of the HV lies within the T1Gd region of hyperintensity, as well as between the T1Gd enhancing rim and the infiltrative edge of the tumor defined by the T2/FLAIR region of hyperintensity. A histogram of FMISO image pixel intensity distributions is shown in Figure 4.11.

FMISO PET imaging protocol 18F-Fluoromisonidazole (FMISO) was prepared following Lim and Berridge [121]. The PET scans were performed on an Advance Tomograph (G.E. Medical Systems) operating in a three-dimensional, high-resolution mode with

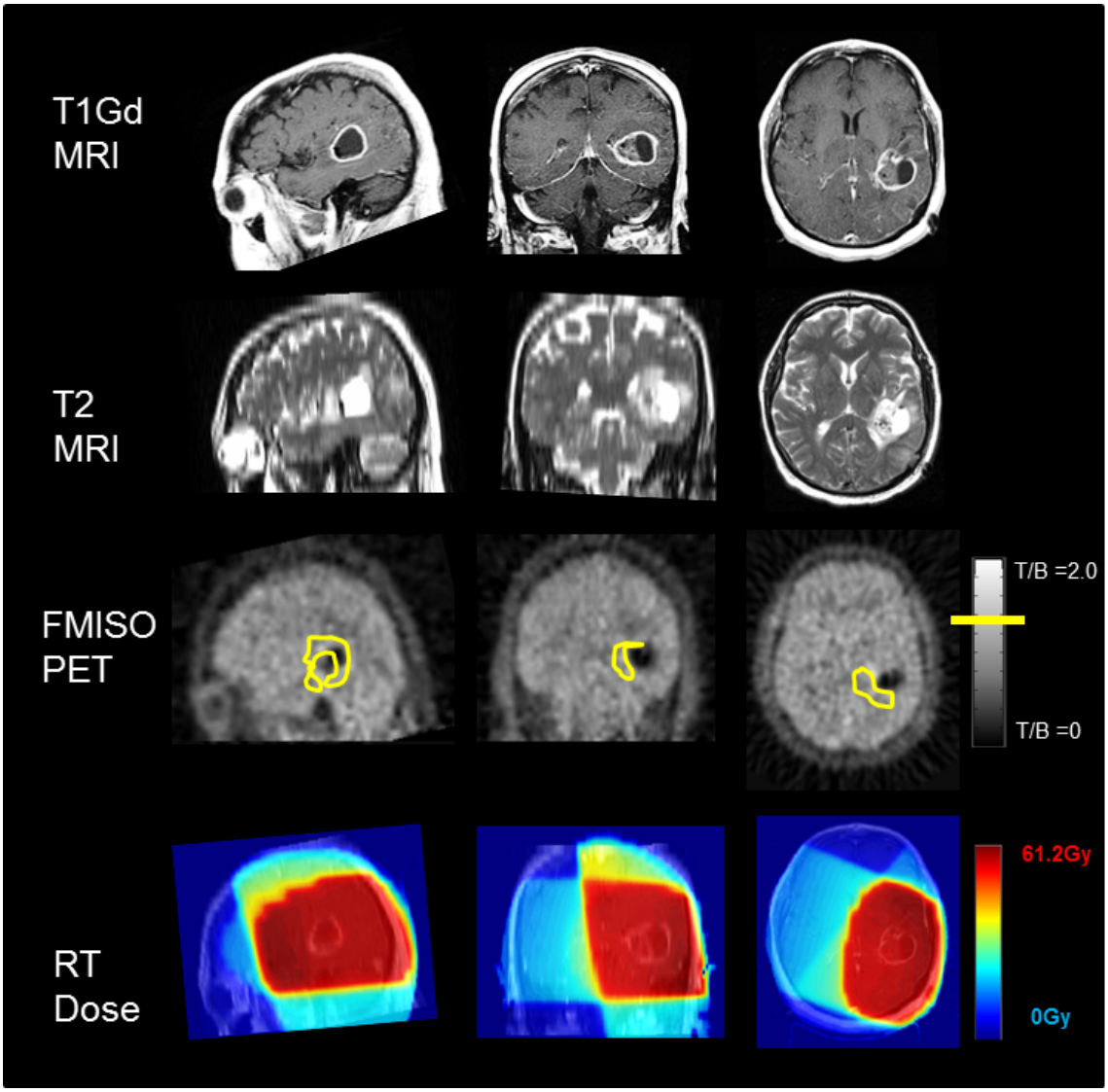

Figure 4.10: Orthogonal views of the patient's diagnostic T1Gd and T2 MRI, FMISO-PET and the composite radiation therapy dose based on MRI-defined margins.

35 imaging planes covering a 15 cm axial field of view. Venous access lines were placed in each arm, one for FMISO injection and the other for blood sampling. Injections of 3.7 MBq/kg (0.1 mCi/kg) of FMISO were then administered, for a maximum of 260 MBq or 7 mCi. A single field-of-view emission scan from 120 to 140 minutes post-injection and an attenuation scan of the brain with tumor were obtained. During emission tomography, four venous blood samples were obtained at intervals of 5 minutes. Whole blood samples of 1 mL each were counted in a Cobra multichannel gamma well counter. Blood activity of 4 samples was averaged and then expressed as MBq/mL decay corrected to time of injection.

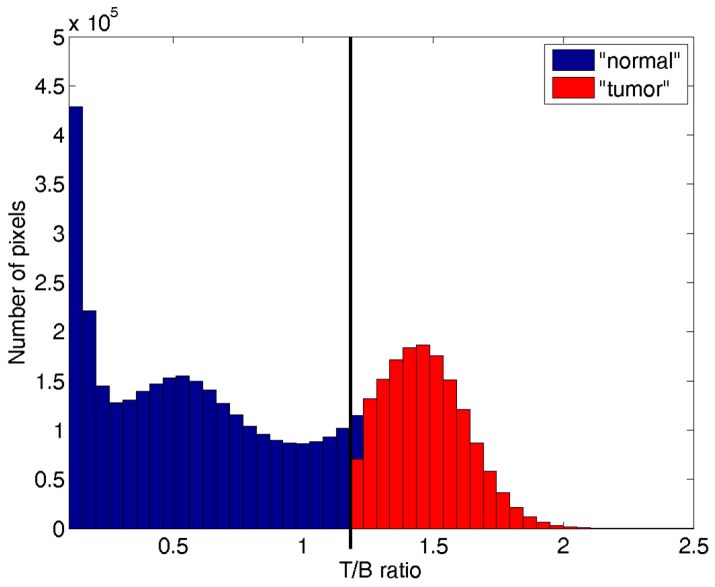

Figure 4.11: Histogram of FMISO pixel intensity distribution. Red bars correspond to pixels greater than or equal to a T/B ratio of 1.2, which is the common threshold to define abnormal FMISO tracer update within the tumor. The blue bars represent normal background uptake of the tracer. Zero and negative pixel values are artifacts of the image reconstruction technique and are note shown.

Clinical radiation therapy protocol Following diagnosis, the patient was treated with radiation therapy delivered with a 3D conformal treatment plan using 6 MV photons. The target volumes were defined as the T2-defined abnormality with a 2.5 cm margin, which had a planned target dose of 54 Gy delivered in 30 daily fractions of 1.8 Gy per fraction (Figure

4.12). An additional dose was delivered to a smaller volume defined by the gadolinium-enhancing region plus a 2 cm margin of 7.2 Gy delivered in an additional 4 daily fractions of 1.8 Gy per fraction for a total of 61.2 Gy to this region. Radiation was delivered with concurrent temozolomide following EORTC/NCIC 26981-22981/CE.3 (75 mg/m^2 given daily 7 days a week during course of RT).

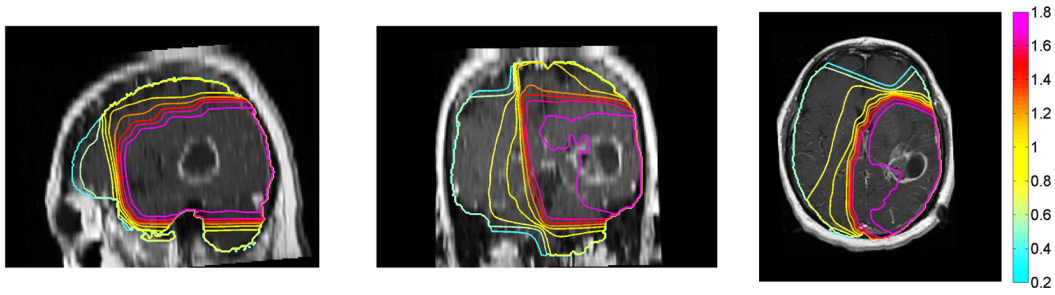

Figure 4.12: A single daily fraction of the prescribed 3D conformal 6 MV photon radiation therapy treatment plan superimposed on the pre-treatment T1Gd MRI for the study patient: from left to right, sagittal, coronal, and axial planes. The daily fraction is dosed to 1.8 Gy.

4.4 Patient-specific mathematical model of radiation response and resistance

The proliferation-invasion radiation therapy (PIRT) is a reaction-diffusion partial differential equation that characterizes the density of glioma cancer cells ($c(x,t)$) in terms of two net rates: proliferation (ρ 1/yr) and invasion ($D(x)$ mm^2/yr) and incorporates the delivery and biological effects of radiation therapy (PIRT model). The net invasion of tumor cells is a function of the spatial variable x so that glioma cells migrate ten times faster in the white matter than in the more dense grey matter, $Dw = 10Dg$ see Equation 4.31. This differential motility characterizes the diffuse invasion of the glioma cells within the brain ($\mathcal{B}$) and has been shown to play a critical role in the morphologic evolution of these tumors [122, 178]. The model describes tumor cell density $c = c(x,t)$ at time t and location x in units cells/mm^3 in terms of logistic growth which uses K is the tumor cell carrying capacity

of the tissue.

$$\overbrace{\frac{\partial c}{\partial t}}^{\substack{\text{rate of change}\\ \text{of glioma cell}\\ \text{concentration}}} = \overbrace{\nabla \cdot (D(\mathbf{x})\nabla c)}^{\substack{\text{net dispersal}\\ \text{of glioma cells}}} + \overbrace{\rho c\left(1-\frac{c}{K}\right)}^{\substack{\text{net proliferation}\\ \text{of glioma cells}}} \overbrace{-R(\alpha, Dose(\mathbf{x},t)c\left(1-\frac{c}{K}\right)}^{\substack{\text{loss due to}\\ \text{radiation therapy}}} \tag{4.28}$$

$$\mathbf{x} \in \mathcal{B}, \quad t \geq 0 \tag{4.29}$$

$$\mathbf{n} \cdot \nabla c = 0 \text{ on } \partial\mathcal{B}, \quad c((x_0, y_0, z_0), t = 0) = c_0, \tag{4.30}$$

with $\mathbf{x} = (x, y, z)$ and initial condition located at the center of mass of the T1Gd defined tumor volume.

$$D(\mathbf{x}) = \begin{cases} D_w & \text{for } \mathbf{x} \in \text{ white matter} \\ D_g & \text{for } \mathbf{x} \in \text{ grey matter} \\ 0 & \text{for } \mathbf{x} \in \text{ CSF or outside the brain.} \end{cases} \tag{4.31}$$

The proliferation-invasion (PI) model To connect histopathological cellular density to that estimated from imaging, we assume T1-weighted gadolinium (T1Gd) and T2-weighted MRIs correspond to densities of 80% and 16% of the tissues total tumor cell carrying capacity, respectively. One corollary of this estimate is the modeling of a diffuse gradient of tumor cells invisible to imaging. The relative proportion of occult disease is characterized by an invisibility index, the ratio of the model parameters D/ρ [83] which has been inversely related to relative hypoxia within the tumor [186]. The model (Equation 4.28) estimates a nearly linear radial growth of the abnormality seen on imaging, which approaches a constant velocity defined by Fishers approximation $v = 2\sqrt{D\rho}$ [62, 132]. A constant velocity of MRI imageable growth has been demonstrated for 27 untreated low grade gliomas computed from serial MRI observations. The invisibility index and velocity of growth are computed from gross tumor volumes (GTV) and combined to calculate patient-specific net rates of diffusion (D) and proliferation (ρ).

Velocity (mm/yr)	Net invasion rate D (mm^2/yr)	Net proliferation rate ρ (/yr)	Relative invasiveness D/ρ (mm^2)	Radio-sensitivity α (/Gy)	Days Gained (days)
27.7	13.93	13.82	1.01	0.055	92.4

Table 4.2: Mathematical model characteristics for the study patient.

4.4.1 Model of hypoxia-modulated radiation-resistance

The last term in Equation 4.28 represents the loss of tumor cells (cell kill) due to radiation therapy and is defined in space and time by the clinically prescribed dose given in Equations 4.32 and 4.33. For low cell densities, the effect of RT is simply the fraction of tumor cells killed as a result of RT. However, at large cell densities close to the carrying capacity K, it is assumed that the effect saturates in the same manner as the net proliferation of tumor cells saturates. This assumption is consistent with the common understanding that cells actively undergoing mitosis are more susceptible to DNA damage [79, 102, 155]. This same assumption is embedded in the linear-quadratic model of radiation as the biological mechanism of radiation induced cell kill [155],

$$R(S, c(x,t)) = [1 - S(Dose(x,t), \alpha, \beta)]\, c \left(1 - \frac{c}{K}\right) \tag{4.32}$$

$$S(Dose(x,t), \alpha, \alpha/\beta) = \exp\left(-\alpha\left(Dose + \frac{Dose^2}{\alpha/\beta}\right)\right). \tag{4.33}$$

Equation 4.33 is the survival probability after each fraction from the linear-quadratic dose-response model for biological radiation effect in units Gy. The interpretation of the coefficients α Gy^{-1} and β Gy^{-2} as damage related to one-track ionizing radiation damage and two-track action induced damage to the cells DNA respectively [155, 75] is not essential to its compatibility with the assumptions of the PIRT tumor growth model. The linear-quadratic model is the most widely used dose-response model of radiation therapy in clinical applications, making it the most appropriate model to account for radiation induced cell kill in our analysis. We do not include the first-order repair kinetics described by the Lea-Catcheside

dose-protraction function, since these effects are negligible at 3D conformal daily fraction doses of less than 2 Gy.

For each point in space and time, an effective dose and probability of cell survival can be calculated that corresponds uniquely to the individual patients treatment plan and the linear-quadratic dose-response model parameter α. Increasing α decreases the probability of cell survival, S, and therefore increases the probability of radiation therapy-induced cell death. The dose distribution is determined by the individual patients GTV data and clinical radiation therapy dose plan. The parameter α can be fitted to either the T1GD or T2 post chemo-radiation MRI using a bootstrap optimization technique, yielding a one-to-one relationship between α and model prediction error, as described in Rockne 2010 [151].

The ratio of the parameters α/β in the linear-quadratic model provides information about the tissue response to radiation exposure: if α/β is large that tissue is more radiosensitive than when the ratio is small. The ratio is modulated by the presence of hypoxia. Following Titz [194], we utilize the oxygen enhancement ratio (OER) scaling, which determines relative resistance to radiation therapy in regions of low oxygen. In our treatment simulations, the ratio α/β is held constant at 10 /Gy within the tumor volume with OER = 3 within regions of hypoxia [166, 102] as determined by the patients FMISO-PET scan and OER = 1 otherwise. The implementation of the OER to the linear-quadratic model is given as

$$S(Dose(x,t),\alpha(x),\alpha/\beta(x)) = \exp\left(-\alpha(x)\left(Dose + \frac{Dose^2}{\alpha/\beta(x)}\right)\right) \tag{4.34}$$

where the radiobiological parameters α and α/β are spatially defined so that

$$\alpha(x) = \begin{cases} \dfrac{\alpha}{OER} & \text{if } x \in \text{ hypoxic region} \\ \alpha & \text{if } x \notin \text{ hypoxic region} \end{cases} \tag{4.35}$$

$$\frac{\alpha}{\beta}(x) = \begin{cases} \dfrac{\alpha}{\beta}OER & \text{if } x \in \text{ hypoxic region} \\ \dfrac{\alpha}{\beta} & \text{if } x \notin \text{ hypoxic region.} \end{cases} \tag{4.36}$$

We assume the delivery and effect of radiation therapy to be an instantaneous, deterministic event using the linear-quadratic equation and its corresponding probability of cell

survival/death. Concurrent chemotherapy is included in the net effect of radiation therapy, and is not modeled explicitly. Damage to and response of normal tissue is not modeled.

4.4.2 Radiation therapy treatment simulations

Several distinct scenarios are simulated to investigate the role of hypoxia in radiographic changes to the tumor in response to radiation therapy.

1. Clinical radiation dose delivered with spatially uniform treatment response. This corresponds to a value for the oxygen enhancement ratio equal to one (OER = 1) at all locations in the brain, and assumes that all tumor cells are equally susceptible to radiation therapy damage.

2. Clinical radiation dose with localized radio-resistance due to hypoxia via a binary relationship. This quantifies focal radio-resistance defined by the patients FMISO-PET scan, where the tissue to blood ratio is greater than or equal to 1.2 [169], where the OER is set to 3, as

$$\mathrm{OER}(x) = \begin{cases} 1 & \text{if} \quad T/B(x) < 1.2 \\ 3 & \text{if} \quad T/B(x) \geq 1.2. \end{cases} \tag{4.37}$$

3. Acknowledging that the distinction between pixel intensity and hypoxic density is not clear, we consider a linear scaling of hypoxic resistance with T/B pixel intensity such that FMISO pixels with low T/B are relatively less hypoxic than pixels with higher T/B ratio and are therefore more hypoxic and therefore in aggregate, relatively less and more resistant to ionizing DNA damage, respectively. The maximum T/B pixel value in the FMISO image is given by $\max_{T/B}$ and the corresponding formula to determine the voxel-wise defined oxygen enhancement ratio for the treatment simulation is given by

$$\mathrm{OER}(x) = \begin{cases} 1 & \text{if} \quad T/B(x) < 1.2 \\ \dfrac{2}{\max_{T/B} - 1.2}(T/B(x) - 1.2) & \text{if} \quad 1.2 \leq T/B(x) \leq \max_{T/B}. \end{cases} \tag{4.38}$$

4. Due to the somewhat small volume of hypoxia relative to the bulk tumor mass defined by T1Gd, we consider omitting the FMISO altogether, and simply use the T1Gd abnormality as a surrogate for hypoxia. The T1Gd abnormality corresponds to leaky vasculature due to tumor-induced neoangiogensis, which is where a preponderance of FMISO tracer uptake is often found. The T1Gd abnormality is heterogeneous and includes regions of focal necrosis, which would have no viable tumor cells and therefore no hypoxic tumor cells, well perfused, normoxic tumor cells near the newly formed blood vessels, as well as regions of hypoxia. Performing this simulation directly addresses the choice of the logistic loss term for the radiation effect, by illustrating increased resistance in the hyperdense core of the tumor through mechanisms of interstitial pressure, hypoxia, and relative dose per cell. Formally, this approach is determined by

$$\mathrm{OER}(x) = \begin{cases} 1 & \text{if} \quad c(x,t) < 0.8K \\ 3 & \text{if} \quad c(x,t) \geq 0.80K. \end{cases} \tag{4.39}$$

5. Untreated virtual control (UVC) which includes no radiation therapy delivery or response. The UVC simulation is used to quantify model-based response metrics as well as a benchmark between other simulation scenarios.

The OER scalings are illustrated in Figure 4.13.

Each simulation was run using an anatomically accurate 3D brain phantom [45] and the patients 3-dimensional conformal radiation dose prescription extracted from the treatment planning system (Philips Pinnacle). Additionally, we incorporated the effects of regional hypoxia as a response resistance mechanism using the OER modification to the linear-quadratic dose-response relationship. The radiation response parameter α was fitted to the first T2 MRI following chemo-radiation creating heterogeneity of radiation-response and resistance in regions of high cell density. We use the T2 scan for this fit due to the localization of FMISO-PET activity in the T1Gd enhancing region. Moreover, the patient-specific, three-dimensional PIRT model as well as the spherically symmetric counterpart, significantly under-predict the T1Gd tumor size following RT when fitted to the T2 data without an OER effect incorporated.

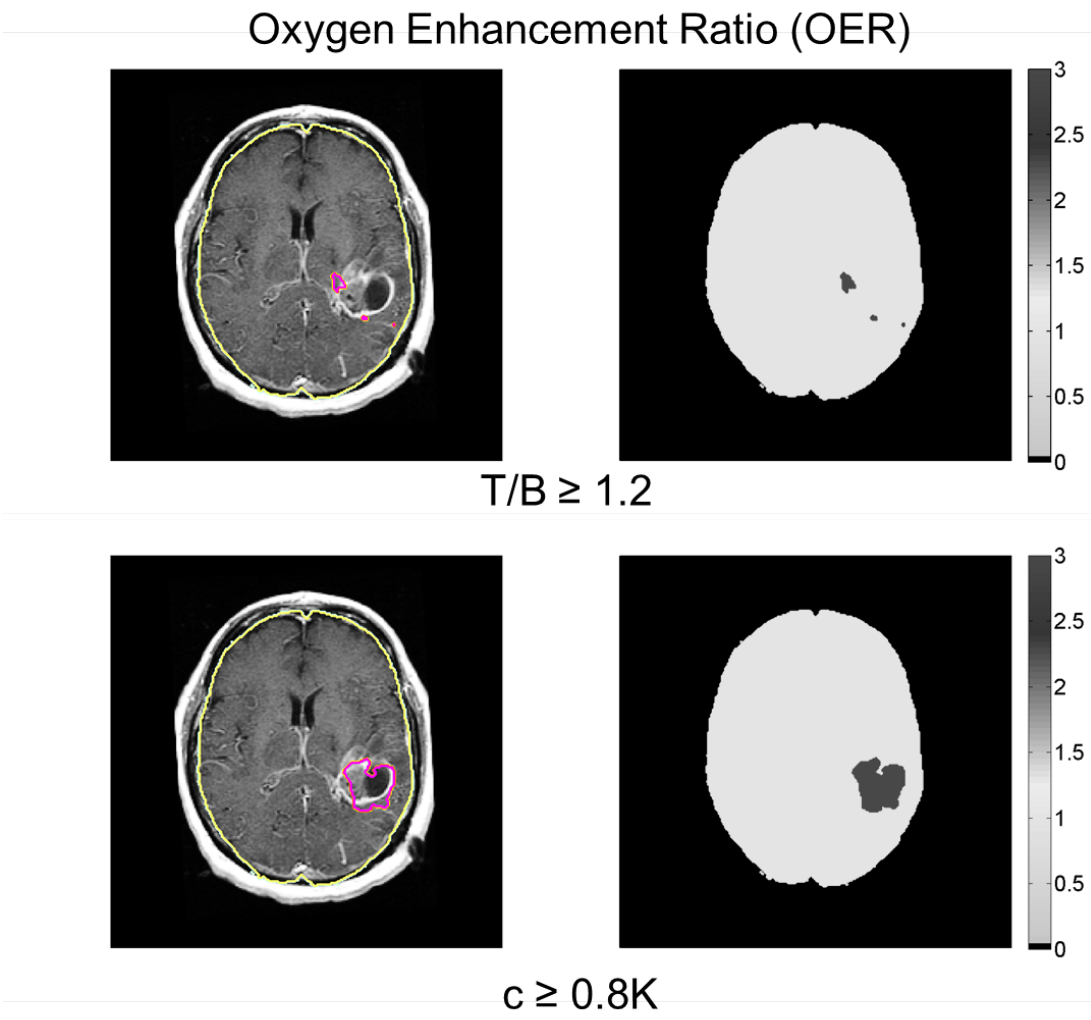

Figure 4.13: Scalings of oxygen enhancement ratio for *in vivo* hypoxic resistance to ionizing radiation induced DNA damage based on FMISO-PET tissue/blood (T/B) pixel intensity. Top: binary on/off function which counts any pixel above the T/B = 1.2 threshold as hypoxic with uniform OER =3. Bottom: cell density threshold scaling of OER such that pixels in the model-predicted T1Gd region of hyper-dense tumor cell density is assigned OER = 3.

The patient's stereotactic needle biopsy was not modeled, as the volume of tissue removed was at the core of the tumor and not a significant portion of the overall tumor mass. The inflammatory response of the tumor and normal appearing surrounding brain may impact MRI abnormalities, particularly on the T2/FLAIR modality. We assume any such effects arising from the biopsy did not impact response to radiation therapy, presentation of disease on follow-up imaging or impact tumor progression.

Patient-specific model parameters As shown in Table 4.1, model parameters D, ρ and α are calculated based on baseline tumor growth kinetics based on pre-treatment MRI. Specifically, within the spectrum of dynamics observed in glioblastoma [135], the patient's net rates of invasion and proliferation which characterize the tumor growth lie within one standard deviation of the population mean observed in 62 patients [135]. Similarly for the patient-specific radio-sensitivity parameter α, the calculated value of $\alpha = 0.055$ (/Gy) reflects neither an exceptionally resistant or sensitive response.

Spatial metrics of model accuracy In order to assess the accuracy of model predictions, we compare the simulated tumor regions to the observed GTV on T1-weighted gadolinium enhanced (T1Gd) and T2-weighted MRI using a suite of metrics summarized in Table 4.4. All of the metrics listed use voxel by voxel comparisons, giving a 3-dimensional quantification of model accuracy. All spatial metrics return a single value indicating the quality of agreement between model and observed tumor growth except for the level-set distance, which returns a distribution of distances between the simulated and actual tumor surfaces. A value of zero in this distribution indicates an exact agreement between simulated and actual tumor surfaces; therefore, we report the mean, median and standard deviation of this distribution - the closer to zero, the better the model prediction (Figure 4.15).

In order to perform our voxel-wise spatial metrics, we segmented the tumor abnormality, creating a boolean mask of the same dimension as the MRI, in which tumor-positive pixels are set to one, and others are set to zero.

Numerical methods

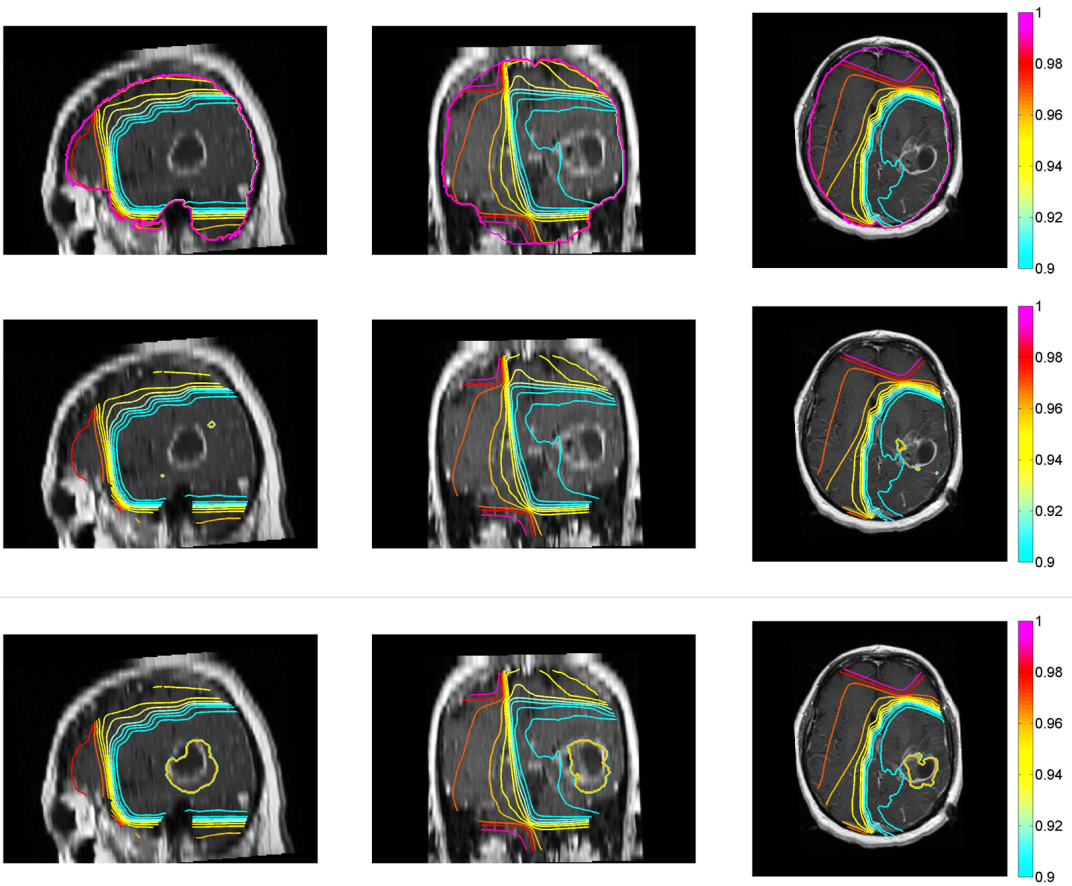

Figure 4.14: Linear-quadratic predicted surviving fraction after one fraction of 1.8 Gy, shown in Figure 4.12. Top row: uniform radio-sensitivity in space. This corresponds to the case with no hypoxia-mediated radiation-resistance and a uniform oxygen enhancement ratio, OER = 1. Middle row: FMISO-defined hypoxia with T/B $\geq$ 1.2 corresponding to OER = 3. This can be seen as orange islands of increased survival probability peripheral to the T1Gd MRI imaging abnormality in the axial view. Bottom row: Cell-density defined hypoxia, with hypoxic volume and OER = 3 where $c \geq 0.8K$.

Table 4.3: Spatial analysis metrics used to asses model prediction accuracy and fidelity (top) and a subset of the response metrics provided by UVC simulations (bottom).

Spatial Metric	Definition
Level set distance (mm)	Level set distance (mm) Euclidean distance between model-predicted tumor surface and observed tumor enhancement
Positive Predictive Value (PPV)[a]	Voxel-wise assessment of simulation versus observed imaging enhancement. PPV = TP / (TP + FP)
Sensitivity, Specificity	Sensitivity = TP / (TP + FN), Specificity = TN / (FP + TN)
Jaccard Index	Similarity metric between two data sets. Jaccard = TP/(FP+TP+FN)
Volume similarity	Volume similarity = 1 - (|FP-FN| / (FP+2TP+FN))
Response Metric	**Definition**
Model Effect	Radial distance between UVC[b] and observed tumor post-treatment
Cell Kill	Number of cells lost as a result of therapy -comparison of UVC at post-treatment time point and observed tumor burden on MRI post-treatment
Days Gained	The days required for the UVC to grow from the size of the measured tumor after therapy to the UVC size at the post-therapy time point based on either the change in mean T1Gd radius or the number of cells killed. In other words, the days the tumor was delayed from its path of untreated growth as a result of therapy.

[a] True Positive (TP), True Negative (TN), False Positive (FP) and False Negative (FN)

[b] Untreated virtual control (UVC)

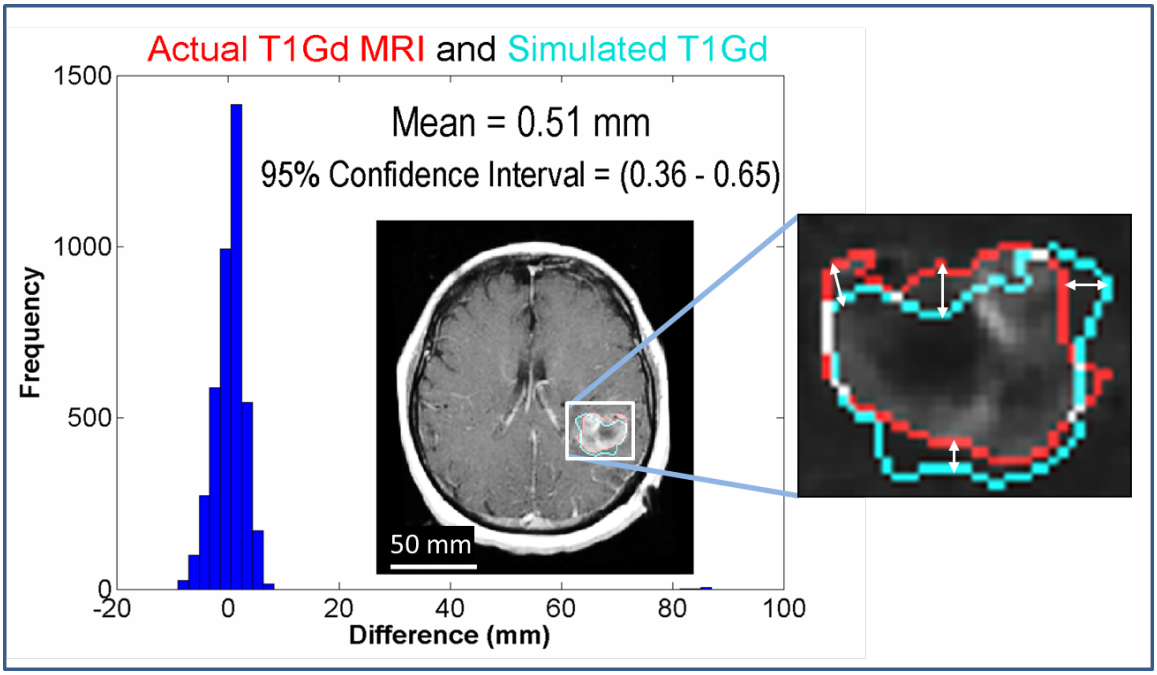

Figure 4.15: Spatial metric between the model-predicted T1Gd surface (light /cyan contour) and the observed tumor boundary (dark/red contour), indicating a mean deviation of 0.51 mm using the observed tumor region (dark/red) as true (see Table 4.4). Negative distances indicate an under-estimation of the model-predicted tumor front, whereas positive distances indicate an over-estimation, with zero distance indicating overlap of the surfaces.

Time	MRI Region	Mean error (mm)	95% Confidence interval (mm)
1st PreRT	T1Gd / T2	0.8 / 2.5	(0.6 – 1.0) / (2.3 – 2.8)
2nd PreRT	T1Gd / T2	0.5 / 3.0	(0.4 – 0.6) / (2.8 – 3.3)
PostRT with OER	T1Gd / T2	0.8 / 2.5	(0.6 – 1.0) / (2.3 – 2.8)
PostRT without OER	T1Gd / T2	0.8 / 2.5	(0.6 – 1.0) / (2.3 – 2.8)

Table 4.4: Euclidean distances between actual and simulated tumor surfaces. This metric produces a distribution of distances between the simulated and observed tumor surfaces. A value of zero indicates exact agreement between model and observed tumor on a voxel-wise basis, therefore the closer the mean of the distribution is to zero, the better the agreement between model and actual tumor burden, in 3-dimensions. Inter-observer error in gross tumor volume measurement has been computed as ± 1 mm [200], indicating that simulation predictions are not much greater than our estimated uncertainty in measurable tumor size.

Region	HV mm^3	T/B min	T/B mean	T/B max
Brain	10637	0	0.001	1.601
T2Buff	2095	0	0.009	1.601
T2-T1Gd	98	0	0.005	1.413
T1	473	0	0.020	1.537

Table 4.5: Hypoxic volue (HV) distributed within MRI regions.

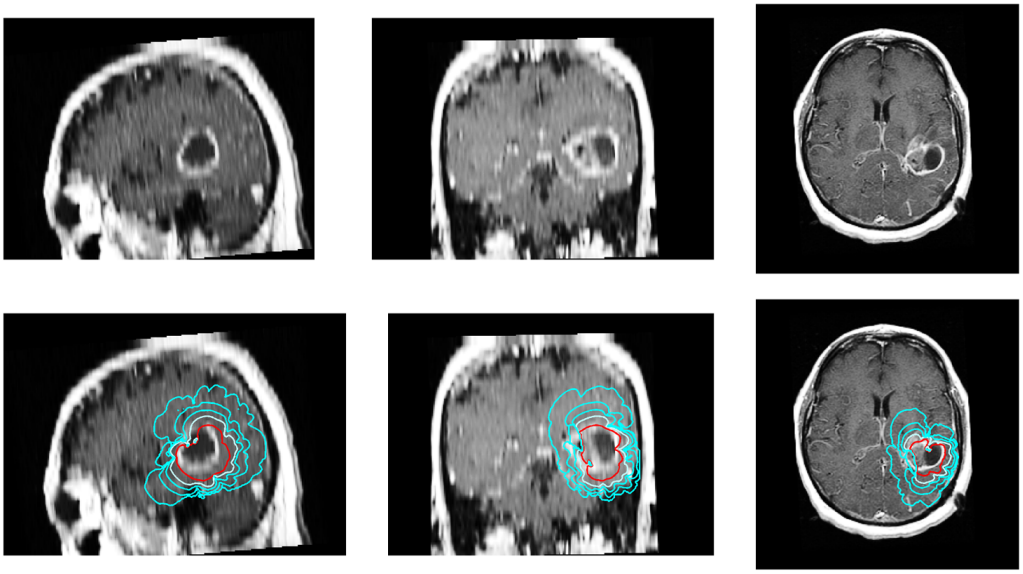

Figure 4.16: Patient-specific 3-dimensional simulation of glioma growth and invasion in the architecture of the brain reveals diffuse infiltration of the surrounding brain well beyond the abnormality revealed on T1Gd clinical imaging. Top: T1Gd MRI following stereotactic needle biopsy, prior to radiation therapy. Bottom: PI model solutions superimposed on the MRI in the top row. Red contour corresponds to the model-predicted T1GD tumor extent. Differential motility of tumor cells reveal invasion into the let temporal lobe as well as imminent infiltration across the corpus collosum into the contra-lateral hemisphere.

Theta methods Consider reaction-diffusion equations of the form

$$c_t = \kappa c_{xx} + \gamma f(c), \tag{4.40}$$

which models a diffusion with reaction term $f(c)$. In the PI model, $f(c)$ is the logistic growth term. Let C_j^n represent the approximation to the solution $c(x_j, t_n)$ at spatial grid point j and time point n. The theta method is given by

$$\begin{aligned} C_j^{n+1} &= C_j^n + k/2h^2 \left[\left(C_{j-1}^n - 2U_j^n + C_{j+1}^n \right) + \left(C_{j-1}^{n+1} - 2C_j^{n+1} + C_{j+1}^{n+1} \right) \right] && (4.41) \\ &+ k\gamma \left[(1-\theta) f(C_j^n) + \theta f(C_j^{n+1}) \right] && (4.42) \end{aligned}$$

where θ is a parameter. In particular, if $\theta = 1/2$ then the reaction term is modeled with the same centered-in-time approach as the diffusion term and the method can be obtained

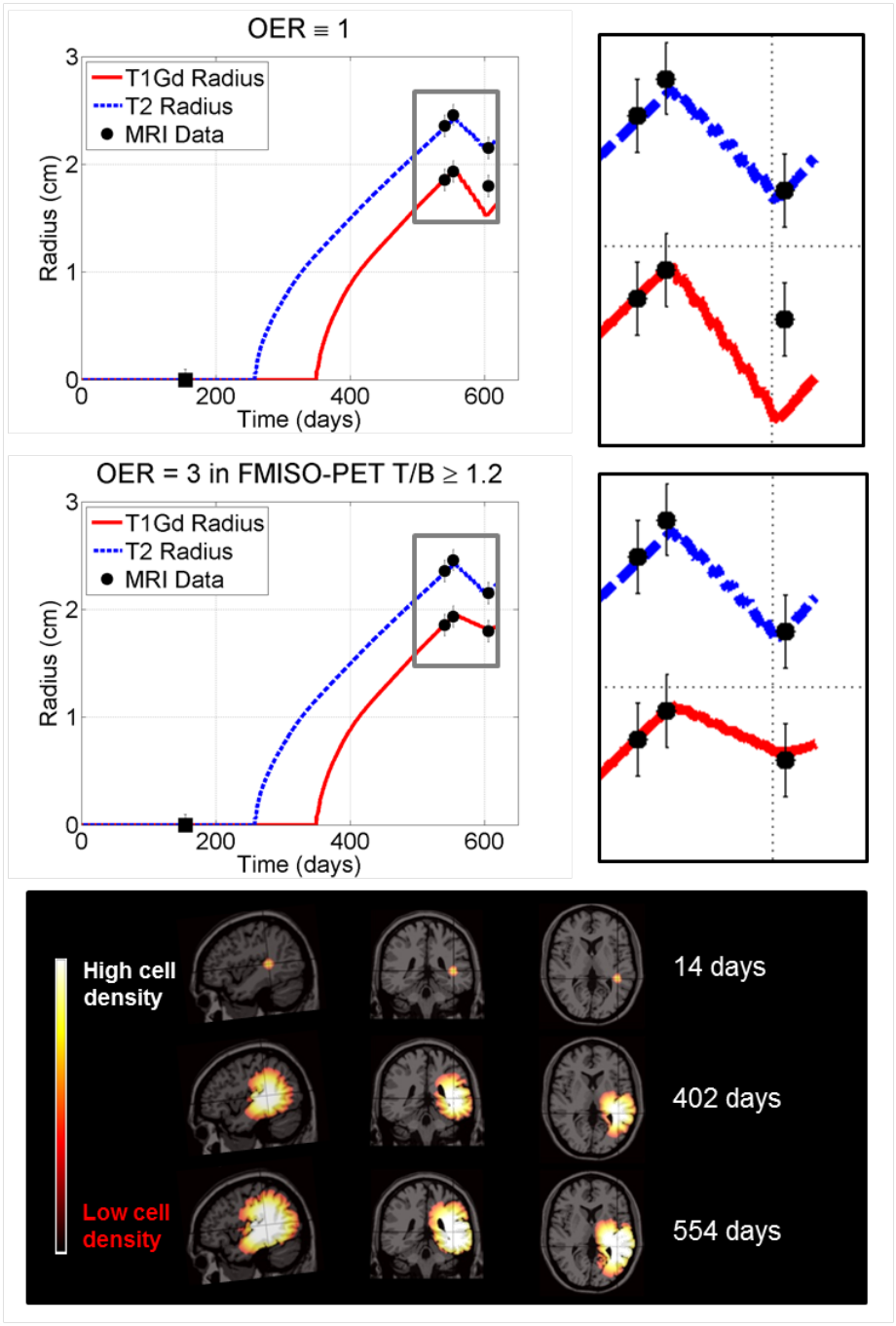

Figure 4.17: Dashed line is the model-predicted tumor size on T2-weighted MRI, solid line is T1-weighted gadolinium enhanced (T1Gd) MRI size. Black circles are observed tumor sizes calculated volumetrically with 1 mm error bars based on inter-observer measurement uncertainty. Top: Patient-specific simulation of radiation therapy without the oxygen enhancement ratio (OER) to model homogeneous response to external-beam radiation therapy. Middle: three-fold reduction in radiation-induced cell kill observed with in vivo radiographic changes in tumor volume with (OER = 3) in regions of FMISO T/B activity greater than 1.2. Bottom: Three dimensional tumor volume prediction using the brainweb atlas reveals diffuse tumor invasion prior to RT.

by applying the trapezoidal method to the method of lines (MOL) formulation of the PDE. If $\theta = 0$ then the reaction term is handled explicitly. For more general reaction-diffusion equations it may be advantageous to handle the reaction terms explicitly since these terms are generally nonlinear, so making them implicit would require solving nonlinear systems in each time step, whereas handling the diffusion term implicitly only gives a linear system to solve in each time step. The conjugate gradient method is used as an iterative method to solve the resulting nonlinear system of equations [72]. This method is $\mathcal{O}(k^p + h^2)$ accurate, where k is the time step, h is the spatial step and $p = 2$ if $\theta = 1/2$ and $p = 1$ otherwise, which is more than sufficient to resolve tumor growth on clinical time and spatial scales, which are approximately $k = \mathcal{O}(\text{ day})$, and $h = \mathcal{O}(1 \text{ mm})$. The Crank-Nicolson (CN) method is a special case of the theta methods where $\theta = 1/2$. The CN method is based on centered differences in space and the trapezoidal rule in time. This method is unconditionally stable, although the time step should be chosen to give sufficient accuracy for the MRI data to be compared with [119]. In order to resolve the wave front, we take

$$k \leq \frac{h^2}{(2\max(D_w, D_g))} \tag{4.43}$$

since we have $D_w > D_g$, we take $k \leq h^2/(2D_w)$.

We implement the treatment simulations in FORTRAN 90. The diffusion and reaction terms were solved simultaneously with a Crank-Nicolson formulation. The CN implementation is straight forward with the notable exception of differencing the spatial derivative with $D(x)$ which must be computed at the half-steps. In one spatial dimension, this is given as

$$\frac{\partial}{\partial \mathbf{x}}\left(D(\mathbf{x})\frac{\partial c(\mathbf{x},t)}{\partial \mathbf{x}}\right) \approx \tag{4.44}$$

$$\frac{1}{h}\left(\frac{D(\mathbf{x}+h/2)(c(\mathbf{x}+h,t)-c(\mathbf{x},t)) - D(\mathbf{x}-h/2)(c(\mathbf{x},t)-c(\mathbf{x}-h,t))}{h}\right) \tag{4.45}$$

$$= \frac{1}{h^2}\left[\left(D\left(\mathbf{x}+\frac{h}{2}\right)+D\left(\mathbf{x}-\frac{h}{2}\right)\right)c(\mathbf{x},t) - \ldots \right. \tag{4.46}$$

$$\left. D\left(\mathbf{x}+\frac{h}{2}\right)(c(\mathbf{x}+h,t)) - D\left(\mathbf{x}-\frac{h}{2}\right)c(\mathbf{x}-h,t)\right] \tag{4.47}$$

where h is the resolution of the spatial grid, which is uniform in each spatial dimension so that $h_x = h_y = h_z = h = \Delta x$. The formula above can be easily extended to non-

cubic Cartesian grids for which $h_x \neq h_y \neq h_z$. The large linear system resulting from the implicit method was solved with the conjugate gradient method. We used the brainweb atlas to determine the grey, white and CSF tissue architectures of the brain [45], and spatially aligned the MRIs and FMISO images to the atlas [190, 107]. We applied a no-flux boundary condition to prevent tumor cells from leaving the brain or entering the cerebro-spinal fluid. The order accuracy of the numerical method was sufficient to resolve the solution to the scale of the input data, which is 1 mm^3 in space and 1 day in time. A point-source of tumor cells corresponding to the carrying capacity K in one voxel at the geometric center of the pre-treatment T1Gd abnormality was used to initiate the simulation,

$$c((x_0, y_0, z_0), t = 0) = K \tag{4.48}$$

where $\mathbf{x}_0 = (x_0, y_0, z_0)$ is the center of mass. Simulations in spherical symmetry were performed in MATLAB using the second order accurate partial differential equation solver pdepe [165].

4.5 Results

Using our patient-specific model for glioma growth and response to radiation therapy, we find a three-fold increase in radiation-resistance in areas of hypoxia leads to a ten-fold increase in accuracy of our model predictions, from 14.6% to 1.1% relative volumetric error (Table 4.4). Additionally, when comparing the PIRT model simulation with and without incorporating the OER, 238% more tumor cells survived due to local hypoxia resistance effects and 24% of the model-predicted tumor cells prior to treatment were killed by the radiation. Incorporation of hypoxia-mediated resistance provided better qualitative and quantitative predictive value to the model in regions of high cellular density where the hypoxia was localized (T1GD), Figure 4.10. Spatial concordance between the model-predicted disease burden prior to, and following radiation therapy was measured through spatial, volume, and similarity metrics, summarized in Tables 4.4, 4.3 and Figure 4.15. Voxel-wise similarity metrics using true positive, false positive, false negative and true negative are challenged by issues of spatial registration and a large number of true negatives for pixels far outside the gross tumor region. With this limitation in mind, a two-fold increase in sensitivity of voxel-

wise concordance of model-predicted disease burden and observed tumor by incorporation of localized hypoxia-modulated radiation resistance. Volume similarity was increased from 0.844 to 0.91, and the Jaccard metric was increased from 0.72 to 0.83.

Sensitivity analysis To investigate sensitivity of our predictions to variation in hypoxic volume delineation, we varied the tissue to blood cutoff from T/B = 1.0, larger regions less specific to hypoxia, to T/B = 1.4 smaller regions specific to concentrated or intense hypoxia. Model accuracy was positively correlated to the FMISO T/B threshold used to determine hypoxic tissue, with a maximal value between 1.3 and 1.4 ($1.3 \leq T/B_{OPT} \leq 1.4$). In addition to binary representations of hypoxic regions, we considered a gradient of hypoxia such that OER was set to unity for pixels below T/B = 0.98 [169] and scaled linearly to OER = 3 at the maximum pixel intensity to give a spatial average of OER = 1.5. This scaling also mitigates partial volume effects inherent in PET imaging [168]. This produced an increased survival probability beyond the infiltrative leading edge of the tumor in normal brain due to the substantial tracer activity between 0.98 and 1.2 T/B, despite this region having a relatively high dose per cell ratio relatively low degree of hypoxia. This resulted in model predictions which over-estimated T2- and under-estimated T1Gd-MRI associated isodensities and therefore decreased overall model prediction accuracy.

To further investigate the role of spatial localization of radiation-resistance, simulations were also performed in isotropic 3-dimensional spherical symmetry without anatomical complexity, using the T1Gd isodensity as a lower bound threshold to determine the hypoxic region. In these simulations we observed the same outcome, that is, that model-data agreement is substantially improved with the inclusion of a three-fold OER in regions of hypoxia. This suggests that tumor kinetics characterize radiation response on a macroscopic scale and are not an artifact of our 3-dimensional atlas or data. Sensitivity of model predictions to uncertainty in imaging data inputs and model parameters is discussed in detail in the supplement to Rockne 2010 [151] and would be insufficient to account for the improvement observed.

4.5.1 Discussion

We have improved a mathematical model of human glioma growth to incorporate hypoxia-induced radiation response for better prediction of patient-specific radiation-response. This model is based on a methodology of proliferation-invasion of tumor spread and incorporates the linear-quadratic model for radiation efficacy of tumor kill. We present a case study in which our model is used to predict glioma growth and response to radiation therapy in a 3D representation of human brain and patient-specific clinical radiation therapy plan (Figure 4.10) in 3D using a phantom [45]. The accuracy of the model in predicting response to radiation therapy is improved by the incorporation of an oxygen-enhancement ratio (OER) to approximate the degree of radio-resistance created by hypoxic conditions within the tumor, see Figure 4.10 and Table 4.4. Without the incorporation of OER and localize radiation resistance, the model is unable to fully capture post-RT tumor size in regions of high cellular density, motivating the addition of the biologically driven OER parameter derived from *in vivo* clinical data.

Limitations and considerations This study assumes no changes to hypoxia through the course of radiotherapy, which ignores one of the four "R's" of radiobiology, re-oxygenation, which surely takes place [12, 106, 102]. The linear-quadratic model is a robust expression of dose-response in the 0–5 Gy dose range but does not reflect myriad repair processes and micro-environmental changes induced by radiotherapy [15], although extensions to the L-Q model exist to approximate the effects of re-oxygenation and hypoxia [29]. Ideally, a more patient-specific, biologically driven model of the process of angiogenesis, hypoxia and necrosis utilizing a modeling approach which integrates multi-modality imaging is desired, [185, 73]. Hypoxia dynamics can be studied with kinetic FMISO imaging [38] to improve differentiation between transient and chronic hypoxic conditions, however this approach remains relegated to the imaging time point. Prospective interventional imaging studies which capture changes in intra-tumoral hypoxia throughout the course of therapy is needed in order to improve models of hypoxia-driven resistance to radiation therapy, as the metronomic nature of daily fractionated conformal radiotherapy likely introduces pheotypic and

genotypic selection pressures which eliminate the sensitive tumor cells and leave the most aggressive, resistant clones to repopulate following therapy completion [120].

The goal of modeling biological response to therapy has been long sought after, but there have been no demonstrable successes with the potential for impacting individual treatment planning. Although previous studies have investigated targeting radiotherapy to regions of hypoxia, [147] or using regions of hypoxia to predict tumor recurrence [194, 41] based solely on imaging, this approach does not account for inter-tumoral differential sensitivity to radiation therapy *across patients* based on growth and invasion kinetics. Other efforts to incorporate biological effect into radiation treatment plans have either relied on static features of the tumor [155] or are not capable of being truly patient-specific because of the large number of parameters to be estimated [54, 53, 60, 172]. We have developed a technique to incorporate the dynamic proliferation and invasion of the tumor over the time course of treatment within the 3D anatomy of the brain. Granting all the assumptions and limitations of the simple proliferation-invasion tumor growth model, this framework has provided a methodology to investigate the role of the OER in modulating radiation response *in vivo*, quantitatively.

Chapter 5

CONCLUSIONS

5.1 Mathematical radiation oncology

In order for there to be a clinical reality in radiation-oncology which utilizes mathematical models to make treatment decisions, the models must be validated and capable of addressing the clinical challenges in the field. For example, high dose per fraction and high energy/charged particle therapies are being reconsidered in the glioblastoma therapy paradigm. Therefore, the field of "mathematical radiation oncology" must include tools to translate understanding of the physics and radiation biology relevant to these scenarios to clinically relevant model predictions. Moreover, individual treatment response and resistance mechanisms must be incorporated into the model in a way which relies on routinely collected clinical data, so that model predictions can be most broadly applied to clinical practice.

5.2 Model selection

The best models are ones that both recapitulate the empirical observations that motivate them as well as provide insight into the fundamental principles governing the system being observed. The scale and complexity of a model is a function of the nature of the question being asked of it, and the data from which it is based. In the case of clinical scale models in which the observations are macroscopic, tissue-scale behavior of the disease, the data dictates the complexity of the model. Likewise in the context of radiation biology, the mechanistic model must both describe the physical properties of the situation, and also be able to reproduce the characteristic dose-response relationships that have been observed for nearly one hundred years. I believe that the PI, PIRT, PIRT-D, and RMF models are well designed models to answer specific questions that can directly translate to clinical challenges in radiation oncology.

5.3 Summary

The results from this dissertation can be summarized as follows:

1. Analytic solutions are found for a one-way coupled ODE model of radiation-induced DNA damage and repair (RMF) which illustrates orders of magnitude differences between the linearized solution used pervasively in the literature and the analytic solution to the fully nonlinear model. This mathematical analysis speaks directly to a current debate regarding the relevance of mathematical models in high radiation dose treatment regimes and provides a new formalism for calculating biological effects of radiation, derived from a mechanistic model.

2. Data-driven parameterization of the RMF DNA damage model reveals superior model prediction and parameter stability across a wide range of experimental conditions compared to current model paradigms.

3. Patient-specific calibration of a proliferation-invasion (PI) model for brain tumor growth which enables characterization of the tumor phenotype in terms of the relative relationship between net rates of diffusion/migration and proliferation.

    (a) This patient-specific model is expanded to include delivery and temporally delayed response to radiation therapy (PIRT-D) to yield a predictive relationship between the net rate of proliferation and radiation sensitivity, and provide a means to infer biological mechanisms of brain tumor growth and response to therapy.

4. The patient-specific radiation therapy (PIRT) model is expanded to include spatially and temporally defined treatment delivery and hypoxia-mediated response. This extension advances the patient-specific response model into 3D as well as improves model accuracy.

Is mathematical modeling the future of prognosis and treatment? Mathematical models have been applied to cancer for over a century. We are currently engaged in a dialog as to whether or not mathematics is "ready for prime time"[52] and speculate it is the future of prognosis and treatment [146] with patient-specific models approaching 20 years old [204]. What do we need to move patient-specific modeling forward towards clinical applicability? Progress is well summarized by Neal et al. [134]. I believe we are *very close* to clinically relevant, personalized models which are capable of transforming clinical decision making by providing doctors with patient-specific quantifications of growth and response to therapy to inform treatment decision making. I believe the next steps in the road to clinical adoption of patient-specific mathematical models are:

1. Prospective validation of model predictions. Uncertainty quantification and validations of models on test data sets distinct from those from which the model is trained/derived is required to have confidence in model predictions.

2. Clinical trials designed with patient-specific, model-derived metrics of response which are prognostic [136].

3. We as a field need to develop more truly patient-specific calibration methodologies which utilize *routinely available data* like those developed by [95, 116].

4. Direct marketing of model predictions to a clinical application will facilitate and accelerate clinical translation through publications in high impact medical and medical physics journals [135, 126, 139, 208].

5. When appropriate, the use of minimal models which can be parameterized for individual patients and predictive of prognosis and/or response to a specific therapy [135]. However, this is a double edged sword: take for instance the RTOG RPA [160] methodology which prognostic, and to an extent, patient-specific, however, this statistical analysis does not make predictions for patients who deviate from a predetermined formula and does not enable virtual investigation of alternative therapies for those patients predicted to not respond to therapy.

6. Increased availability of advanced imaging techniques. Many additional "advanced MRI," PET, SPECT, and other imaging methods can enable greater model calibration and biological complexity *in vivo*. We need not only the incorporation of advanced imaging in models [208, 58], but we need to increase our investment as a society in obtaining as much patient-specific disease kinetic information as is possible, to the extent which it is safe for the patient.

Overcoming the major hurdles for advancing the understanding and effective treatment of gliomas calls for new and innovative techniques. This is where mathematical modeling has already begun to play an important role. The fundamental definition of cancer includes uncontrolled proliferation and invasion, which forms the basis of the bio-mathematical model. We believe that this model represents a truly revolutionary and relevant approach to assessing and predicting the interactions of these two most salient features of glioma growth – proliferation and migration (dispersal) – *in vivo*. Modeling of such complex systems allows for iterative comparisons between virtual and real situations. Thus far, this iterative comparison has provided new directions in our understanding of gliomas and has provided direction for testing new hypotheses.

ACKNOWLEDGMENTS

First, I wish to thank my wife Sarah for enduring long evening and weekend work hours, and my daughters Chloe and Ella for sleeping as much as possible during the preparation of this thesis work. I could not have completed this work without Sarah's constant support, and care taking of me and the family. Further, I wish to thank all of my friends and family for their support of my return to school. Many thanks go to the reading committee for guidance and helpful edits.

Special thanks go to Addie Boone for the "clinical challenge" and "model opportunity" paradigm. Thanks to clinical collaborators Dr. Peter Canoll M.D., Ph.D., Dr. Maciej M. Mrugala M.D., Ph.D., M.P.H., Dr. Jason K. Rockhill M.D., Ph.D., Dr. Jacob Scott M.D., and Dr. Andrew D. Trister M.D., Ph.D., for their valuable perspectives on how mathematical model predictions can be made most clinically relevant. Thank you to Alexander "Sandy" R. A. Anderson Ph.D. for challenging me to communicate the impact of my work, and for talking me through the subtleties of a life and career in academics. Thank you to all members of the Swanson Lab, who endured my relative isolation during the final dissertation writing phase. I wish to thank the national institutes of health (NIH) and the James S. McDonnell foundation for their financial support.

Last, but certainly not least, I wish to thank Kristin R. Swanson Ph.D.. Without her, this work would not have happened. She has been an incredible mentor and I am constantly amazed by her effortless insight into complicated problems. Further, everyone in the field of "Mathematical Neuro-Oncology" is indebted to Ellsworth "Buster" C. Alvord, Jr. M.D., whose vision and collaboration with James D. Murray D.Phil., initiated this line of research.

BIBLIOGRAPHY

[1] S. A. Airapetov and V. K. Ivanov. Optimal-control of radiation-therapy in a heterogeneous population-model of tumor-cells. *Automation and Remote Control*, 51(10):1442–1448, 1990.

[2] N. S. Akella, Q. Ding, I. Menegazzo, W. Wang, G. Y. Gillespie, J. R. Grammer, C. L. Gladson, and L. B. Nabors. A novel technique to quantify glioma tumor invasion using serial microscopy sections. *J Neurosci Methods*, 153(2):183–9, 2006.

[3] K. Aldape, P. C. Burger, and A. Perry. Clinicopathologic aspects of 1p/19q loss and the diagnosis of oligodendroglioma. *Arch Pathol Lab Med*, 131(2):242–51, 2007.

[4] G. A. Alexiou, S. Tsiouris, A. P. Kyritsis, S. Voulgaris, M. I. Argyropoulou, and A. D. Fotopoulos. Glioma recurrence versus radiation necrosis: accuracy of current imaging modalities. *J Neurooncol*, 2009.

[5] E. C. Alvord Jr. Why do gliomas not metastasize. *Arch Neurol*, 33(2):73–5, 1976.

[6] E. C. Alvord Jr. Simple model of recurrent gliomas. *J Neurosurg*, 75(2):337–8, 1991.

[7] V. Amberger-Murphy. Hypoxia helps glioma to fight therapy. *Curr Cancer Drug Targets*, 9(3):381–90, 2009.

[8] A. R. Anderson and V. Quaranta. Integrative mathematical oncology. *Nat Rev Cancer*, 8(3):227–34, 2008.

[9] R. P. Araujo and D. L. McElwain. A history of the study of solid tumour growth: the contribution of mathematical modelling. *Bull Math Biol*, 66(5):1039–91, 2004.

[10] J. Ashburner, G. Flandin, R. Henson, S. Kiebel, J. Kilner, J. Mattout, W. Penny, and K. Stephan. Statistical parametric mapping (SPM), 2005.

[11] N. C. Atuegwu, L. R. Arlinghaus, X. Li, A. B. Chakravarthy, V. G. Abramson, M. E. Sanders, and T. E. Yankeelov. Parameterizing the logistic model of tumor growth by DW-MRI and DCE-MRI data to predict treatment response and changes in breast cancer cellularity during neoadjuvant chemotherapy. *Transl Oncol*, 6(3):256–64, 2013.

[12] A. O. Badib and J. H. Webster. Changes in tumor oxygen tension during radiation therapy. *Acta Radiol Ther Phys Biol*, 8(3):247–57, 1969.

[13] D.L. Bailey, D.W. Townsend, P.E. Valk, and M.N. Maisey, editors. *Imaging tumor hypoxia*, pages 689–96. Springer-Verlag, London, 2002.

[14] A. L. Baldock, R. C. Rockne, A. D. Boone, M. L. Neal, A. Hawkins-Daarud, D. M. Corwin, C. A. Bridge, L. A. Guyman, A. D. Trister, M. M. Mrugala, J. K. Rockhill, and K. R. Swanson. From patient-specific mathematical neuro-oncology to precision medicine. *Front Oncol*, 3:62, 2013.

[15] J. Bampoe and M. Bernstein. Advances in radiotherapy of brain tumors: radiobiology versus reality. *J Clin Neurosci*, 5(1):5–14, 1998.

[16] L. Barazzuol, N. G. Burnet, R. Jena, B. Jones, S. J. Jefferies, and N. F. Kirkby. A mathematical model of brain tumour response to radiotherapy and chemotherapy considering radiobiological aspects. *Journal of Theoretical Biology*, 262(3):553–65, 2010.

[17] G. W. Barendsen, T. L. Beusker, A. J. Vergroesen, and L. Budke. Effects of different radiations on human cells in tissue culture. ii. biological experiments. *Radiat Res*, 13:841–9, 1960.

[18] G. W. Barendsen, C. J. Koot, G. R. Van Kersen, D. K. Bewley, S. B. Field, and C. J. Parnell. The effect of oxygen on impairment of the proliferative capacity of human cells in culture by ionizing radiations of different LET. *International journal of radiation biology and related studies in physics, chemistry, and medicine*, 10(4):317–27, 1966.

[19] F. G. Barker II, M. D. Prados, S. M. Chang, P. H. Gutin, K. R. Lamborn, D. A. Larson, M. K. Malec, M. W. McDermott, P. K. Sneed, W. M. Wara, and C. B. Wilson. Radiation response and survival time in patients with glioblastoma multiforme. *J Neurosurg*, 84(3):442–8, 1996.

[20] D. Basanta, M. Simon, H. Hatzikirou, and A. Deutsch. Evolutionary game theory elucidates the role of glycolysis in glioma progression and invasion. *Cell Prolif*, 41(6):980–7, 2008.

[21] S. Bauer, R. Wiest, L. P. Nolte, and M. Reyes. A survey of MRI-based medical image analysis for brain tumor studies. *Phys Med Biol*, 58(13):R97–R129, 2013.

[22] G. S. Bauman, B. J. Fisher, W. McDonald, V. R. Amberger, E. Moore, and R. F. Del Maestro. Effects of radiation on a three-dimensional model of malignant glioma invasion. *Int J Dev Neurosci*, 17(5-6):643–51, 1999.

[23] G. S. Bauman, L. E. Gaspar, B. J. Fisher, E. C. Halperin, D. R. Macdonald, and J. G. Cairncross. A prospective study of short-course radiotherapy in poor prognosis glioblastoma multiforme. *Int J Radiat Oncol Biol Phys*, 29(4):835–9, 1994.

[24] G. S. Bauman, W. MacDonald, E. Moore, D. A. Ramsey, B. J. Fisher, V. R. Amberger, and R. M. Del Maestro. Effects of radiation on a model of malignant glioma invasion. *J Neurooncol*, 44(3):223–31, 1999.

[25] N. Bellomo, M. Chaplain, and E. de Angelis, editors. *Modeling Diffusely Invading Brain Tumors: An Individualized Approach to Quantifying Glioma Evolution and Response to Therapy*, chapter 8, pages 207–218. Birkhuser, Cambridge, Massachusetts, 2008.

[26] C. M. Bender and S. A. Orszag. *Advanced mathematical methods for scientists and engineers*. Springer, New York, 1999.

[27] S. M. Blinkov and I. Glezer. *The human brain in figures and tables; a quantitative handbook*. Basic Books, New York, 1968. Translated from the Russian by Basil Haigh.

[28] D. J. Brenner. The linear-quadratic model is an appropriate methodology for determining isoeffective doses at large doses per fraction. *Semin Radiat Oncol*, 18(4):234–9, 2008.

[29] D. J. Brenner, L. R. Hlatky, P. J. Hahnfeldt, E. J. Hall, and R. K. Sachs. A convenient extension of the linear-quadratic model to include redistribution and reoxygenation. *Int J Radiat Oncol Biol Phys*, 32(2):379–90, 1995.

[30] D. J. Brenner, L. R. Hlatky, P. J. Hahnfeldt, Y. Huang, and R. K. Sachs. The linear-quadratic model and most other common radiobiological models result in similar predictions of time-dose relationships. *Radiat Res*, 150(1):83–91, 1998.

[31] M.A. Brown and R.C. Semelka. *MRI: Basic Principles and Applications*. Wiley-Liss Inc., New York, 2nd edition, 1999.

[32] P. K. Burgess, P. M. Kulesa, J. D. Murray, and E. C. Alvord Jr. The interaction of growth rates and diffusion coefficients in a three-dimensional mathematical model of gliomas. *J Neuropathol Exp Neurol*, 56(6):704–13, 1997.

[33] H. L. Byrne, A. L. McNamara, W. Domanova, S. Guatelli, and Z. Kuncic. Radiation damage on sub-cellular scales: beyond DNA. *Phys Med Biol*, 58(5):1251–67, 2013.

[34] M. Carlone, D. Wilkins, and P. Raaphorst. The modified linear-quadratic model of guerrero and li can be derived from a mechanistic basis and exhibits linear-quadratic-linear behaviour. *Phys Med Biol*, 50(10):L9–13; author reply L13–5, 2005.

[35] D. J. Carlson. *Mechanisms of Intrinsic Radiation Sensitivity: The Effects of DNA Damage Repair, Oxygen, and Radiation Quality*. Ph.D., Purdue University, 2006.

[36] D. J. Carlson, R. D. Stewart, and V. A. Semenenko. Effects of oxygen on intrinsic radiation sensitivity: A test of the relationship between aerobic and hypoxic linear-quadratic (LQ) model parameters. *Med Phys*, 33(9):3105–15, 2006.

[37] D. J. Carlson, R. D. Stewart, V. A. Semenenko, and G. A. Sandison. Combined use of monte carlo DNA damage simulations and deterministic repair models to examine putative mechanisms of cell killing. *Radiat Res*, 169(4):447–59, 2008.

[38] J. J. Casciari, M. M. Graham, and J. S. Rasey. A modeling approach for quantifying tumor hypoxia with [F-18]fluoromisonidazole PET time-activity data. *Med Phys*, 22(7):1127–39, 1995.

[39] J. L. Chan, S. W. Lee, B. A. Fraass, D. P. Normolle, H. S. Greenberg, L. R. Junck, S. S. Gebarski, and H. M. Sandler. Survival and failure patterns of high-grade gliomas after three-dimensional conformal radiotherapy. *J Clin Oncol*, 20(6):1635–42, 2002.

[40] J. D. Chapman. The detection and measurement of hypoxic cells in solid tumors. *Cancer*, 54(11):2441–9, 1984.

[41] J. D. Chapman, E. L. Engelhardt, C. C. Stobbe, R. F. Schneider, and G. E. Hanks. Measuring hypoxia and predicting tumor radioresistance with nuclear medicine assays. *Radiother Oncol*, 46(3):229–37, 1998.

[42] M. R. Chicoine and D. L. Silbergeld. Assessment of brain tumour cell motility in vivo and in vitro. *J Neurosurg*, 82:615–622, 1995.

[43] A. Claes, A. J. Idema, and P. Wesseling. Diffuse glioma growth: a guerilla war. *Acta neuropathologica*, 114(5):443–58, 2007.

[44] L. P. Clarke, R. Velthuizen, M. A. Camacho, Heine J. J., Vaidyanathan M., L. O. Hall, R. W. Thatcher, and Silbiger M. L. MRI segmentation: methods and applications. *Magnetic Resonance Imaging*, 13(3):343–368, 1995.

[45] C. A. Cocosco, V. Kollokian, R. K.-S. Kwan, and A. C. Evans. Brainweb: Online interface to a 3D simulated brain database. *Neuroimage*, 5:S425, 1997.

[46] J. P. Concannon, S. Kramer, and R. Berry. The extent of intracranial gliomata at autopsy and its relationship to techniques used in radiation therapy of brain tumors. *Am J Roentgenol Radium Ther Nucl Med*, 84:99–107, 1960.

[47] J. R. Cunningh and J. Niederer. Mathematical-model for cellular response to radiation. *Phys Med Bio*, 17(5):685, 1972.

[48] R. G. Dale. Dose-rate effects in targeted radiotherapy. *Phys Med Biol*, 41(10):1871–84, 1996.

[49] S. J. Dalrymple, J. E. Parisi, P. C. Roche, S. C. Ziesmer, B. W. Scheithauer, and P. J. Kelly. Changes in proliferating cell nuclear antigen expression in glioblastoma multiforme cells along a stereotactic biopsy trajectory. *Neurosurgery*, 35(6):1036–1044; discussion 1044–1045, 1994.

[50] M. C. de Wit, H. G. de Bruin, W. Eijkenboom, P. A. Sillevis Smitt, and M. J. van den Bent. Immediate post-radiotherapy changes in malignant glioma can mimic tumor progression. *Neurology*, 63(3):535–7, 2004.

[51] J. M. R. Dealmodovar, M. I. Nunez, T. J. McMillan, N. Olea, C. Mort, M. Villalobos, V. Pedraza, and G. G. Steel. Initial radiation-induced DNA-damage in human tumor-cell lines - a correlation with intrinsic cellular radiosensitivity. *British Journal of Cancer*, 69(3):457–462, 1994.

[52] T. S. Deisboeck, L. Zhang, J. Yoon, and J. Costa. In silico cancer modeling: is it ready for prime time? *Nat Clin Pract Oncol*, 6(1):34–42, 2009.

[53] D. D. Dionysiou, G. S. Stamatakos, D. Gintides, N. Uzunoglu, and K. Kyriaki. Critical parameters determining standard radiotherapy treatment outcome for glioblastoma multiforme: a computer simulation. *Open Biomed Eng J*, 2:43–51, 2008.

[54] D. D. Dionysiou, G. S. Stamatakos, N. K. Uzunoglu, K. S. Nikita, and A. Marioli. A four-dimensional simulation model of tumour response to radiotherapy in vivo: parametric validation considering radiosensitivity, genetic profile and fractionation. *J Theor Biol*, 230(1):1–20, 2004.

[55] T. A. Dolecek, J. M. Propp, N. E. Stroup, and C. Kruchko. CBTRUS statistical report: primary brain and central nervous system tumors diagnosed in the united states in 2005-2009. *Neuro-oncology*, 14 Suppl 5:v1–49, 2012.

[56] S. E. Eikenberry, T. Sankar, M. C. Preul, E. J. Kostelich, C. J. Thalhauser, and Y. Kuang. Virtual glioblastoma: growth, migration and treatment in a three-dimensional mathematical model. *Cell Prolif*, 42(4):511–28, 2009.

[57] B. M. Ellingson, P. S. LaViolette, S. D. Rand, M. G. Malkin, J. M. Connelly, W. M. Mueller, R. W. Prost, and K. M. Schmainda. Spatially quantifying microscopic tumor invasion and proliferation using a voxel-wise solution to a glioma growth model and serial diffusion mri. *Magnetic resonance in medicine*, 65(4):1131–43, 2011.

[58] B. M. Ellingson, M. G. Malkin, S. D. Rand, J. M. Connelly, C. Quinsey, P. S. LaViolette, D. P. Bedekar, and K. M. Schmainda. Validation of functional diffusion

maps (fDMs) as a biomarker for human glioma cellularity. *J Magn Reson Imaging*, 31(3):538–48, 2010.

[59] B. M. Ellingson, M. G. Malkin, S. D. Rand, P. S. Laviolette, J. M. Connelly, W. M. Mueller, and K. M. Schmainda. Volumetric analysis of functional diffusion maps is a predictive imaging biomarker for cytotoxic and anti-angiogenic treatments in malignant gliomas. *J Neurooncol*, 2010.

[60] H. Enderling, M. A. Chaplain, and P. Hahnfeldt. Quantitative modeling of tumor dynamics and radiotherapy. *Acta Biotheor*, 58(4):341–53, 2010.

[61] Sydney M. Evans, Kevin D. Judy, Isolde Dunphy, W. Timothy Jenkins, Wei-Ting Hwang, Peter T. Nelson, Robert A. Lustig, Kevin Jenkins, Deirdre P. Magarelli, Stephen M. Hahn, Ruth A. Collins, M. Sean Grady, and Cameron J. Koch. Hypoxia is important in the biology and aggression of human glial brain tumors. *Clin Cancer Res*, 10(24):8177–8184, 2004.

[62] R. A. Fisher. The wave of advance of advantageous genes. *Ann. Eugenics*, 7:353–369, 1937.

[63] J. R. Flynn, L. Wang, D. L. Gillespie, G. J. Stoddard, J. K. Reid, J. Owens, G. B. Ellsworth, K. L. Salzman, A. Y. Kinney, and R. L. Jensen. Hypoxia-regulated protein expression, patient characteristics, and preoperative imaging as predictors of survival in adults with glioblastoma multiforme. *Cancer*, 113(5):1032–42, 2008.

[64] E. Galanis, J. C. Buckner, M. J. Maurer, R. Sykora, R. Castillo, K. V. Ballman, and B. J. Erickson. Validation of neuroradiologic response assessment in gliomas: measurement by RECIST, two-dimensional, computer-assisted tumor area, and computer-assisted tumor volume methods. *Neuro Oncol*, 8(2):156–65, 2006.

[65] L.M. Garcia, J. Leblanc, D. Wilkins, and G.P. Raaphorst. Fitting the linear-quadratic model to detailed data sets for different dose ranges. *Phys Med Biol*, 51:2813–2823, 2006.

[66] W. J. Gardner, L. J. Karnosh, Jr. McClure, C. C., and A. K. Gardner. Residual function following hemispherectomy for tumour and for infantile hemiplegia. *Brain : a journal of neurology*, 78(4):487–502, 1955.

[67] R. A. Gatenby and P. K. Maini. Mathematical oncology: cancer summed up. *Nature*, 421(6921):321, 2003.

[68] M. Gerosa, A. Nicolato, and R. Foroni. The role of gamma knife radiosurgery in the treatment of primary and metastatic brain tumors. *Curr Opin Oncol*, 15(3):188–96, 2003.

[69] A. Giese, B. Laube, S. Zapf, U. Mangold, and M. Westphal. Glioma cell adhesion and migration on human brain sections. *Anticancer Res*, 18(4A):2435–47, 1998.

[70] A. Giese and M. Westphal. Glioma invasion in the central nervous system. *Neurosurgery*, 39(2):235–50; discussion 250–252, 1996.

[71] Q. Y. Gong, P. R. Eldridge, A. R. Brodbelt, M. Garcia-Finana, A. Zaman, B. Jones, and N. Roberts. Quantification of tumour response to radiotherapy. *Br J Radiol*, 77(917):405–13, 2004.

[72] A. Greenbaum. *Iterative Methods for Solving Linear Systems*. Society for Industrial and Applied Mathematics, Philadelphia, 1997.

[73] S. Gu, G. Chakraborty, K. Champley, A. M. Alessio, J. Claridge, R. Rockne, M. Muzi, K. A. Krohn, A. M. Spence, Jr. Alvord, E. C., A. R. Anderson, P. E. Kinahan, and K. R. Swanson. Applying a patient-specific bio-mathematical model of glioma growth to develop virtual [18F]-FMISO-PET images. *Mathematical medicine and biology : a journal of the IMA*, 29(1):31–48, 2012.

[74] R. Guenther and J. Lee. *Partial Differential Equations of Mathematical Physics and Integral Equations*. Prentice Hall, Englewood Cliffs, 1988.

[75] M. Guerrero and M. Carlone. Mechanistic formulation of a lineal-quadratic-linear (LQL) model: split-dose experiments and exponentially decaying sources. *Med Phys*, 37(8):4173–81, 2010.

[76] M. Guerrero and X. A. Li. Extending the linear-quadratic model for large fraction doses pertinent to stereotactic radiotherapy. *Phys Med Biol*, 49(20):4825–35, 2004.

[77] M. Guerrero, R. D. Stewart, J. Z. Wang, and X. A. Li. Equivalence of the linear-quadratic and two-lesion kinetic models. *Phys Med Biol*, 47(17):3197–209, 2002.

[78] P. Hahnfeldt and L. Hlatky. Resensitization due to redistribution of cells in the phases of the cell cycle during arbitrary radiation protocols. *Radiation Research*, 145(2):134–143, 1996.

[79] E. J. Hall and A. J. Giaccia. *Radiobiology for the radiologist*. Lippincott Williams & Wilkins, Philadelphia, 7th edition, 2011.

[80] M. A. Hammoud, R. Sawaya, W. Shi, P. F. Thall, and N. E. Leeds. Prognostic significance of preoperative MRI scans in glioblastoma multiforme. *J Neurooncol*, 27(1):65–73, 1996.

[81] S. M. Haney, P. M. Thompson, T. F. Cloughesy, J. R. Alger, and A. W. Toga. Tracking tumor growth rates in patients with malignant gliomas: a test of two algorithms. *AJNR Am J Neuroradiol*, 22(1):73–82, 2001.

[82] L. Hanin and M. Zaider. A mechanistic description of radiation-induced damage to normal tissue and its healing kinetics. *Phys Med Biol*, 58(4):825–39, 2013.

[83] H. L. Harpold, Jr. Alvord, E. C., and K. R. Swanson. The evolution of mathematical modeling of glioma proliferation and invasion. *J Neuropathol Exp Neurol*, 66(1):1–9, 2007.

[84] H. Hatzikirou, D. Basanta, M. Simon, K. Schaller, and A. Deutsch. 'go or grow': the key to the emergence of invasion in tumour progression? *Math Med Biol*, 29(1):49–65, 2012.

[85] H. Hatzikirou, A. Chauviere, A. L. Bauer, A. Leier, M. T. Lewis, P. Macklin, T. T. Marquez-Lago, E. L. Bearer, and V. Cristini. Integrative physical oncology. *Wiley Interdiscip Rev Syst Biol Med*, 4(1):1–14, 2012.

[86] H. Hatzikirou, A. Deutsch, C. Schaller, M. Simon, and K. R. Swanson. Mathematical modelling of glioblastoma tumour development: A review. *Mathematical Models and Methods in Applied Sciences,*, 11:1779–1794, 2005.

[87] A. Hawkins-Daarud, R. C. Rockne, A. R. Anderson, and K. R. Swanson. Modeling tumor-associated edema in gliomas during anti-angiogenic therapy and its impact on imageable tumor. *Front Oncol*, 3:66, 2013.

[88] M. A. Heesters, J. Koudstaal, K. G. Go, and W.M. Molenaar. Analysis of proliferation and apoptosis in brain gliomas: Prognostic and clinical value. *J. Neurooncol*, 44:255–266, 1999.

[89] J. C. Helton and F. J. Davis. Illustration of sampling-based methods for uncertainty and sensitivity analysis. *Risk Anal*, 22(3):591–622, 2002.

[90] K. R. Hess. Extent of resection as a prognostic variable in the treatment of gliomas. *J Neurooncol*, 42(3):227–231, 1999.

[91] L. Hlatky, R. K. Sachs, M. Vazquez, and M. N. Cornforth. Radiation-induced chromosome aberrations: insights gained from biophysical modeling. *Bioessays*, 24(8):714–23, 2002.

[92] C. Holdsworth, M. Kim, J. Liao, and M. H. Phillips. A hierarchical evolutionary algorithm for multiobjective optimization in imrt. *Med Phys*, 37(9):4986–97, 2010.

[93] C. H. Holdsworth, D. Corwin, R. D. Stewart, R. Rockne, A. D. Trister, K. R. Swanson, and M. Phillips. Adaptive IMRT using a multiobjective evolutionary algorithm integrated with a diffusion-invasion model of glioblastoma. *Phys Med Biol*, 57(24):8271–83, 2012.

[94] R. P. Holloway and R. G. Dale. Theoretical implications of incorporating relative biological effectiveness into radiobiological equivalence relationships. *The British journal of radiology*, 86(1022):20120417, 2013.

[95] A. Z. Hyun and P. Macklin. Improved patient-specific calibration for agent-based cancer modeling. *J Theor Biol*, 317:422–4, 2013.

[96] E. P. M. Jansen, L. G. H. Dewit, M. van Herk, and H. Bartelink. Target volumes in radiotherapy for high-grade malignant glioma of the brain. *Radiotherapy and Oncology*, 56:151–156, 2000.

[97] S. Jbabdi, E. Mandonnet, H. Duffau, L. Capelle, K. R. Swanson, M. Pelegrini-Issac, R. Guillevin, and H. Benali. Simulation of anisotropic growth of low-grade gliomas using diffusion tensor imaging. *Magnetic Resonance in Medicine*, 54(3):616–24, 2005.

[98] R. Jena, S. J. Price, C. Baker, S. J. Jefferies, J. D. Pickard, J. H. Gillard, and N. G. Burnet. Diffusion tensor imaging: possible implications for radiotherapy treatment planning of patients with high-grade glioma. *Clin Oncol (R Coll Radiol)*, 17(8):581–90, 2005.

[99] J. Jeong, K. I. Shoghi, and J. O. Deasy. Modelling the interplay between hypoxia and proliferation in radiotherapy tumour response. *Phys Med Biol*, 58(14):4897–919, 2013.

[100] B. N. Joe, M. B. Fukui, C. C. Meltzer, Q. Haung, R. S. Day, P. J. Greer, and M. E. Bozik. Brain tumor volume measurement: comparison of manual and semiautomated methods. *Radiology*, 212:811–816, 1999.

[101] D. Johnson, S. McKeever, G. Stamatakos, D. Dionysiou, N. Graf, V. Sakkalis, K. Marias, Z. Wang, and T. S. Deisboeck. Dealing with diversity in computational cancer modeling. *Cancer Inform*, 12:115–24, 2013.

[102] M. Joiner and A. van der Kogel. *Basic clinical radiobiology*. Hodder Arnold ;, London, 4th edition, 2009.

[103] B. Jones and R. G. Dale. Mathematical models of tumour and normal tissue response. *Acta Oncol*, 38(7):883–93, 1999.

[104] B. Jones and R.G. Dale. Cell loss factors and the linear-quadratic model. *Radiother Oncol*, 37:136–139, 1995.

[105] J.B. Keller, D.W. McLaughlin, and G.C. Papanicolaou, editors. *Diffusion in random media*, volume I, pages 205–254. Plenum Press, New York, 1995.

[106] C. J. Kelly and M. Brady. A model to simulate tumour oxygenation and dynamic [18F]-Fmiso PET data. *Phys Med Biol*, 51(22):5859–73, 2006.

[107] S. J. Kiebel, J. Ashburner, J. B. Poline, and K. J. Friston. Mri and pet coregistration–a cross validation of statistical parametric mapping and automated image registration. *Neuroimage*, 5(4 Pt 1):271–9, 1997.

[108] Y. Kim and W. A. Tom. Dose-painting imrt optimization using biological parameters. *Acta Oncol*, 49(8):1374–84, 2010.

[109] Y. S. Kim, S. H. Kim, J. Cho, J. W. Kim, J. H. Chang, D. S. Kim, K. S. Lee, and C. O. Suh. MGMT gene promoter methylation as a potent prognostic factor in glioblastoma treated with temozolomide-based chemoradiotherapy: a single-institution study. *Int J Radiat Oncol Biol Phys*, 84(3):661–7, 2012.

[110] N. F. Kirkby, N. G. Burnet, and D. B. F. Faraday. Mathematical modelling of the response of tumour cells to radiotherapy. *Nuclear Instruments & Methods in Physics Research Section B-Beam Interactions with Materials and Atoms*, 188:210–215, 2002.

[111] J. P. Kirkpatrick, D. J. Brenner, and C. G. Orton. Point/counterpoint. the linear-quadratic model is inappropriate to model high dose per fraction effects in radiosurgery. *Med Phys*, 36(8):3381–4, 2009.

[112] J. P. Knisely and S. Rockwell. Importance of hypoxia in the biology and treatment of brain tumors. *Neuroimaging Clin N Am*, 12(4):525–36, 2002.

[113] W. J. Koh, J. S. Rasey, M. L. Evans, J. R. Grierson, T. K. Lewellen, M. M. Graham, K. A. Krohn, and T. W. Griffin. Imaging of hypoxia in human tumors with [f-18]fluoromisonidazole. *Int J Radiat Oncol Biol Phys*, 22(1):199–212, 1992.

[114] E Konukoglu. *Modeling Glioma Growth and Personalizing Growth Models in Medical Images*. Ph.D., University of Nice, 2009.

[115] E. Konukoglu, O. Clatz, P. Y. Bondiau, H. Delingette, and N. Ayache. Extrapolating glioma invasion margin in brain magnetic resonance images: suggesting new irradiation margins. *Medical image analysis*, 14(2):111–25, 2010.

[116] E. Konukoglu, O. Clatz, P. Y. Bondiau, M. Sermesant, H. Delingette, and N. Ayache. Towards an identification of tumor growth parameters from time series of images. *Med Image Comput Comput Assist Interv Int Conf Med Image Comput Comput Assist Interv*, 10(Pt 1):549–56, 2007.

[117] S.P. Lee, M.Y. Leu, J.B. Smathers, W.H. McBride, R.G. Parker, and H.R. Withers. Biologically effective dose distribution based on the linear quadratic model and its clinical relevance. *Int J Radiat Oncol Biol Phys*, 33(2):375–389, 1995.

[118] Randall J. LeVeque. *Finite volume methods for hyperbolic problems*. Cambridge texts in applied mathematics. Cambridge University Press, Cambridge ; New York, 2002.

[119] Randall J. LeVeque. *Finite difference methods for ordinary and partial differential equations : steady-state and time-dependent problems*. Society for Industrial and Applied Mathematics, Philadelphia, PA, 2007.

[120] B. C. Liang. Effects of hypoxia on drug resistance phenotype and genotype in human glioma cell lines. *J Neurooncol*, 29(2):149–55, 1996.

[121] J. L. Lim and M. S. Berridge. An efficient radiosynthesis of [18f]fluoromisonidazole. *Appl Radiat Isot*, 44(8):1085–91, 1993.

[122] D.N Louis, H. Ohgaki, O.D. Wiestler, and W.K. Cavenee. *WHO Classification of Tumours of the Central Nervous System*. Renouf Publishing Co. Ltd, Geneva, Switzerland, 4th edition, 2007.

[123] D. R. MacDonald, T. L. Cascino, Jr. Schold, S. C., and J. G. Cairncross. Response criteria for phase II studies of supratentorial malignant glioma. *J Clin Oncol*, 8(7):1277–80, 1990.

[124] E. Mandonnet, P. Brot, K. R. Swanson, A. F. Carpentier, J. Y. Delattre, and L. Capelle. Linear growth of mean tumor diameter in low grade gliomas. *Neurology*, 58:A13–A13, Suppl 3, 2002.

[125] E. Mandonnet, J. Y. Delattre, M. L. Tanguy, K. R. Swanson, A. F. Carpentier, H. Duffau, P. Cornu, R. Van Effenterre, Jr. Alvord, E. C., and L. Capelle. Continuous growth of mean tumor diameter in a subset of grade II gliomas. *Ann Neurol*, 53(4):524–528, 2003.

[126] E. Mandonnet, J. Pallud, O. Clatz, L. Taillandier, E. Konukoglu, H. Duffau, and L. Capelle. Computational modeling of the who grade ii glioma dynamics: principles and applications to management paradigm. *Neurosurg Rev*, 31(3):263–9, 2008.

[127] MATLAB. *The MathWorks, Inc.*, 2013.

[128] H. McAneney and S. F. O'Rourke. Investigation of various growth mechanisms of solid tumour growth within the linear-quadratic model for radiotherapy. *Phys Med Biol*, 52(4):1039–54, 2007.

[129] F. L. Moghaddasi, E. Bezak, and L. Marcu. In silico modelling of tumour margin diffusion and infiltration: review of current status. *Comput Math Methods Med*, 2012:16, 2012.

[130] L. Moghaddasi, E. Bezak, and L. G. Marcu. Current challenges in clinical target volume definition: tumour margins and microscopic extensions. *Acta Oncol*, 51(8):984–95, 2012.

[131] J. D. Murray. *Asymptotic analysis*. Applied mathematical sciences. Springer-Verlag, New York, [springer edition, 1984.

[132] J. D. Murray. *Mathematical biology I: an introduction*, volume 1. Springer-Verlag, New York, 3rd edition, 2002.

[133] J. D. Murray. *Mathematical Biology II. Spatial Models and Biological Applications*, volume 2. Springer-Verlag, New York, 3rd edition, 2003.

[134] M. L. Neal and R. Kerckhoffs. Current progress in patient-specific modeling. *Brief Bioinform*, 11(1):111–26, 2010.

[135] M. L. Neal, A. D. Trister, S. Ahn, A. Baldock, C. A. Bridge, L. Guyman, J. Lange, R. Sodt, T. Cloke, A. Lai, T. F. Cloughesy, M. M. Mrugala, J. K. Rockhill, R. C. Rockne, and K. R. Swanson. Response classification based on a minimal model of glioblastoma growth is prognostic for clinical outcomes and distinguishes progression from pseudoprogression. *Cancer Res*, 73(10):2976–86, 2013.

[136] M. L. Neal, A. D. Trister, T. Cloke, R. Sodt, S. Ahn, A. L. Baldock, C. A. Bridge, A. Lai, T. F. Cloughesy, M. M. Mrugala, J. K. Rockhill, R. C. Rockne, and K. R. Swanson. Discriminating survival outcomes in patients with glioblastoma using a simulation-based, patient-specific response metric. *PLoS One*, 8(1):e51951, 2013.

[137] S. J. Nelson and S. Cha. Imaging glioblastoma multiforme. *Cancer J*, 9(2):134–45, 2003.

[138] A. R. Padhani and L. Ollivier. The RECIST (Response Evaluation Criteria in Solid Tumors) criteria: implications for diagnostic radiologists. *Brit J Radiol*, 74(887):983–6, 2001.

[139] J. Pallud, M. Blonski, E. Mandonnet, E. Audureau, D. Fontaine, N. Sanai, L. Bauchet, P. Peruzzi, M. Frenay, P. Colin, R. Guillevin, V. Bernier, M. H. Baron, J. Guyotat, H. Duffau, L. Taillandier, and L. Capelle. Velocity of tumor spontaneous expansion predicts long-term outcomes for diffuse low-grade gliomas. *Neuro Oncol*, 15(5):595–606, 2013.

[140] J. Pallud, E. Mandonnet, H. Duffau, M. Kujas, R. Guillevin, D. Galanaud, L. Taillandier, and L. Capelle. Prognostic value of initial magnetic resonance imaging growth rates for World Health Organization grade II gliomas. *Ann Neurol*, 60(3):380–3, 2006.

[141] A. K. Paulsson, K. P. McMullen, A. M. Peiffer, W. H. Hinson, W. T. Kearns, A. J. Johnson, G. J. Lesser, T. L. Ellis, S. B. Tatter, W. Debinski, E. G. Shaw, and M. D. Chan. Limited margins using modern radiotherapy techniques does not increase marginal failure rate of glioblastoma. *Am J Clin Oncol*, 2012.

[142] W. B. Pope, J. Sayre, A. Perlina, J. P. Villablanca, P. S. Mischel, and T. F. Cloughesy. MR imaging correlates of survival in patients with high-grade gliomas. *AJNR Am J Neuroradiol*, 26(10):2466–74, 2005.

[143] G. Powathil, M. Kohandel, S. Sivaloganathan, A. Oza, and M. Milosevic. Mathematical modeling of brain tumors: effects of radiotherapy and chemotherapy. *Phys Med Biol*, 52(11):3291–306, 2007.

[144] X. S. Qi, C. J. Schultz, and X. A. Li. An estimation of radiobiologic parameters from clinical outcomes for radiation treatment planning of brain tumor. *Int J Radiat Oncol Biol Phys*, 64(5):1570–80, 2006.

[145] E. C. Quant and P. Y. Wen. Response assessment in neuro-oncology. *Curr Oncol Rep*, 2010.

[146] V. Quaranta, A. M. Weaver, P. T. Cummings, and A. R. Anderson. Mathematical modeling of cancer: the future of prognosis and treatment. *Clin Chim Acta*, 357(2):173–9, 2005.

[147] J. G. Rajendran, K. R. Hendrickson, A. M. Spence, M. Muzi, K. A. Krohn, and D. A. Mankoff. Hypoxia imaging-directed radiation treatment planning. *Eur J Nucl Med Mol Imaging*, 33 Suppl 13:44–53, 2006.

[148] J. S. Rasey, J. J. Casciari, P. D. Hofstrand, M. Muzi, M. M. Graham, and L. K. Chin. Determining hypoxic fraction in a rat glioma by uptake of radiolabeled fluoromisonidazole. *Radiat Res*, 153(1):84–92, 2000.

[149] B. Ribba, T. Colin, and S. Schnell. A multiscale mathematical model of cancer, and its use in analyzing irradiation therapies. *Theor Biol Med Mod*, 3(7), 2006.

[150] R. Rockne, Jr. Alvord, E. C., J. K. Rockhill, and K. R. Swanson. A mathematical model for brain tumor response to radiation therapy. *J Math Biol*, 58(4-5):561–78, 2009.

[151] R. Rockne, J. K. Rockhill, M. Mrugala, A. M. Spence, I. Kalet, K. Hendrickson, A. Lai, T. Cloughesy, E. C. Alvord, and K. R. Swanson. Predicting the efficacy of radiotherapy in individual glioblastoma patients in vivo: a mathematical modeling approach. *Phys Med Biol*, 55(12):3271–3285, 2010.

[152] P. Romanelli, A. Conti, A. Pontoriero, G. K. Ricciardi, F. Tomasello, C. De Renzis, G. Innocenzi, V. Esposito, and G. Cantore. Role of stereotactic radiosurgery and fractionated stereotactic radiotherapy for the treatment of recurrent glioblastoma multiforme. *Neurosurg Focus*, 27(6):E8, 2009.

[153] R. K. Sachs and D. J. Brenner. The mechanistic basis of the linear-quadratic formalism. *Medical physics*, 25(10):2071–3, 1998.

[154] R. K. Sachs, P. Hahnfeld, and D. J. Brenner. The link between low-let dose-response relations and the underlying kinetics of damage production/repair/misrepair. *Int J Radiat Biol*, 72(4):351–74, 1997.

[155] R. K. Sachs, L. R. Hlatky, and P. Hahnfeldt. Simple ode models of tumor growth and anti-angiogenic or radiation treatment. *Mathematical and Computer Modelling*, 33:1297–1305, 2001.

[156] H. J. Scherer. The forms of growth in gliomas and their practical significance. *Brain*, 63:1–35, 1940.

[157] P. Schmitt, E. Mandonnet, A. Perdreau, and E. D. Angelini. Effects of slice thickness and head rotation when measuring glioma sizes on mri: in support of volume segmentation versus two largest diameters methods. *J Neurooncol*, 2013.

[158] V. A. Semenenko and R. D. Stewart. Fast monte carlo simulation of DNA damage formed by electrons and light ions. *Physics in Medicine and Biology*, 51(7):1693–706, 2006.

[159] J. Shao. Linear model selection by cross-validation. *J Amer Stat Assoc*, 88(422):486–494, 1993.

[160] E. G. Shaw, W. Seiferheld, C. Scott, C. Coughlin, S. Leibel, W. Curran, and M. Mehta. Reexamining the radiation therapy oncology group (RTOG) recursive partitioning analysis (RPA) for glioblastoma multiforme (GBM) patients. *Intl J Radiat Oncol Biol Phys*, 57(2, Supplement 1):S135–S136, 2003.

[161] J. P. Sheehan, M. E. Shaffrey, B. Gupta, J. Larner, J. N. Rich, and D. M. Park. Improving the radiosensitivity of radioresistant and hypoxic glioblastoma. *Future Oncol*, 6(10):1591–601, 2010.

[162] N. Shigesada and K. Kawasaki. *Biological Invasions: Theory and Practice*. Oxford University Press, Oxford, 1997.

[163] D. L. Silbergeld and M. R. Chicoine. Isolation and characterization of human malignant glioma cells from histologically normal brain. *J Neurosurg*, 86(3):525–531, 1997.

[164] D. L. Silbergeld, R. C. Rostomily, and Jr. Alvord, E. C. The cause of death in patients with glioblastoma is multifactorial: clinical factors and autopsy findings in 117 cases of supratentorial glioblastoma in adults. *J Neurooncol*, 10(2):179–85, 1991.

[165] R. D. Skeel and M. Berzins. A method for the spatial descretization of parabolic equations in one space variable. *J Sci Stat Comput*, 11(1):1–32, 1990.

[166] C. von Sonntag. *Free-radical-induced DNA damage and its repair : a chemical perspective*. Springer, Berlin, 2006.

[167] W. Sontag. Comparison of six different models describing survival of mammalian cells after irradiation. *Radiat Environ Biophys*, 29(3):185–201, 1990.

[168] M. Soret, S. L. Bacharach, and I. Buvat. Partial-volume effect in PET tumor imaging. *J Nucl Med*, 48(6):932–45, 2007.

[169] A. M. Spence, M. Muzi, K. R. Swanson, F. O'Sullivan, J. K. Rockhill, J.G. Rajendran, T.C.H. Adamsen, J. M. Link, P. E. Swanson, K.J. Yagle, R. C. Rostomily, D.L. Silbergeld, and K. Krohn. Regional hypoxia in glioblastoma multiforme quantified with [18f]fluoromisonidazole positron emission tomography before radiotherapy: correlation with time to progression and survival. *Clin Cancer Res*, 14(9):2623–2630, 2008.

[170] M. A. Stackhouse and J. S. Bedford. An ionizing radiation-sensitive mutant of CHO cells: irs-20. i. isolation and initial characterization. *Radiat Res*, 136(2):241–9, 1993.

[171] M. A. Stackhouse and J. S. Bedford. An ionizing radiation-sensitive mutant of CHO cells: irs-20. ii. dose-rate effects and cellular recovery processes. *Radiat Res*, 136(2):250–4, 1993.

[172] G. Stamatakos, V. P. Antipas, and N. K. Ozunoglu. A patient-specific in vivo tumor and normal tissue model for prediction of the response to radiotherapy. *Methods Inf Med*, 46(3):367–75, 2007.

[173] R. D. Stewart, V. K. Yu, A. G. Georgakilas, C. Koumenis, J. H. Park, and D. J. Carlson. Effects of radiation quality and oxygen on clustered dna lesions and cell death. *Radiat Res*, 176(5):587–602, 2011.

[174] R. Stupp and et al. Effects of radiotherapy with concomitant and adjuvant temozolomide versus radiotherapy alone on survival in glioblastoma in a randomised phase III study: 5-year analysis of the EORTC-NCIC trial. *Lancet Oncol*, 10(5):459–66, 2009.

[175] R. Stupp, W. P. Mason, M. J. van den Bent, M. Weller, B. Fisher, M. J. Taphoorn, K. Belanger, A. A. Brandes, C. Marosi, U. Bogdahn, J. Curschmann, R. C. Janzer, S. K. Ludwin, T. Gorlia, A. Allgeier, D. Lacombe, J. G. Cairncross, E. Eisenhauer, and R. O. Mirimanoff. Radiotherapy plus concomitant and adjuvant temozolomide for glioblastoma. *N Engl J Med*, 352(10):987–96, 2005.

[176] K. R. Swanson. *Mathematical Modeling of the Growth and Control of Tumors*. Ph.D., University of Washington, 1999.

[177] K. R. Swanson and Jr. Alvord, E. C. Serial imaging observations and postmortem examination of an untreated glioblastoma: A traveling wave of glioma growth and invasion. *Neuro-Oncol*, 4:340, 2002.

[178] K. R. Swanson, Jr. Alvord, E. C., and J. D. Murray. A quantitative model for differential motility of gliomas in grey and white matter. *Cell Prolif*, 33(5):317–329, 2000.

[179] K. R. Swanson, Jr. Alvord, E. C., and J. D. Murray. Quantifying efficacy of chemotherapy of brain tumors with homogeneous and heterogeneous drug delivery. *Acta Biotheoretica*, 50(4):223–237, 2002.

[180] K. R. Swanson, Jr. Alvord, E. C., and J. D. Murray. Virtual brain tumours (gliomas) enhance the reality of medical imaging and highlight inadequacies of current therapy. *Brit J Cancer*, 86(1):14–18, 2002.

[181] K. R. Swanson, C. Bridge, J. D. Murray, and Jr. Alvord, E. C. Virtual and real brain tumors: using mathematical modeling to quantify glioma growth and invasion. *J Neurol Sci*, 216(1):1–10, 2003.

[182] K. R. Swanson, G. Chakraborty, C. H. Wang, R. Rockne, H. L. Harpold, M. Muzi, T. C. Adamsen, K. A. Krohn, and A. M. Spence. Complementary but distinct roles for MRI and 18F-fluoromisonidazole PET in the assessment of human glioblastomas. *J Nucl Med*, 50(1):36–44, 2009.

[183] K. R. Swanson, H. L. Harpold, D. L. Peacock, R. Rockne, C. Pennington, L. Kilbride, R. Grant, J. M. Wardlaw, and Jr. Alvord, E. C. Velocity of radial expansion of contrast-enhancing gliomas and the effectiveness of radiotherapy in individual patients: a proof of principle. *Clin Oncol (R Coll Radiol)*, 20(4):301–8, 2008.

[184] K. R. Swanson, J. D. Murray, Jr. Alvord, E. C., and R. Rockne. Method and system for characterizing tumors. US 12/709,367(US20110208490 A1):Aug 25, 2011, 2013.

[185] K. R. Swanson, R. C. Rockne, J. Claridge, M. A. Chaplain, Jr. Alvord, E. C., and A. R. Anderson. Quantifying the role of angiogenesis in malignant progression of gliomas: in silico modeling integrates imaging and histology. *Cancer Res*, 71(24):7366–75, 2011.

[186] M. D. Szeto, G. Chakraborty, J. Hadley, R. Rockne, M. Muzi, Jr. Alvord, E. C., K. A. Krohn, A. M. Spence, and K. R. Swanson. Quantitative metrics of net proliferation and invasion link biological aggressiveness assessed by MRI with hypoxia assessed by FMISO-PET in newly diagnosed glioblastomas. *Cancer Res*, 69(10):4502–9, 2009.

[187] W. Taal, D. Brandsma, H. G. de Bruin, J. E. Bromberg, A. T. Swaak-Kragten, P. A. Smitt, C. A. van Es, and M. J. van den Bent. Incidence of early pseudo-progression in a cohort of malignant glioma patients treated with chemoirradiation with temozolomide. *Cancer*, 113(2):405–10, 2008.

[188] R. Taleei and H. Nikjoo. The non-homologous end-joining (NHEJ) pathway for the repair of DNA double-strand breaks: I. a mathematical model. *Radiat Res*, 179(5):530–9, 2013.

[189] M. L. Tanaka, W. Debinski, and I. K. Puri. Hybrid mathematical model of glioma progression. *Cell Prolif*, 2009.

[190] PMOD Technologies. Pfus, 2010.

[191] P. Therasse, E. A. Eisenhauer, and J. Verweij. RECIST revisited: a review of validation studies on tumour assessment. *Eur J Cancer*, 42(8):1031–9, 2006.

[192] J. Thibault, S. Bergeron, and H. W. Bonin. On finite-difference solutions of the heat equation in spherical coordinates. *Numerical Heat Transfer*, 12(4):457–474, 1987.

[193] J. P. Tian, A. Friedman, J. Wang, and E. A. Chiocca. Modeling the effects of resection, radiation and chemotherapy in glioblastoma. *J Neurooncol*, 91(3):287–93, 2009.

[194] B. Titz and R. Jeraj. An imaging-based tumour growth and treatment response model: investigating the effect of tumour oxygenation on radiation therapy response. *Phys Med Biol*, 53(17):4471–88, 2008.

[195] A. Toma, K. Holl-Ulrich, S. Becker, A. Mang, T. A. Schtz, M. M. Bonsanto, V. Tronnier, and T. M. Buzug. A mathematical model to simulate glioma growth and radiotherapy at the microscopic level. *Biomed Tech (Berl)*, 57 Suppl 1, 2012.

[196] P. Tracqui, G. C. Cruywagen, D. E. Woodward, G. T. Bartoo, J. D. Murray, and Jr. Alvord, E. C. A mathematical model of glioma growth: the effect of chemotherapy on spatio-temporal growth. *Cell Prolif*, 28(1):17–31, 1995.

[197] C. Tsien, D. Gomez-Hassan, T. L. Chenevert, J. Lee, T. Lawrence, R. K. Ten Haken, L. R. Junck, B. Ross, and Y. Cao. Predicting outcome of patients with high-grade gliomas after radiotherapy using quantitative analysis of t1-weighted magnetic resonance imaging. *Int J Radiat Oncol Biol Phys*, 67(5):1476–83, 2007.

[198] C. Tsien, D. Gomez-Hassan, R. K. Ten Haken, D. Tatro, L. Junck, T. L. Chenevert, and T. Lawrence. Evaluating changes in tumor volume using magnetic resonance imaging during the course of radiotherapy treatment of high-grade gliomas: Implications for conformal dose-escalation studies. *Int J Radiat Oncol Biol Phys*, 62(2):328–32, 2005.

[199] R. G. Verhaak and et al. Integrated genomic analysis identifies clinically relevant subtypes of glioblastoma characterized by abnormalities in PDGFRA, IDH1, EGFR, and nf1. *Cancer Cell*, 17(1):98–110, 2010.

[200] M. J. Vos, B. M. J. Uitdehaag, F. Barkhof, J. J. Heimans, H. C. Baayen, W. Boogerd, J. A. Castelijns, P. H. M. Elkhuizen, and T. J. Postma. Interobserver variability in the radiological assessment of response to chemotherapy in glioma. *Neurology*, 60(5):826–830, 2003.

[201] C. H. Wang, J. K. Rockhill, M. Mrugala, D. L. Peacock, A. Lai, K. Jusenius, J. M. Wardlaw, T. Cloughesy, A. M. Spence, R. Rockne, Jr. Alvord, E. C., and K. R. Swanson. Prognostic significance of growth kinetics in newly diagnosed glioblastomas revealed by combining serial imaging with a novel biomathematical model. *Cancer Res*, 69(23):9133–40, 2009.

[202] J. Z. Wang, Z. Huang, S. S. Lo, W. T. Yuh, and N. A. Mayr. A generalized linear-quadratic model for radiosurgery, stereotactic body radiation therapy, and high-dose rate brachytherapy. *Sci Transl Med*, 2(39):39ra48, 2010.

[203] Y. X. Wang, A. D. King, H. Zhou, S. F. Leung, J. Abrigo, Y. L. Chan, C. W. Hu, D. K. Yeung, and A. T. Ahuja. Evolution of radiation-induced brain injury: MR imaging-based study. *Radiology*, 254(1):210–8, 2010.

[204] R. Wasserman, R. Acharya, C. Sibata, and K. H. Shin. A patient-specific in vivo tumor model. *Mathematical Biosciences*, 136(2):111–140, 1996.

[205] R. L. Wells and J. S. Bedford. Dose-rate effects in mammalian cells. iv. repairable and nonrepairable damage in noncycling c3h 10t 1/2 cells. *Radiat Res*, 94(1):105–34, 1983.

[206] P. Y. Wen and S. Kesari. Malignant gliomas in adults. *N Engl J Med*, 359(5):492–507, 2008.

[207] P. Y. Wen, A. D. Norden, J. Drappatz, and E. Quant. Response assessment challenges in clinical trials of gliomas. *Curr Oncol Rep*, 12(1):68–75, 2010.

[208] T. E. Yankeelov, N. Atuegwu, D. Hormuth, J. A. Weis, S. L. Barnes, M. I. Miga, E. C. Rericha, and V. Quaranta. Clinically relevant modeling of tumor growth and treatment response. *Sci Transl Med*, 5(187):187ps9, 2013.

[209] L. Zhang, L. L. Chen, and T. S. Deisboeck. Multi-scale, multi-resolution brain cancer modeling. *Math Comput Simul*, 79(7):2021–2035, 2009.

VITA

Russell Christian Rockne

Current position

Research Associate

Department of Neurological Surgery

Northwestern University

Chicago, IL

Education

Ph.D. Applied Mathematics, University of Washington, Seattle, WA 2013

M.S. Applied Mathematics,University of Washington, Seattle, WA 2006

B.S. Mathematics, Fine Art, University of Colorado, Boulder, CO 2002

Professional Experience

2012 – present Research Associate, Department of Neurological Surgery

Northwestern University, Chicago, IL

2006 – 2012 Research Scientist, Departments of Pathology and Applied Mathematics

University of Washington, Seattle, WA

2002 – 2004 Mathematics Instructor, Edmonds Community College, Privett Academy

Seattle, WA

Professional Society Memberships

European Society for Theoretical and Mathematical Biology (ESTMB)

Society of Mathematical Biology (SMB)

Society of Industrial and Applied Mathematics (SIAM)

Society for Neuro-Oncology (SNO)

Society for Nuclear Medicine (SNM)

American Mathematical Society (AMS)

Radiation Research Society (RRS)

American Association for Cancer Research (AACR)

Awards

1. Roberts prize nominee

   Top 10 paper of the year for Physics in Medicine and Biology 2011

   Rockne, R, Rockhill JK, Mrugala M, Spence AM, Kalet I, Hendrickson K, Lai A, Cloughsey T, Alvord EC Jr., Swanson KR: Predicting the efficacy of radiotherapy in individual glioblastoma patients in vivo: a mathematical modeling approach. *Physics in Medicine and Biology*, 55: 3271-3285 2010.
   PubMed ID: 20484781

2. Best Abstract 2011

   36th Annual Western Regional Society for Nuclear Medicine
   Rockne R, Champley K, Alessio A, Muzi M, Krohn KA, Kinahan PE, Swanson KR. Patient-specific simulations allow prediction of hypoxia and [18F]FMISO-PET in human glioblastoma. Seattle, WA

3. Clinical research paper of the year 2009

   Swanson KR, Chakraborty G, Wang CH, Rockne R, Harpold HLP, Muzi M, Anderson TCH, Krohn KA, Spence AM: Complimentary but Distinct Roles for MRI and 18F-Fluoromisonidazole PET in the Assessment of Human Glioblastomas. *Journal of Nuclear Medicine*, 50: 36-44 2009.
   PubMed ID: 19091885

4. Landahl Travel Award 2008

   European Society for Theoretical and Mathematical Biology (ESMTB) Annual Meeting in Edinburgh Scotland

5. Landahl Travel Award 2013

   Society for Mathematical Biology (SMB) Annual Meeting in Phoenix Arizona

Patents Filed

Method and system for characterizing tumors
K. R. Swanson. E. C. Alvord, Jr., J. D. Murray, R. Rockne
Application #: US 12/709,367

Articles - Peer Reviewed

1. Rockne R, Alvord EC Jr., Rockhill J K, Swanson K R: A mathematical model for brain tumor response to radiation therapy. *Journal of Mathematical Biology*, Special Issue on Computational Oncology, 2009 58(4-5):561-78
   PubMed ID: 18815786

2. Rockne R, Alvord E C Jr., Reed P, Swanson K R: Modeling the growth and invasion of gliomas, from simple to complex: the Goldie Locks paradigm. BIOMAT 2007 International Symposium on Mathematical and Computational Biology. Ed. Mondaini R. 2008 World Scientific

3. Swanson K R, Harpold H L P, Peacock D L, Rockne R, Pennington C, Kilbride L, Grant R, Wardlaw J, Alvord E C, Jr. Velocity of Radial Expansion of Contrast-Enhancing Gliomas and Effectiveness of Radiotherapy in Individual Patients: A Proof of Principle. *Clinical Oncology*, 2008 20: 301-308
   PubMed ID: 18308523

4. Swanson KR, Chakraborty G, Wang CH, Rockne R, Harpold HLP, Muzi M, Anderson TCH, Krohn KA, Spence AM: Complimentary but Distinct Roles for MRI and 18F-Fluoromisonidazole PET in the Assessment of Human Glioblastomas. *Journal of Nuclear Medicine*, 2009 50: 36-44.
PubMed ID: 19091885

5. Szeto MD, Chakraborty G, Hadley J, Rockne R, Muzi M, Alvord E C Jr., Krohn K, Spence A M, Swanson K R: Quantitative Metrics of Net Proliferation and Invasion Link Biological Aggressiveness Assessed by MRI with Hypoxia Assessed by FMISO-PET in Newly Diagnosed Glioblastomas. *Cancer Research*, 2009 69(10):4502-9
PubMed ID: 19934335

6. Wang C, Rockhill JK, Mrugala M, Peacock DL, Lai A, Jusenius K, Wardlaw JM, Cloughesy T, Spence AM, Rockne R, Alvord EC Jr., Swanson KR: Prognostic significance of growth kinetics in newly diagnosed glioblastomas revealed by combining serial imaging with a novel bio-mathematical model. *Cancer Research*, 2009 69(23): 9133-9140
PubMed ID: 19366800

7. Assefa M, Rockne R, Szeto M, Swanson KR. Mathematical Modeling of Glioma Proliferation and Diffusion. *Ethnicity and Disease*, 2009 19:2, Supplement 3
PubMed ID: 19554787

8. Swanson KR, Chakraborty G, Wang CH, Rockne R, Harpold HLP, Muzi M, Anderson TCH, Krohn KA, Spence AM: Complimentary but Distinct Roles for MRI and 18F-Fluoromisonidazole PET in the Assessment of Human Glioblastomas. *Journal of Nuclear Medicine*, 2009 50: 36-44.
PubMed ID: 19091885

9. Rockne, R, Rockhill JK, Mrugala M, Spence AM, Kalet I, Hendrickson K, Lai A, Cloughsey T, Alvord EC Jr., Swanson KR: Predicting the efficacy of radiotherapy in

individual glioblastoma patients in vivo: a mathematical modeling approach. *Physics in Medicine and Biology*, 2010 55: 3271-3285.
PubMed ID: 20484781
*Roberts prize nominee for paper of the year 2010

10. Basanta D, Scott JG, Rockne R, Swanson KR, Anderson ARA: The role of IDH1 mutated tumor cells in secondary glioblastomas: an evolutionary game theoretical view. *Physical Biology.* 8(2011)
PubMed ID: 21301070

11. Bohman LE, Swanson KR, Moore JL, Rockne R, Mandigo C, Hankinson T, Assanah M, Canoll P, Bruce JN. Preoperative MRI Characteristics of Glioblastoma Multiforme: Implications for Understanding Glioma Ontogeny. *Neurosurgery*, 67(5):1319-27, 2010
PubMed ID: 20871424

12. Gu S, Chakraborty G, Champley K, Alessio A, Claridge J, Rockne R, Muzi M, Krohn KA, Spence AM, Alvord EC Jr., Anderson ARA, Kinahan P, Swanson KR. Applying A Patient-Specific Bio-Mathematical Model of Glioma Growth to Develop Virtual [18F]-FMISO PET Images. Mathematics in Medicine and Biology 2011 DOI: 10.1093/imammb/dqr002 In: *Computation modeling in cancer special double issue: IMA Mathematical Medicine and Biology.* Ed. Rejniak K, Anderson ARA.
PubMed ID: 21562060

13. Swanson KR, Rockne R, Claridge J, Chaplain MA, Alvord EC Jr., Anderson ARA. Quantifying the role of angiogenesis in malignant progression of gliomas: In silico modeling integrates imaging and histology. *Cancer Research.* 71(24):7366-75, 2011
PubMed ID: 21900399

14. Sodt R, Rockne R, Neal M L, Kalet I, Swanson K R. Quantifying the role of anisotropic invasion in human glioblastoma. Accepted *in press*

15. Alvord E C, Jr., Rockne R, Rockhill J K, Mrugala M M, Rostomily R, Lai A, Cloughessy T, Wardlaw J M, Spence A M, Swanson K R. Know thy enemy: Paradoxes to be exploited in the war against glioblastoma. *Submitted*

16. Holdsworth C, Corwin D, Stewart R D, Rockne R C, Trister A D, Swanson K R, Philips M. Adaptive IMRT using a multiobjective evolutionary algorithm integrated with a diffusion-invasion model of glioblastoma. *Physics in Medicine and Biology*, 57(24):8271-83, Nov 2012
PubMed ID: 23190554

17. Neal M L, Trister A D, Cloke T, Sodt R, Ahn S, Baldock A L, Bridge C, Lai A, Cloughesy T, Mrugala M, Rockhill J K, Rockne R C, Swanson K R. Discriminating survival outcomes in patients with glioblastoma using a simulation-based, patient-specific response metric. 8(1): e51951 *PLOS One*, Jan 2013
PubMedID: 23372647

18. Neal M L, Trister A D, Ahn S, Baldock A L, Bridge C A, Guyman L, Lange J, Sodt R, Cloke T, Lai A, Cloughesy T, Mrugala M M, Rockhill J K, Rockne R C, Swanson K R. Response classification based on a minimal model of glioblastoma growth is prognostic for clinical outcomes and distinguishes progression from pseudoprogression. *Cancer Research*, 3588 Feb 2013
PubMedID: 23400596

19. Baldock A, Rockne R, Boone A, Neal M, Bridge C, Guyman L, Hawkins-Daarud H, Corwin D, Mrugala M M, Rockhill J K, Swanson K R. From Patient-Specific Mathematical Neuro-Oncology to Precision Medicine. *Frontiers in Molecular and Cellular Oncology.* doi: 10.3389/fonc.2013.00062, Mar 2013

20. Hawkins-Daarud A, Rockne R C, Anderson A R A, Swanson K R. Modeling tumor-associated edema in gliomas during anti-angiogenic therapy and its impact on imageable tumor. *Frontiers in Molecular and Cellular Oncology.* doi: 10.3389/fonc.2013.00066, Mar 2013

21. Corwin D, Holdsworth C, Rockne R C, Trister A D, Mrugala M M, Rockhill J K, Stewart R D, Phillips M, Swanson K R. Patient-specific, biologically optimized IMRT plans for the treatment of glioblastoma. *In revision*

22. Massey S, Rockne R C, Canoll P, Swanson K R. Differential chemotaxis of tumor cells to platelet-derived growth factor in murine gliomas.*In final preparation*

23. Rockne R C, Trister A D, Neal M L, Hendrickson K, Mrugala M M, Rockhill J K, Krohn K, Swanson K R. Quantifying hypoxia-modulated radiation-resistance in human glioblastoma in vivo. *Submitted*

Contributed Works

1. Rockne R, Alvord EC Jr., Szeto M, Gu S, Chakraborty G, Swanson KR: Modeling Diffusely Invading Brain Tumors: An Individualized Approach to Quantifying Glioma Evolution and Response to Therapy. In: Selected Topics in Cancer Modeling: Genesis, Evolution, Immune Competition, and Therapy. Ed. Bellomo N, Chaplain M, de Angelis E. Birkhauser, Boston MA. 2008 ISBN-13 13 978-0817647124

2. Chakraborty G, Sodt R, Massey S, Gu S, Rockne R, Alvord EC Jr., Swanson KR. Bridging from Multi-scale Modeling to Practical Clinical Applications in the Study of Human Gliomas. In: Multiscale Cancer Modeling. Ed. Deisboeck T, Stamatakos G. CRC Press. ISBN-10 1439814406

Theses

A Mathematical Model for Brain Tumor Response to Radiation Therapy.
Masters in Applied Mathematics
University of Washington, Seattle, WA, 2006.
Advisor: Kristin R. Swanson Ph.D.

Theses cont.

Towards Patient-Specific Mathematical Radiation Oncology

Doctor of Philosophy in Applied Mathematics

University of Washington, Seattle, WA, 2013.

Advisor: Kristin R. Swanson Ph.D.

Minisymposia

2013 Society for Mathematical Biology Annual Meeting

Title: Mathematical Radiation Oncology

R. C. Rockne Chair

A. D. Trister Speaker

H. Enderling Speaker

X. Gao Speaker

Graduate Course Work

Applied Linear Analysis, Numerical Methods, Mathematical Ecology, Mathematical Biology, Stochastic Methods, Scientific Computing, Advanced Methods for ODEs, PDEs, Finite Volume Methods, Fluid Mechanics, Optimization, Biomedical Imaging & Contrast Agents, Perturbations and Asymptotic Analysis

Current Research Support

7/01/2009 – 6/30/2014 NIH (R01)

Novel Tools for Evaluation and Prediction of Radiotherapy Response

in Individual Glioma Patients

PI: K. R. Swanson

9/01/2009 – 8/31/2014 NIH/NCI Physical Sciences Oncology Center (U54)

PD: R. Gatenby (Moffitt Cancer Center), PI: K. R. Swanson

Current Research Support cont.

6/01/2011 – 5/31/2014 James S. McDonnell Foundation Collaborative Activity Award Brain Oncology Network of Knowledge (BONK)"
MPIs: K. R. Swanson, P. Canoll, (Columbia), A. R. A. Anderson. (Moffitt)

9/27/2011 – 9/31/2016 NIH (R01)
UVIC: Untreated virtual imaging control
MPIs: K. R. Swanson, P. Kinahan